FLOW PATTERNS AROUND GROYNES IN THE COASTAL ZONE

by

PierLuigi Antonio Lucca

Submitted in fulfilment of the requirements for the degree of
Master of Science in Engineering
In the
Civil Engineering Programme
College of Agriculture, Engineering and Science, University of KwaZulu-Natal
Durban
2013

Supervisor: Professor D.D. Stretch

PREFACE

As the candidate's Supervisor I agree/do not agree to the submission of this thesis.

……. …….

Prof D.D Stretch Date

COLLEGE OF AGRICULTURE, ENGINEERING AND SCIENCE

DECLARATION - PLAGIARISM

I, PierLuigi Antonio Lucca, declare that

1. The research reported in this thesis, except where otherwise indicated, is my original research.
2. This thesis has not been submitted for any degree or examination at any other university.
3. This thesis does not contain other persons' data, pictures, graphs or other information, unless specifically acknowledged as being sourced from other persons.
4. This thesis does not contain other persons' writing, unless specifically acknowledged as being sourced from other researchers. Where other written sources have been quoted, then:

a. Their words have been re-written but the general information attributed to them has been referenced

b. Where their exact words have been used, then their writing has been placed in italics and inside quotation marks, and referenced.

5. This thesis does not contain text, graphics or tables copied and pasted from the Internet, unless specifically acknowledged, and the source being detailed in the thesis and in the References sections.

……. …….

P. L. A. Lucca Date

ACKNOWLEDGEMENTS

I would like to express my acknowledgement of the following:

My family for their support over the last two years.

Justin Pringle for his help in the field and the debates in the office.

eThekwini Municipality Coastal Department for providing bathymetry surveys of the Durban Beach front. Thank you, in providing permission to carry out the testing on the Durban beach front.

eThekwini Chair and supervisor, Professor D.D Stretch for the subsistence funding and his continual advice on the research.

National Research Foundation (NRF) for their scarce skills scholarship that was received for post graduate studies. The financial assistance of the National Research Foundation (NRF) towards this research is hereby acknowledged. Opinions expressed and conclusions arrived at, are those of the author and are not necessarily to be attributed to the NRF.

SA National Port Authority for their wave data near the Durban Harbour.

Environmental Mapping and Surveying (EMS) for the use of their custom built instrumentation. A special thanks to Zane Thackeray and Rio Leuci who went above and beyond to help with the required data collection.

SA lifesaving, for the use of their motorized boats at the Durban Beach front

South African Weather Service for their contribution in providing wind data.

ABSTRACT

Semi-permeable groynes are used to modulate the long-shore transport for beach management purposes, but the optimal design of these structures remains unresolved. This in part is due to their ability to behave as both a permeable and an impermeable structure.

A 2D depth-averaged flow model for an isolated groyne was developed to undertake a parametric study to investigate the characteristic flow patterns and how these flow patterns change under different conditions. These include various constrictions to the alongshore flow; changing water levels, groyne permeability, and geometric parameters. The flow model was coupled with a spectral wave model to simulate wave-driven flow near the groyne. The alongshore tip velocities, cross-shore rip currents and the flow separation length were analysed for different wave conditions and groyne lengths. A method was developed to model the permeability of the groyne by manipulating friction that impeded the through-flow. This was compared with an alternative model using a permeable pile screen.

Parametric studies using the models show how flow patterns are sensitive to changes in permeability and the geometry of the groyne but also sensitive to the level of constriction of cross-sectional flow. The level of constriction is the ratio of the groyne length to the width of the breaker zone. The change in constriction affects the predominant flow pattern at the tip of the groyne, where either the cross-shore or alongshore current velocity is larger. Alongshore current tip velocities increase and rip current velocities decrease when the constriction is low and vice versa when the constriction is high. Changes in the permeability of the structure also significantly affect the circulation patterns - the influence of the groyne's constriction reduces as permeability increases.

Field measurements were carried out in Durban, South Africa. An array of current meters was deployed to map the flow field around an existing groyne for comparison with the numerical simulations from the parametric studies. Groyne tip velocities, rip currents, separation length and velocity vectors were consistent with the flow patterns from the simulations. Severe scour has been observed near groyne tips at the case study site. This can be explained in terms of the above-mentioned flow patterns and how they change for different wave and tide conditions. The observed flows are shown to be sufficient to cause bedload sediment transport around the groyne.

TABLE OF CONTENTS

PREFACE ii

ACKNOWLEDGEMENTS iii

ABSTRACT iv

TABLE OF CONTENTS v

LIST OF FIGURES xii

LIST OF TABLES xxiii

LIST OF SYMBOLS xxvi

CHAPTER 1 1

INTRODUCTION 1

1. Introduction 1

1.1 Background of the Durban Central Coastline 2

1.2 Motivation 5

1.2.1 South Africa – East Coast 7

1.3 Topic 10

1.4 Research Question 10

1.5 Aim 10

1.6 Objectives 10

1.7 Dissertation Outline 11

CHAPTER 2 13

LITERATURE REVIEW 13

2.1 Introduction 13

2.1.1 Mechanisms of coastal erosion and coastal variability 13

2.2 Surf Zone Processes 15

2.2.1 Waves 16

2.2.1.1 Wave Breaking 17

2.2.3 Wave-induced currents 19

2.2.4 Beach Morphological Type 20
2.2.5 Durban Wave Climate 21
2.3 Groynes 22
2.3.1 Impermeable Groynes 24
2.3.1.1 Impermeable groyne flow 25
2.3.2 Permeable Groynes 27
2.3.2.1 Permeable groyne flow 28
2.3.3 Wave Breaking in the context of groynes 30
2.3.3.1 Effects of the level of constriction on groynes 30
2.3.3.2 Effects of the level of constriction on groyne erosion 31
2.4 Summary 34
CHAPTER 3 35
METHODOLOGY - NUMERICAL MODELLING 35
3.1 MIKE 21 - General Description 35
3.1.1 Spectral Wave-model 35
3.1.2 Flow-model 36
3.2 Overview of the simulation methodology 37
3.2.1 Study 1: Pattiaratchi Comparison 37
3.2.2 Study 2: Simulation of flow around impermeable groynes 38
3.2.3 Study 3: Changes to permeability by friction manipulation 38
3.2.4 Study 4: Simulation of flow around permeable pile screen groynes 39
3.2.5 Study 5: Field study analysis 40
3.3 Configuration of Models 40
3.3.1 Standard Model Parameters 40
3.3.3 Flow Model Parameters 44
3.3.4 Coupling Parameters 45
3.4 Discussion of Models 46
3.5 Calculation Methods 49
3.5.1 Level of constriction of the cross-sectional flow 49

CHAPTER 4 50

METHODOLOGY – FIELD WORK 50

4.1 Field work objectives 50

4.1.1 Instrumentation 50

4.2 Field Study – Flow Data Collection 53

4.2.1 Data Collection 53

4.2.2 Problems encountered 56

4.2.3 Current Meter Velocity Calibration 56

4.2.4 Current Meter Directional Calibration 57

4.3 Field Study – Sediment Data Collection 58

4.3.1 Data Collection 58

4.3.2 Grain Size Analysis 60

4.3.2.1 Data Analysis 60

4.3.3 Bedload transport 61

CHAPTER 5 63

RESULTS & DISCUSSION – PATTIARATCHI COMPARISON 63

5.1 Introduction to Study 1 63

5.2 Peak radiation stress zone 64

5.3 Eddy circulations in the lee of the groyne 65

5.4 Rip currents 66

5.5 Convergence zone 67

5.6 Divergence of the alongshore currents 73

5.7 Comparison of Pattiaratchi vs. Impermeable Groyne with a beach slope 74

5.7.1 Radiation stress field 74

5.7.2 Eddy circulations in the lee of the groyne 75

5.7.3 Rip currents 75

5.7.4 Alongshore currents 75

5.7.5 Convergence 76

5.7.6 Divergence 77

5.7.7 Wave setup and run-up 78
5.8 Summary 79
5.8.1 Pattiaratchi Comparison 79
5.8.2 Impermeable Groyne with a beach slope 79
CHAPTER 6 80
RESULTS & DISCUSSION – IMPERMEABLE GROYNES 80
6.1 Introduction to Study 2 80
6.2 Water Level Changes 81
6.3 Groyne width change 85
6.4 Groyne length change 87
6.5 Rip currents 89
6.6 Alongshore Current 93
6.7 Predominant flow pattern vs. level of constriction 99
6.8 Summary of Impermeable Groynes Parametric Study 103
CHAPTER 7 105
RESULTS & DISCUSSION – FRICTION MANIPULATION 105
7.1 Introduction to Study 3 105
7.2 Alongshore current 105
7.3 Permeability 109
7.4 Impermeable Groyne vs. Friction Manipulation 111
7.6 Summary of Friction Manipulation 113
CHAPTER 8 114
RESULTS & DISCUSSION – PERMEABLE PILE SCREEN GROYNES 114
8.1 Introduction to Study 4 114
8.2 Eddy circulations 114
8.3 Groyne length change 115
8.4 Rip currents 117
8.5 Alongshore currents 123
8.6 Predominant flow pattern vs. the level of constriction 127

8.7 Permeable pile screens vs. Friction manipulation 130
8.8 Summary of Permeable Pile Groynes 133
CHAPTER 9 134
RESULTS & DISCUSSION – FIELD INVESTIGATION 134
9.1 Introduction to Study 5 134
9.1.1 Durban Conditions 134
9.1.2 Current Meter Measurements 135
9.1.2.1 Tide 138
9.1.3 Level of Constriction 140
9.2 Results for Bedload transport assessment 143
9.2.1 Threshold velocities 143
9.2.2 Bedload transport due to currents and waves 146
9.3 Summary for Field Study 150
CHAPTER 10 151
SUMMARY & CONCLUSIONS 151
10.1 Comparison with previous modelling work 151
10.2 Level of Constriction 152
10.3 Modelling groynes with varying permeability 155
10.4 Bay of Plenty Pier 155
10.5 Summation 157
10.6 Recommendations 158
REFERENCES 159
APPENDIX A 169
MIKE 21 – NUMERICAL MODELLING 169
A1. Spectral Wave Governing Equations 170
A1.1 Radiation stress 170
A1.1.1 Radiation stress induced forces 172
A1.2 Bottom Friction 172
A1.3 Wave Breaking 173

A2. Flow Model Governing Equations 174
A2.1 Flow 174
A2.2 Horizontal eddy viscosity 176
A2.3 Bottom Stress 176
A2.4 Radiation Stress 177
A3. MIKE 21 Model Runs 178
A3.1 Part 1 – Comparison of Pattiaratchi Impermeable Groynes 178
A3.2 Part 2 – Impermeable Groynes 178
A3.3 Part 3 – Friction Manipulation 180
A3.4 Part 4 – Permeable Pile Groynes 182
APPENDIX B 183
CURRENT METERS & ADCP 183
B1. Current Meter Analysis 184
B2. Current Rose Plots 185
B2.1 Current meters 1 second intervals 185
B2.2 Current meters 10 minute averaging 191
APPENDIX C 197
Pattiarachi Comparison 197
C1. Model Run Results 198
APPENDIX D 199
IMPERMEABLE GROYNES 199
D1. Model Run Results 200
APPENDIX E 203
PERMEABLE GROYNES 203
E1. Model Run Results 204
APPENDIX F 205
SEDIMENT GRADING AND SEDIMENT TRANSPORT ANALYSIS 205
F1. Sieve Analysis 206
F2. Sediment Transport Modelling 214

F2.1 Depth Envelopes 214

F2.2 Sediment Transport – Currents 215

F2.3 Sediment Transport – Waves 223

F2.4 Sediment Transport – Combination of Waves & Currents 229

LIST OF FIGURES

FIGURE 1-1: OVERVIEW OF PROJECT LOCATION, HIGHLIGHTING DURBAN AND THE BEACHFRONT PIERS (ADAPTED FROM GOOGLE EARTH, 2013). 2
FIGURE 1-2: PHOTOGRAPH OF CENTRAL DURBAN BEACHFRONT SHOWING THE BAY OF PLENTY, NORTH BEACH AND DAIRY BEACH PIERS FROM CLOSEST TO FURTHEST (SOUTH AFRICAN TOURISM, 2013). 4
FIGURE 1-3: PHOTOGRAPH OF BAY OF PLENTY PIER SOUTH SIDE PILE FAILURE, HIGHLIGHTED IN RED (ADAPTED FROM EMS, 2013). 5
FIGURE 1-4: BATHYMETRY OF DURBAN CENTRAL BEACH FRONT JULY 2011 RELATIVE TO CD, BAY OF PLENTY PIER HIGHLIGHTED IN BLACK (ADAPTED ON MIKE FROM EMS, 2013). 8
FIGURE 1-5: BATHYMETRY OF BAY OF PLENTY PIER RELATIVE TO CD, MARCH 2012 (ADAPTED ON MIKE FROM EMS, 2013). 8
FIGURE 2-1: SKETCH OF THE SURF ZONE, SOURCE (UCAR, 2012A)..... 15
FIGURE 2-2: APPROXIMATE PARTICLE ORBIT MOTION FOR: (A) DEEP WATER, (B) SHALLOWER WATERS (BROOKE, 2003). 17
FIGURE 2-3: MAP OF SOUTH AFRICA SHOWING KWAZULU-NATAL WITH LOCATIONS OF WAVERIDER BUOYS AND ADCP (CORBELLA AND STRETCH, 2012C)……..21
FIGURE 2-4: (A) EXAMPLE OF IMPERMEABLE GROYNES (LAMBERTI AND ZANUTTIGH, 2010) AND (B) EXAMPLE OF PERMEABLE GROYNES (RAUDKIVI, 1996). 22
FIGURE 2-5: SCHEMATIC SKETCH OF THE RECIRCULATION ZONE FOR A SINGLE GROYNE. 25
FIGURE 2-6: SCHEMATIC OF RESULTING FLOW PATTERNS AND SHORELINE CONFIGURATION IN GROYNE FIELDS WITH IMPERMEABLE GROYNES (AFTER TRAMPENAU, OUMERACI AND DETTE, 2004). 26
FIGURE 2-7: SCHEMATIC OF RESULTING FLOW PATTERNS AND SHORELINE CONFIGURATION IN GROYNE FIELDS WITH PERMEABLE GROYNES (TRAMPENAU, OUMERACI AND DETTE, 2004). 29
FIGURE 2-8: ACCRETION/EROSION ZONES FOR G_L/B_Z = 2.0 (WALKER, DONG AND ANASTASIOU, 1991). 31
FIGURE 2-9: ACCRETION/EROSION ZONES FOR G_L/B_Z = 1.0 (WALKER, DONG AND ANASTASIOU, 1991). 32

FIGURE 2-10: ACCRETION/EROSION ZONES FOR G_L/B_Z = 0.67 (WALKER, DONG AND ANASTASIOU, 1991). 32
FIGURE 2-11: NEARSHORE CURRENTS FOR G_L/B_Z = 0.67 (WALKER, DONG AND ANASTASIOU, 1991). 33
FIGURE 4-1: CURRENT METER DEVELOPED BY EMS (EMS, 2013). 51
FIGURE 4-2: DEPLOYMENT CONFIGURATION AROUND BAY OF PLENTY PIER, CURRENT METERS LOST IN YELLOW, PROPELLERS LOST IN BLUE (BACKGROUND IMAGE FROM GOOGLE EARTH, 2013). 54
FIGURE 4-3: (A) THE 25 CURRENT METERS PRIOR TO DEPLOYMENT AND (B) SCHEMATIC OF A CURRENT METER ONCE DEPLOYED. 55
FIGURE 4-4: ADCP PRIOR TO DEPLOYMENT, WITH WEIGHTS, FLOATS AND MARKERS. 56
FIGURE 4-5: LOCATIONS OF SEDIMENT SAMPLE COLLECTION (BACKGROUND IMAGE FROM GOOGLE EARTH, 2013). 59
FIGURE 4-6: (A) SEDIMENT SAMPLES AND (B) SIEVE STACK 61
FIGURE 5-1: CONTOUR PLOT OF RADIATION STRESS FIELD FOR THE S_{XX} COMPONENT. FOR THE (H_S = 2M; T_P = 14S; Θ = 45°) WAVE CONDITIONS (TABLE A3.1.1, MODEL RUN 14). 68
FIGURE 5-2: CONTOUR PLOT OF RADIATION STRESS FIELD FOR THE S_{YY} COMPONENT. FOR THE (H_S = 2M; T_P = 14S; Θ = 45°) WAVE CONDITIONS (TABLE A3.1.1, MODEL RUN 14). 68
FIGURE 5-3: CONTOUR PLOT OF RADIATION STRESS FIELD FOR THE S_{XY} COMPONENT. FOR THE (H_S = 2M; T_P = 14S; Θ = 45°) WAVE CONDITIONS (TABLE A3.1.1, MODEL RUN 14). 68
FIGURE 5-4: VECTOR PLOT SHOWING THE PREDICTED CURRENT VECTORS AND THE WAVE SET-UP FOR (H_S = 1M; T_P = 14S; Θ = 45°) (TABLE A3.1.1, MODEL RUN 1). 69
FIGURE 5-5: VECTOR PLOT SHOWING THE PREDICTED CURRENT VECTORS AND THE WAVE SET-UP FOR MODEL RUN 1 (H_S = 1M; T_P = 14S; Θ = 45°). (PATTIARATCHI ET AL., 2009). 69
FIGURE 5-6: VECTOR PLOT SHOWING THE PREDICTED CURRENT VECTORS AND THE WAVE SET-UP FOR (H_S = 2M; T_P = 14S; Θ = 10°) (TABLE A3.1.1, MODEL RUN 16). 70
FIGURE 5-7: VECTOR PLOT SHOWING THE PREDICTED CURRENT VECTORS AND THE WAVE SET-UP FOR MODEL RUN 16 (H_S = 2M; T_P = 14S; Θ = 10°). (PATTIARATCHI ET AL., 2009). 70

FIGURE 5-8: VECTOR PLOT SHOWING THE PREDICTED CURRENT VECTORS AND THE WAVE SET-UP FOR (HS = 2M; TP = 14S; Θ = 45°) (TABLE A3.1.1, MODEL RUN 14). 71
FIGURE 5-9: VECTOR PLOT SHOWING THE PREDICTED CURRENT VECTORS AND THE WAVE SET-UP FOR MODEL RUN 14 (H_S = 2M; T_P = 14S; Θ = 45°). (PATTIARATCHI ET AL., 2009). 71
FIGURE 5-10: VECTOR PLOT SHOWING THE PREDICTED CURRENT VECTORS AND THE WAVE SET-UP FOR (HS = 3M; TP = 14S; Θ = 45°) (TABLE A3.1.1, MODEL RUN 19). 72
FIGURE 5-11: VECTOR PLOT SHOWING THE PREDICTED CURRENT VECTORS AND THE WAVE SET-UP FOR MODEL RUN 19 (H_S = 3M; T_P = 14S; Θ = 45°). (PATTIARATCHI ET AL., 2009). 72
FIGURE 5-12: VECTOR PLOT SHOWING THE PREDICTED CURRENT VECTORS. THE COLOUR REPRESENTS THE CURRENT SPEED FOR THE (H_S=1M; T_P=14S; Θ=45°) WAVE CONDITIONS (REFER TABLE A3.2.2, MODEL RUN 1). 76
FIGURE 5.13: VECTOR PLOT SHOWING THE PREDICTED CURRENT VECTORS. THE COLOUR REPRESENTS THE CURRENT SPEED FOR THE (H_S=1M; T_P=14S; Θ=45°) WAVE CONDITIONS (REFER TABLE A3.1.1, MODEL RUN 1). 77
FIGURE 6-1: VECTOR PLOT SHOWING THE PREDICTED CURRENT VECTORS FOR MSL = 0 (H_S = 1M; T_P = 14S; Θ = 45°) (REFER TO TABLE A3.2.3, MODEL RUN 1). 83
FIGURE 6-2: VECTOR PLOT SHOWING THE PREDICTED CURRENT VECTORS FOR MSL = -1 (H_S = 1M; T_P = 14S; Θ = 45°) (REFER TO TABLE A3.2.3, MODEL RUN 2). 83
FIGURE 6-3: VECTOR PLOT SHOWING THE PREDICTED CURRENT VECTORS FOR MSL = 0 (H_S = 2M; T_P = 14S; Θ = 45°) (REFER TO TABLE A3.2.3, MODEL RUN 9). 84
FIGURE 6-4: VECTOR PLOT SHOWING THE PREDICTED CURRENT VECTORS FOR MSL = 1 (H_S = 2M; T_P = 14S; Θ = 45°) (REFER TO TABLE A3.2.3, MODEL RUN 10). 84
FIGURE 6-5: VECTOR PLOT OF THE 20M WIDE GROYNE SHOWING THE PREDICTED CURRENT VECTORS AND THE CURRENT SPEED FOR THE (H_S = 1M; T_P = 14S; Θ = 45°) WAVE CONDITIONS (REFER TO TABLE A3.2.2, MODEL RUN 1)..... 86
FIGURE 6-6: VECTOR PLOT OF THE 1M WIDE GROYNE SHOWING THE PREDICTED CURRENT VECTORS AND THE CURRENT SPEED FOR THE (H_S = 1M; T_P = 14S; Θ = 45°) WAVE CONDITIONS (REFER TO TABLE A3.2.3, MODEL RUN 1)..... 86
FIGURE 6-7: VECTOR PLOT SHOWING THE PREDICTED CURRENT VECTORS AND THE WAVE SET-UP FOR THE 100M GROYNE (H_S = 1M; T_P = 14S; Θ = 45°) (REFER TO TABLE A3.2.4, MODEL RUN 1). 88

FIGURE 6-8: VECTOR PLOT SHOWING THE PREDICTED CURRENT VECTORS AND THE WAVE SET-UP FOR THE 200M GROYNE (H_S = 1M; T_P = 14S; Θ = 45°) (REFER TO TABLE A3.2.3, MODEL RUN 1). 88
FIGURE 6-9: GRAPH OF PEAK RIP CURRENTS VS. LEVEL OF CONSTRICTION FOR THE (H_S=1M; T_P=14S; Θ=45°) WAVE CONDITIONS. POINTS ARE JOINED TO LINES FOR CLARITY. 89
FIGURE 6-10: GRAPH OF PEAK RIP CURRENTS VS. LEVEL OF CONSTRICTION FOR THE (H_S = 2M; T_P = 14S; Θ = 45°) WAVE CONDITIONS. POINTS ARE JOINED TO LINES FOR CLARITY. 90
FIGURE 6-11: GRAPH OF PEAK RIP CURRENTS VS. LEVEL OF CONSTRICTION FOR THE (H_S = 2M; T_P = 14S; Θ = 60°) WAVE CONDITIONS. POINTS ARE JOINED TO LINES FOR CLARITY. 90
FIGURE 6-12: GRAPH OF PEAK RIP CURRENTS VS. LEVEL OF CONSTRICTION FOR THE (H_S = 3M; T_P = 14S; Θ = 45°) WAVE CONDITIONS. POINTS ARE JOINED TO LINES FOR CLARITY. 91
FIGURE 6-13: GRAPH OF CROSS-SECTION FLOW AT THE TIP OF THE GROYNE FOR THE DIFFERENT DATUMS AND G_L/B_Z. FOR THE (H_S = 1M; T_P = 14S; Θ = 45°) WAVE CONDITIONS. 93
FIGURE 6-14: GRAPH OF CROSS-SECTION FLOW AT THE TIP OF THE GROYNE FOR THE DIFFERENT DATUMS AND G_L/B_Z. FOR THE (H_S = 2M; T_P = 14S; Θ = 45°) WAVE CONDITIONS. 94
FIGURE 6-15: GRAPH OF CROSS-SECTION FLOW AT THE TIP OF THE GROYNE FOR THE DIFFERENT DATUMS AND G_L/B_Z. FOR THE (H_S = 3M; T_P = 14S; Θ = 45°) WAVE CONDITIONS. 94
FIGURE 6-16: GRAPH OF CROSS-SECTION FLOW AT THE TIP OF THE 100M GROYNE FOR THE DIFFERENT DATUMS AND G_L/B_Z. FOR THE (H_S = 1M; T_P = 14S; Θ = 45°) WAVE CONDITIONS. 95
FIGURE 6-17: GRAPH OF CROSS-SECTION FLOW AT THE TIP OF THE 200M GROYNE FOR THE DIFFERENT DATUMS AND G_L/B_Z. FOR THE (H_S = 1M; T_P = 14S; Θ = 45°) WAVE CONDITIONS. 95
FIGURE 6-18: GRAPH OF CROSS-SECTION FLOW AT THE TIP OF THE 100M GROYNE FOR THE DIFFERENT DATUMS AND G_L/B_Z. FOR THE (H_S = 2M; T_P = 14S; Θ = 45°) WAVE CONDITIONS. 96
FIGURE 6-19: GRAPH OF CROSS-SECTION FLOW AT THE TIP OF THE 200M GROYNE FOR THE DIFFERENT DATUMS AND G_L/B_Z. FOR THE (H_S = 2M; T_P = 14S; Θ = 45°) WAVE CONDITIONS. 97

FIGURE 6-20: GRAPH OF CROSS-SECTION FLOW AT THE TIP OF THE 100M GROYNE FOR THE DIFFERENT DATUMS AND G_L/B_Z. FOR THE (H_S = 3M; T_P = 14S; Θ = 45°) WAVE CONDITIONS. 97
FIGURE 6-21: GRAPH OF CROSS-SECTION FLOW AT THE TIP OF THE 200M GROYNE FOR THE DIFFERENT DATUMS AND G_L/B_Z. FOR THE (H_S = 3M; T_P = 14S; Θ = 45°) WAVE CONDITIONS. 98
FIGURE 6-22: GRAPH OF CROSS-SECTION VELOCITIES AT THE TIP OF THE GROYNE WITH A MSL = -1 AND G_L/B_Z = 0.89. FOR THE (H_S = 1M; T_P = 14S; Θ = 45°) WAVE CONDITIONS (TABLE A3.2.3, MODEL RUN 2). 99
FIGURE 6-23: GRAPH OF CROSS-SECTION VELOCITIES AT THE TIP OF THE GROYNE WITH A MSL = 0 AND G_L/B_Z = 1.12. FOR THE (H_S = 1M; T_P = 14S; Θ = 45°) WAVE CONDITIONS (TABLE A3.2.3, MODEL RUN 1). 100
FIGURE 6-24: GRAPH OF CROSS-SECTION VELOCITIES AT THE TIP OF THE GROYNE WITH A MSL = 0.75 AND G_L/B_Z = 0.80. FOR THE (H_S = 2M; T_P = 14S; Θ = 45°) WAVE CONDITIONS (TABLE A3.2.3, MODEL RUN 11). 100
FIGURE 6-25: GRAPH OF CROSS-SECTION VELOCITIES AT THE TIP OF THE GROYNE WITH A MSL = 0.75 AND G_L/B_Z = 0.60. FOR THE (H_S = 3M; T_P = 14S; Θ = 45°) WAVE CONDITIONS (TABLE A3.2.3, MODEL RUN 19). 101
FIGURE 6-26: GRAPH OF CROSS-SECTION VELOCITIES AT THE TIP OF THE GROYNE WITH A MSL = 0.5 AND G_L/B_Z = 0.55. FOR THE (H_S = 3M; T_P = 14S; Θ = 45°) WAVE CONDITIONS (TABLE A3.2.3, MODEL RUN 20). 101
FIGURE 6-27: GRAPH OF CROSS-SECTION VELOCITIES AT THE TIP OF THE GROYNE WITH A MSL = 1 AND G_L/B_Z = 0.50. FOR THE (H_S = 2M; T_P = 14S; Θ = 60°) WAVE CONDITIONS (TABLE A3.2.4, MODEL RUN 14). 102
FIGURE 6-28: SCHEMATIC OF RIP CURRENT DOMINANT FLOW PATTERN AROUND AN IMPERMEABLE GROYNE..... 103
FIGURE 6-29: SCHEMATIC OF ALONGSHORE CURRENT DOMINANT FLOW PATTERN AROUND AN IMPERMEABLE GROYNE..... 104
FIGURE 7-1: GRAPH OF CROSS-SECTION FLOW ALONG THE FRICTION COEFFICIENT GEOMETRIC AREA FOR DIFFERENT CASES. THIS IS FOR THE (H_S = 2M; T_P = 14S; Θ = 10°) WAVE CONDITIONS. 106
FIGURE 7-2: GRAPH OF CROSS-SECTION FLOW ALONG THE FRICTION COEFFICIENT GEOMETRIC AREA MULTIPLIED BY THE DEPTH FOR DIFFERENT CASES. THIS IS FOR THE (H_S = 2M; T_P = 14S; Θ = 10°) WAVE CONDITIONS. 107

FIGURE 7-3: GRAPH OF CROSS-SECTION FLOW ALONG THE FRICTION COEFFICIENT GEOMETRIC AREA MULTIPLIED BY DEPTH FOR DIFFERENT CASES. THIS IS FOR THE (H_S = 3M; T_P = 14S; Θ = 45°) WAVE CONDITIONS..... 107

FIGURE 7-4: GRAPH OF CROSS-SECTION FLOW ALONG THE FRICTION COEFFICIENT GEOMETRIC AREA MULTIPLIED BY DEPTH FOR DIFFERENT CASES. THIS IS FOR THE (H_S=2M; T_P=14S; Θ=45°) WAVE CONDITIONS. 108

FIGURE 7-5: GRAPH OF THE FLOW & SPEED REDUCTION FOR THE FRICTION COEFFICIENT MANIPULATION. FOR THE (H_S = 2M; T_P = 14S; Θ = 10°) WAVE CONDITIONS. 109

FIGURE 7-6: GRAPH OF PERMEABILITY REDUCTION FOR FRICTION COEFFICIENT MULTIPLIED BY THE DEPTH. FOR THE (H_S = 2M; T_P = 14S; Θ = 10°) WAVE CONDITIONS. 110

FIGURE 7-8: IMPERMEABLE GROYNE VECTOR PLOT SHOWING THE PREDICTED CURRENT VECTORS AND THE WAVE SET-UP FOR (H_S = 2M; T_P = 14S; Θ = 45°) (TABLE A3.2.3, MODEL RUN 9)..... 111

FIGURE 7-9: VECTOR PLOT SHOWING THE PREDICTED CURRENT VECTORS AND THE WAVE SET-UP FOR (H_S = 2M; T_P = 14S; Θ = 45°). FOR THE C_F X H MANIPULATION OVER A 20M WIDTH (TABLE A3.3.3, MODEL RUN 9)..... 112

FIGURE 8-1: VECTOR PLOT OF A 50.13 PER CENT PERMEABLE PILE SCREEN SHOWING THE PREDICTED CURRENT VECTORS AND THE WAVE SET-UP FOR (H_S = 2M; T_P = 14S; Θ = 45°) (TABLE A3.4.1, MODEL RUN 5)..... 116

FIGURE 8-2: VECTOR PLOT OF A 33.33 PER CENT PERMEABLE PILE SCREEN SHOWING THE PREDICTED CURRENT VECTORS AND THE WAVE SET-UP FOR (H_S = 2M; T_P = 14S; Θ = 45°) (TABLE A3.4.1, MODEL RUN 6)..... 116

FIGURE 8-3: VECTOR PLOT OF A 33.33 PER CENT PERMEABLE PILE SCREEN SHOWING THE PREDICTED CURRENT VECTORS AND THE WAVE SET-UP FOR (H_S = 1M; T_P = 14S; Θ = 45°) (TABLE A3.4.1, MODEL RUN 3). SHOREWARD RIP CURRENT HIGHLIGHTED IN RED..... 117

FIGURE 8-4: VECTOR PLOT OF A 70.32 PER CENT PERMEABLE PILE SCREEN SHOWING THE PREDICTED CURRENT VECTORS AND THE WAVE SET-UP (H_S = 2M; T_P = 14S; Θ = 45°) (TABLE A3.4.1, MODEL RUN 4). LOCATION OF SHOREWARD RIP CURRENT HIGHLIGHTED IN RED. 118

FIGURE 8-5: GRAPH OF 200M PILE SCREEN PERMEABILITY VS. PEAK RIP CURRENTS FOR G_L/B_Z=1.14 AND (H_S = 1M; T_P = 14S; Θ = 45°) WAVE CONDITIONS. POINTS ARE JOINED TO LINES FOR CLARITY..... 118

FIGURE 8-6: GRAPH OF 100M PILE SCREEN PERMEABILITY VS. PEAK RIP CURRENTS FOR G_L/B_Z=0.63 AND (H_S = 1M; T_P = 14S; Θ = 45°) WAVE CONDITIONS. POINTS ARE JOINED TO LINES FOR CLARITY. 119
FIGURE 8-7: GRAPH OF 200M PILE SCREEN PERMEABILITY VS. PEAK RIP CURRENTS FOR G_L/B_Z=0.72 AND (H_S = 2M; T_P = 14S; Θ = 45°) WAVE CONDITIONS. POINTS ARE JOINED TO LINES FOR CLARITY. 119
FIGURE 8-8: GRAPH OF 100M PILE SCREEN PERMEABILITY VS. PEAK RIP CURRENTS FOR G_L/B_Z=0.40 AND (H_S = 2M; T_P = 14S; Θ = 45°) WAVE CONDITIONS. POINTS ARE JOINED TO LINES FOR CLARITY. 120
FIGURE 8-9: GRAPH OF 100M PILE SCREEN PERMEABILITY VS. PEAK RIP CURRENTS FOR G_L/B_Z=0.27 AND (H_S = 3M; T_P = 14S; Θ = 45°) WAVE CONDITIONS. POINTS ARE JOINED TO LINES FOR CLARITY. 120
FIGURE 8-10: GRAPH OF CROSS-SECTION FLOW ALONG 100M PERMEABLE PILE SCREEN GROYNE FOR A CHANGE IN PERMEABILITY AND A G_L/B_Z = 0.63. FOR THE (H_S = 1M; T_P = 14S; Θ = 45°) WAVE CONDITIONS. 123
FIGURE 8-11: GRAPH OF CROSS-SECTION FLOW ALONG 100M PERMEABLE PILE SCREEN GROYNE FOR A CHANGE IN PERMEABILITY AND A G_L/B_Z = 0.40. FOR THE (H_S = 2M; T_P = 14S; Θ = 45°) WAVE CONDITIONS. 124
FIGURE 8-12: GRAPH OF CROSS-SECTION FLOW ALONG 100M PERMEABLE PILE SCREEN GROYNE FOR A CHANGE IN PERMEABILITY AND A G_L/B_Z = 0.27. FOR THE (H_S = 3M; T_P = 14S; Θ = 45°) WAVE CONDITIONS. 124
FIGURE 8-13: GRAPH OF CROSS-SECTION FLOW ALONG 200M PERMEABLE PILE SCREEN GROYNE FOR A CHANGE IN PERMEABILITY AND A G_L/B_Z = 1.14. FOR THE (H_S = 1M; T_P = 14S; Θ = 45°) WAVE CONDITIONS. 125
FIGURE 8-14: GRAPH OF CROSS-SECTION FLOW ALONG 200M PERMEABLE PILE SCREEN GROYNE FOR A CHANGE IN PERMEABILITY AND A G_L/B_Z = 0.72. FOR THE (H_S = 2M; T_P = 14S; Θ = 45°) WAVE CONDITIONS. 125
FIGURE 8-15: GRAPH OF CROSS-SECTION FLOW ALONG 200M PERMEABLE PILE SCREEN GROYNE FOR A CHANGE IN PERMEABILITY AND A G_L/B_Z = 0.49. FOR THE (H_S = 3M; T_P = 14S; Θ = 45°) WAVE CONDITIONS. 126
FIGURE 8-16: GRAPH OF CROSS-SECTION VELOCITIES AT THE TIP OF THE PERMEABLE PILE SCREEN FOR A PERMEABILITY OF 70.32% AND A G_L/B_Z = 1.14. FOR THE (H_S = 1M; T_P = 14S; Θ = 45°) WAVE CONDITIONS (TABLE A3.4.1, MODEL RUN 1). 127
FIGURE 8-17: GRAPH OF CROSS-SECTION VELOCITIES AT THE TIP OF THE PERMEABLE PILE SCREEN FOR A PERMEABILITY OF 50.13% AND A G_L/B_Z =

1.14. FOR THE (H_S = 1M; T_P = 14S; Θ = 45°) WAVE CONDITIONS (TABLE A3.4.1, MODEL RUN 2)..... 128
FIGURE 8-18: GRAPH OF CROSS-SECTION VELOCITIES AT THE TIP OF THE PERMEABLE PILE SCREEN FOR A PERMEABILITY OF 33.33% AND A G_L/B_Z = 1.14. FOR THE (H_S = 1M; T_P = 14S; Θ = 45°) WAVE CONDITIONS (TABLE A3.4.1, MODEL RUN 3)..... 128
FIGURE 8-19: GRAPH OF CROSS-SECTION VELOCITIES AT THE TIP OF THE PERMEABLE PILE SCREEN FOR A PERMEABILITY OF 70.32% AND A G_L/B_Z = 0.72. FOR THE (H_S = 2M; T_P = 14S; Θ = 45°) WAVE CONDITIONS (TABLE A3.4.1, MODEL RUN 4)..... 129
FIGURE 8-20: GRAPH OF CROSS-SECTION VELOCITIES AT THE TIP OF THE PERMEABLE PILE SCREEN FOR A PERMEABILITY OF 50.13% AND A G_L/B_Z = 0.72. FOR THE (H_S = 2M; T_P = 14S; Θ = 45°) WAVE CONDITIONS (TABLE A3.4.1, MODEL RUN 5)..... 129
FIGURE 8-21: VECTOR PLOT SHOWING A 33.33 PER CENT PERMEABLE PILE SCREEN WITH THE PREDICTED CURRENT VECTORS AND THE WAVE SET-UP FOR (H_S = 2M; T_P = 14S; Θ = 45°) (TABLE A3.4.1, MODEL RUN 6)..... 130
FIGURE 8-22: VECTOR PLOT SHOWING THE PREDICTED CURRENT VECTORS AND THE WAVE SET-UP FOR (H_S = 2M; T_P = 14S; Θ = 45°). FOR THE C_F X H MANIPULATION OVER A 1M WIDTH (TABLE A3.3.3, MODEL RUN 13)..... 131
FIGURE 8-23: VECTOR PLOT SHOWING THE PREDICTED CURRENT VECTORS AND THE WAVE SET-UP FOR (H_S = 2M; T_P = 14S; Θ = 45°). FOR THE C_F X H MANIPULATION OVER A 20M WIDTH (TABLE A3.3.3, MODEL RUN 7)..... 132
FIGURE 9-1: WAVE ROSE FOR DURBAN CENTRAL BEACH FRONT, 6 NOVEMBER 2013..... 135
FIGURE 9-2: CURRENT ROSES WITH 10 MINUTE AVERAGING, DISPLAYING THE MOST FREQUENT CURRENT DIRECTION FOR THE CURRENT METERS (BACKGROUND IMAGE FROM GOOGLE, 2012)..... 136
FIGURE 9-3: CURRENT METER AVERAGE VECTOR PLOT (BACKGROUND IMAGE FROM GOOGLE, 2012)..... 137
FIGURE 9-4: HIGH TIDE CURRENT METER VECTOR PLOT (BACKGROUND IMAGE FROM GOOGLE, 2012)..... 138
FIGURE 9-5: LOW TIDE CURRENT METER VECTOR PLOT (BACKGROUND IMAGE FROM GOOGLE, 2012)..... 139
FIGURE 9-6: WAVE BREAKING CONDITIONS AROUND THE BAY OF PLENTY PIER (BACKGROUND IMAGE FROM GOOGLE, 2012)..... 141

FIGURE 9-7: AVERAGE THRESHOLD VELOCITIES FOR THE NORTH SIDE OF THE BAY OF PLENTY PIER. POINTS ARE JOINED TO LINES FOR CLARITY. 144
FIGURE 9-8: AVERAGE THRESHOLD VELOCITIES FOR THE SOUTH SIDE OF THE BAY OF PLENTY PIER. POINTS ARE JOINED TO LINES FOR CLARITY. 144
FIGURE 9-9: AVERAGE BED SHEAR STRESSES FOR THE NORTH SIDE OF THE BAY OF PLENTY PIER USING THE SOULSBY AND CLARKE (2005) METHOD. POINTS ARE JOINED TO LINES FOR CLARITY. 146
FIGURE 9-10: AVERAGE BED SHEAR STRESSES FOR THE SOUTH SIDE OF THE BAY OF PLENTY PIER USING THE SOULSBY AND CLARKE (2005) METHOD. POINTS ARE JOINED TO LINES FOR CLARITY. 147
FIGURE 9-11: AVERAGE BEDLOAD TRANSPORT RATE FOR THE NORTH SIDE OF THE BAY OF PLENTY PIER USING THE SOULSBY AND CLARKE (2005) METHOD WITH THE NEILSEN (1992) METHOD. POINTS ARE JOINED TO LINES FOR CLARITY 148
FIGURE 9-12: AVERAGE BEDLOAD TRANSPORT RATE FOR THE SOUTH SIDE OF THE BAY OF PLENTY PIER USING THE SOULSBY AND CLARKE (2005) METHOD WITH THE NEILSEN (1992) METHOD. POINTS ARE JOINED TO LINES FOR CLARITY 149
FIGURE 10-1: SCHEMATIC OF RIP CURRENT DOMINANT FLOW PATTERN AROUND AN IMPERMEABLE GROYNE 153
FIGURE 10-2: SCHEMATIC OF ALONGSHORE CURRENT DOMINANT FLOW PATTERN AROUND AN IMPERMEABLE GROYNE 154
FIGURE A1-1: TRANSLATION DESCRIPTION OF RADIATION STRESSES (NIELSEN AND APELT, 2003) 171
FIGURE B2-1: CURRENT ROSE (M/S) FOR CURRENT METER NO.1 185
FIGURE B2-2: CURRENT ROSE (M/S) FOR CURRENT METER NO.2 185
FIGURE B2-3: CURRENT ROSE (M/S) FOR CURRENT METER NO.3 185
FIGURE B2-4: CURRENT ROSE (M/S) FOR CURRENT METER NO.4 186
FIGURE B2-6: CURRENT ROSE (M/S) FOR CURRENT METER NO.7 186
FIGURE B2-5: CURRENT ROSE (DIRECTION ONLY) FOR CURRENT METER NO.6.. 186
FIGURE B2-7: CURRENT ROSE (M/S) FOR CURRENT METER NO.8 186
FIGURE B2-8: CURRENT ROSE (M/S) FOR CURRENT METER NO.9 187
FIGURE B2-9: CURRENT ROSE (DIRECTION ONLY) FOR CURRENT METER NO.10 187
FIGURE B2-10: CURRENT ROSE (M/S) FOR CURRENT METER NO.11 187
FIGURE B2-11: CURRENT ROSE (M/S) FOR CURRENT METER NO.12 187
FIGURE B2-12: CURRENT ROSE (M/S) FOR CURRENT METER NO.13 188

FIGURE B2-13: CURRENT ROSE (M/S) FOR CURRENT METER NO.14 188
FIGURE B2-14: CURRENT ROSE (M/S) FOR CURRENT METER NO.15 188
FIGURE B2-15: CURRENT ROSE (M/S) FOR CURRENT METER NO.16 188
FIGURE B2-16: CURRENT ROSE (M/S) FOR CURRENT METER NO.17 189
FIGURE B2-17: CURRENT ROSE (M/S) FOR CURRENT METER NO.18 189
FIGURE B2-18: CURRENT ROSE (M/S) FOR CURRENT METER NO.19 189
FIGURE B2-19: CURRENT ROSE (M/S) FOR CURRENT METER NO.20 189
FIGURE B2-20: CURRENT ROSE (M/S) FOR CURRENT METER NO.22 190
FIGURE B2-21: CURRENT ROSE (DIRECTION ONLY) FOR CURRENT METER NO.24 190
FIGURE B2-22: CURRENT ROSE (M/S) FOR CURRENT METER NO.25 190
FIGURE B2-23: CURRENT ROSE (M/S) FOR CURRENT METER NO.1 191
FIGURE B2-24: CURRENT ROSE (M/S) FOR CURRENT METER NO.2 191
FIGURE B2-25: CURRENT ROSE (M/S) FOR CURRENT METER NO.3 191
FIGURE B2-26: CURRENT ROSE (M/S) FOR CURRENT METER NO.4 192
FIGURE B2-27: CURRENT ROSE (M/S) FOR ADCP AT CURRENT METER NO.6 LOCATION 192
FIGURE B2-28: CURRENT ROSE (M/S) FOR CURRENT METER NO.7 192
FIGURE B2-29: CURRENT ROSE (M/S) FOR CURRENT METER NO.8 192
FIGURE B2-30: CURRENT ROSE (M/S) FOR CURRENT METER NO.9 193
FIGURE B2-31: CURRENT ROSE (M/S) FOR CURRENT METER NO.11 193
FIGURE B2-32: CURRENT ROSE (M/S) FOR CURRENT METER NO.12 193
FIGURE B2-33: CURRENT ROSE (M/S) FOR CURRENT METER NO.13 193
FIGURE B2-34: CURRENT ROSE (M/S) FOR CURRENT METER NO.14 194
FIGURE B2-35: CURRENT ROSE (M/S) FOR CURRENT METER NO.15 194
FIGURE B2-36: CURRENT ROSE (M/S) FOR CURRENT METER NO.16 194
FIGURE B2-37: CURRENT ROSE (M/S) FOR CURRENT METER NO.17 194
FIGURE B2-38: CURRENT ROSE (M/S) FOR CURRENT METER NO.18 195
FIGURE B2-39: CURRENT ROSE (M/S) FOR CURRENT METER NO.19 195
FIGURE B2-40: CURRENT ROSE (M/S) FOR CURRENT METER NO.20 195
FIGURE B2-41: CURRENT ROSE (M/S) FOR CURRENT METER NO.22 195
FIGURE B2-42: CURRENT ROSE (M/S) FOR CURRENT METER NO.25 196
FIGURE F1-1: SIEVE ANALYSIS OF SECTION 1 – SOUTHSIDE SHORE 206
FIGURE F1-2: SIEVE ANALYSIS OF SECTION 2 – SOUTHSIDE MIDDLE OF PIER 207
FIGURE F1-3: SIEVE ANALYSIS OF SECTION 3 – SOUTHSIDE ¾ OF PIER..... 208
FIGURE F1-4: SIEVE ANALYSIS OF SECTION 4 – NORTHSIDE SHORE 209

FIGURE F1-5: SIEVE ANALYSIS OF SECTION 5 – NORTHSIDE MIDDLE OF PIER.... 210
FIGURE F1-6: SIEVE ANALYSIS OF SECTION 6 – NORTHSIDE ¾ OF PIER 211
FIGURE F1-7: SIEVE ANALYSIS OF SECTION 7 – TIP OF THE PIER 212
FIGURE F2-1: DEPTH ENVELOPE OF CURRENT METERS, 10 11 12 & 16 ON THE NORTH SIDE OF THE BAY OF PLENTY PIER. POINTS ARE JOINED TO LINES FOR CLARITY..... 214
FIGURE F2-2: DEPTH ENVELOPE OF CURRENT METERS, 14 15 & 16, ON THE SOUTH SIDE OF THE BAY OF PLENTY PIER. POINTS ARE JOINED TO LINES FOR CLARITY. 214
FIGURE F2-3: FLOW CHART OF DETERMINING CURRENT BEDLOAD TRANSPORT PART 1 221
FIGURE F2-4: FLOW CHART OF DETERMINING CURRENT BEDLOAD TRANSPORT PART 2 222
FIGURE F2-5: FLOW CHART OF DETERMINING WAVE BEDLOAD TRANSPORT.... 228
FIGURE F2-6: FLOW CHART OF DETERMINING MEAN & MAXIMUM BED SHEAR STRESSES FOR LAMINAR, SMOOTH-TURBULENT & ROUGH-TURBULENT WAVE + CURRENT FLOWS 234
FIGURE F2-7: FLOW CHART OF DETERMINING WAVE + CURRENT BEDLOAD TRANSPORT 235

LIST OF TABLES

TABLE 2-1: FUNCTIONAL PROPERTIES ATTRIBUTED TO GROYNES AND THEIR CRITICAL EVALUATION (AFTER KRAUS, HANSON AND BLOMGREN, 1994). .. 23
TABLE 3-1: DOMAIN CONFIGURATIONS FOR NUMERICAL MODELLING STUDIES 40
TABLE 3-2: SW CONFIGURATIONS FOR NUMERICAL MODELLING STUDIES 44
TABLE 3-3: FM CONFIGURATIONS FOR NUMERICAL MODELLING STUDIES 45
TABLE 3-4: OVERVIEW OF STUDY 1 MODEL RUNS 46
TABLE 3-5: OVERVIEW OF STUDY 2 MODEL RUNS 46
TABLE 3-6: OVERVIEW OF STUDY 3 MODEL RUNS 47
TABLE 3-7: OVERVIEW OF STUDY 4 MODEL RUNS 48
TABLE 5-1: DIVERGENCE LOCATION FOR THE DIFFERENT SIMULATIONS 73
TABLE 5-2: DIVERGENCE LENGTH COMPARISON 77
TABLE 6-1: CONSTRICTION RATIO DIFFERENCE FOR THE 200M & 100M GROYNE (AFTER TABLE D1.2-D1.3) 87
TABLE 6-2: EFFECTS OF THE LEVEL OF CONSTRICTION ON THE GROYNE RIP-CURRENTS 92
TABLE 8-1: SUMMARY OF PERMEABILITY EFFECTS ON THE GROYNE RIP-CURRENTS 122
TABLE A3-1-1: MODEL RUN IMPERMEABLE GROYNE INCIDENT WAVE CONDITIONS (AFTER PATTIARATCHI ET AL., 2009) 178
TABLE A3-2-1: MODEL RUN PLANAR BEACH CONDITIONS 178
TABLE A3-2-2: MODEL RUN IMPERMEABLE GROYNE INCIDENT WAVE CONDITIONS & DATUM SHIFT CONDITIONS 179
TABLE A3-2-3: MODEL RUN 200M IMPERMEABLE GROYNE INCIDENT WAVE CONDITIONS & DATUM SHIFT CONDITIONS 179
TABLE A3-2-4: MODEL RUN 100M IMPERMEABLE GROYNE INCIDENT WAVE CONDITIONS & DATUM SHIFT CONDITIONS 180
TABLE A3-3-1: MODEL RUN FRICTION COEFFICIENT CONDITIONS 180
TABLE A3-3-2: MODEL RUN DATUM SHIFT & FRICTION COEFFICIENT CONDITIONS 181
TABLE A3-3-3: MODEL RUN FRICTION COEFFICIENT MULTIPLIED BY VARIED DEPTH CONDITIONS 181
TABLE A3-4-1: MODEL RUN 200M PERMEABLE PILE CONDITIONS 182
TABLE A3-4-2: MODEL RUN 100M PERMEABLE PILE CONDITIONS 182

TABLE B1-1: CURRENT METER CALIBRATION DATA 184
TABLE C1-1: SUMMARY OF PATTIARATCHI RESULTS VS. STUDY RESULTS 198
TABLE D1-1: LEVEL OF CONSTRICTION OF CROSS-SHORE FLOW FOR DEPTH CHANGES FOR 20M X 200M GROYNE 200
TABLE D1-2: LEVEL OF CONSTRICTION OF CROSS-SHORE FLOW FOR DEPTH CHANGES FOR 1M X 200M GROYNE 201
TABLE D1-3: LEVEL OF CONSTRICTION OF CROSS-SHORE FLOW FOR DEPTH CHANGES FOR 1M X 100M GROYNE 202
TABLE E1-1: MODEL RUN PERMEABLE PILE CONDITIONS FOR 1M X 200M GROYNE 204
TABLE E1-2: MODEL RUN PERMEABLE PILE CONDITIONS FOR 1M X 100M GROYNE 204
TABLE F1-1: SIEVE ANALYSIS OF SECTION 1 – SOUTH SIDE SHORE 206
TABLE F1-2: SUMMARY OF SIEVE ANALYSIS SECTION 1 – SOUTH SIDE SHORE . 206
TABLE F1-3: SIEVE ANALYSIS OF SECTION 2 – SOUTH SIDE MIDDLE OF PIER 207
TABLE F1-4: SUMMARY OF SIEVE ANALYSIS SECTION 2 – SOUTH SIDE MIDDLE OF PIER 207
TABLE F1-5: SIEVE ANALYSIS OF SECTION 3 – SOUTH SIDE ¾ OF PIER 208
TABLE F1-6: SUMMARY OF SIEVE ANALYSIS SECTION 3 – SOUTH SIDE ¾ OF PIER 208
TABLE F1-7: SIEVE ANALYSIS OF SECTION 4 – NORTH SIDE SHORE 209
TABLE F1-8: SUMMARY OF SIEVE ANALYSIS SECTION 4 – NORTH SIDE SHORE . 209
TABLE F1-9: SIEVE ANALYSIS OF SECTION 5 – NORTH SIDE MIDDLE OF PIER 210
TABLE F1-10: SUMMARY OF SIEVE ANALYSIS SECTION 5 – NORTH SIDE MIDDLE OF PIER 210
TABLE F1-11: SIEVE ANALYSIS OF SECTION 6 – NORTH SIDE ¾ OF PIER 211
TABLE F1-12: SUMMARY OF SIEVE ANALYSIS SECTION 6 – NORTH SIDE ¾ OF PIER 211
TABLE F1-13: SIEVE ANALYSIS OF SECTION 7 – TIP OF THE PIER 212
TABLE F1-14: SUMMARY OF SIEVE ANALYSIS SECTION 7 – TIP OF THE PIER 212
TABLE F2-1: THRESHOLD VELOCITY DATA FOR THE SOUTH SIDE OF BAY OF PLENTY PIER 237
TABLE F2-2: THRESHOLD VELOCITY DATA FOR THE NORTH SIDE OF BAY OF PLENTY PIER 237
TABLE F2-3: BED SHEAR STRESS DATA FOR THE SOUTH SIDE OF BAY OF PLENTY PIER 238

TABLE F2-4: BED SHEAR STRESS DATA FOR THE NORTH SIDE OF BAY OF PLENTY PIER 238
TABLE F2-5: BEDLOAD TRANSPORT DATA FOR THE SOUTH SIDE OF BAY OF PLENTY PIER 239
TABLE F2-6: BEDLOAD TRANSPORT DATA FOR THE NORTH SIDE OF BAY OF PLENTY PIER 239

LIST OF SYMBOLS

A	=	Semi-orbital excursion (m).
A	=	Horizontal eddy viscosity (m^2/s).
a	=	Wave amplitude (m).
α_{bj}	=	Calibration constant.
B_z	=	Breaker zone width (m).
β	=	Angle of the beach slope (°).
C_c	=	Coefficient of curvature.
c	=	Wave celerity (m/s).
c_0	=	Deep water wave celerity (m/s).
C_D	=	Bed roughness drag coefficient.
C_{Dm}	=	Mean current drag coefficient.
C_{Dmax}	=	Maximum current drag coefficient.
C_{Dr}	=	Rough turbulent flow for current drag coefficient.
C_{Ds}	=	Smooth turbulent flow for current drag coefficient.
C_f	=	Coefficient of drag.
c_g	=	Group wave celerity (m/s).
c_{g0}	=	Deep water group wave celerity (m/s).
c_s	=	Constant used for subgrid scale eddy viscosity.
C_u	=	Coefficient of uniformity.
d	=	Water depth (m).
D^*	=	Particle size parameter.
D_{10}	=	Tenth percentile of the grain sample size (mm).

D_{30} = Thirtieth percentile of the grain sample size (mm).

D_{50} = Median grain (mm).

D_{60} = Sixtieth percentile of the grain sample size (mm).

D_{90} = Ninetieth percentile of the grain sample size (mm).

E = Mean wave energy (J/m^2).

f = Frequency (H_z).

f_c = Coefficient of current friction.

$\bar{f}$ = Mean frequency (H_z).

f_w = Wave friction factor.

f_{wr} = Rough turbulent wave friction factor.

f_{ws} = Smooth turbulent wave friction factor.

G_L = Groyne length (m).

g = Gravitational constant (m/s^2).

γ = Wave breaking index.

H = Wave height (m).

H_b/H_m = Breaking wave height (m).

H_{rms} = Root mean square wave height (m).

H_s = Significant wave height (m).

k = wave number (m^{-1}).

K_3 = Coefficient to allow for the effect of the transformation to irregular waves.

k_n = Nikuradse bed roughness length (m).

k_s = Nikuradse roughness (m).

L = Wave length (m).

L_0 = Deep water wave length (m).

l = Length of eddy viscosity (m).

M = Manning number ($m^{1/3}/s$).

μ = Dynamic viscosity (Ns/m^2).

n = Wave celerity ratio.

v = Kinematic viscosity (m^2/s).

ω = Wave radian frequency (rad/s).

P = Wave power (W/m^2).

p_a = Atmospheric pressure (N/m^2).

P_0 = Deep water wave power (W/m^2).

φ = Bedload transport rate factor.

φ = Angle between waves and currents.

Q_b = Fraction of breaking waves.

q_b = Bedload transport rate ($m^3/m/s$).

R_e = Reynolds number.

Re_c = Reynolds current number.

$Re_{c,cr}$ = Reynolds critical current number.

Re_w = Reynolds wave number.

$Re_{w,cr}$ = Reynolds critical wave number.

ρ_0, ρ_w = Density of water (kg/m^3).

ρ_s = Density of sand (kg/m^3).

S = Magnitude of discharge due to point sources (m^3/s)

s = Ratio of densities of grain and water.

S_{bot} = Source term for bottom friction dissipation rate (J/m^2).

S_{ij} = Deformation rate of eddy viscosity.

S_{surf} = Source term for wave breaking dissipation rate (J/m^2).

S_{xx} = Principle radiation stress component that acts on a vertical plane that is perpendicular to the wave propagation direction (m^3/s^2).

S_{xy} = Shear radiation stress component (m^3/s^2).

S_{yy} = Principle radiation stress component that acts on a vertical plane that is parallel to the wave propagation direction (m^3/s^2).

T, T_p = Wave period (s).

T_{xx} = Lateral stress, viscous friction (N/m^2).

T_{yy} = Lateral stress, turbulent friction (N/m^2).

T_{xy} = Lateral stress, differential advection (N/m^2).

T_0 = Bed shear stress & Skin friction stress (N/m^2).

T_{bx} = X component (sea bed) bottom stress (N/m^2).

τ_{by} = Y component (sea bed) bottom stress (N/m^2).

$\tau_{c,s}$ = Current induced skin friction shear stress (N/m^2).

T_{cs} = Skin friction shear stress for current flow (N/m^2).

T_m = Mean shear stress (N/m^2).

T_{max} = Maximum shear stress (N/m^2).

T_{mr} = Rough turbulent current shear stress (N/m^2).

T_{ms} = Smooth turbulent current shear stress (N/m^2).

T_{sx} = X component surface wind stress (N/m^2).

τ_{sy} = Y component surface wind stress (N/m^2).

T_{wr} = Rough turbulent skin friction shear stress for waves (N/m^2).

$\tau_{w,s}$ = Wave induced skin friction shear stress (N/m^2).

T_{ws}	=	Skin friction shear stress for waves (N/m^2).
T_{ws}	=	Smooth turbulent skin friction shear stress for waves (N/m^2).
τ_x	=	Wave force component that acts on a vertical plane that is perpendicular to the wave propagation direction (N).
τ_y	=	Wave force component that acts on a vertical plane that is parallel to the wave propagation direction (N).
θ	=	Direction of wave propagation (°).
θ_m	=	Mean wave direction (°).
θ_{cr}	=	Critical Shields parameter
θ_s	=	Shields parameter/ Entrainment function.
$\bar{u}$	=	X component depth averaged velocity (m/s).
$\bar{U}_{cr}$,$u_{c,cr}$	=	Current threshold velocity (m/s).
$\bar{U}$	=	Depth averaged velocity (m/s).
u_s	=	X component velocity by which water is discharged into ambient water (m/s).
$u_{w,cr}$	=	Wave threshold velocity (m/s).
U_w,u_w	=	Orbital wave velocity (m/s).
$U_{\tau b}$	=	Friction velocity (m/s).
u_*	=	Shear velocity (m/s).
v	=	Current speed (m/s).
$\bar{v}$	=	Y component depth averaged velocity (m/s).
v_s	=	Y component velocity by which water is discharged into ambient water (m/s).
X	=	Ratio of the total energy in the random wave train to the energy in a wave train with the maximum possible wave height.
z_0	=	Bed roughness length (m).

CHAPTER 1

INTRODUCTION

Chapter One defines and discusses the nature and scope of the research problem. An overview of the case study area and its history as well as a motivation for the investigation is presented. The primary aims and objectives of the study are stated.

1. Introduction

This research thesis investigates the wave driven flow patterns around a single isolated groyne are presented with respect to the following characteristics;

- Geometric parameters such as the ratio of the groyne length to the breaker zone width
- Variation in depth, to assess how tidally-driven water level changes affect the breaker zone width and the resulting flow patterns.
- Variation in permeability and how this affects the dominant flow pattern compared to impermeable groynes.

The focus is on wave driven currents since the coastline at the case study site in Durban, the KwaZulu-Natal coastline is oblique to the dominant wave directions this gives rise to the strong long-shore currents (Corbella and Stretch, 2012b). The aim of the research is to elucidate the dominant circulation patterns that correspond to different wave conditions. This in turn will give insight into erosion in the vicinity of the groyne structure so that mitigation measures can be implemented. The groyne used as a case study was the Bay of Plenty Pier on the central Durban coastline off the KwaZulu-Natal coast, South Africa (refer to figure 1-1).

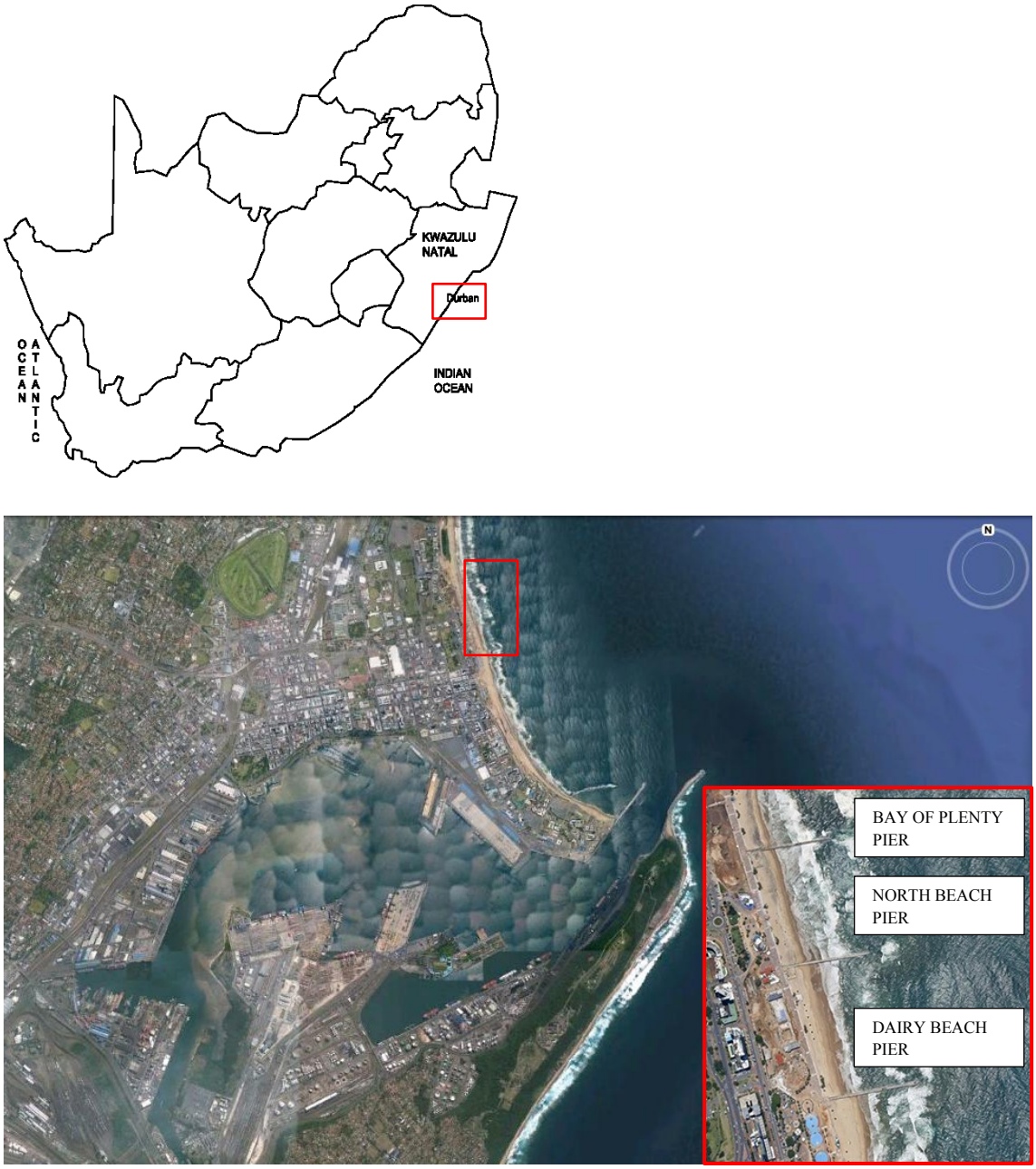

Figure 1-1: Overview of project location, highlighting Durban and the beachfront Piers (adapted from Google Earth, 2013).

1.1 Background of the Durban Central Coastline

The first recorded disturbance of the beaches was during the period 1851-1903 when harbour entrance channel works were initiated. This aggravated the beach equilibrium causing the beach to progress seawards (Jordan, 1970).

During the period 1903-1926 the increase in the harbour channel depth led to beach losses north of Vetch's Bight, the Bight itself still underwent deposition. Since 1905 the primary source of dredging has been from a sand trap south of the harbour entrance and from 1925 onwards the dredging rate has been relatively constant at about 600 000m^3 per annum (Jordan, 1970; Barnett, 1982). Subsequent to 1926 the Vetch's Bight showed more deposition, however the general Durban beaches continued to erode. A huge swell in 1934 caused excessive damage; this led to the Council commissioning the first sand pumping in 1935 in an attempt to nourish the South and Central Beaches (Bronsvoort et al., 2011). Sand was dredged from the moorings at the North Pier and delivered to the Vetch's Pier area where it was re-dredged and pumped as far northwards as the present day South Beach.

The northern Durban beaches continued to erode and during the period 1950-1953 sand was pumped by means of a submarine pipeline across the harbour mouth to the Vetch's Bight, directly, from a location south of the breakwater (Barnett, 1982). This method was considered ineffective due to there being insufficient sand collected from the location being used. The initial pumping scheme of 1935 was resumed.

During the period 1954-1956 two Paterson Groynes were built, this was in an attempt to stabilise the Central beaches by trapping the sand but this did not solve the problem. The erosion of the northern beaches still continued, however rip currents formed around the groynes, that together with the southerly and easterly swells created perfect wave conditions for surfing (Bronsvoort et al., 2011).

Research was carried out to further understand the problems in the current scheme being implemented to replenish the eroded beaches. The Paterson Groynes were replaced by two low level semi permeable groynes, with piers on top, which were constructed in 1983 and 1985. A third groyne was built between 1987 and 1988 to create beach profiles that were more acceptable (Mather, Kasserchun and Wenlock, 2003). The old groynes were replaced with low level groynes to ensure that not all the sediment south of the piers is trapped (Bronsvoort et al., 2011). The new groynes (refer to figure 1-2), the Bay of Plenty, North Beach and Dairy Beach piers, were designed by a partnership between the City Engineer's Department and the CSIR. They were constructed with precast elements and rock-fill was placed between the piles to a predetermined level (eThekwini Municipality, 2011). The rocks inside the pier formed a low level groyne. The new groynes resulted in a reduction of the rip currents reducing the size of waves previously recorded with the older groynes.

In 1998 the Bay of Plenty Groyne required repair; due to a large storm event - the southern seaward piles were undermined by excessive scour (Corbella and Stretch, 2012a).

Figure 1-2: Photograph of central Durban beachfront showing the Bay of Plenty, North Beach and Dairy Beach Piers from closest to furthest (South African Tourism, 2013).

Nourishments are an on-going process to date and there have been some improvements along the coastline. However not all the nourished sand is measured in the bathymetry surveys that the city carries out as half to two thirds is getting carried away by the alongshore current.

A severe storm hit the East coast in March of 2007 producing waves with a significant wave height of 8.5m (Corbella and Stretch, 2012a), causing serious damage along the coastline including Durban city. Since the event, Durban city has been trying to rectify the coastal damage done. Emergency measures were carried out to restore the beaches; making use of geosynthetic sandbags. This however did not remedy the problem as the storm event caused considerable erosion. The harbour sand pumping hopper was no longer available and therefore could not supply the sand to counter the total sand lost during the storm.

In 2007 the port of Durban initiated a widening of the access channel and extension of the breakwaters. The pump/hopper station used for pumping sand from the dredger to the booster stations and from there to the beaches was demolished to make space for the widening. This meant that sand could only be pumped to the first booster station, from where it was dumped onto Vetch's beach by use of the dredger.

During 2009 and 2010 the city had access to the dredger and took the opportunity to nourish beaches approximately 500 000 m^3 from an offshore location. The nourishment of the beaches was carried out in two phases on Addington beach (Corbella and Stretch, 2012a).

Whilst preparing for the 2010 Soccer World Cup, the city restored the low level groins. Due to the energetic wave climate the piers suffered settlement and therefore required restoration as well. There was still erosion taking place northwards of the piers, therefore the city lowered the height of the groynes along two thirds of the groyne length that was out to sea and only restored

one third the length of the stone construction to the original height close to the existing beach. Whilst the city was restoring the piers, they took the initiative to install pipes into them. The pipes were installed to allow for the pumping of sand directly into the surf zone in an attempt to restore the beaches, surf conditions and provide a protective beach front for Durban.

In 2012 the Bay of Plenty Pier was deemed unsafe and closed to the general public due to seaward pile failure (refer to figure 1-3).

Figure 1-3: Photograph of Bay of Plenty Pier south side pile failure, highlighted in red (adapted from EMS, 2013).

1.2 Motivation

Climate change is a serious problem and is one of the major causes due to global warming (Bell, Goring and de Lange, 2000).The warming of our climate system is unequivocal, as is evident from observations of definite increases in the global average air and ocean temperatures (Herbert, 2007). The climate change has been directly correlated with sea level rise, factors attributing to sea level rise include; thermal expansion of sea water, widespread melting of glaciers, small ice caps and ice sheets (Herbert, 2007; Warwick et al., 1996).

Another important consideration not to be overlooked is the increase in storm surges (Bell, Goring and de Lange, 2000) and the associated shift in weather patterns due to climate change. The sea level is elevated above the expected tide level due to; wind stress, low atmospheric pressure and continentally trapped waves (Bell, Goring and de Lange, 2000). This storm surge is superimposed on all other sea level fluctuations that act on the coast at any time.

The changes in storm intensities and rising sea levels have important environmental and socio-economic implications as they are adversely affecting the coastlines. The knowledge of changes is crucial for engineers and planners with regards to any form of coastal developments due to short term beach fluctuations and shoreline recession.

It is estimated that over seventy per-cent of the sandy shorelines around the world are eroding (Bird, 1985). The extent of such erosion would suggest that sea level rise is a large factor. However, there are many other processes that would contribute to this problem, that would need to be considered (Stive, Roelvink and De Vriend, 1990). There has been an increasing awareness of the impact that anthropogenic activities are having on various coastlines around the world, harbour constructions, maintenance of inlets, burgeoning worldwide of coastal populations leading to the expansion and development of coastal communities (IPCC, 1990). When faced with shoreline retreat and the loss of the natural protective and recreational beaches, a coastal community has very few alternatives; according to the IPCC (1990):

1. Retreat (relocation of structures landward)
2. Accommodate (raising of structures to projected flood levels)
3. Protect (building of soft or hard structures)

The preferred approach due to highly developed infrastructures and densely populated areas is protection (Fulford and Grosskopf, 1989). Groynes of varying design, both impermeable and permeable, have been used for coastal protection for many years. Their expected effects have only been marginally quantifiable (Raudkivi, 1996) and so their performance is still relatively poor, the design as such is still far from an exact science (Dong, 2004).

The understanding of morphological evolution in the vicinity of hard engineering structures is necessary for their design optimisation. The issue however is that the near-shore hydrodynamics and sediment transport processes, near coastal structures are highly complex (Nam et al., 2011).

Therefore, quantitative analyses on the flow patterns for groynes and the permeability rates are considered of practical use in evaluating their performance in field applications.

1.2.1 South Africa – East Coast

The Durban bight is continuously under attack by the Indian Ocean; as Durban is a morphologically active coast that is dominated by Easterly and Southerly swells. In general the Durban's beach profiles have been showing a decreasing trend (Corbella, 2010). The rough sea and yearly storms are responsible for the erosion and therefore retreat of the Durban coastline. There is also a mean long shore sediment transport loss rate in the Northward direction along the Durban bight averaging 300,000 m^3/year (Schoonees, 2000).

To protect the harbour from the energetic ocean, breakwaters were constructed. Not only do the breakwaters protect the harbour from the ocean but they also reduce sedimentation inside the harbour. The construction and extension of the breakwaters in later years has affected sediment flow to the Durban beaches. The breakwaters led to an interruption of the natural flow from South to North along the coastline which has changed the surroundings (Laubscher et al., 1990). The sand from the natural flow gets trapped and accumulates by the breakwater south of the harbour mouth (Mather, Kasserchun and Wenlock, 2003); the area of accumulation is known as a sand trap (Saxena, Vaidyaraman and Srinivasan, 1976). The rate of sediment transported into the trap at Durban is 500,000 m^3/year (Schoonees, 2000).

Due to the erosion of the beaches during swells and the breakwater hindrance of sediment flow, the semi-permeable low groynes are insufficient to trap sand and maintain the beaches. Nourishments are therefore necessary to restore the beaches. The sand necessary for the nourishments makes use of the harbour dredger; dredging sand from the sand trap by means of the sand bypass scheme (Barnett, 1999).

The depositing of sand nourishment on the beaches is only a temporary reprieve against long shore sediment transport. There is also insufficient sand quantities being dredged and dumped onto the beaches as nourishment, to counter the erosion taking place. This is due to operation being limited by availability of sand from the sand trap and when appropriate conditions are available for dredging (Corbella and Stretch, 2012b). The current soft measures have not improved the surf conditions.

A bathymetry survey in July 2011, as seen in figure 1-4, revealed severe scour occurring at the latter third of the trunks and tips of the Piers; Bay of Plenty, North Beach and Dairy Beach Piers. The Bay of Plenty Pier showed the worst scour conditions. There was a similar scour occurrence almost a year later in March 2012. The scour conditions at the Bay of Plenty Pier were far more severe in March of 2012, reaching a water depth of 10 metres, as seen in figure 1-5, than in July 2011 where it only reached a water depth of 8.3 metres.

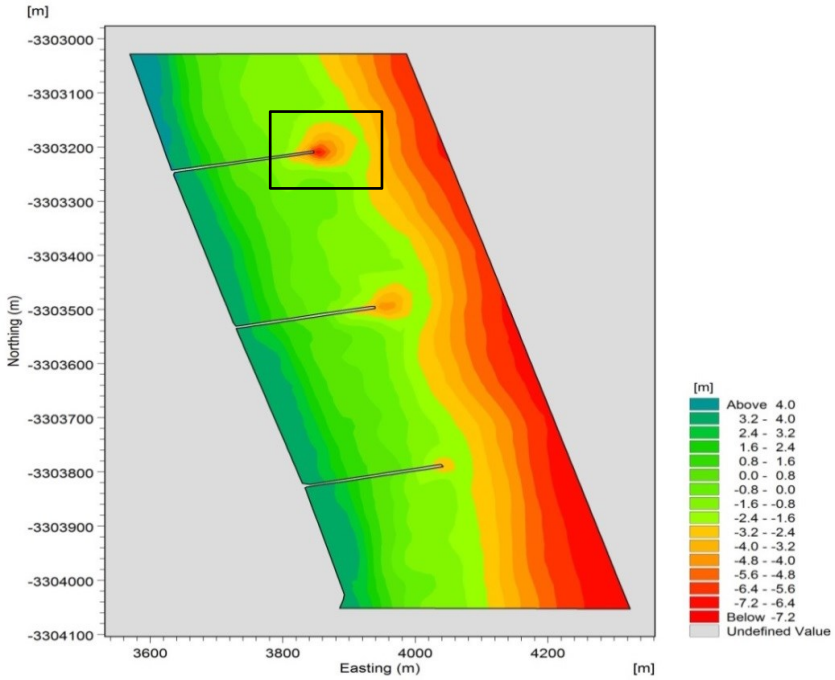

Figure 1-4: Bathymetry of Durban central beach front July 2011 relative to CD, Bay of Plenty Pier highlighted in black (adapted on MIKE from EMS, 2013).

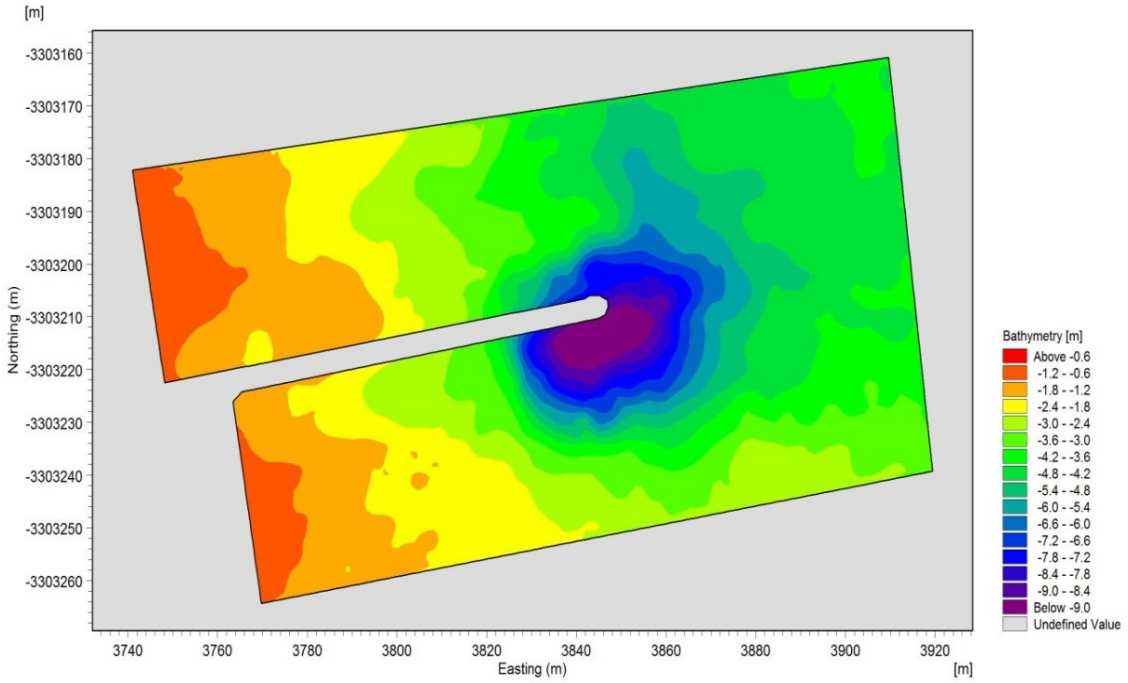

Figure 1-5: Bathymetry of Bay of Plenty Pier relative to CD, March 2012 (adapted on MIKE from EMS, 2013).

The pipes that were installed into the piers, if implemented effectively could potentially solve the various issues; the new sand bypass scheme is due to be operational by 2013 (Corbella and Stretch, 2012a). Insufficient sand quantities are being dredged to nourish the beaches. By applying sand nourishment directly into the surf by use of the pipes, it may lead to bathymetric changes. These changes could positively affect not only the surf conditions but the restoration of the beaches, by effectively using the sand that is available.

The piers, as stated previously, are low level crested groynes that act as semi-permeable groynes and have an uncertain permeability factor. The uncertain permeability factor is due to the groyne characteristics changing with wave and tide conditions. The functioning of any groyne system depends on a variety of hydraulic, morphodynamic and morphological factors (Trampenau, Oumeraci and Dette, 2004). One needs to consider the severe scour occurrences around the groynes and the failing of the Bay of Plenty Pier on two occasions. A better understanding of the situation is required before nourishment is carried out. The nourishments, be they onshore or in the nearshore, due to the pier pipes, could have an adverse effect on the coastal system.

It is important to therefore understand how the flow patterns around the groyne differ due to wave conditions; as nearshore processes are not only subject to complex spatial and temporal variations but also act interdependently of each other (Trampenau, Oumeraci and Dette, 2004; Nam et al., 2011). This will determine how the groyne reacts with the nourishments; this is with respect to erosion due to cross shore or alongshore dominant currents in the vicinity of the groyne.

If the research on flow pattern generation due to wave conditions around the Durban piers, based on permeability variations, shows adequate similarities it would allow for erosion predictions. By knowing how and when dominant currents occur due to waves, one can implement mitigation measures such as nourishment to reduce erosion. It will also determine when the optimum wave conditions are to release nourishment from the pier pipes. Early action would protect coastal structures and developments and minimise the adverse effects of the rough sea on the Durban coastline.

1.3 Topic

Flow patterns around groynes in the coastal zone.

1.4 Research Question

What flow circulation patterns develop due to the wave radiation stresses and the change in the wave field conditions with the tide? How do variations in the permeability factor affect the developing patterns around the groyne?

Can this be used to predict the effect of the wave conditions on the strength and dominance of flow patterns around a groyne, such that it allows for erosion prevention?

1.5 Aim

- To evaluate different types of flow patterns that develop in the vicinity of the groyne due to wave breaking.
- To evaluate how the permeability of the groyne affects the flow patterns around the groyne.
- To approximate how the wave breaking and flow around the groyne affects the bedload sediment.

1.6 Objectives

In order to achieve the overall aims various objectives need to be achieved. The objectives focus is on understanding the requirements, processes and techniques necessary for the accurate flow assessment of the parametric studies:

- To become fluent in the relevant modelling/simulating software by DHI.
    - MIKE 21 – Spectral Wave Model FM (Flexible Mesh)
    - MIKE 21 – Flow Model FM
- To understand, through both research and model studies, the fundamental hydraulic principles revolving around groynes.

  - To find out how circulation patterns generally occur around impermeable and permeable groynes.
  - An alternative method for the modelling of permeable groynes.
- To collect and consolidate the required data surrounding the area of interest;
  - Central Durban beach front.
  - Bay of Plenty Pier.
- To assess, using the collected field data, the validity of the parametric study results with the actual flow patterns occurring in the field.
- To consolidate the results from the model studies and the case study to evaluate whether or not it can explain the erosion occurring along the trunk and tip of the Bay of Plenty Pier.
- To estimate, using collected field data, the threshold velocities required for sediment motion and bedload sediment transport loads.
- To mention recommendations, concerns and mitigation measures with regards to groynes generically and then specifically towards the Durban beach front.

1.7 Dissertation Outline

This dissertation comprises of the following chapters:

Chapter Two pertains to a review of literature; the breaking of waves in the surf zone and how this affects currents and the effects thereof on erosion/ sediment transport. The hydrodynamics and effects on hydrodynamics due to permeability variance of groynes are discussed, followed by previous research on groynes.

Chapter Three discusses the numerical modelling; the methods, configurations and conditions for the simulations. It lists the details of all the simulations undertaken, according to their sections and the relevant reasoning behind the modelling for each section.

Chapter Four outlines the field work for the case study at the Bay of Plenty Pier, Durban Central Beach. This includes a breakdown of the preparations, procedures and analyses to be undertaken.

Chapter Five presents the results obtained for the first numerical modelling study where an attempt is made to reproduce existing work from a publication. It is a comparative discussion of the results and the differences between them.

Chapter Six displays the results obtained for the second numerical modelling study where simulations are carried out to observe the flow pattern behaviour around impermeable groynes. The result findings are discussed and summarised.

Chapter Seven presents the results obtained for the third numerical modelling study where uniform drag is applied to the column of water over an area in an attempt to mimic permeability. This is an assessment of the research considering the noticeable strengths and weaknesses of the methods developed to mimic permeability.

Chapter Eight displays the results for the fourth numerical modelling study where simulations are carried out to observe the flow pattern behaviour around permeable pile screens. This compares the differences in flow behaviour with respect to impermeable groynes as well. The result findings are discussed and summarised.

Chapter Nine presents the results obtained in the field investigation. A discussion of the results, explaining issues and observations are made during the case study. This is an assessment of the Eularian data and how it ties into the result findings of *Chapter Six* and *Chapter Eight*.

Chapter Ten contains a summary of the research conducted and conclusions for the respective investigations. Recommendations are made for future research according to the conclusions. The objectives of the research are met in this chapter.

The following appendices will form part of the report:

- Appendix A: Numerical Modelling
- Appendix B: Current meter and ADCP result data
- Appendix C: Pattiaratchi comparison result data
- Appendix D: Impermeable groyne result data
- Appendix E: Permeable groyne result data
- Appendix F: Sediment grading and sediment transport analysis

CHAPTER 2

LITERATURE REVIEW

Chapter Two consists of a literature review. The review explains the information required in understanding the processes around the Durban groynes. This comprises of mechanisms of erosion, wave breaking and the hydrodynamic processes that are present around groynes. It discusses how breaking waves in the surf zone and permeability variations affect the circulation patterns within the vicinity of the groynes. The effects of the groynes on sediment transport are also reviewed.

2.1 Introduction

Coastal erosion is a large problem occurring worldwide at various coastal sites due either to human activities or natural effects. To deal with this problem both hard and soft remedial measures for sandy beaches are undertaken, groynes are of course a hard engineering structure. They are specifically designed for the protection and stabilisation of shorelines (Bruun, Mehta and Johnson, 1978).

Coastal structures are built to reduce the coastal erosion and to maintain the beach width for the use of recreation. A hard structure however, is not a mitigation measure for storm-induced erosion of sandy dunes during conditions with high surge levels (Kraus, Hanson and Blomgren, 1994; Marchand, 2010).

2.1.1 Mechanisms of coastal erosion and coastal variability

The erosion of sandy beach systems due to waves during storms is a constant threat to the coastline. During storm events, sediment may either be transported onshore or offshore from the seafloor seaward of the surf zone. This implies that the nearshore area acts either as a source or sink for the shore sediment (Komar, 1996; Patsch and Griggs, 2006; Marchand, 2010). The severity of the coastal erosion threat is due to the permanent loss of sand from the beach system

and the level of erosion is dependent on the type of coast with respect to (Beach and Sternberg, 1996; Stive, Ranasinghe and Cowell, 2010);

- Beach slope
- Sediment composition
- Surge levels
- Exposure
- Wave climate

When considering coastal erosion it has both longshore and cross-shore components (Stive, Ranasinghe and Cowell, 2010). During extreme events, dune erosion is mainly a cross-shore process whereby the sediment from the static dune front is brought into the dynamic littoral system. The erosion of the dunes and beach is also an alongshore process and is due to the existence of longshore eroding currents and tidal currents. The shoreline within the littoral cell system is time dynamic since it changes with the seasons, the rhythmic changes of the tides, and climatic shifts on a long term scale e.g. sea level fluctuation (Patsch and Griggs, 2006).

Coastal variability, or shoreline variations, is the temporary loss of sand from the beach system (Stive et al., 2002). This is generally visible through the use of a trend line to note the variation of the shoreline. The erosion at the trend line is either due to natural causes or due to man-made developments such as groynes.

2.2 Surf Zone Processes

The surf zone or breaker zone shown in figure 2-1 is a region of utmost importance as most of the hydrodynamic forces driving sediment transport occur within this region. It is the region where the majority of waves break, dissipating their energy. The surf zone hydrodynamic forces are what typically determine the coastline's shape. This zone is characterised by water depths varying from 0 metres to 10 metres or up to depths that are two to three times the significant wave breaker height (Schoonees and Theron, 2002). When considering how hydrodynamic processes affect a coast there are three identifiable types of coastline (Davis and Hayes, 1984);

- Coast dominated by a balance of tides and waves
- Coast dominated by waves
- Coast dominated by tides

The South African coastline has an energetic wave climate (Mather and Stretch, 2011). The Durban coast is wave dominated and is therefore the driving factor behind the cross-shore and alongshore currents.

Section 2.2.1 will explain the forces that waves produce in a surf zone to gain insight into these important processes.

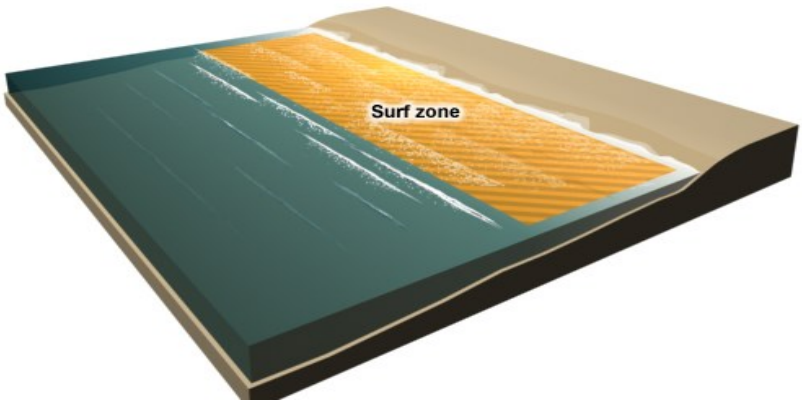

Figure 2-1: Sketch of the surf zone, source (UCAR, 2012a).

2.2.1 Waves

Waves are typically considered to be the driving force behind long-shore current development, transport of sediment and coastal morphology within the surf zone (Davis and Hayes, 1984). In reality wave fields tend to be very irregular and may vary in space and time.

- Long-shore currents bring new sediments from other locations as well as permanently removing sediment from the shore, this process is known as littoral drift; the littoral drift rate is dependent upon the wave energy, orientation of the shoreline, the angle of the dominant wave approach (Patsch and Griggs, 2006) and whether or not there are artificial obstructions.

Ocean waves are generally defined as the oscillation of the ocean surface due to tides, mean direction, wind and storm surges. For modelling purposes, waves are simplified making use of regular waves with sinusoidal shapes (Visser, 2002). The characteristics of a wave field are summarised by means of statistics into the properties of a single wave. The wave field is then characterised by the peak period (T_p [s]), direction of propagation (θ [°]) and a significant wave height in deep water (H_s [m]). This allows for the determination of the wave length (L [m]) and the celerity (c [m/s]) (Reeve, Chadwick and Fleming, 2004a).

There are two classifications of waves; deep water waves and shallow water waves. Emphasis will be placed on shallow water waves as the research carried out pertains to the surf zone near the shore, around groynes. Shallow water waves are affected by the sea bed, as the waves propagate shoreward the fluid particles' orbital motions tend from circular to elliptical due to the interaction with the sea bed (Brooke, 2003), as shown in figure 2-2. It is the continuously changing magnitude and direction of the orbital velocities that induce variations in the shear stresses along the seabed. This stirs up material for transportation by currents, this stirring affect increases when both waves and currents are present (Soulsby and Clarke, 2005).

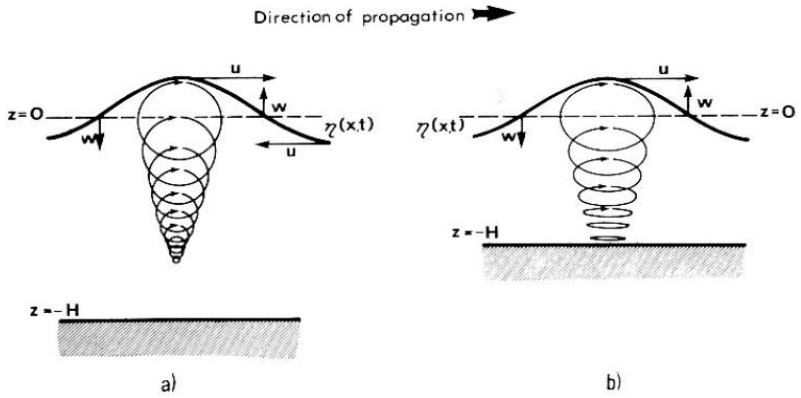

Figure 2-2: Approximate particle orbit motion for: (a) Deep water, (b) Shallower waters (Brooke, 2003).

2.2.1.1 Wave Breaking

As a group of waves propagate shoreward the waves begin to deform where the wavelength decreases and the wave height increases, thus becoming steeper. The wave will either become too steep or the wave height will become too high relative to the water depth, either case will result in the wave breaking (Visser, 2002; Reeve, Chadwick, and Fleming, 2004a).

The location or point at which wave breaking occurs is defined by two parameters, the breaker index and the wave steepness. The breaker index is the ratio between the wave height and the water depth (H/d) and the wave steepness is the ratio of the wave height to the wave length (H/L) (Battjes, 1974). In accordance with linear wave theory, as the wave approaches the coastline the wave height increases and the wave length decreases, this affects the breaker index (refer to equation 2-1) and the wave steepness (refer to equation 2-2). The two parameters are given by (Reeve, Chadwick and Fleming, 2004b):

$$\gamma = \frac{H}{d} = 0.78 \qquad \text{(Standard breaking index)} \qquad (2\text{-}1)$$

$$\frac{H}{L} < \frac{1}{7} \qquad \text{(Steepness limit)} \qquad (2\text{-}2)$$

Taking into consideration that waves over steepen, the breaking of waves occurs in water approximately as deep as the waves are high (Komar, 1998). Waves break, on average, when the wave height to water depth ratio value is 0.78 (McCowen, 1894), this value can reach 1.2 on steep beaches, and drop to 0.6 on flatter beaches (Galvin, 1972).

There were many empirical formulas proposed over the years for computing the breaking wave height, for example, Goda (1970), Weggel (1972) and Hansen (1990). There were however no conclusions as to which is the most reliable. Goda (1970) did however develop his breaking

criterion (refer to equation 2-3) from a number of experiments, boasting a wide range of results. This is the ratio detailing the limiting breaker height for regular waves, based on a collection of laboratory results was provided by Goda (2000). The only difference between Goda's (1970) and (2000) breaking criterion, is that the coefficient K_3 is given by 0.17 (regular waves). The equation that approximates the design diagram is given by:

$$\frac{H_b}{L_0} = K_3\{1 - \exp\left[-\frac{1.5\pi H}{L_0}\left(1 + 15\tan^{4/3}\beta\right)\right]\} \quad (2\text{-}3)$$

In which;

- H_b = Breaking wave height (m)
- L_0 = Deep water wave length (m)
- K_3 = Coefficient to allow for the effect of the transformation to irregular waves
- β = angle of the bottom slope/beach slope

To take into consideration that at the certain point where waves usually break, one must assess the probability of waves breaking, commonly referred to as the fraction of breaking waves (Kuriyama, 1996; Rattanapitikon and Shibayama, 1998). This the ratio of the number of breaking/broken waves to the total number of occurring waves. This ratio affects a variety of phenomena in the surf zone; nearshore currents, sediment suspension and morphological changes. The reason being breaking/broken waves has a much greater effect on the surf zone than non-breaking waves with respect to the wave induced turbulence, mass flux and momentum flux (Kuriyama, 1996). It is important therefore to consider this probability when determining the flow structures.

Battjes and Janssen (1978) assumed that the probability density function of wave heights is of a Rayleigh-type distribution. It was truncated at the breaking wave height H_b, for simulated variations in wave height H within the surf zone. This was carried out by giving breaking and broken waves the same H_b value. In accordance with the assumption; the root mean square wave height H_{rms} and the breaking/broken wave height H_b were used to estimate Q_b. Planar beach results from field and laboratory measurements carried out by Battjes and Stive (1985), Roelvink (1993) and Southgate and Nairn (1993) were compared to the estimated Q_b values from Battjes and Janssen's (1978) model. The estimated Q_b values were smaller than the Q_b values measured, the cross-shore estimated distributions of Q_b however, qualitively agreed with the field and laboratory measurements.

Battjes and Janssen's (1978) model for the probability of waves breaking; for a random wave train with a truncated Raleigh distribution of wave heights, the fraction of breaking waves Q_b is determined by equation 2-4:

$$\frac{Q_b - 1}{lnQ_b} = \left(\frac{H_{rms}}{H_m}\right)^2 \rightarrow Q_b = exp\left(\frac{-(1-Q_b)}{\left(\frac{H_{rms}}{H_m}\right)^2}\right) \quad (2\text{-}4)$$

In which;

- Q_b = fraction of breaking waves
- H_{rms} = root mean square wave height (m)
- H_m = maximum wave height, in shallow water, also known as H_b. (m)

The maximum wave height can be calculated from $H_m = \gamma d$, refer to equation (2-1).

When the wave breaks, the energy is dissipated in the form of a bore; due to the dissipation nearshore currents are induced. The energy dissipation causes radiation stress. Radiation stresses are important to consider as they drive long-shore currents.

2.2.3 Wave-induced currents

As waves break, the collected wave energy is dissipated which induces nearshore currents as well as a wave induced set up within the water level. With regards to coastal morphology; the induced nearshore currents are important processes in the overall behaviour of a given stretch of coast as they drive sediment transport. Research carried out by Longuet-Higgins and Stewart (1960) showed that swells or obliquely incident waves approaching a straight coastline will induce a mean current that is parallel to the coastline. These parallel currents, long-shore currents, are the cause for the alongshore transport of sediments and therefore influence morphological changes along the coast. Based off his earlier research on radiation stress generated by waves (Longuet-Higgins and Stewart, 1964), Longuet-Higgins (1970) derived the formulation of the long-shore current.

Waves contribute to the transfer of momentum in the water, known as radiation stress (Longuet-Higgins and Stewart, 1964). As energy is dissipated in the breaker zone, the radiation stress will decrease. Following in accordance with the balance of momentum; it results in a pressure gradient forming, or simply put the generation of a current (Longuet-Higgins, 1970). The propagation of oblique waves towards the coast, when breaking, decrease the radiation stress resulting in wave-driven current in the alongshore direction and wave-setup in the cross-shore direction. The radiation stress is therefore dependent on the wave characteristics.

Radiation stress plays a crucial role later in this study, for more in depth theory; please refer to appendix A, section A1.1.

2.2.4 Beach Morphological Type

When considering beaches it is important to know the relevant beach categories for wave formation. Research done by Wright and Short (1984) categorized beaches into three main morphological types as a function of the wave characteristics and the beach grain size. The types are; dissipative, intermediate and reflective.

- Dissipative beaches have low slopes (flat beach) such that short waves break far offshore and continue to lose energy as they cross the wide stretching surf zone with multiple low bars and generally comprised of fine sand.
- Intermediate beaches display morphodynamic states that occur between dissipative and reflective states. This beach has an intermediate slope, with one or two bars in the surf zone, rip currents, shore indentations such as cusps, and generally comprised of medium sand.
- Reflective beaches have steep slopes, no bars and the incident waves are forced to break close to the shore where they immediately wash up the beach face. This beach is generally comprised of coarse sand.

The area around the Durban central beach is that of an intermediary beach when considering its behaviour and natural composition (eThekwini, 2011).

2.2.5 Durban Wave Climate

At the Durban central beach the three Durban piers, semi-permeable groynes, modify the incoming waves adjusting their shape and generating strong rip currents to produce custom waves, the average swell ranges between 1.0 and 2.0 m (Preston-Whyte, 2002). Corbella and Stretch (2012c) re-analysed 18 years' worth of wave data off the KwaZulu-Natal coast using existing Waverider buoy and ADCP records (refer to figure 2-3 for Waverider and ADCP locations). They determined that the average peak period from the data set is 10.0 seconds, the average significant wave height is 1.65m and the average incident angle is 130 degrees.

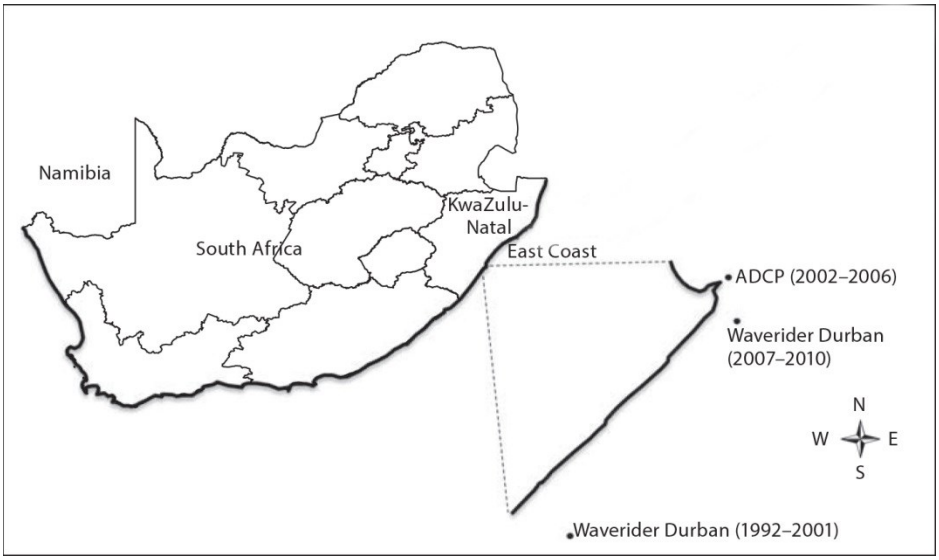

Figure 2-3: Map of South Africa showing KwaZulu-Natal with locations of Waverider buoys and ADCP (Corbella and Stretch, 2012c).

2.3 Groynes

Groynes are relatively long slender structures built into the sea, often perpendicularly to the coast (refer to figure 2-4). The application of a groyne is to reduce the alongshore currents and therefore reduce the littoral drift in the shore side surf zone, protecting against coastal erosion. This retains an amount of beach sand between the groynes allowing the beach to stabilise and widen seaward (Fleming, 1990) due to accumulation and/or redistribution of sand on the upstream side of the groyne resulting in a steeper coast profile (Sorenson, 1960). Groynes reduce the long-shore sand transport not only on the beach itself but also indirectly along the entire coast profile (Sorenson, 1960). The upstream accumulation affects the downstream sediment transport, considerably reducing it which leads to erosion on the downstream area.

There are two main types of beach groynes:

- Impermeable groynes
- Permeable groynes

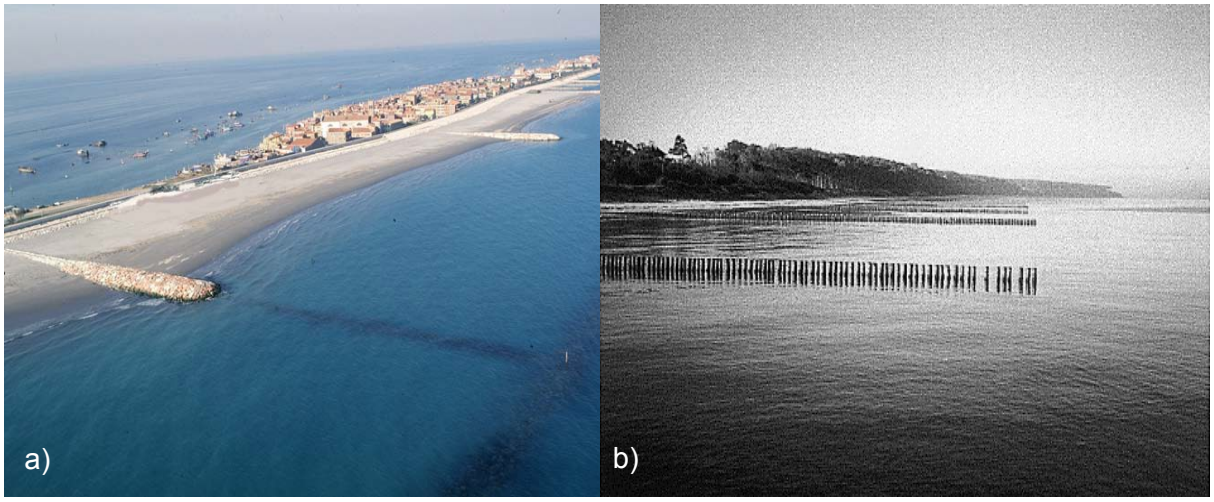

Figure 2-4: (a) Example of impermeable groynes (Lamberti and Zanuttigh, 2010) and (b) Example of permeable groynes (Raudkivi, 1996).

There is a fair amount of laboratory research with regards to the hydraulics of permeable and impermeable groynes. This however is related mainly to river groynes and was carried out in flumes, e.g. Rajaratnam and Nwachukwu, (1983); Uijttewaal, (2005); Teraguchi et al., (2008) and Kang et al., (2011).

There is detailed research regarding the functional design of groynes in a coastal environment such as that by Kraus, Hanson and Blomgren (1994) (refer to the comments shown in table 2-1).

This study deals with not only flow but the action of waves as well and with respect to this investigation there is very little decent research. The majority of the available research discusses only rip currents along the groyne, e.g. Shepard, Emery and La fond, (1941); Dolan et al., (1987); and Komar, (1998). The most detailed research on flow patterns around groynes with varied permeability was carried out by Trampenau, Oumeraci and Dette (2004), a large portion of this section will therefore refer to this work.

Table 2-1: Functional Properties attributed to groynes and their critical evaluation (after Kraus, Hanson and Blomgren, 1994).

Property	Comment
1. Wave angle and wave height are leading parameters (long-shore transport).	Verified through research. For fixed groyne length, these parameters determine by passing and the net and gross long-shore transport rates.
2. Groyne length is a leading parameter for single groynes. (Length controls depth at the tip of the groyne.)	Verified through research, with groyne length defined relative to the surf zone width.
3. Groynes should be permeable	Verified through research. Permeable groynes allow water and sand to move alongshore, and reduce rip current formation and cell circulation.
4. Groynes function best on beaches with a pre-dominant long-shore transport direction.	Verified through research. Groynes act as rectifiers of transport. As the ratio of gross to net transport increases, the retention functioning decreases
5. The up drift shoreline at a groyne seldom reaches the seaward end of the groyne.	Verified through research. Due to sand bypassing, groyne permeability, and reversals in transport, the up drift shoreline cannot reach the end of a groyne by long-shore transport processes alone. Onshore transport is required for the shoreline to reach a groyne tip.

6. Groynes cause impoundment to the farthest point of the up drift beach and erosion to the farthest point of the down drift beach.	Verified through research. Sand will be impounded along the entire up drift reach, causing erosion down drift of the groyne.
7. Groynes erode the offshore profile.	Questionable and doubtful. No clear physical mechanism has been proposed.
8. Groynes erode the beach by rip current jetting of sand far offshore.	Questionable. Short groynes cannot jet material far offshore, and permeable groynes reduce the rip current effect. However, long impermeable jetties might produce large rip currents and jet material beyond the average surf zone width.
9. For beaches with a large predominant wave direction, groynes should be orientated perpendicular to the breaking wave crests.	Tentatively accepted. Oblique orientation may reduce rip current generation.

2.3.1 Impermeable Groynes

Impermeable groynes generally block the entire long-shore transport and current acting over the full length of the groyne diverting the long-shore transport system seawards (Trampenau, Oumeraci and Dette, 2004). This may differ with design due to low crested weirs which allow through flow under certain conditions such as high tide. The alongshore blockage induces circulations and rip currents which result in a transportation of sediment seawards on the up drift side of the groyne. If the groyne is built in a wave climate with one predominant wave direction then this will result in the typical saw-tooth bathymetry with scouring near the groyne heads due to rip currents.

An impermeable groyne typically creates a sheltered zone on the lee side where the flow past this zone due to fluid drag on the open boundary generates a circulation (i.e. a large scale eddy); the greater the velocity differential the greater the vorticity within the circulation pattern (Raudkivi, 1996).

The issue with a groyne is that it introduces excessive local down drift erosion and long-shore variability (van Rijn, 2011). This is not beneficial towards controlling erosion when other sustainable methods are available for use.

2.3.1.1 Impermeable groyne flow

Irrespective of groyne permeability, it is the change in water level conditions that play an important role in the hydraulic functioning of the groyne. Water level change induces gravity currents (Trampenau, Oumeraci and Dette, 2004). Impermeable groynes induce stronger gravity currents due to the sheltering of the lee side of the groyne.

A recirculation zone is produced on the lee side of a groyne due to the groyne geometric parameters affecting the water level and constricting flow; this develops an eddy flow in the alongshore current (Raudkivi, 1996).

The flow patterns in the alongshore and the recirculation zone differ because the groyne geometric parameters and the permeability can affect not only the groyne tip velocity angle but the magnitude of the flow separation at the tip. A separation layer represents the spatial extent of the recirculation zone, and the distance between the groyne and the end of the separation layer is defined as the separation length (Teraguchi et al., 2008). A field study carried out by Pattiaratchi et al., (2009) using both Lagrangian and Eularian methods confirmed the lee side recirculation zone, where a large eddy was occurring. Figure 2-5 shows the schematic of a recirculation zone.

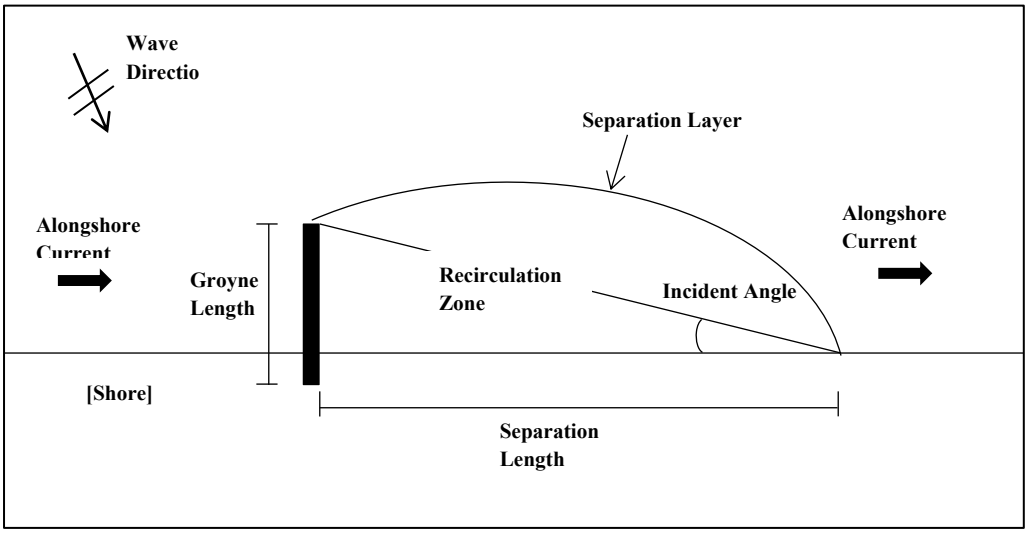

Figure 2-5: Schematic sketch of the recirculation zone for a single groyne.

When angled waves approach the groyne, wave refraction and diffraction produce smaller waves in the leeward side of the groyne this results in a wave set-up field producing an alongshore current flowing towards the groyne (Pattiaratchi et al., 2009). Strong and narrow currents that flow seaward through the surf zone are known as rip currents (MacMahan et al., 2004; MacMahan, Thornton and Reniers, 2006); they affect shoreline migration and nearby sediment transport process (Brander, 1999). The groyne deflects the alongshore generated current offshore, forming rip currents adjacent to the groyne. The deflecting influence of the groyne evidently plays an important part in localizing these currents. When rip currents dominate sediment is sent back out to sea (Dolan et al., 1987), creating channels around the structure (Shepard, Emery and La Fond, 1941).

Figure 2-6 is a schematic displaying the resultant flow patterns in an impermeable groyne field. For the resultant flow patterns of a single impermeable groyne only; zone 1 is taken as the upstream flow and zone 3 is taken as the downstream flow, excluding zone 2.

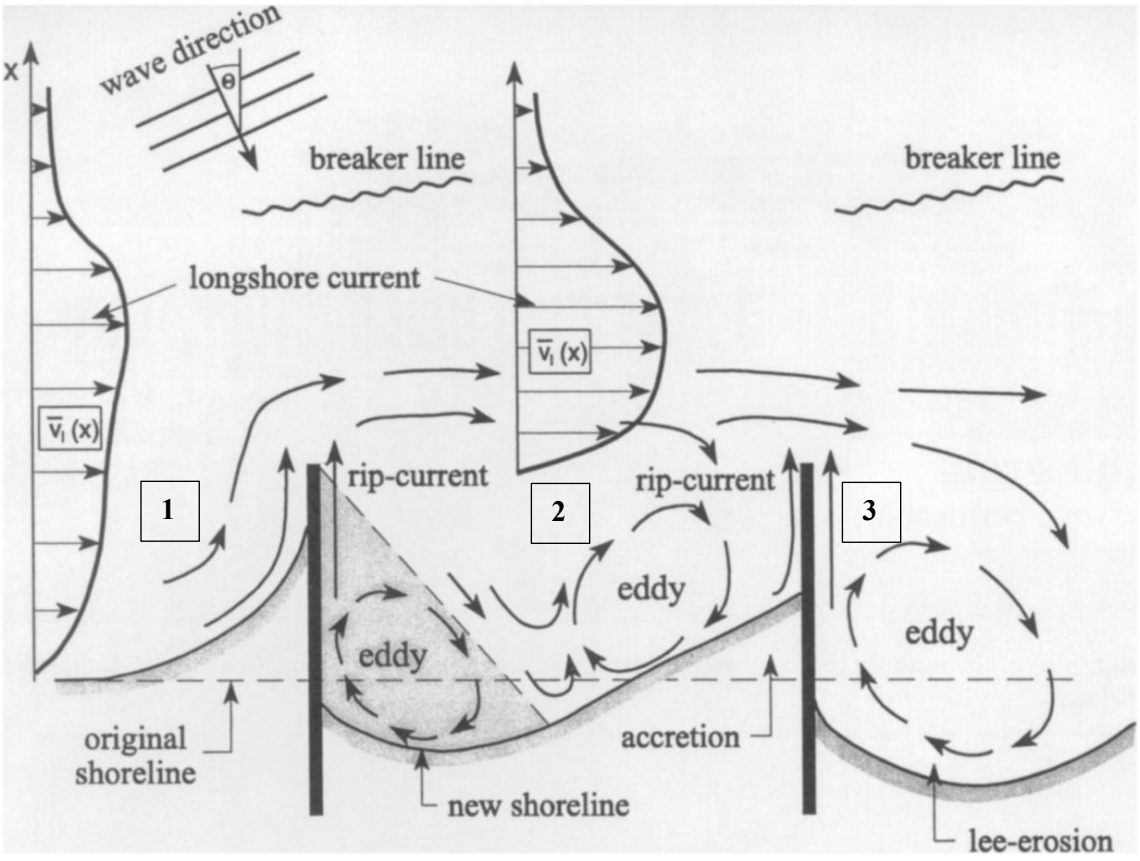

Figure 2-6: Schematic of resulting flow patterns and shoreline configuration in groyne fields with impermeable groynes (after Trampenau, Oumeraci and Dette, 2004).

Large scale physical models carried out by Trampenau, Oumeraci and Dette (2004) showed that for a single groyne with permeability ≤ 10 per cent (impermeable behaviour as there was no noticeable flow through the groyne) there was a rip current both on the upstream and downstream trunk of the groyne, a large eddy on the lee side of the groyne and a deviation of the alongshore current seaward of the tip of the groyne due to the flow obstruction of the impermeable structure. This coincides with previous research. Water level induced currents were listed as dominant for this groyne.

2.3.2 Permeable Groynes

Permeable groynes can range drastically in characteristics depending on the percentage of permeability. Bakker led the first known attempts in systematically studying the functioning of pile groynes and their relative effectiveness; this was summarised in Bakker et al (1984). Permeable groynes tend to make use of piles placed with varying spaces between centres. The purpose of permeable pile screens is to act as an artificial hydraulic resistance, this decreases the alongshore current velocity and thus decreases the rate of alongshore sediment transport (Bakker et al., 1984). By varying the openings between the piles the flow gradient along the shore can be adjusted (Shiereck, 2004).

Over the whole length of the groyne the alongshore velocities are reduced, the seaward velocities are far less than those of the impermeable groyne (Trampenau, Oumeraci and Dette, 2004) due to through flow between the piles. Permeable pile groynes are designed to reduce the littoral current velocity such that rip currents and large scale circulations are minimized.

The pile screens therefore reduce the stirring up and the transporting of sediment, without directly inducing a decrease in the primary wave action (Shiereck, 2004). The groyne allows for sediment bypassing which reduces leeside erosion of the groyne and produces a more natural, continuous, shoreline. The permeable groyne results in a more continuous beach line compared to the saw-tooth beach line which is predominant with impermeable groynes (Bakker et al., 1984). The saw-tooth beach line does occur however if the permeability of the groynes is too low, as illustrated by Kolp (1970) in the use of luminescent sands.

Permeable groyne structures are known to have a few problems occurring as observed by (Bakker et al., 1984);

- Failure at seaward side, where piles are dislodged
- Erosion at the groin toe

- A decrease in permeability due to mussel growth in the sea zone, increasing the velocities within the groyne
- Increased rip-current magnitudes, leading to the attraction of rip channels, with consequent seaward sand loss

2.3.2.1 Permeable groyne flow

To flow through the cross sectional slots in the piles the water has to accelerate, on the lee side the flow loses energy due to expansion (Raudkivi, 1996; Dette, Raudkivi and Oumeraci, 2004). This accelerated flow has been found on occasion to induce scour around the piles (Bakker et al., 1984). The wave setup creates the necessary build-up of water; the setup also generates a gradient for flow seaward along the groyne (Raudkivi, 1996).

The effect of pile groynes on waves is small (Dette, Raudkivi and Oumeraci, 2004) therefore the pile groynes must function dominantly on the velocity, velocity distribution and turbulence within the vicinity of the permeable groyne. To the waves, a pile groyne acts as a permeable breakwater; a large permeability will cause little decay of the waves (Raudkivi, 1996) and as the permeability increases the effect on the alongshore current becomes less.

Research carried out by Kolp (1970) indicated that the pile groynes should not be too closely positioned near the shore; there should be a certain level of permeability thereby allowing shore parallel movement within the swash zone, reducing any tendency for rip currents to occur.

Pile groynes reduce the velocity through the groyne and increase the velocity in the alongshore direction seaward of the structure (Dette, Raudkivi and Oumeraci, 2004; Trampenau, Oumeraci and Dette, 2004), as shown in figure 2-7.

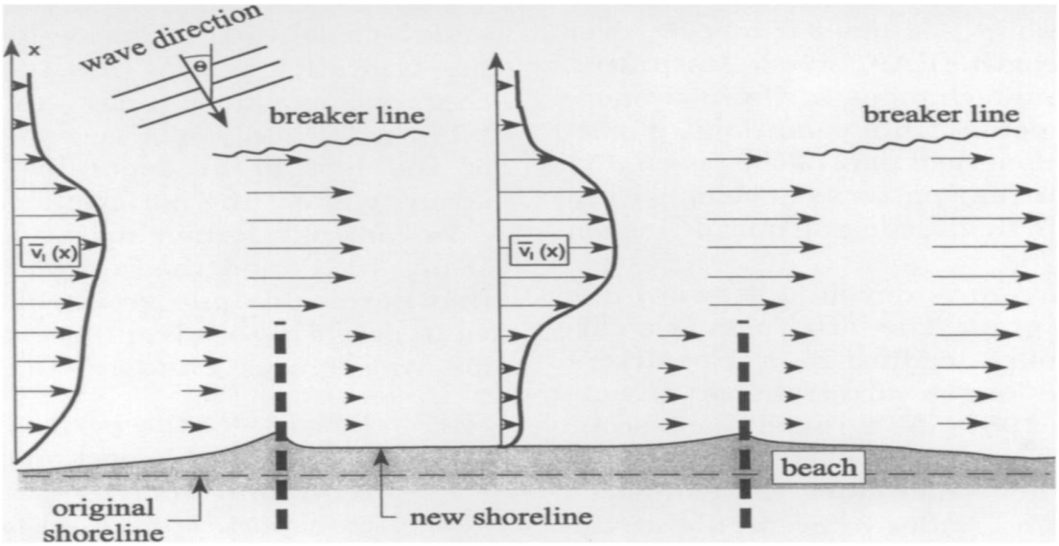

Figure 2-7: Schematic of resulting flow patterns and shoreline configuration in groyne fields with permeable groynes (Trampenau, Oumeraci and Dette, 2004).

The interaction between the slower currents downstream of the groyne piles and the faster currents seaward of the groyne is an area of steep velocity gradients; this induces circulation and therefore numerous small eddies are formed (Raudkivi, 1996; Dette, Raudkivi and Oumeraci, 2004).

When the permeability of a groyne is less than 20 per cent, large eddies form in the lee of the groyne (Trampenau, Oumeraci and Dette, 2004) and less than equal to 10 per cent behaves impermeable (Teraguchi et al,. 2008).

For a wave energetic climate, the long-shore current is wave induced; as such the current downstream will be accelerated by the wave action. At some distance downstream of the groyne it will reach a velocity as that with a coast without any groynes. A permeable groyne also undergoes a recirculation zone on the lee side like an impermeable groyne where there is a separation length, however this occurs with many small eddies (Bakker et al., 1984).

Large scale physical models carried out by Trampenau, Oumeraci and Dette (2004) showed that for a single groyne of permeability $\geq$ 20 per cent there was a minor rip current on the upstream side of the groyne, no rip current downstream of the groyne and a minor deviation of the alongshore current seaward of the tip of the groyne. Alongshore currents are dominant for this groyne.

2.3.3 Wave Breaking in the context of groynes

Waves interact with groynes by: diffraction around the groyne tip, reflection off the groyne structure and/or propagation over the groyne. These interactions contribute to the complex flow patterns, moving sediment alongshore and offshore of the groyne's location (Dean, 1978). The interactions will vary during the tidal cycle when the water depth changes.

The relative ratio of the groyne length to some statistical measure of the breaking/surf zone width, is an important factor in sand bypassing due to alongshore currents. A parameter was established by, Taranowska (1985) (Trampenau, Oumeraci and Dette, 2004) to describe the functioning of groynes. The ratio of groin length to the width of the breaker zone (G_L/B_z) represents the level of constriction of the cross-sectional flow. The issue however is that this concept was initially developed for impermeable groynes and the permeability factor on groynes has been neglected from this concept.

2.3.3.1 Effects of the level of constriction on groynes

Trampenau, Oumeraci and Dette (2004) made the following observations for a groyne with permeability $\leq$ 10 per cent;

For a $G_L/B_z = 1.0$;

- There is a rip current on the upstream side of the groyne and a lee side rip current due to a large circular lee side eddy in the recirculation zone with low velocities. The alongshore current is increased seaward of the tip of the groyne. The strongest alongshore currents at the tip of the groyne.

For a $G_L/B_z = 0.7$;

- Rip currents become negligible.

For a $G_L/B_z = 0.625$;

- A decrease in the level of constriction was observed to decreases the alongshore current seaward of the tip of the groyne. An elliptical lee side eddy in the recirculation zone with increased vorticity.

Trampenau, Oumeraci and Dette (2004) made the following observations for a groyne with permeability ≥ 20 per cent;

For a $G_L/B_z = 1.0$;

- There was a minor rip current on the upstream side of the groyne, no rip current downstream of the groyne and a minor deviation of the alongshore current seaward of the tip of the groyne as there was through flow. The alongshore through flow was uniform.

For a $G_L/B_z = 0.625$;

- Similar to $G_L/B_z = 1.0$. Alongshore currents are smaller in magnitude.

2.3.3.2 Effects of the level of constriction on groyne erosion

Walker, Dong and Anastasiou (1991) carried out research with respect to the sediment transport near groynes in the nearshore zone. The research made use of a bathymetric evolution model to predict bottom changes around groynes. The calculations assumed that the sediment responded quickly to changes in the capacity of the flow to transport sediment, to result in local equilibrium. The results of the sediment transport near groynes were displayed using a level of constriction, as shown in figures 2-8 to 2-10.

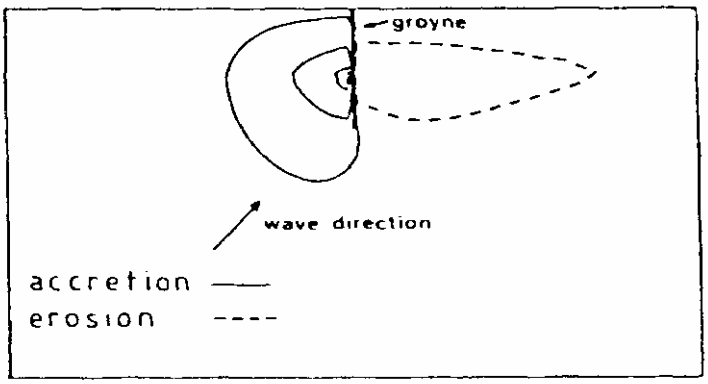

Figure 2-8: Accretion/erosion zones for $G_L/B_z = 2.0$ (Walker, Dong and Anastasiou, 1991).

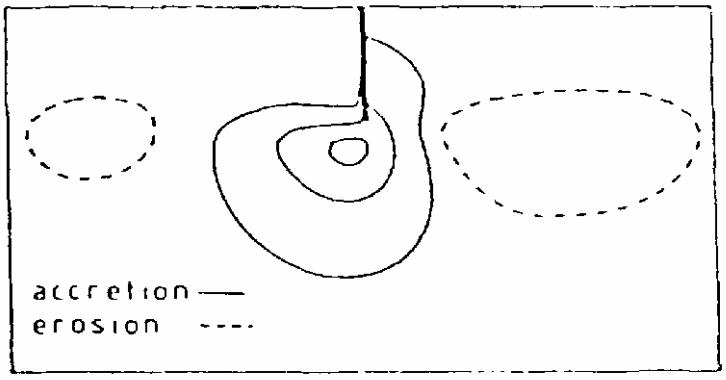

Figure 2-9: Accretion/erosion zones for $G_L/B_z = 1.0$ (Walker, Dong and Anastasiou, 1991).

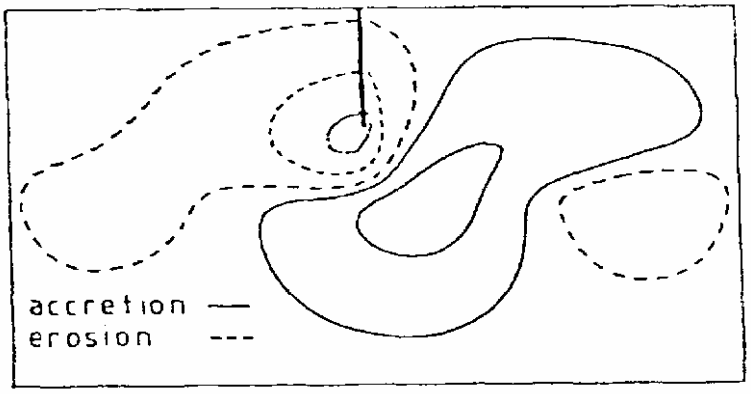

Figure 2-10: Accretion/erosion zones for $G_L/B_z = 0.67$ (Walker, Dong and Anastasiou, 1991).

Figure 2-8 is similar to the typical groyne pattern displaying a build-up of sediment on the updrift side, leading to the saw tooth behaviour. As the level of constriction decreases and the breaker zone increases in width the pattern changes significantly as seen in figures 2-9 and 2-10. The groyne begins to deflect the nearshore currents, leading to increased erosion off the end of the groyne tip; leading to downstream accretion.

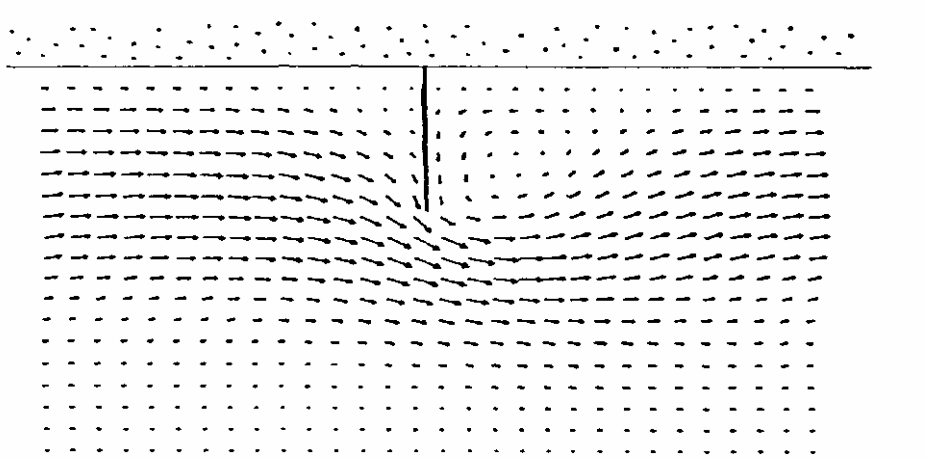

Figure 2-11: Nearshore currents for $G_L/B_z = 0.67$ (Walker, Dong and Anastasiou, 1991).

Figure 2-11 is the modelled current flow around the groyne for figure 2-10. In this instance the groyne is two thirds the width of the breaker zone from the shoreline. The diversion of the flow along the breaker line is evident. The strong groyne tip currents and lee side rip current caused by the eddy coincide with figure 2-9 erosion zones. A similar behaviour to figure 2-10 and figure 2-11 was observed by Hulsbergen, Bakker and van Bochove (1976) during physical model studies; where groyne tip erosion led to downstream accretion of the groyne.

The research carried out by Walker, Dong and Anastasiou (1991) as displayed in figures 2-8 to 2-11 consisted of numerical models only. They were not tested against actual field data where structures were present nor against laboratory experiments.

2.4 Summary

Though there is an abundance of research on groynes, there is little on the topic of groynes in the coastal zone and the flow patterns surrounding them. The research that is available made use of observations (e.g. Bakker et al., 1984; Raudkivi, 1996), physical laboratory models (e.g. Trampenau, Oumeraci and Dette, 2004) or numerical modelling (e.g. Walker, Dong and Anastasiou, 1991). There was only one instance where field data was used to display the flow pattern around a groyne (e.g. Pattiaratchi et al., 2009). The published paper was on lee side circulation due to waves. There were no models tested against, or compared with actual field data where the groyne was present.

Our understanding of groynes needs to be enhanced to improve the functionality of these structures (Hanson and Larson, 2004). This was seen with respect to the comments made by Kraus, Hanson and Blomgren (1994) as shown in table 2-1. There has been little improvement on the functional properties attributed to groynes since then.

From the literature about groynes it can be seen that there are similarities between the observed flow patterns around groynes, (Bakker et al., 1984; Dolan et al., 1987; Trampenau, Oumeraci and Dette, 2004) but insufficient research towards how the patterns change and what affects these changes. Walker, Dong and Anastasiou (1991) and Trampenau, Oumeraci and Dette (2004) made reference towards the groyne length in context of the breaker zone width. The breaker zone width with respect to the probability of waves breaking is an important factor to consider, as its area of action and intensity determines the alongshore currents (Longuet-Higgins and Stewart, 1964; Longuet-Higgins, 1970).

Walker, Dong and Anastasiou (1991) showed that the breaker zone width affects the sediment transport around a groyne. To understand how sediment is transported, an understanding of the flow patterns around a groyne is required. By varying the breaker zone width for the same groyne length changes in the flow patterns were observed in the literature. This ratio of groyne length to breaker zone width was only overviewed however and not discussed in detail by the literature found. The ratio of groyne length to breaker zone width or level of constriction of cross-sectional flow (Taranowska, 1985) will be used to identifying and classifying the flow patterns around a groyne. This is for the purpose of determining the flow conditions for any groyne.

CHAPTER 3

METHODOLOGY - NUMERICAL MODELLING

Chapter Three presents a general description of the numerical modelling undertaken using the DHI MIKE 21 package. The MIKE 21 modules used in the study, and key assumptions, are outlined. Furthermore, idealised test cases modelled in MIKE 21 are described and compared to published results in order to develop the basic methods for application in the main schematized simulations.

3.1 MIKE 21 - General Description

The MIKE 21 numerical model developed by DHI was used for the present study. MIKE 21 is a two-dimensional (depth averaged) process-based numerical modelling package. It comprises of different modules that focus on specific processes (hydrodynamics, waves, sediment transport, morphological changes, and water quality). Modules can be coupled to interact with each other. This study focuses on computations of wave-driven flow patterns around impermeable and permeable groyne structures. Only the Spectral Wave and Flow modules were used in this study.

3.1.1 Spectral Wave-model

MIKE 21 SW FM is a spectral wind-wave model that uses an unstructured (flexible) mesh for the numerical solutions. It is used to simulate waves in coastal and offshore areas and describes the growth, decay and transformation of wind generated waves. MIKE 21 SW computes the wave spectra as they approach the shoreline and the associated radiation stresses that drive a nearshore flow field.

MIKE 21 SW FM has been used extensively for other investigations and has been thoroughly validated, particularly in engineering applications e.g. Johnson et al., (2005).

Refer to appendix A section A1 for in-depth detail of the governing equations used for the spectral wave modelling, which are based on the principle of wave action conservation.

3.1.2 Flow-model

MIKE 21 HD FM is a flexible mesh flow model that is used for simulating unsteady hydrodynamics using a two-dimensional (depth averaged) formulation. Documentation provided by DHI (Sorenson et al., (2004); MIKE21 (2011)) provides detailed descriptions of transport and flow governing equations, and numerical solution methods.

The flow model was developed for applications in coastal, oceanographic and estuarine environments.

Refer to appendix A section A2 for in-depth detail of the governing equations used for the flow modelling, which are based on the principle of continuity and horizontal motion.

3.2 Overview of the simulation methodology

There were four separate numerical modelling sections carried out for the purpose of understanding the hydraulics around groynes in coastal waters. The first comprised of a comparison with a previous study of impermeable groynes, followed by three parametric studies that expand on previous work to include a wider range of conditions including changes to the depth and effective permeability of the structures. The fifth section was not a numerical modelling study it did however make use of the numerical modelling sections in conjunction with the field measurements carried out at the case study site. The studies are listed below:

- Study 1: Pattiaratchi Comparison
- Study 2: Simulation of flow around impermeable groynes
- Study 3: Changes to permeability by friction manipulation
- Study 4: Simulation of flow around permeable pile screen groynes
- Study 5: Field study analysis

The remainder of section 3.2 gives an overview of what each of these numerical modelling studies entailed.

3.2.1 Study 1: Pattiaratchi Comparison

A paper written by Pattiaratchi et al (2009) made use of MIKE 21 software to assess "Wave-driven circulation patterns in the lee of groynes". The paper made use of an idealized, schematized problem comprising of a straight coastline, uniform beach slope and simplified wave conditions. As the problem was idealized it made for a good first test case. An attempt was therefore made to reproduce the simulation results reported in that publication.

The same model setup and configuration described by Pattiaratchi et al., (2009) was used to run simulations and to compare the results against those published in their paper. In addition simulations were carried out with the same incident wave conditions but with a modified shoreline boundary condition comprising of a sloping beach instead of the closed boundary used by Pattiaratchi et al., (2009). The sloping beach allows for wave run-up and reduces wave reflection that can occur at closed boundaries.

In addition to numerical simulations, Pattiaratchi et al., (2009) also carried out some limited Lagrangian and Eularian measurements at a case study site to measure the flow patterns and rip

current speeds generated around an impermeable groyne. The data can be used for general validation of the numerical model, although details, such as bathymetry, were not reproduced in the modelling.

3.2.2 Study 2: Simulation of flow around impermeable groynes

A detailed parametric study of the effect of the breaker zone width on flow characteristics surrounding impermeable groynes was undertaken. The onshore boundary condition comprised of a uniform beach slope. Simulations were run by varying the water depth, groyne length and wave parameters in order to change the breaker zone width which in turn changed the flow patterns.

This study comprised of only numerical experiments - no field or laboratory measurements were carried out to validate the model.

3.2.3 Study 3: Changes to permeability by friction manipulation

The purpose of this parametric study was an attempt to develop a simplified method to mimic the effects of semi-permeability by manipulating the drag terms in the governing equations. This included both bottom friction and applying a uniform drag through the water column at the location of the groyne so as to impede flow to varying degrees. This approach obviates the need to model the flow through complex geometric elements such as pile screen structures which require detailed mesh generation to resolve the resulting small scale flow structure. Such models can lead to problems with numerical stability and accuracy, and add considerably to computational resource requirements.

The Spectral Wave model (SW) and the Flow model (FM) use different formulation for the bed friction, for this reason the models use different bed friction terms. The SW model uses the friction coefficient value C_f and the FM model uses the Manning's M value. When manipulating the C_f value in the SW model, the M value in the FM model has to change as well to correspond with the change in C_f. This study will attempt to use the bed friction terms to induce drag.

This section comprised of two friction manipulation methods to mimic permeability, whereby the coefficient of friction in the Spectral Wave model and the Manning friction number in the Flow Model were manipulated:

1. A constant coefficient of friction and varying Manning values. (As depth increases the drag will decrease).
2. A coefficient of friction proportional to the depth (i.e. drag assumed distributed uniformly over the water column in the depth-averaged formulation) and varying Manning values.

For the FM model the governing equations are depth averaged. This is why if the C_f is made proportional to the depth i.e. C_f x h, the friction term becomes independent of the depth. This has an effect equivalent to applying a uniform drag over the water column rather than only a friction at the bed.

When adjusting the drag, the drag terms were consistent for both the spectral wave and the flow model. This study comprised of only numerical experiments - no measurements were carried out to validate the model.

3.2.4 Study 4: Simulation of flow around permeable pile screen groynes

This parametric study focussed on understanding the flow around a permeable pile screen structure. A single row permeable pile screen was simulated with varying permeability. The permeability was varied by adjusting the size and spacing of the pile screen. Other parameters that were varied included the following:

1. Permeable pile screens of varying permeability over a 100m length
2. Permeable pile screens of varying permeability over a 200m length

The results of this parametric study were compared with those of the impermeable groyne parametric study (Study 2) and the changes to permeability by friction manipulation parametric study (Study 3). The comparison focussed on the flow patterns, alongshore flow fluxes, cross-shore and alongshore velocities as well as level of constriction of cross-sectional flow values.

This study comprised of only numerical experiments – no measurements were carried out to validate the model.

3.2.5 Study 5: Field study analysis

This study used the level of constriction of cross-sectional flow data from the impermeable and permeable groyne parametric study simulations, to comparatively assess the flow patterns observed at the case study site. The comparison was carried out for the purpose of evaluating whether or not the data simulated correlated well with Eularian measurements from the case study site.

In Study 2 and Study 4, no measurements were carried out to validate the models. The models were however compared with field measurements to discern the general terms with respect to flow patterns around groynes.

3.3 Configuration of Models

3.3.1 Standard Model Parameters

The idealised model setup for the four numerical modelling sections comprised of the following standard parameters with regards to the domain configurations (refer table 3-1):

- A constant linear beach profile with a slope of 1/50
- The domain extended 1500m in the cross-shore direction and 4000m in the alongshore direction. Study 1 was an exception - refer to table 3-1.
- The groyne central axis lay midway on the alongshore axis, at 2000m.
- A triangular mesh with a grid resolution ranging from 100m^2 in the region around the groyne to a maximum 6400m^2 offshore was used. Exceptions were study 1 and study 4 where the resolutions were 100m^2 to 900m^2 and 25m^2 to 3200m^2 respectively (refer to table 3-1).

Table 3-1: Domain configurations for numerical modelling studies

Numerical Modelling Study	Overview
Study 1: Pattiaratchi Comparison	<u>Groyne Geometry:</u> • Shore-normal impermeable groyne; 20m wide, extending 200m in the cross-shore direction and was modelled as a land boundary. <u>Domain:</u> • The domain extended 1000m in the cross-shore

	direction and 4000m in the alongshore direction. The domain depth range according to a 1:50 slope is therefore 0m above sea level and 20m below sea level. <u>Mesh solving:</u> • A triangular mesh with a grid resolution ranging from 100m^2 in the region around the groyne to a maximum 900m^2 offshore was used. The grid resolution used was significantly finer than that used by Pattiaratchi et al., (2009) who used grid sizes ranging from 10m to 80m (grid areas from 100m^2 to 6400m^2). A finer resolution was used in this study in an attempt to better resolve the flow throughout the domain.
Study 2: Impermeable Groynes	<u>Groyne Geometry:</u> (Three groyne configurations) 1. 20m wide, extending 200m beyond the 0 MSL in the cross-shore direction, however it is 500m long with 300m on land and 200m extending into the water. It was modelled as a land boundary. 2. 1m wide, extending 200m in the cross-shore direction, however it is 500m long with 300m on land and 200m extending into the water. It was modelled as a land boundary 3. 1m wide, extending 100m in the cross-shore direction, however it is 500m long with 300m on land and 100m extending into the water. It was modelled as a land boundary
Study 3: Friction Manipulation	<u>Drag Geometry:</u> • The geometric area over which the coefficient of drag and Manning's numbers were manipulated were as follows; shore-normal 20m wide, extending 200m beyond the 0 MSL in the

	cross-shore direction, however it is 500m long with 300m on land and 200m extending into the water. This geometry was used to approximate the previous groyne model runs.
Study 4: Permeable Pile Screen Groynes	<u>Groyne Geometry:</u> • For the permeable pile screen geometry a 1m x 1m square pile was used for all cases. The permeability was determined by the spacing between the piles. The different permeability cases required specialised meshes for the pile screens, where each and every pile had to be positioned and sequenced as a closed boundary with refined meshes surrounding the piles. <u>Mesh solving:</u> • A triangular mesh with a grid resolution ranging from 25m^2 in the region near the pile screen groyne to a maximum 3200m^2 offshore was used. Around the pile screen groyne the grid resolution was $\leq$ 1m^2

3.3.2 Spectral Wave Model Parameters

The spectral wave model setup for the four numerical modelling sections comprised of the following standard parameters:

- The spectral formulation used; the directionally decoupled parametric formulation. This is based on a parameterization of the wave action conservation equation. The formulation is in accordance with Holthuijsen (1989); where the parameterization is made in the frequency domain by introducing the zeroth and first moment of the wave action spectrum as dependent variables.
- The time formulation used; the quasi-stationary formulation. This formulation method removes time as an independent variable and calculates a steady state solution at each time step. For quasi-stationary calculations the inclusion of diffraction can cause convergence problems. To reduce these problems a smoothing is introduced for the

discrete values of the square root of the directional spectral energy density, which is used in the calculation of the diffraction parameter. The steady state solution at each time step is solved using two methods:

  - Modified Newton Rhaphson iteration
  - Iteration in the time domain

- A significant wave height H_s, peak wave period T_p, and mean wave direction θ_m were defined in the shore normal direction at the offshore boundary using the default directional spreading index. The shore normal direction acts as an open wave boundary. The shore parallel direction boundaries act as lateral boundaries (i.e. a one-dimensional calculation of the basic equations is solved along this boundary line. The information of incoming waves required for this boundary line is obtained from the connected boundary lines.).
- Wind forcing was excluded from the model runs.
- The initial conditions were of the spectra from empirical formula type, and were based on a JONSWAP fetch growth expression (using a peak enhancement factor of 3.3) at the offshore boundary to force the wave model.
- Wave dissipation due to breaking was modelled using the Battjes and Janssen's (1978) formulation. To parameterise dissipation due to wave breaking a breaker index of γ = 0.8 was used (for details refer to MIKE21, 2011a).
- Wave refraction/diffraction effects in the area of the groyne were modelled using the Hothuijsen et al. (2003) phase-decoupled refraction-diffraction approximation method with the standard pre-set values. The approximation is based on the mild-slope equation where phase information is omitted. It was noted that including diffraction in the SW made quite a difference to the final flow result file. When diffraction was not included there was noticeably less flow around the groyne.
- Following Weber (1991) the wave dissipation due to bottom friction was modelled using a constant Nikuradse bed roughness length of k_n = 0.004m. An exception was study 3 where the drag coefficient C_f was used (refer to Table 3-2).
- Boundary conditions: the cross-shore used a lateral boundary (Neumann boundary) and the offshore used a wave parameter boundary where the incident wave conditions were specified.

The specialised parameters for the individual numerical modelling sections are listed in table 3-2:

Table 3-2: SW configurations for numerical modelling studies

Numerical Modelling Study	Overview
Study 1: Pattiaratchi Comparison	• Standard parameters only
Study 2: Impermeable Groynes	• Water level changes were applied
Study 3: Friction Manipulation	• Water level changes were applied • In accordance with Komen et al., (1994) formulation; to parameterise the rate of bottom friction induced wave dissipation the drag coefficient C_f was used.
Study 4: Permeable Pile Screen Groynes	• Standard parameters only

3.3.3 Flow Model Parameters

The flow model setup for the four numerical modelling sections used the following standard parameters:

- The higher order numerical solver option was used for both the time integration and the spatial discretization. A Courant-Friedrich-Lévy (CFL) number of 1.0 was preset for 2D modelling.
- The Smagorinsky model was used for horizontal eddy viscosity with a default constant of 0.28 in order to parameterise the turbulent, subgrid-scale horizontal momentum transfer (for details refer to MIKE21, 2011b).
- To parameterise the bed shear stress in the numerical simulation a quadratic drag law with a Manning number of $32 m^{1/3} s^{-1}$ was used. An exception was study 3 where the drag coefficient M was varied (refer to table 3-3).
- Wind forcing was excluded from the model runs.
- Wave radiation stress was specified for S_{xx}, S_{yy} and S_{xy} from the MIKE 21 SW FM wave radiation output. The output varied in time and space.
- For the boundary conditions both the cross-shore and the offshore were set to specified water levels. The water level conditions were set to constant values (0m MSL, 1m MSL) and tidal variations were not modelled for these simulations.

The specialised parameters for the individual numerical modelling sections are listed in table 3-3:

Table 3-3: FM configurations for numerical modelling studies

Numerical Modelling Study	Overview
Study 1: Pattiaratchi Comparison	• Standard parameters only
Study 2: Impermeable Groynes	• Water level changes were applied
Study 3: Friction Manipulation	• Water level changes were applied • To parameterise the bed shear stress for bed resistance in the numerical simulation a quadratic drag law with a Manning *M* number is required. The values vary in the domain.
Study 4: Permeable Pile Screen Groynes	• Standard parameters only

3.3.4 Coupling Parameters

To simulate the flow using radiation stress requires the coupling of the spectral wave model and the flow model. The coupling parameters are as follows:

- Study 1: Pattiaratchi Comparison
    - Coupling occurred every 7 seconds instead of every 60 seconds as carried out by Pattiaratchi et al., (2009). In an attempt to resolve eddy shedding.
- Study 2: Impermeable Groynes
    - coupling occurred every 60 seconds
- Study 3: Friction Manipulation
    - coupling occurred every 60 seconds
- Study 4: Permeable Pile Groynes
    - coupling occurred every 60 seconds

'Spin-up' was allowed for both models until such time as quasi-steady wave fields and currents were attained; this occurred after approximately three hours of simulation time.

For the spectral wave model the time integration is based on a fractional step approach. This comprises an initial propagation step using an explicit Euler scheme. To overcome the severe stability restriction, a multi-sequence integration scheme is employed following the idea by Vilsmeier and Hänel (1995). Here, the maximum time step is increased by locally employing a sequence of integration steps, where the number of steps may vary from element to element. Using the explicit Euler scheme, the time step is limited by the CFL condition. As stated in

Section 3.3.3 a CFL of 1.0 was used as a preset for the 2D modelling. The second approach is the correction step which is performed using an implicit method.

For the flow model the time integration was determined using a second order accurate Runge Kutta method.

3.4 Discussion of Models

Each numerical modelling section had specific outcomes. Some of the sections comprised of more than one set of model runs to meet objectives. A comprehensive list of all the model runs for the studies can be found in appendix A section A3.

The sections will be discussed with respect to specific objectives, refer to table 3-4 to table 3-7.

Table 3-4: Overview of Study 1 Model runs

Study 1: Pattiaratchi Comparison	
Objective	Overview
1	A comparison of Pattiaraitchi et al., (2009) simulation results for rip-currents, convergence points, divergence points and eddy formations.
2	A comparison of Pattiaratchi et al., (2009) closed land boundary flow pattern results with open boundary beach slope flow pattern results.

Table 3-5: Overview of Study 2 Model runs

Study 2: Impermeable Groynes	
Objective	Overview
1	Planar beach simulations were run to evaluate where the alongshore current should be prior to the placement of groynes. This allowed for cross-section comparisons of the alongshore flow at groyne positions.
2	Impermeable groyne simulations were run applying depth changes to the datum configuration. The depth change affected the breaker zone width changing the location of the wave driving forces. This was used to ascertain the effects depth change had on the levels of constriction of cross-sectional flow and how the depth change affected the surrounding flow characteristics. The depth change was carried out in an attempt to observe how the tide may affect the flow when it is high or low.
3	A comparison was carried out between the 20m wide groyne simulations and the

	1m wide groyne simulations to see if the width change of the groyne had a large effect on the surrounding flow characteristics even though the level of constriction of cross-sectional flow remained unchanged.
4	Groyne simulations were run applying length changes to the groyne geometry. This was another attempt at evaluating how a change in the level of constriction of cross-sectional flow affects the surrounding flow characteristics.
5	Using the results from objective 1 to 4 a comparison of rip-currents and alongshore currents for specific levels of constriction could be made. Time averaging was done to remove noise from the graphs due to eddy shedding. This was carried out to evaluate dominant flow patterns surrounding groynes depending on the level of constriction.

Table 3-6: Overview of Study 3 Model runs

Study 3: Friction Manipulation	
Objective	Overview
1	A set of simulations were carried out making use of a domain where both the drag coefficient and Mannings M value were manipulated over a pre-set geometric area resembling that of a 20m wide groyne (A constant drag and a variable Mannings M). This was done to ascertain whether or not resistance to flow can be used to mimic permeability in a numerical model. For this approach as depth increased the effect due to drag decreased. Ideally, as the drag coefficients are increased, the model results should tend towards those of an impermeable groyne.
2	Water level changes were applied to the simulations with the friction manipulated geometric area to evaluate how the flow pattern changes around that area. This datum change also had the purpose of evaluating if a change in water level would affect the permeability of the friction manipulated area.
3	The same principle as objective 1 was carried out however the constant drag coefficient values for the manipulated geometric area were multiplied by the depth prior to the simulations. The purpose of this was to attempt to mimic a constant drag through the whole water column in the depth averaged formulations. This should ideally improve the efficacy of the friction manipulation for modelling semi-permeability.
4	Objective 1 and 3 were then compared to evaluate which of the two developed methods behaved better when mimicking permeability. For this evaluation cross sections of alongshore current speed and flow were taken midway through the manipulated geometric area of all simulations. The cross-

	sections were time averaged and compared against cross-sections of alongshore current speed and flow for planar beach simulations that had no friction manipulation. This allowed for a comparison of the two methods.

Table 3-7: Overview of Study 4 Model runs

Study 4: Permeable Pile Screen Groynes	
Objective	Overview
1	Two sets of simulations were carried out. One set made use of a 100m long permeable pile screen groyne. The second set made use of a 200m permeable pile screen groyne. Both sets of simulations had varied permeability applied to the groynes. The permeability was applied by varying the pile spacing. The purpose of the simulations was to assess the effects of permeability on the level of constriction of cross-sectional flow. The reason is that changing the permeability does not change the groyne length nor the breaker zone width. The level of constriction will therefore remain the same.
2	Time averaged cross-sections of the alongshore flow upstream, downstream and along the groyne tip were compared to evaluate how the permeability affects the alongshore currents with respect to strength and possible deviation of the alongshore current in the cross-shore direction.
3	Time averaged cross-shore and alongshore plots were compared to evaluate dominant flow patterns in correlation with the level of constriction.
4	Objectives 1 through 3 were used to compare the effects of the level of constriction on the flow pattern around a permeable groyne against those around an impermeable groyne from study 2.
5	Study 3 was compared against study 4 to evaluate whether or not manipulating the drag could accurately simulate the flow patterns around a permeable groyne for approximately the same permeability.

3.5 Calculation Methods

The majority of the numerical modelling methodology calculations tie into the source functions and governing equations of appendix A. This is inclusive of the relationship between the drag coefficient C_f and Mannings M calculations of study 3: Friction Manipulation. This is however not the case for the level of constriction of cross-sectional flow calculations. This particular parameter calculation is fundamental to most of the parametric studies and shall therefore be explained in detail.

3.5.1 Level of constriction of the cross-sectional flow

The cross-sectional flow constriction factor was estimated thusly: the groyne length G_L was determined by the length of the groyne in contact with the active water zone i.e. including the swash zone. The breaker zone width B_z was determined from the fraction of breaking waves Q_b also known as the probability of waves breaking as stated in appendix A section A1.3. The probability range used was from 100 per cent of the waves being broken on-shore to 0.01 per cent of the waves breaking offshore to give a total 99.99 per cent of the breaker zone; If you know where the probability of waves breaking occurs with regards to depth and you know the bathymetry, you can determine the distance of the breaker zone width with relative accuracy.

The following should be emphasized: Based on laboratory data and field data it has been shown that the breaking parameter γ varies significantly depending on the wave conditions and the bathymetry. For this study Kaminsky and Kraus (1993) γ values were used, where γ is in the range of 0.6 and 1.59 with an average of 0.79. The probability range will be used to parameterize the level of constriction of the cross-sectional flow; the smaller the probability used the greater the level of constriction value, a reasonable probability range is 99.99 per cent. It is not necessary to use 100 per cent as this implies assessing a probability of waves breaking less than 1 in 100, the distance that waves break from the shore then becomes unrealistic.

To evaluate the predominant flow patterns required further analysis. The wave action in the breaker zone is the driving force of the currents and therefore the flow pattern around a groyne. The ratio of groyne length to the width of the breaker zone (G_L/B_z) introduced by Taranowska (1985), was used to place the predominant flow patterns into context. This was undertaken by running different simulations.

CHAPTER 4

METHODOLOGY – FIELD WORK

Chapter Four describes the methodology used to undertake field measurements at a case study site. The procedures and preparations for the field tests and sediment data sampling are listed as well. These include the calibration of the current meters that were deployed for the field study. Finally the methods used for the data analysis are also described.

4.1 Field work objectives

The main objective behind the field work is to collect current data around a groyne for the purpose of plotting the flow pattern. The flow pattern will then be compared against the parametric studies for the same levels of constriction of cross-sectional flow. This will show whether or not the level of constriction of cross-sectional flow can be used to characterise flow patterns around groynes.

The secondary objective is to collect sediment samples from around the groyne where the current data was collected. The sediment will then be graded and the threshold velocities will be calculated to allow for a sediment transport evaluation around the case study site.

4.1.1 Instrumentation

To carry out the main objective of collecting current data, custom instrumentation was required. The device implemented was developed by EMS (2013), it is a simplified analogue current meter (refer to figure 4-1) shaped like a dart with a single outer water-proof casing and a fitted propeller. It has on-board programmable electronics with a magnetic compass and a logger. The measurement principle is based on a pulse generator and a counter that records the rotations of the propeller.

Figure 4-1: Current meter developed by EMS (EMS, 2013).

Though the current meter propellers were crafted from the same mould, each current meter's propeller rotation speed varied due to them having different rotational resistances. Each propeller had a slightly different rotation per metre and required a standardised count per metre. The current meters were tested to ensure they had the same number of counts per rotation.

To evaluate the count-velocity relationship a pool was used. The parameters measured in the pool were distance and the number of propeller counts.

The following apparatus were used:

- A measuring tape, was used to measure distance (m)
- The current meter, was used to measure counts
- Stop watch, used to measure time (s)

<u>The method for data collection may be summarised as follows:</u>

1. The measuring tape was laid out along the side of the pool for a distance of 10m
2. The current meter circuit board was programmed to collect data over 30 second intervals.
3. The current meter circuit board (inclusive of battery pack and SD card) was connected to the propeller relay wire and inserted into the current meter.
4. The current meter was affixed to a custom built rod to be pulled through the water.
5. The current meter was pulled through the water for 10 m, taken out, turned round and pulled back along the 10 m stretch. This process was carried out 3 times with varying speeds; slow, medium, and fast. The stop watch was checked continuously to ensure every process was carried out within the 30 second recording interval.

6. The SD card was removed and the data stored.
7. Steps 1 through 6 were repeated for all 5 propellers.

During the trial tests in the pool it was noted that in one direction the propeller remained still but when turned to face the other direction there was a very slight current that induced propeller motion. This is why a total distance of 20 m is travelled; 10 m one way followed by returning the 10 m distance, to average out the number of counts due to the slight current in the one direction.

The 20 m distance was carried out 3 times for each propeller at varied speeds to determine by how much the speed varies the number of counts. Theoretically it shouldn't vary at all as the distance travelled is the same. The counts logged at the 3 different speeds were then averaged for each propeller.

When testing propeller 4 and propeller 5, for some reason their logged SD data showed unusually high counts; the tests for propeller 4 and 5 were redone. For the current meter calibration data on the pool test refer to appendix B, section B1.

Section 4.2 will discuss in detail the deployment of the instrumentation and collection of current data around the case study site.

4.2 Field Study – Flow Data Collection

A field study was conducted at the Bay of Plenty Pier, Durban Central Beach off the coast of KwaZulu-Natal South Africa on 6th November 2012. The main objective of the field study was measure the currents' velocity, (both magnitude and direction) in the vicinity of the Pier.

Measurements were needed at a number of locations near and around the Bay of Plenty Pier to investigate the spatial variability in magnitude and direction of the current velocity.

There are no prior measurements available for this site. For further information regarding the case study site, please refer back to chapter 1 section 1.1 and section 1.2.1 where it was covered in detail.

4.2.1 Data Collection

The parameters that were measured in the field were: Velocity (m/s), Direction (°), temperature and pressure (Dbar).

The following apparatus were used:

- 25 x Custom made current meters equipped with on-board magnetic compasses, were used to measure velocity (m/s) and direction (°)
- 1 x A Sontek Argonaut 300khz Acoustic Doppler Current Profiler, was used to measure velocity (cm/s), direction (degrees), pressure (Dbar) and temperature (°C)
- A motorized boat, supplied by the local lifeguards, was used as a platform for the deployment and collection of instrumentation whilst moving around the Bay of Plenty Pier
- A Garmin eTrex handheld GPS to record the current meter locations

The swell conditions were mild with the swell direction coming from South-East to East, easy conditions for deployment. The current meters were deployed between 07:30am – 09:00am during high tide. During deployment two current meters were lost, no.21 and no.23. The industrial cable ties snapped on no.21 and no.23 due to the waves breaking on top of them, this required onsite improvisation for the rest of the current meters. The industrial cable ties were removed and nylon cord was knotted through the remaining current meter cable holes.

Initially instrumentation was to be retrieved after 6 hours of run time however the low tide surf zone was far too rough for the motor boat. The retrieval was postponed till the following day, 07th November 2012 between 07:00am – 09:00am during high tide. During retrieval no.5 could not be found, whether it was stolen or it followed a similar fate to that of no.21 and no.23 this could not be determined.

A total of three current meters were lost (no.5, 21, 23) and a total of 3 current meters lost their propellers (no.6, 10, 24), either due to assembly faults or fouling of the propeller.

Twenty-Five current meters were deployed. The deployment configuration (refer to figure 4-2) consisted of four devices per row and three rows on either side of the pier in an approximate grid deployment. This was an approximate configuration as the boat was shifting position due to wave action. An ADCP (Acoustic Doppler Current Profiler) was deployed as well in conjunction with the current meters. It was positioned on the seabed, approximately 100 metres in front of the tip of the pier, with the no.6 current meter attached to it. The ADCP was used in an attempt to compare the data recorded with that of current meter no.6.

Figure 4-2: Deployment configuration around Bay of Plenty Pier, Current meters lost in yellow, Propellers lost in blue (background image from Google Earth, 2013).

The method for data collection may be summarised as follows:

1. The current meters were set to continuously log current and direction data at a rate of 0.5 Hz.
2. The current meter circuit boards (inclusive of battery pack and SD card) were connected to the propeller relay wires and inserted into the current meter shell using rubber seals to ensure the circuit boards remained dry during operation.
3. The 25 current meters were individually attached to drop weights with a 1 meter length of nylon cord so that the current meter sat 1 meter above the seabed. The current meters were then attached to custom cut floats for buoyancy and then the floats were attached to markers to ensure visibility on retrieval. (refer to figure 4-3)
4. The ADCP was affixed to a stainless steel mounting sled/bracket (refer to figure 4-4) to ensure it remained firmly seated on the seabed and that it wouldn't roll due to wave action. The ADCP was programmed to continuously log data at 0.0167Hz, and to take the average log every 0.0167Hz.
5. The current meters and the ADCP were dropped into position via motor boat and left in the surf for a 24 hour duration. At which point they were collected by motor boat.

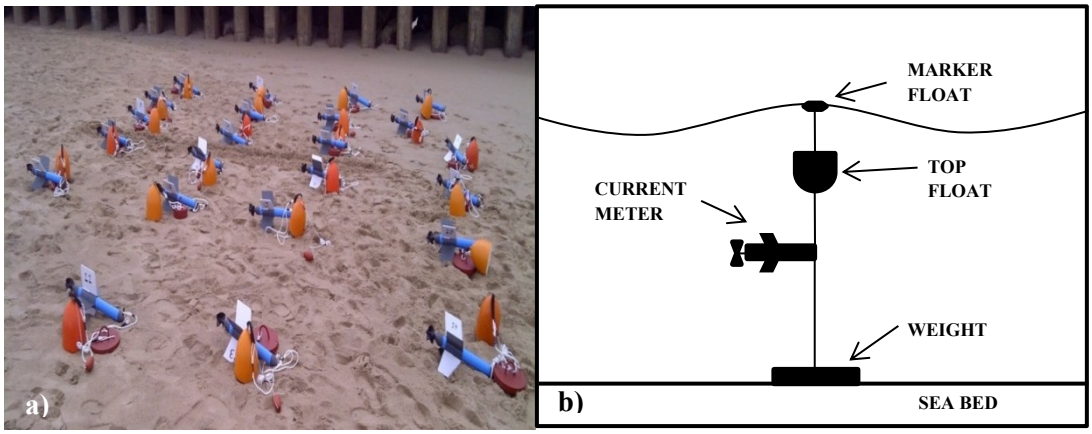

Figure 4-3: (a) The 25 current meters prior to deployment and (b) Schematic of a current meter once deployed.

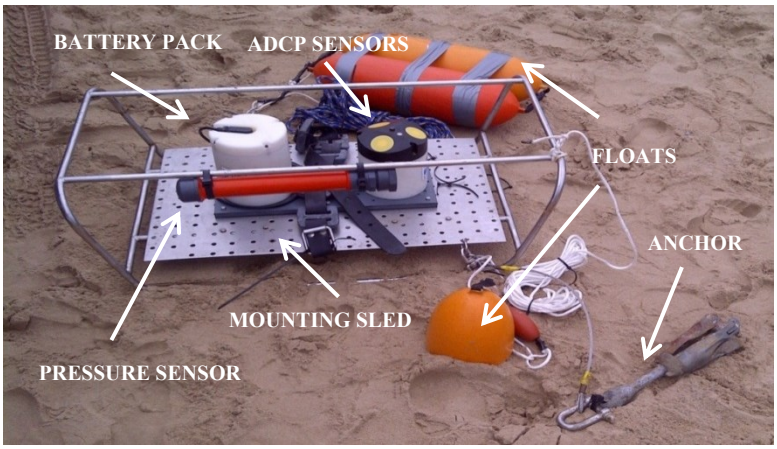

Figure 4-4: ADCP prior to deployment, with weights, floats and markers.

4.2.2 Problems encountered

- Fouling in the propeller, tangling of the dynamo in the propeller. The slack in the cord caused an issue with the one current meter; this was noted as a lost propeller.
- The floats were not sufficiently visible; the dark red floats were at times hard to locate in the waves.
- Seaweed may cause cowling. The occurrence is unpredictable, and may vary due to conditions. This occurred with one current meter; this was noted as a lost propeller.
- Waves crashing on the propeller fins in the shallow water breaking zone; changing the instrument stability. This is dependent on the water depth.
- Battery batch errors, alkaline batteries running continuously have at most an 8-10 hour run time for the custom current meters.
- Cable ties snapped under wave conditions; this led to a couple current meters being dragged out to sea. Cable ties were removed, replaced by nylon cord.

4.2.3 Current Meter Velocity Calibration

To determine the velocity the first thing required is to divide the recorded count number for each logged count by two, due to the current meter logging at 0.5 Hz. Then use equation 4-1:

$$V = \frac{(counts/second)}{(counts/metre)_{avg}} \tag{4-1}$$

Equation 4-1 originated from the pool experiment where each propeller was rotated a full revolution to determine the number of counts per revolution (counts/rev).

From the count readings logged in the pool, the average counts were calculated for each propeller. The average number of counts for each propeller was then divided by the total distance travelled (20m) to determine the number of counts per metre (counts/m) for each propeller. The average counts per metre were then determined from all the propellers and used as a standard value for inferring the velocity.

The average propeller count per metre value of 17.85 was used for all propellers as their counts per revolution were 4 and their propellers were all from the same mould.

4.2.4 Current Meter Directional Calibration

Prior to deployment the current meters were aligned on the beach, with the propeller side facing shoreward, parallel to the Bay of Plenty Pier. This allowed for the calibration of the on-board magnetic compasses by making use of a reference direction. Once data was recorded from the field test, a correction factor could be applied to the directional data displaying the direction via nautical bearing. The correction factor was a deduction of 90 degrees from all 25 current meters' directional data.

4.3 Field Study – Sediment Data Collection

A field study was conducted at the Bay of Plenty Pier, Durban Central Beach. The reason for the field study was due to their being no previous records of collected sediment samples. During coastal construction eThekweni municipality uses a standard value of 250 μm for their median grain value. This is however insufficient to estimate the initiation of scour surrounding the groyne; requires location specific sampling. Sampling was carried out on the 16/05/2013.

The aim for the field study was to obtain a good data set of sediment samples. This implied that data would need to be collected from a number of locations around the Bay of Plenty Pier. This would show the spatial variability in the sediment grain size due to the wave and current interactions that frequent the Pier. The sediment samples will be used to approximate the threshold velocities of the sediment grains so that the threshold velocities can be compared against the velocity data collected from the current meter field test. This in conjunction with an approximated bedload transport will be used to assess erosion around the groyne due to the recorded current meter data.

4.3.1 Data Collection

There were no parameters measured on the day, this field study was purely the collection of sediment samples to undergo grain grading.

The following apparatus were used:

- Surfboards were used as floatation devices to move around the Bay of Plenty Pier whilst diving
- Diving gear; merely flippers and goggles
- Ziploc plastic bags to hold and seal the sediment inside; both fine and coarse sediment.
- Pegs to ensure the Ziploc bags remained sealed
- 3 x Water proof buckets with lids to store the samples in, without having to worry over the loss of fine sediment due to wave action and for the purpose of floatation; to bring the samples back to shore safely.

The sampling was carried out under mild swell conditions, with the swell direction coming from the South-East. The majority of the waves were breaking inside the groyne's length due to high tide. The collection of sediment samples required free diving down to the seabed and collecting

of sediment on the north side trunk, south side trunk and at the tip of the pier (refer to figure 4-5). Collecting sediment along the trunk of the groyne on the South and North side was relatively easy. This was not the case however for the groyne tip; on the day of collection it was over 5m deep and this required multiple dives to retrieve samples.

Figure 4-5: Locations of sediment sample collection (background image from Google Earth, 2013).

The sampling procedure for the groyne tip (S7) may be summarized as follows:

1. The surf board was paddled out to the approximate position.
2. All excess equipment was rigged to the surfboard to ensure it didn't float away
3. The flippers and goggles were used to ease the dive down to the seabed
4. At the seabed, the Ziploc bag was opened and the mouth of the bag was placed on the surface of the seabed. The bag was then pressed down into the bed and sealed, this ensured both the fine top layer and coarse under layer was collected. The bag was closed and the sample was then returned to the surface.
5. On returning to the surfboard, the sealed Ziploc bag was twisted, pegged and stored inside a bucket.
6. The surfboard was then paddled back to shore.

The rest of the sample collections were relatively the same as summarised above, however they did not require the use of a surfboard.

4.3.2 Grain Size Analysis

This test was performed to determine the percentage of different grain sizes contained within the soil of each sample from the 7 different locations. The mechanical or sieve analysis was performed in order to determine the distribution of the coarser, larger sized particles.

The grain size analysis was carried out in accordance with the ASTM D 422; the standard test method for particle-size analysis of soils with the exception of the hydrometer analysis.

4.3.2.1 Data Analysis

The following equipment was used:

- Oven
- Balance
- Sample dishes
- Set of sieves; 4.75mm, 2.00mm, 1.40mm, 1.18mm, 0.60mm, 0.425mm, 0.30mm, 0.15mm, 0.075mm and a pan.
- Cleaning brush
- Sieve shaker

The test procedure may be summarised as follows:

1. Samples, in dishes (refer to figure 4-6a), were placed in the oven at 108°C for 24 hours to remove all moisture content.
2. All sieves and pan were cleaned to remove contaminants.
3. The weight of each sieve and pan were recorded.
4. Sieves were assembled in ascending order (refer to figure 4-6b), with the pan on the bottom and the 4.75mm sieve at the top. Oven dried soil from a sample location was then carefully poured into the top sieve after which the cap was placed over it to seal the sieve stack.
5. The sieve stack was then placed in the mechanical shaker and shaken for 10 minutes.
6. The stack was removed from the shaker and each sieve, and the pan, with its retained soil was weighed and recorded.
7. The above test procedure was carried out for all samples.

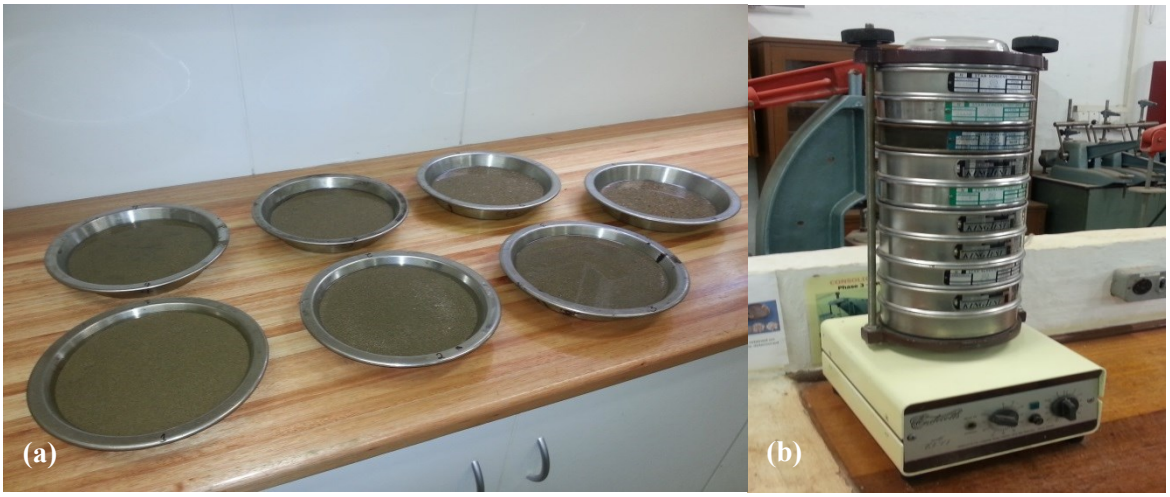

Figure 4-6: (a) Sediment samples and (b) Sieve stack

The sieve analysis may be summarised as follows:

1. The mass of soil retained on each sieve was obtained; the weight of the empty sieve subtracted from the mass of the sieve + retained soil. This was recorded as the weight retained on the data sheet. The sum of all retained masses is approximately equal to the initial mass of the poured soil sample. A loss of more than two per cent is unsatisfactory by ASTM D 422 standards.
2. The per cent retained on each sieve is calculated by dividing the weight retained on each sieve by the original sample mass.
3. The per cent passing is calculated by starting at 100 per cent and then subtracting the per cent retained on each sieve as a cumulative procedure.
4. A semi-logarithmic graph of grain size vs. per cent finer is then plotted.
5. C_c and C_u is then calculated for the soil.

Refer to appendix F section F1 for sieve analysis equations and results.

4.3.3 Bedload transport

Due to the relative length and complexity of this section's method, designed sediment models and literature it was moved to appendix F section F2. Below is merely an overview of the procedures for section F2.

This section comprises of three parts respectively;

1. Sediment transport due to currents
2. Sediment transport due to waves
3. Sediment transport due to the combination of waves and currents

The purpose for steps 1 and 2 is to evaluate the predominant scour factor i.e. currents or waves. Step 3 is then to evaluate, through the combination of step 1 and 2 methods, how currents and waves in combination affect the bedload transport.

Prior to the evaluation of bedload transport, several inputs were required; median grain (D_{50}), ninety per cent of the grain sample (D_{90}), water depth (h), depth average velocity ($\bar{\upsilon}$).

- The D_{50} and D_{90} are relatively simple to determine; it merely requires reading the grain size of the semi-logarithmic graphs, from section F1, for the respective percentages
- h was determined through the use of depth envelopes (section F2.1 - figure F2-1 and F2-2). Past bathymetric surveys of the Bay of Plenty Pier (July 2011, March 2012 and June 2012) were compiled on MIKE21. Then using the current meter coordinates as reference points, the depths at those reference points on the bathymetric surveys were recorded. This yielded the minimum and maximum depth for each current meter located along the North and South side trunk of the Pier.
- $\bar{\upsilon}$ was determined by weighted average. The purpose for the weighted average velocity was to place more dependence on the frequency of a particular current speed occurring in the data set. This would then display the most likely scour conditions.

The main values calculated for each section were;

- The skin friction bed shear stress ($\tau_{c,s}$, $\tau_{w,s}$); as this shear stress acts directly on the grains and is thus the parameter used when calculating the threshold of motion for bedload transport.
- Threshold of motion ($u_{c,cr}$, $u_{w,cr}$); the velocity due to current or wave action that initiates motion of the grains lying on the bed surface
- Bedload transport (q_b); merely the volume of sand displaced per metre per second from the surface of the seabed.

CHAPTER 5

RESULTS & DISCUSSION – PATTIARATCHI COMPARISON

Chapter Five comprises of the results for Pattiaratchi et al., (2009) comparison and a discussion thereof. It details the differences between the reproduced simulations and the publicised findings with possible reasons for discrepancies. It also evaluates the findings for a closed boundary versus a beach slope for impermeable groynes.

5.1 Introduction to Study 1

Numerical simulations of an idealised beach with a shore-normal groyne were conducted using a flow circulation model driven by waves for the present study and compared with the work of Pattiaratchi et al., (2009). The results indicated several things; the incident wave angle, wave period, and especially the wave height controlled the circulation. The results also indicated that the present study displayed a different circulation pattern to Pattiaratchi et al., (2009). Pattiaratchi et al., (2009) results showed an onshore rip current forming on the lee side at the tip of the groyne whereas the present study showed no such onshore rip current forming.

Simulated radiation stress fields S_{xx}, S_{yy} and S_{xy} (refer to figure 5-1, 5-2 & 5-3) show the peak radiation stress zone, and the distribution around the groyne. Different wave conditions changed the spatial distribution of the radiation stress' that in turn affects the flow fields. Therefore the peak radiation stress zone will be discussed in further detail in section 5.2.

Flow vector fields, from Pattiaratchi et al. (2009) and from the present study are shown in figures 5-1 to 5-8. They show the dominant circulation pattern that occurs around the groyne. Irrespective of changing wave conditions the pattern includes:

- an eddy in the lee of the groyne associated with flow separation around the groyne tip and subsequent re-circulation into the separation zone.
- rip currents on both sides of the groyne.

- Pattiaratchi et al., (2009) shows a convergence zone near the tip of the groyne (refer to figure 5-5, 5-7, 5-9 and 5-11), but this feature is not evident in the results from the present study (refer to figure 5-4, 5-6, 5-8 and 5-10).
- Divergence occurs in the alongshore currents at the down drift extent of the lee eddy where the flow re-attaches to the shoreline.
- Water levels are set up on the updrift side of the groyne and set down on the downdrift side
- The magnitude of the abovementioned features are amplified with increasing wave heights and the obliqueness of the wave approach angle i.e. flow velocities and water level changes increase.

5.2 Peak radiation stress zone

(For theory regarding wave radiation stresses, refer to appendix A: section A1.1)

The simulations showed that the radiation stress fields on the lee side of the groyne were offset from those on the updrift side (refer to figure 5-1, 5-2 & 5-3). The offset is more predominant for S_{xy}, see Figure 5-3. This is the same as field observations of waves breaking where the lee side is sheltered and the waves breaking are offset from that of the upstream side.

For a given significant wave height, a change in the wave period T_p or mean wave direction θ_m, affected the radiation stress components S_{xx} and S_{yy}. As T_p increased it was found that the peak radiation stress zone increased in intensity but the location remained almost constant for both the S_{xx} and the S_{yy} components. This leads to an increase in the current strength. As θ_m increased from 10° to 60°, the peak radiation stress components S_{xx} and S_{yy} increased in intensity and their locations moved further offshore, this moves the location of the peak alongshore current further offshore, reducing the tip velocity angle. The S_{yy} zone moved not only offshore with an increase in mean wave direction but also upward in the alongshore direction from the lee side of the groyne to the upstream side of the groyne. This increases the strength of the current velocity acting at the tip of the groyne.

For a given significant wave height, a change in the wave period T_p or mean wave direction θ_m, affected the S_{xy} radiation stress component. As T_p increased it was found that the peak radiation stress zone increased in intensity however the location remained almost constant, the same as the S_{xx} and the S_{yy} components. This increased the strength of the alongshore current. As θ_m

increased from 10° to 60° it was found that the peak radiation stress zone moved further offshore and that 45° yielded the largest peak radiation stress for the S_{xy} component, not 60°.

For a fixed wave period and mean wave direction, a change in the significant wave height affected the radiation stress in the $S_{xx,}$ S_{yy} and the S_{xy} components. As the wave height increased the radiation stress zone moved further offshore, this is due to the breaker/surf zone moving further offshore as the wave height increased; the change in location of the breaker zone changes the location of the peak alongshore current. Not only did the radiation stress zone move further offshore, but it increased in intensity and the area over which the zone acts, i.e. the width of the peak radiation stress zone increased. With a set wave incident angle, 45°, by increasing the offshore wave height from 1 m to 3 m the peak radiation stress increased from 1.14 m^3/s^2 to 6.78 m^3/s^2 for the S_{xx} component and from 0.55 m^3/s^2 to 3.79 m^3/s^2 in the S_{yy} component and from 0.21 m^3/s^2 to 1.68 m^3/s^2 in the S_{xy} component.

5.3 Eddy circulations in the lee of the groyne

A complex eddy structure was formed in the lee of the groyne where the radiation stress had the greatest variation in the S_{xx} and S_{yy} components. A lee eddy occurred in all 20 simulations (eg; figures 5-4, 5-6, 5-8 and 5-10). As the significant wave height increased, the current speed nearshore increased in magnitude as well as in the spatial extent of the current; the width of the alongshore current. It was observed that the eddy structure became less complex and more circular with an increase in significant wave height (the complexity of the eddy is with respect to the number of smaller eddies within the larger eddy.). This is due to an increase in the breaker zone width. As the breaker zone width extended offshore of the groyne so too did the generated alongshore current. This led to a decrease in the current velocity tip angle which decreases the spatial extent of the recirculation zone, making the eddy more circular and compact.

With a set wave incident angle θ_m, 45°, by increasing the offshore wave height from 1 m to 3 m the maximum rip current speed parallel to the groyne increased from 0.29 m/s to 0.93 m/s (Figures 5-4, 5-6, 5-8 and 5-10). The onshore maximum current speeds along the boundary also increased (from 0.095 m/s to 0.37 m/s). This shows an increase in the eddy vorticity with an increase in wave height.

A comparison of the current vector values for runs with set significant wave heights H_s, and incident angles of 10°, 30°, 45° and 60° yielded the conclusion that the eddy was strongest when the incident wave was at a 45° angle to the shore.

While keeping H_s constant with waves propagating at angles tending from 45° to 10° (almost perpendicular) to the shore, it produced eddy circulations with larger spatial extents and weaker current velocities. By increasing the wave period T_p, for the same conditions it produced eddy circulations with similar spatial extents however the current velocities were stronger; increased vorticity.

While keeping the T_p and θ_m the same as H_s increased the eddy centre remained relatively constant in the alongshore direction. It did however move closer to the shore in the cross-shore direction. This can be explained by the reduction in the tip velocity angle. When the mean wave direction θ_m was closer to 0° the eddy like structure was relatively large, however as it tended towards 45° the structure decreased in size and became more compact. While keeping the T_p and H_s the same while increasing θ_m from 10° to 60°, the eddy centre remained relatively constant in the alongshore direction. The eddy centre did however move closer to the shore in the cross-shore direction.

The lee side eddies of the different model runs were not as ideally circular as those found in Pattiaratchi et al., (2009), they were more irregular.

5.4 Rip currents

Rip currents with speeds ranging from 0.29 m/s to 0.93 m/s (refer to appendix B table B1.1), occurred along the lengths of the groyne and were strongest near the groyne. On the lee side, the rip currents were strongly attached to the eddy structure. The rip current spatial extent in the lee of the groyne was equal to or greater than the rip currents up-drift of the groyne. The up-drift peak rip current always occurred further offshore along the groyne trunk than the lee side peak rip current. The cross-shore location, of the strongest currents, on the lee side of the groyne was almost in line with the centre of the eddy.

As the H_s increased, the location of the peak rip current changed; moving offshore along the trunk of the groyne.

The H_s was kept constant at 2m, to examine the effects of changing the T_p and the wave direction θ_m. As the mean wave direction tended from 10° to 60° the peak rip current moved

offshore along the lee side of the groyne. It moved towards the tip of the groyne while the spatial extent increased outward from the groyne. For a given height, as the wave period increased from 8s to 14s the peak rip current location remained unchanged. It did however increase in strength and spatial extent near the tip of the groyne.

Rip currents were apparent in all simulations. They were however weaker when H_s and T_p were small and θ_m was close to either 0° (alongshore) or 90° (cross-shore). They were stronger when H_s and T_p were large and θ_m was between 45° - 60°. The strongest rip currents however occurred when the mean wave direction θ_m was 60°. The greatest variation in rip current speed was due to changes in the incident wave height.

The strongest current velocity was always at the tip of the groyne on the up-drift side, due to the rip currents and alongshore currents interacting.

5.5 Convergence zone

In all their model runs Pattiaratchi et al (2009) found that "the rip current in the lee of the groyne encountered a shoreward current around the groyne tip" (refer to figure 5-5, 5-7, 5-9 and 5-11). In the present simulations no shoreward currents were formed whilst using the same model description and configurations (refer to figures 5-4, 5-6, 5-8 and 5-10). The following factors were manipulated in an approach to reproduce the convergence zone occurrence:

- The mesh type was changed from triangular to quadrangular and even a hybrid of both was attempted.
- The grid resolution was changed using both higher and lower resolutions.
- The horizontal eddy viscosity was changed by varying the Smagorinsky variation constant. The constant was varied between 0.28 and 2.0. By varying the constant eddy shedding and numerical instability can be dampened creating more idealised circulation patterns.
- The North and South boundary conditions (cross-shore boundaries) were changed to other available options from the model configuration parameters; making use of reflective, lateral and zero normal velocity boundaries.

None of the model runs could reproduce the convergence zone as displayed in Pattiaratchi et al's (2009) paper.

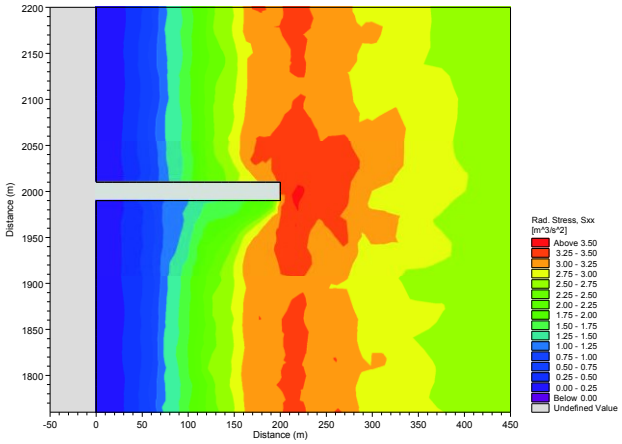

Figure 5-1: Contour plot of radiation stress field for the S_{xx} component. For the (H_s = 2m; T_p = 14s; θ = 45°) wave conditions (Table A3.1.1, model run 14).

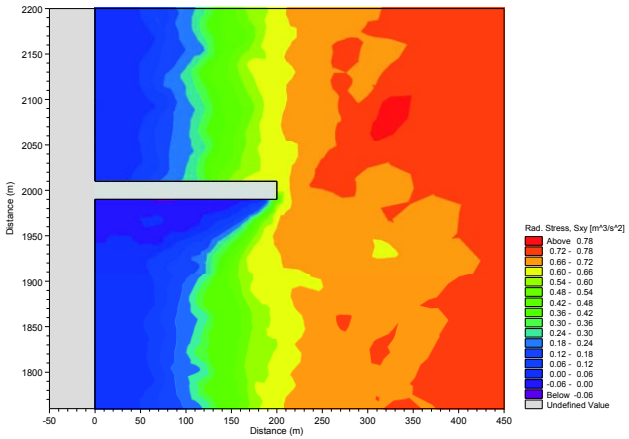

Figure 5-3: Contour plot of radiation stress field for the S_{xy} component. For the (H_s = 2m; T_p = 14s; θ = 45°) wave conditions (Table A3.1.1, model run 14).

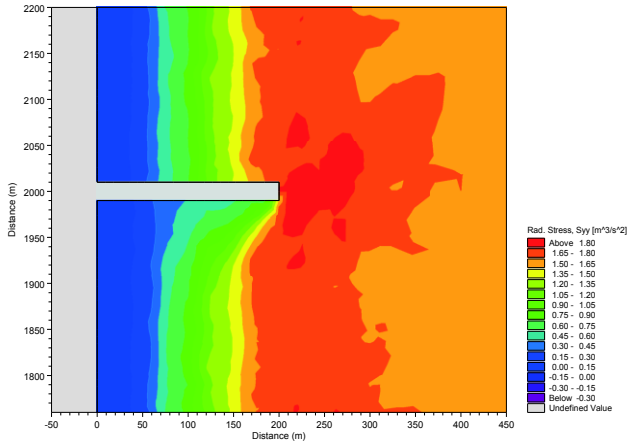

Figure 5-2: Contour plot of radiation stress field for the S_{yy} component. For the (H_s = 2m; T_p = 14s; θ = 45°) wave conditions (Table A3.1.1, model run 14).

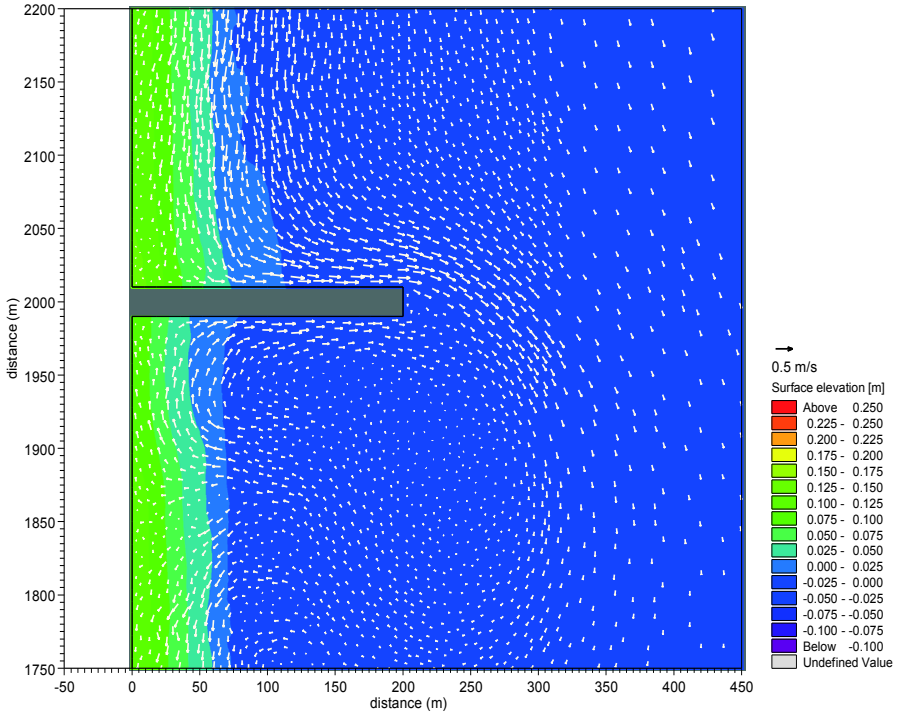

Figure 5-4: Vector plot showing the predicted current vectors and the wave set-up for (H_s = 1m; T_p = 14s; θ = 45°) (Table A3.1.1, model run 1).

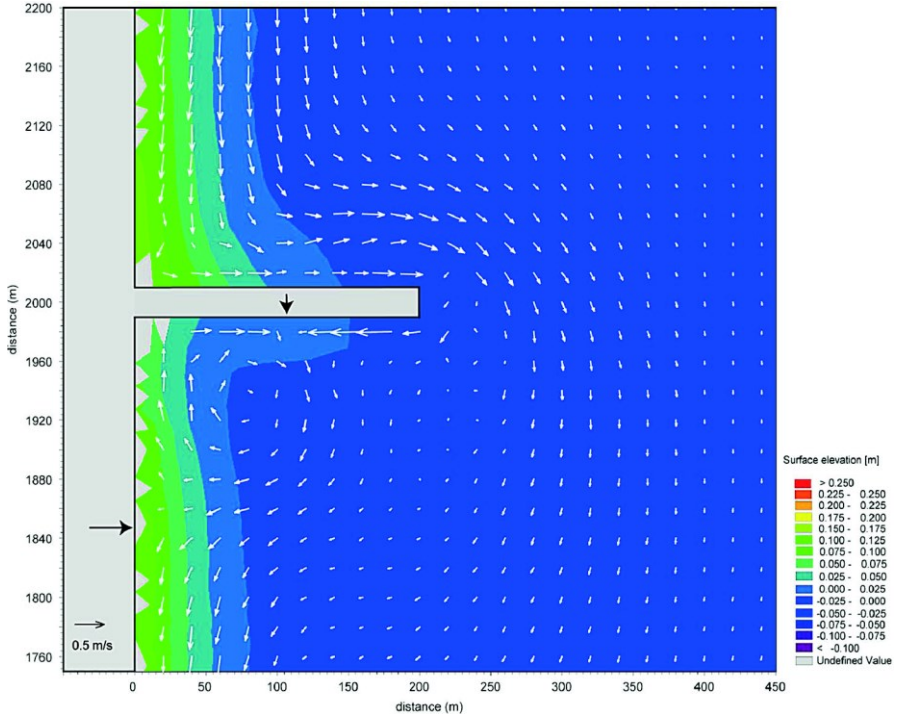

Figure 5-5: Vector plot showing the predicted current vectors and the wave set-up for model run 1 (H_s = 1m; T_p = 14s; θ = 45°). (Pattiaratchi et al., 2009).

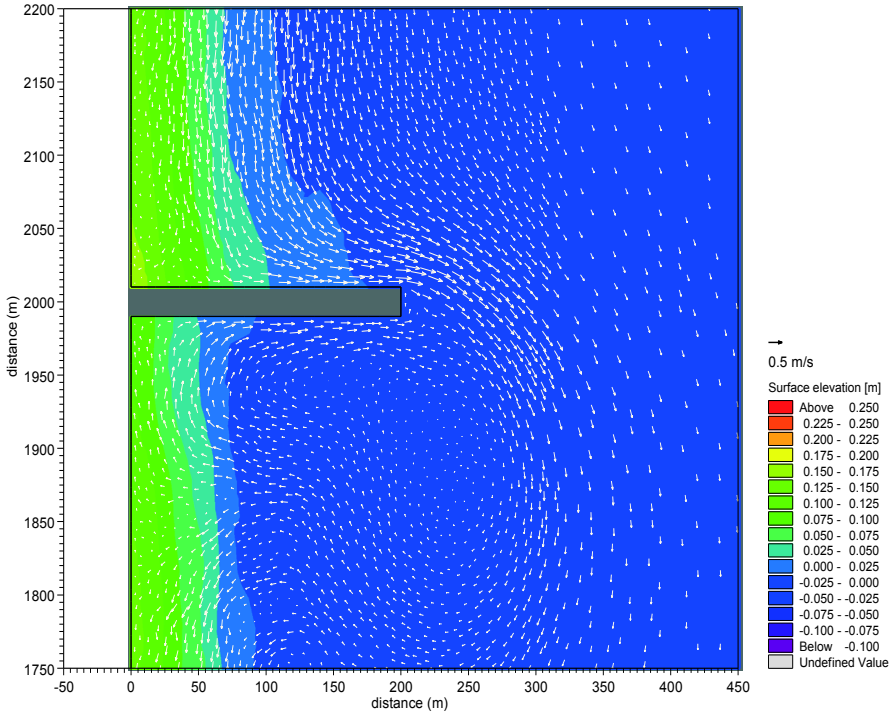

Figure 5-6: Vector plot showing the predicted current vectors and the wave set-up for (H_s = 2m; T_p = 14s; θ = 10°) (Table A3.1.1, model run 16).

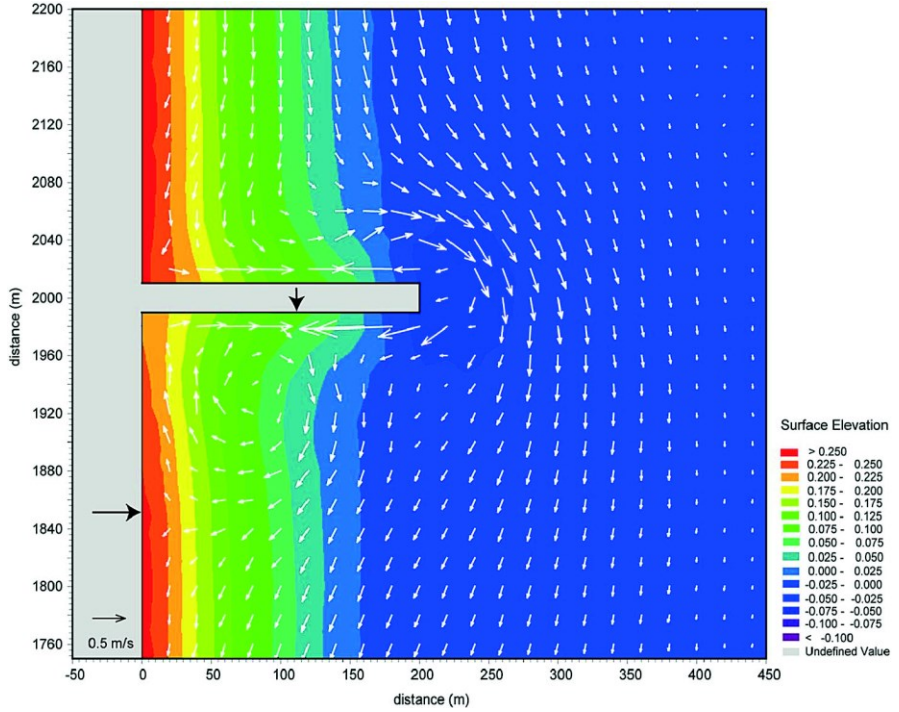

Figure 5-7: Vector plot showing the predicted current vectors and the wave set-up for model run 16 (H_s = 2m; T_p = 14s; θ = 10°). (Pattiaratchi et al., 2009).

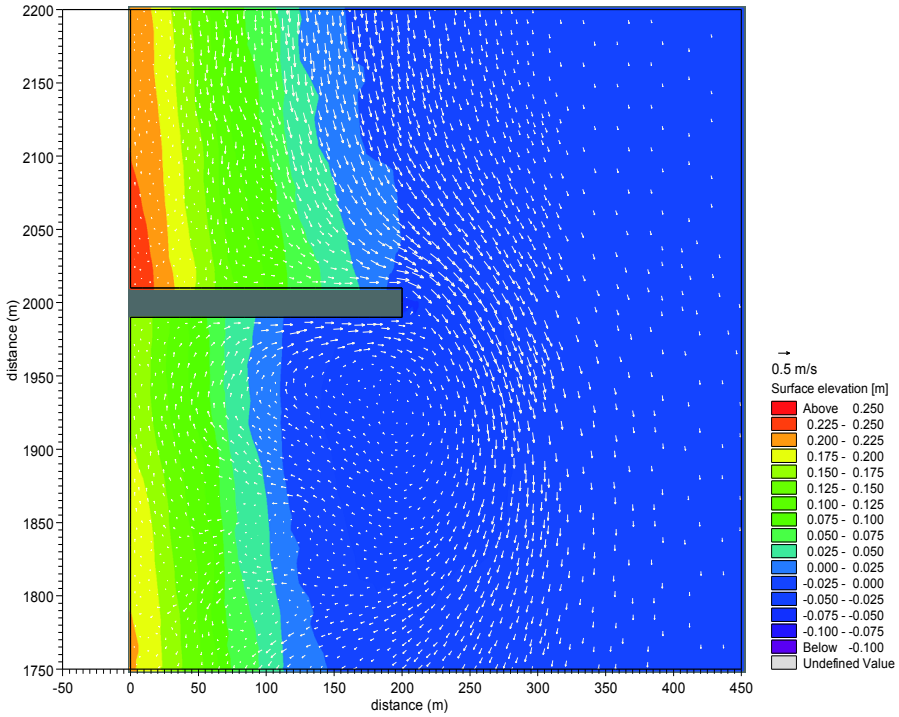

Figure 5-8: Vector plot showing the predicted current vectors and the wave set-up for (Hs = 2m; Tp = 14s; θ = 45°) (Table A3.1.1, model run 14).

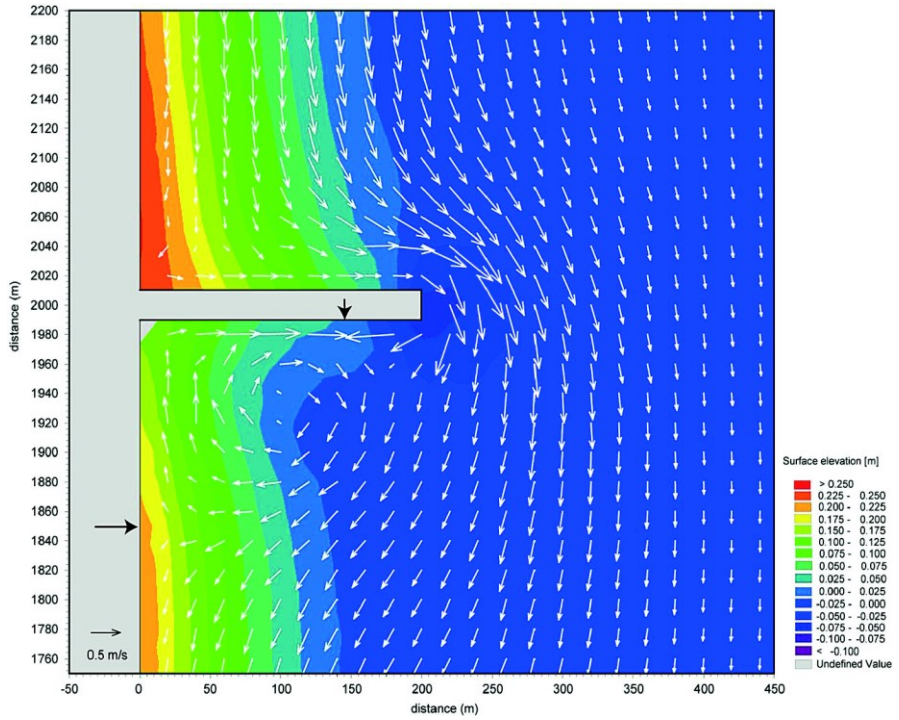

Figure 5-9: Vector plot showing the predicted current vectors and the wave set-up for model run 14 (H_s = 2m; T_p = 14s; θ = 45°). (Pattiaratchi et al., 2009).

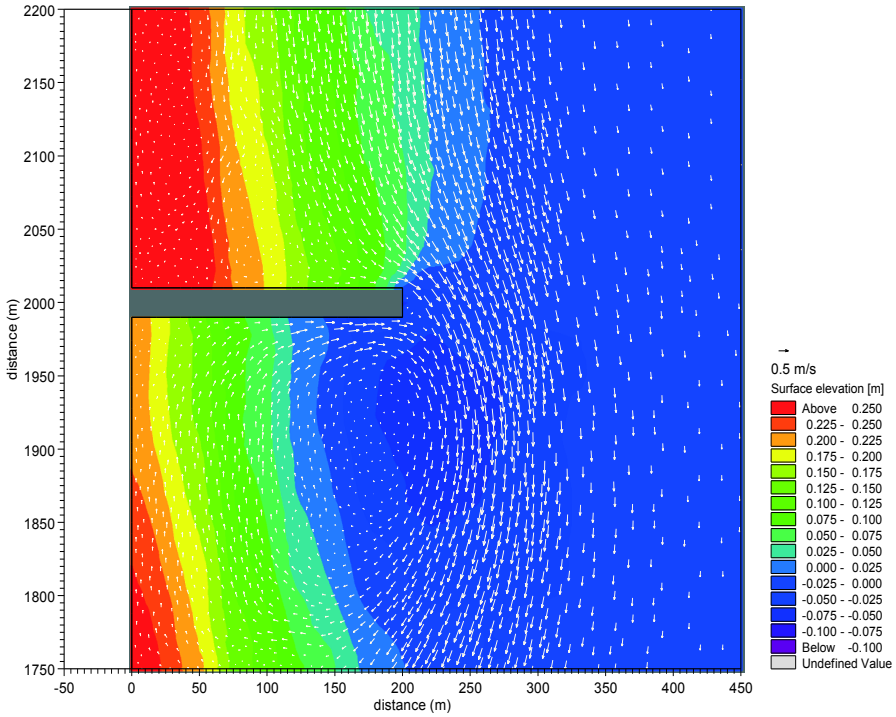

Figure 5-10: Vector plot showing the predicted current vectors and the wave set-up for (Hs = 3m; Tp = 14s; θ = 45°) (Table A3.1.1, model run 19).

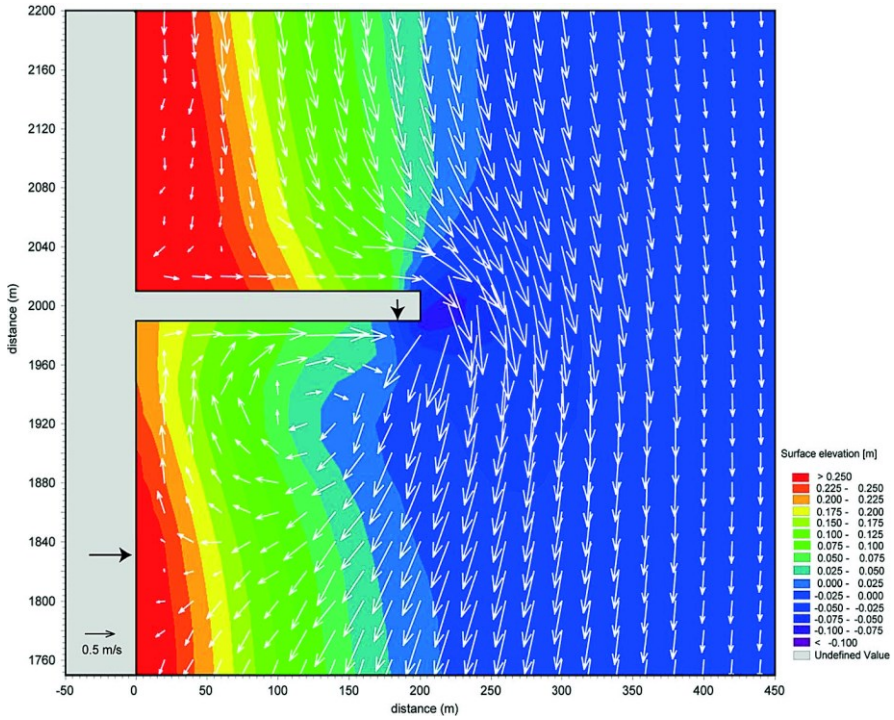

Figure 5-11: Vector plot showing the predicted current vectors and the wave set-up for model run 19 (H_s = 3m; T_p = 14s; θ = 45°). (Pattiaratchi et al., 2009).

5.6 Divergence of the alongshore currents

In all simulations a divergence point occurred downstream of the groyne at the reattachment location. Between the divergent point and the groyne (recirculation zone) nearshore current flows towards the groyne. Beyond the divergent point the alongshore current flows away from the groyne. Pattiaratchi et al (2009) showed a divergence point occurring between 20 m and 60 m from the groyne. The divergence point appears prominently in figures 5-5, 5-7, 5-9, and 5-11 because the current vectors were interpolated onto a structured mesh. This smooths the results because the vectors are averaged. Although Pattiaratchi et al (2009) states that the divergence points occurred between 20 and 60m from the groyne, in figures 5-5, 5-7, 5-9, and 5-11 they occur at 140, 140, 160 and 140m away from the groyne. This may be a simple typographical error in their paper.

In the present study vector interpolation onto a structured mesh was not used for plotting the flow fields. The divergence point is less prominent but greater detail is evident in the flow fields due to a finer grid resolution (refer to figures 5-4, 5-6, 5-8 and 5-10). The location of the reattachment points vary with wave height and the divergence point occurs between 135 m and 365 m away from the groyne. The differences in divergence point location between this study and Pattiarachi et al (2009) are summarised in table 5-1:

Table 5-1: Divergence location for the different simulations

Figures	H_s (m)	θ_m	T_p (s)	Divergence Location (m)
5.4	1	45	14	135
5.5	1	45	14	140
5.6	2	10	14	174
5.7	2	10	14	140
5.8	2	45	14	230
5.9	2	45	14	140
5.10	3	45	14	370
5.11	3	45	14	160

Through vector plot analysis it was observed that larger waves with a stronger downstream eddy caused the divergence point to move away from the groyne. Smaller waves with a weaker eddy caused it to move towards the groyne. Larger waves developed larger recirculation zones. Small changes in T_p resulted in only minor influences on the overall location of the divergence point.

For the same wave heights, as θ_m increased from 10° to 60° the divergence point moved further away from the groyne.

5.7 Comparison of Pattiaratchi vs. Impermeable Groyne with a beach slope

This section of results comprises of a discussion comparing Pattiaratchi et al. (2009) who used a closed boundary condition at the land boundary against an open boundary with a beach slope at the land boundary. The discussion evaluates the following:

- The radiation stress field
- The lee side eddy
- Rip currents on both sides of the groyne
- Flow convergence zones
- Divergence occurring in the alongshore flow at the down drift extent of the lee eddy.

5.7.1 Radiation stress field

The radiation stress S_{xx} component was greater for the model runs with a beach slope than for the model runs with the closed boundary. The radiation stress S_{yy} component had a greater spatial extent for the model runs with the closed boundary condition, and the radiation stress values were higher. It was noted however this was mainly apparent for the 1m significant wave height model runs whereas the model runs with a 2m and 3m significant wave height had very similar S_{yy} component radiation stress values.

It was found that when comparing the model runs with a beach slope to the model runs with the closed boundary, the closed boundary model runs had a higher radiation stress in S_{xy} across the domain with a definite increase further offshore than the model runs with a beach slope. The differences however became less apparent when comparing the model runs with 3m significant wave heights.

5.7.2 Eddy circulations in the lee of the groyne

For the (Hs = 1m, θ = 45°, T = 14s) wave conditions a compact circular eddy formed for the model run with a beach slope, where as the model runs with a closed boundary did not show this. It was the same occurrence for the (Hs = 2m, θ = 10°, T = 14s) wave conditions. When comparing the other model runs, the eddy structure was very similar, and the differences became negligible with increasing wave height.

5.7.3 Rip currents

A strong offshore directed rip current occurred on the upstream side of the groyne for the model runs with a beach slope boundary condition and with (Hs = 1m, θ = 45°, T = 14s) wave conditions (refer to figure 5-12). This did not occur for the model runs with the closed boundary (refer to figure 5-13). Model comparisons for the (Hs = 2m, θ = 10°, T = 14s) wave conditions showed a similar rip current where there were large tip velocity angles. The rip currents were greater for the model runs with a closed land boundary condition compared to the model runs with a beach slope boundary condition.

Refer to tables C1.1 and table D1.1 in the appendices for details comparing rip currents from the closed and beach slope boundary conditions.

5.7.4 Alongshore currents

The (Hs = 1m, θ = 45°, T = 14s) wave condition model run with a beach slope boundary condition showed an alongshore current acting within the length of the groyne (Figure 5-12). Whereas for the model run with a closed boundary condition the alongshore current acted well outside of the length of the groyne (refer to figure 5-13). For the (Hs = 2m, θ = 10°, T = 14s) wave condition there was a more intense alongshore current spatially and in magnitude for the closed boundary model run. The alongshore current had a greater width in the cross-shore direction for all model runs with a closed land boundary.

5.7.5 Convergence

The model run with a beach slope land boundary condition, for the (Hs = 1m, θ = 45°, T = 14s) wave condition showed a weak convergence near the tip of the groyne on the lee side. This did not occur for a closed boundary condition simulation. No other model runs in the present study showed this feature.

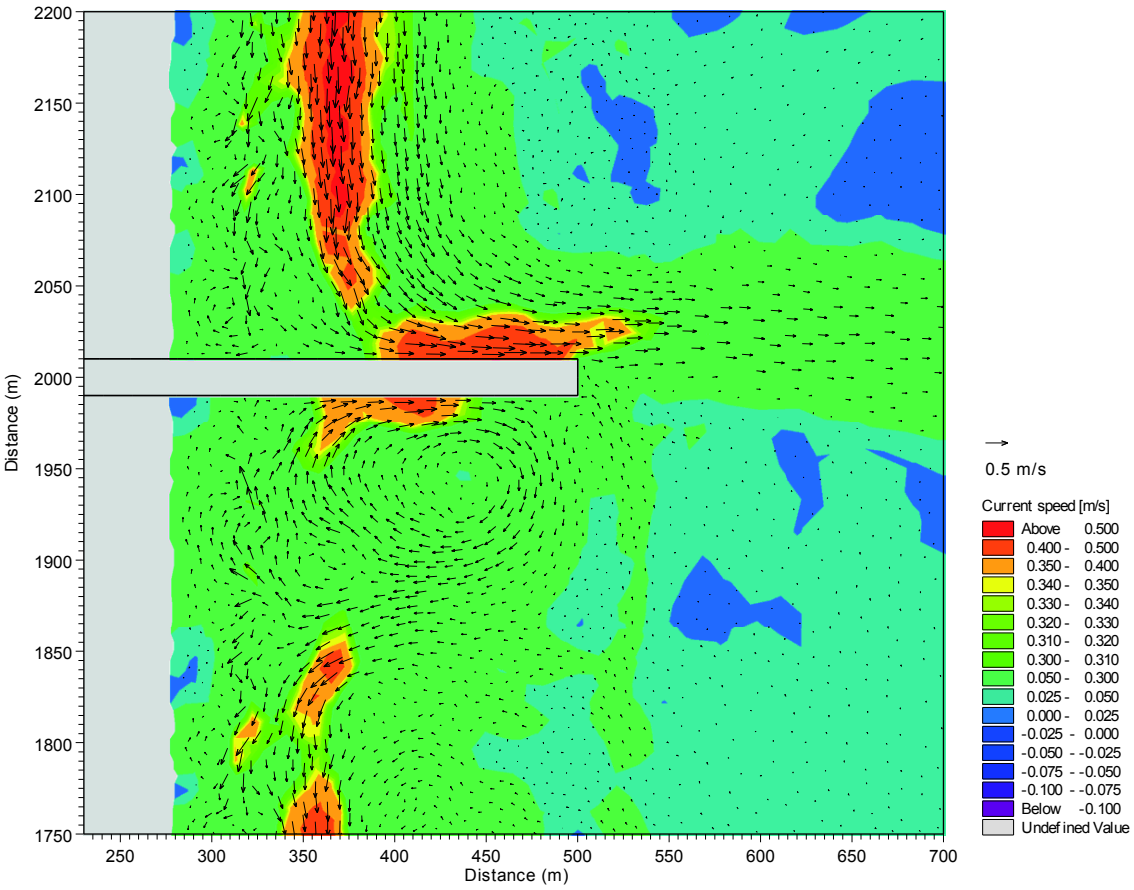

Figure 5-12: Vector plot showing the predicted current vectors. The colour represents the current speed for the (H_s=1m; T_p=14s; θ=45°) wave conditions (refer Table A3.2.2, model run 1).

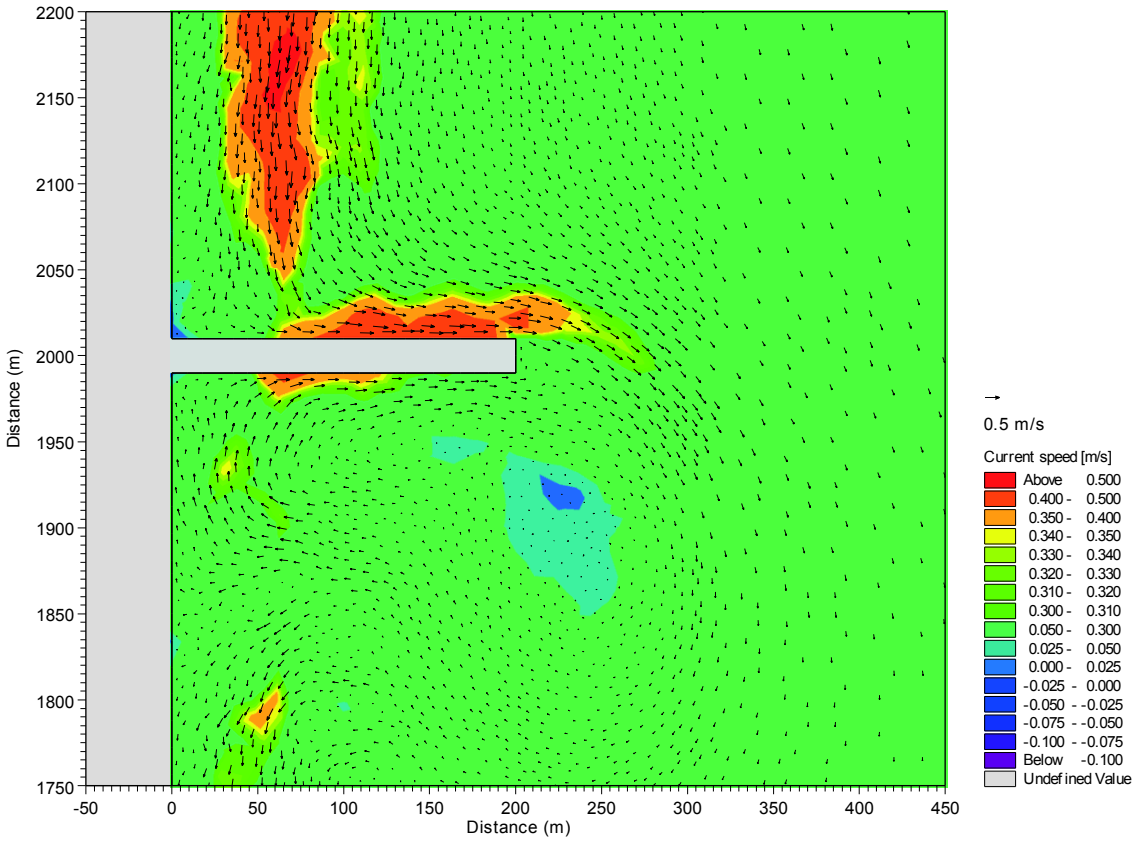

Figure 5.13: Vector plot showing the predicted current vectors. The colour represents the current speed for the (H_s=1m; T_p=14s; θ=45°) wave conditions (refer Table A3.1.1, model run 1).

5.7.6 Divergence

In general the model runs with a beach slope had smaller divergence lengths (i.e. length of the downstream re-circulation zone) than those with closed boundaries, as seen in table 5-2:

Table 5-2: Divergence length comparison

Incident Wave Conditions			Divergence Length (m)	
H_s (m)	Θ_m	T_p (s)	Beach Slope	Closed Boudary
1	45	14	130	135
2	10	14	130	170
2	45	14	140	200
3	45	14	300	370

The physical reason(s) for these differences are not clear, but they should be noted when making comparisons between models that are set up differently. A sloping beach at the landward boundary is a more realistic model for sandy shorelines.

5.7.7 Wave setup and run-up

The model runs with a beach slope boundary condition showed significant water level setup above 0 MSL position of the SWL landward boundary location. This may be the main reason for the differences between the simulations with a beach slope boundary condition and those with a closed land boundary condition. This allowed for the wave power to reach zero at the land boundary. The spectral wave model incorporates bottom friction that affects wave dissipation. The closed boundary at the 0 MSL changes the dissipation rate of the wave energy spectrum in comparison to a sloped beach boundary.

5.8 Summary

5.8.1 Pattiaratchi Comparison

There are significant discrepancies between the results published by Pattiaratchi et al., (2009) and those from the present simulations, although the model configurations were consistent. The only changes were the resolution and the time step for the solving i.e. the resolution was made finer and the time step was reduced. These two changes refined the flow patterns but did not change them.

It was noted that some of Pattiaratchi et al., (2009) results were incorrectly stated, as with the divergence lengths (section 5.6). There was also the lee side onshore rip current at the tip of the groyne as shown in Pattiaratchi et al., (2009) simulated results. This did not occur for any of the present simulations nor has it been reported in any other impermeable groyne literature (Kraus, Hanson & Blomgren, 1994; Raudkivi, 1996; Trampenau, Oumeraci and Dette, 2004).

The impermeable structure deflects the alongshore current offshore causing a rip current on the upstream side of the groyne. The sheltering of the lee side leads to a decrease in the radiation stress due to wave attenuation. The wave attenuation then leads to a water level change in the wave set-up which in turn generates gravitational currents directed towards the lee side of the groyne.

The present simulations generally agree with observed and documented flow patterns reported in the literature.

5.8.2 Impermeable Groyne with a beach slope

The reason behind the differences in the closed boundary impermeable groyne simulations and those of the open boundary beach slope simulations is due to the rate of dissipation of the wave energy spectrum. The governing equation for bottom friction in the spectral wave model affects the wave dissipation rate and so an open boundary with a slope had a higher dissipation rate than that of a closed boundary. This explains the discrepancies in the simulations as to why Pattiaratchi et al., (2009) simulations yielded higher radiation stresses, wave set-up and stronger currents.

CHAPTER 6

RESULTS & DISCUSSION – IMPERMEABLE GROYNES

Chapter Six comprises of a detailed discussion on the impermeable groyne simulation results. It is an evaluation of the change in flow pattern due to the change in the breaker zone width using the level of constriction of cross-sectional flow.

6.1 Introduction to Study 2

Multiple scenarios of impermeable groyne simulations were run in an attempt to evaluate the relationship between the resultant flow patterns and the levels of constriction of cross-sectional flow. This study was separated into several subsections:

- Datum change – manipulation of the water depth
- Groyne width change
- Groyne length change
- Rip currents
- Alongshore current
- Predominant flow pattern vs. the level of constriction

6.2 Water Level Changes

When the water levels were changed the level of constriction of the cross-section flow changed. It would either increase or decrease depending on whether or not a positive or negative datum shift was applied.

Following in accordance with model runs for the 200m long x 20m wide groyne:

When the water level decreased by 1m for the model runs with the (H_s = 1m, θ = 45°, T = 14s) wave conditions, the G_L/B_z value changed by a factor of 0.293 (from 1.152 to 0.859). As the water level decreased so too does the length of the groyne that is actively in the breaker zone width; the breaker zone moves further offshore.

When the water level increased by 1m for the model runs with the (H_s = 2m, θ = 45°, T = 14s) wave conditions, the G_L/B_z value changed by a factor of 0.168 (from 0.709 to 0.877). For the (H_s = 3m, θ = 45°, T = 14s) wave conditions, it was found that the G_L/B_z value changed by a factor of 0.110 (from 0.494 to 0.604). As the water level increased, so too does the length of the groyne that is actively in the breaker zone width; the breaker zone moves shoreward.

When comparing the change in G_L/B_z for the 2m and 3m significant wave heights, it can be seen that the change in depth has less of an effect on the G_L/B_z value for larger significant wave heights. The reason is that the larger significant wave height has a larger breaker zone width.

When comparing the model runs for the 2m significant wave height with incident angles 10°, 45° and 60°, there were differences in the change in G_L/B_z. The following differences were observed as the water level increased by 1m; the 10° G_L/B_z value changed by a factor of 0.277 (from a value of 1.087 to 1.364), the 45° G_L/B_z value changed by a factor of 0.168 (from a value of 0.709 to 0.877) and the 60° G_L/B_z value changed by a factor of 0.157 (from a value of 0.637 to 0.794). There was a definite decrease in the change in G_L/B_z with a depth change as the incident angle increased. This was not due to a change in depth but due to the fact that the change in incident angle affects the breaker zone width. An increase in the incident angle increases the breaker zone width. This can be explained earlier in section 5.2, where the incident angle increase affects the peak radiation stress conditions.

The level of constriction of cross-sectional flow increases with a water level increase; and decreases when the water level decreases. It will therefore act similarly with tidal changes.

When comparing the flow patterns for the (H_s = 1m, θ = 45°, T = 14s) wave conditions, as the depth decreased by 1m, the alongshore current moved offshore in the cross-shore direction

(refer to figure 6-1 and 6-2). As it moved further offshore, the area of interaction between the groyne and the alongshore current decreased. This decrease in the area of interaction decreases the tip velocity angle at the head of the groyne. It was also observed that the depth change affected the flow pattern. This change in the flow pattern was more apparent when assessing the (H_s = 2m, θ = 45°, T = 14s) wave conditions. When the depth increased by 1m the alongshore current moved shoreward (refer to figure 6-3 and 6-4) and the tip velocity angle increased.

As the water depth increases the flow pattern around the groyne starts to change from alongshore dominant to rip current dominant. As the water depth decreases the flow pattern around the groyne starts to change from rip current dominant to alongshore current dominant.

Refer to appendix D, tables D1.1 - D1.3 for level of constriction of the cross-sectional flow values for different model runs. Section 6.2 only used table A3.2.3 values to determine the general effects on the level of constriction of the cross-sectional flow values due to depth changes.

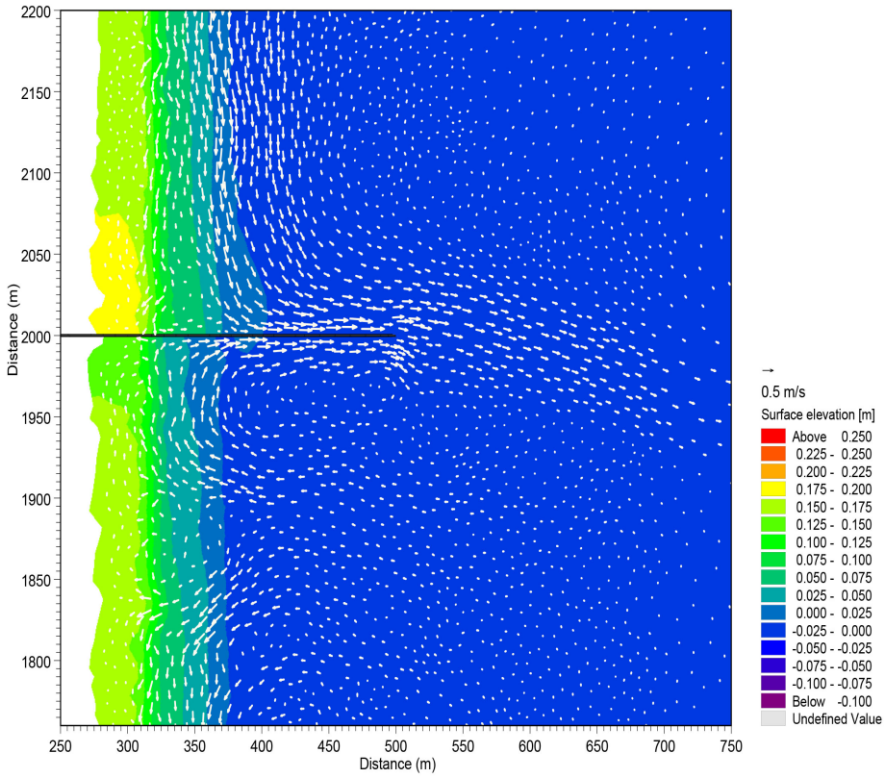

Figure 6-1: Vector plot showing the predicted current vectors for MSL = 0 (H_s = 1m; T_p = 14s; θ = 45°) (refer to table A3.2.3, model run 1).

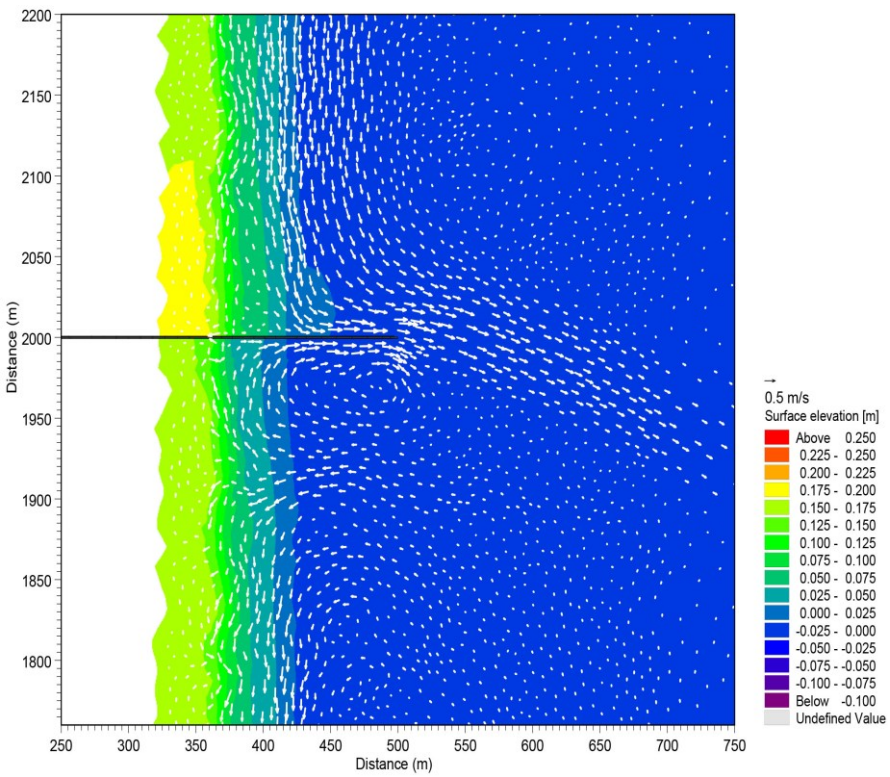

Figure 6-2: Vector plot showing the predicted current vectors for MSL = -1 (H_s = 1m; T_p = 14s; θ = 45°) (refer to table A3.2.3, model run 2).

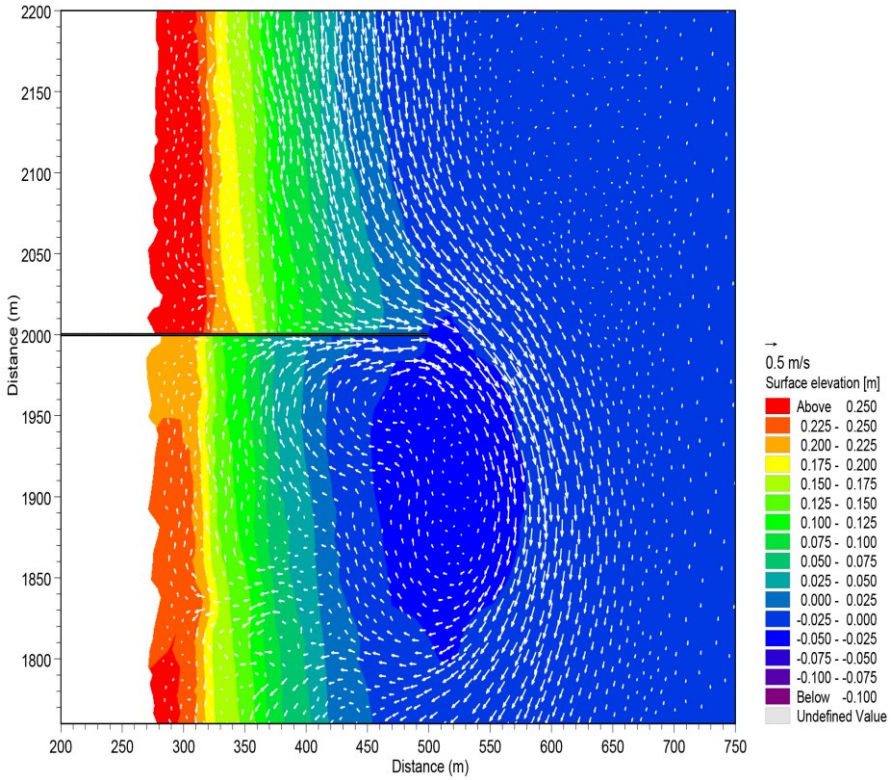

Figure 6-3: Vector plot showing the predicted current vectors for MSL = 0 (H_s = 2m; T_p = 14s; θ = 45°) (refer to table A3.2.3, model run 9).

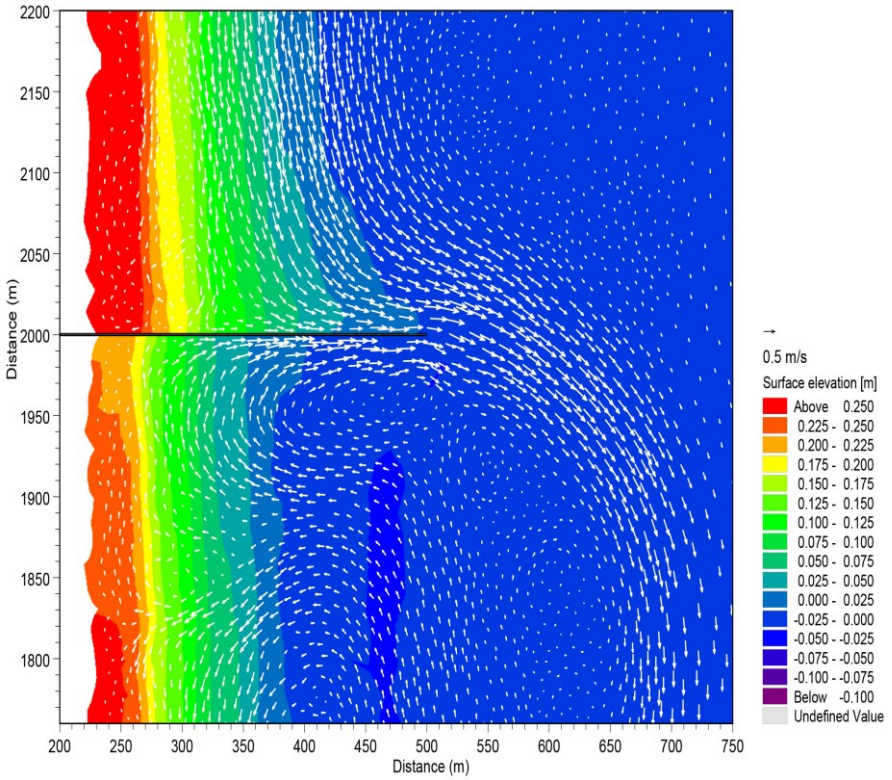

Figure 6-4: Vector plot showing the predicted current vectors for MSL = 1 (H_s = 2m; T_p = 14s; θ = 45°) (refer to table A3.2.3, model run 10).

6.3 Groyne width change

When comparing the level of constriction of the cross-sectional flow between the 20m x 200m groyne and the 1m x 200m groyne (refer to appendix D, table D1.1-D1.2) there were only minor differences:

- Model run 1 (Hs = 1m, θ = 45°, T = 14s), the 20m wide G_L/B_z value was 1.152, the 1m wide G_L/B_z value was 1.117, with a difference in value of 0.035.
- Model run 9 (Hs = 2m, θ = 45°, T = 14s), the 20m wide G_L/B_z value was 0.709, the 1m wide G_L/B_z value was 0.717, with a difference in value of 0.008.
- Model run 17 (Hs = 3m, θ = 45°, T = 14s), the 20m wide G_L/B_z value was 0.494, the 1m wide G_L/B_z value was 0.485, with a difference in value of 0.009.

From a larger view point there should not be any differences in the level of constriction of the cross-sectional flow as the breaker zone width is determined by the bathymetry, the water levels and the wave conditions. These parameters are identical in the compared model runs, the only difference is the groyne widths. It is possible that the wider groyne can affect the breaker zone width but only in the vicinity of the groyne tip.

What was interesting however was that differences were observed between the compared current vector plots. The upstream flow structures were similar but the downstream flow structures in the lee of the groyne for model run 1 (Hs = 1m, θ = 45°, T = 14s) were not. In the lee of the groyne, the 20m wide groyne (refer to figure 6-5) had an eddy, circular in nature. The narrow 1m groyne (refer to figure 6-6) did not show a completely formed eddy. The narrow groyne also displayed a rip current tending far offshore on both the upstream and downstream sides. This however was not the case for the wide groyne, the rip current tending far offshore only occurred on the upstream side. On the downstream side there was a convergent flow impeding the rip current and feeding it back into the eddy.

Only the model runs from 1 to 4 displayed differences in the surrounding flow patterns. The differences in the flow patterns between a wide and narrow groyne were only observed for a 1m significant wave height. The compared model runs for a 2m and a 3m significant wave height showed very similar flow patterns between the 20 m wide and the 1m narrow groynes. It is therefore apparent that the larger the significant wave height is, the smaller the affect the groyne width has on the surrounding flow patterns due to the larger breaker zone width.

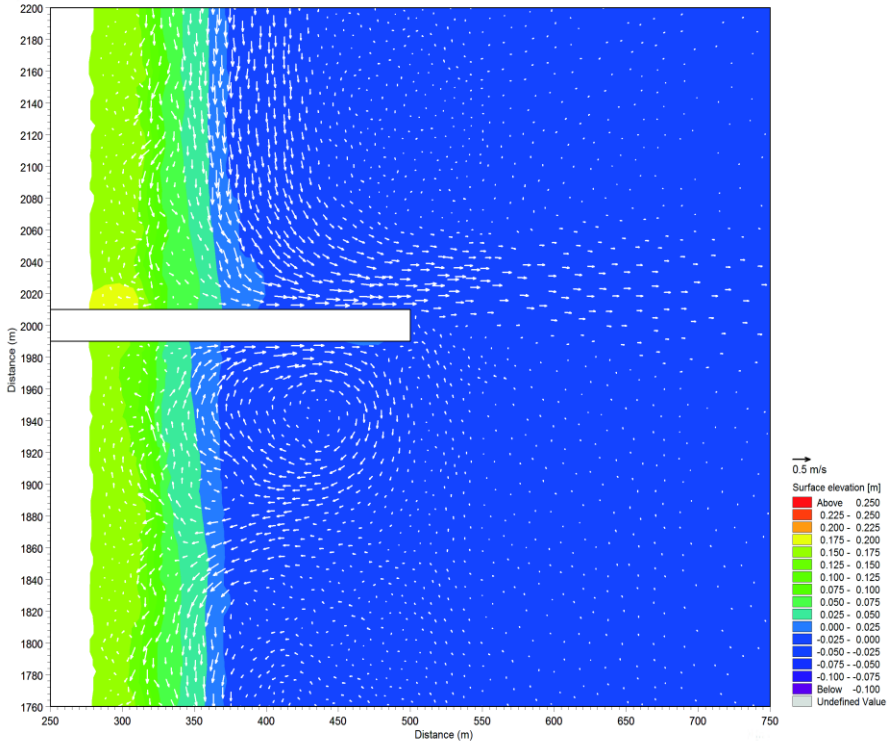

Figure 6-5: Vector plot of the 20m wide groyne showing the predicted current vectors and the current speed for the (H_s = 1m; T_p = 14s; θ = 45°) wave conditions (refer to table A3.2.2, model run 1).

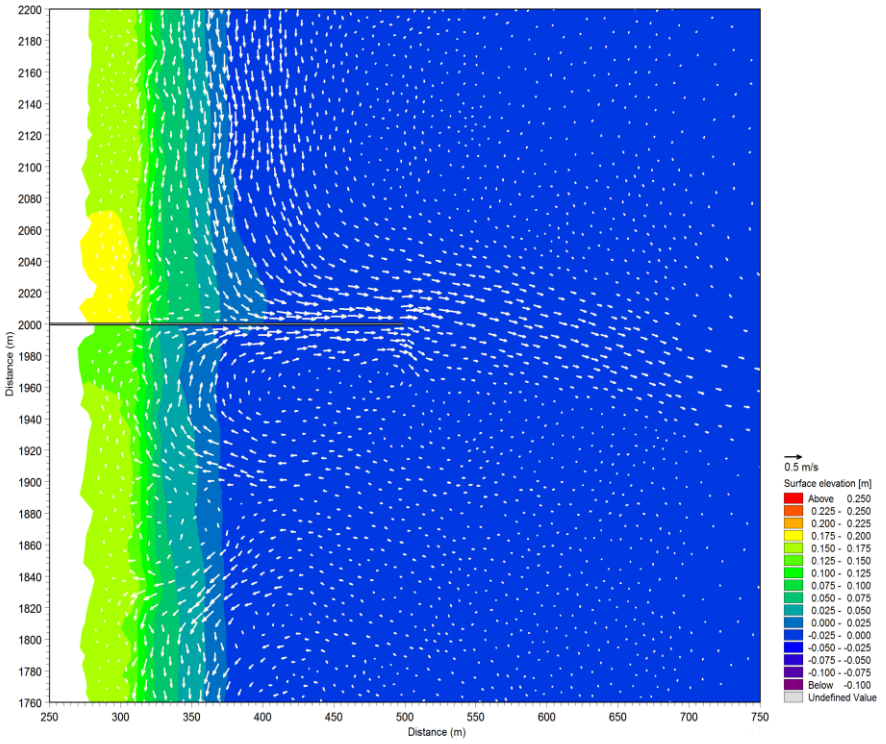

Figure 6-6: Vector plot of the 1m wide groyne showing the predicted current vectors and the current speed for the (H_s = 1m; T_p = 14s; θ = 45°) wave conditions (refer to table A3.2.3, model run 1).

6.4 Groyne length change

The affect that a change in groyne length has on the flow pattern varies depending on how much the groyne length changes. Changing the groyne length will have the same effect as changing the water level. The only factor that is actually changing is the effective length of the groyne actively in the water. In this case the groyne length was reduced to half the initial length, from 200m to 100m. Ideally this should halve the level of constriction of the cross-sectional flow however there are some slight discrepancies in this relationship, as shown in table 6-1, due to how a groyne affects the surrounding swash zone.

Table 6-1: Constriction ratio difference for the 200m & 100m groyne (after Table D1.2-D1.3)

Model Run	G_L/B_z		Difference
	1m x 200m	1m x 100m	%
1	1.117	0.630	56.40
5	1.053	0.590	56.03
9	0.717	0.394	54.95
13	0.641	0.349	54.46
17	0.485	0.264	54.43

The main effect that the change in groyne length has is the degree to which it changes the level of constriction of cross-sectional flow. If the length is increased then the level of constriction decreases and if the length is decreased then the level of constriction increases.

When the groyne length is decreased it has a higher probability that the groyne in its entire length will act within the alongshore current zone. This occurred for all model runs where the groyne was 100m long in the active water zone. A reduction in the groyne length will lead to a decrease in the tip velocity angle. As the angle decreases the current will change direction from cross-shore flow (tending offshore) to alongshore flow. If the groyne acts within the alongshore current zone and the groyne length does not exceed the width of the alongshore current flow, then the flow structure is predominantly in the alongshore direction (refer to figure 6-7).

It can also be stated that as the groyne length is increased the tip velocity angle increases as well. If the groyne length exceeds the width of the alongshore current flow, then the flow will be predominantly rip-current (refer to figure 6-8) or in a state of transition between the two different flow patterns.

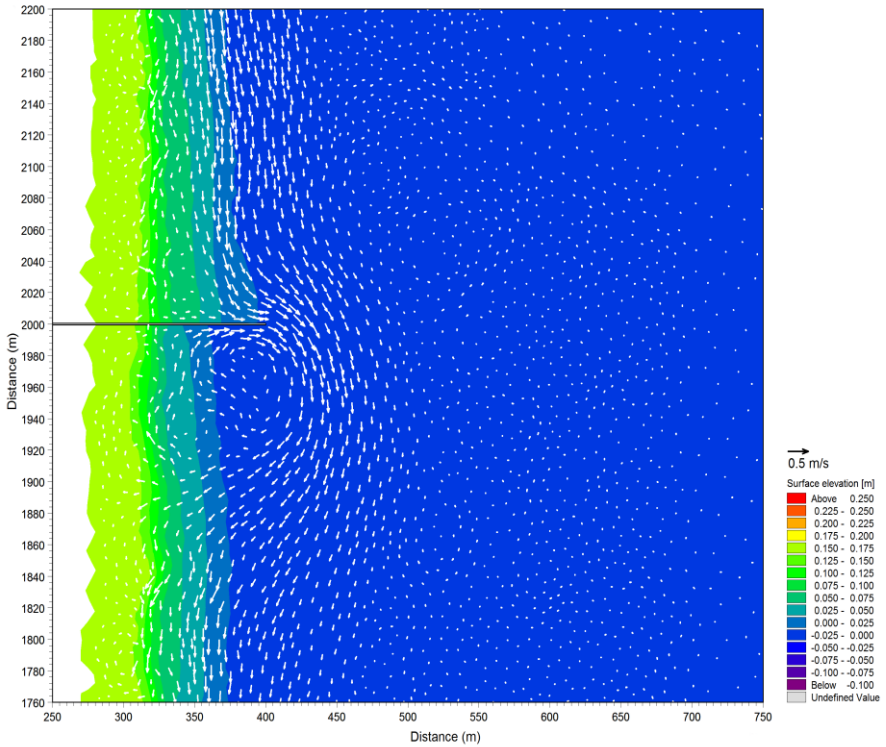

Figure 6-7: Vector plot showing the predicted current vectors and the wave set-up for the 100m groyne (H_s = 1m; T_p = 14s; θ = 45°) (refer to table A3.2.4, model run 1).

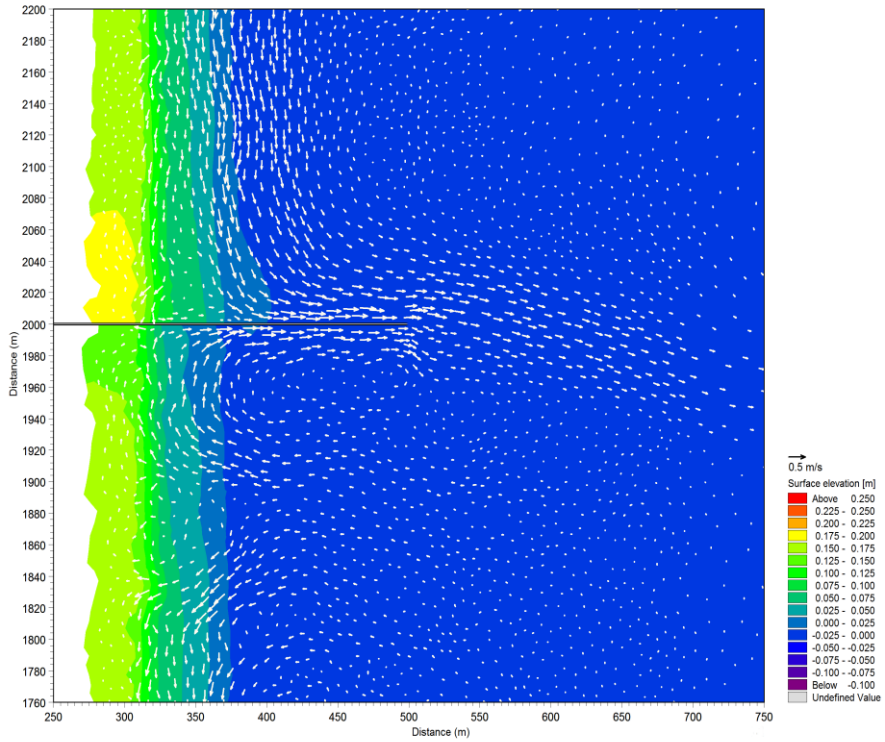

Figure 6-8: Vector plot showing the predicted current vectors and the wave set-up for the 200m groyne (H_s = 1m; T_p = 14s; θ = 45°) (refer to table A3.2.3, model run 1).

6.5 Rip currents

The core alongshore current occurs where the greatest intensity of radiation stress acts in the S_{xx} and the S_{yy} (the wave set up), this is where the ratio of the breaking waves Q_b ranged between 9 and 50 per-cent which relates to the standard breaking index number γ ranging between 0.5 - 0.8 ($\gamma = H_b/L_o$). The strongest rip currents formed along the groyne behind the 0.8 breaking index number. In the event the standard breaking index of 0.8 occurred outside of the groyne length then the strongest rip current occurred at the very tip of the groyne for levels of constriction of cross-sectional flow less than 0.6.

A comparison of the upstream and downstream maximum rip-currents along the trunk of the groyne was undertaken. This was done to correlate these values with the level of constriction of the cross-sectional flow. The following results are a collective of the 1m x 200m groyne and the 1m x 100m groyne:

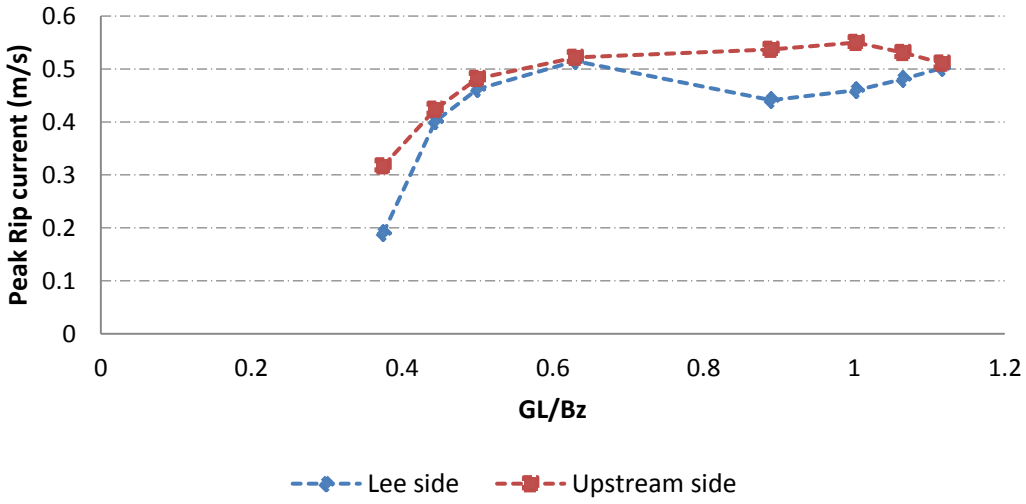

Figure 6-9: Graph of Peak rip currents vs. level of constriction for the (H_s=1m; T_p=14s; θ=45°) wave conditions. Points are joined to lines for clarity.

Figure 6-9 shows that for a 1m significant wave height as the G_L/B_z decreased from 0.9 to 0.6, the peak rip current on the upstream side of the groyne decreased while the peak rip current on the lee side increased. As G_L/B_z decreased from 0.6 to 0.4 both the peak rip currents on either side of the groyne trunk decreased.

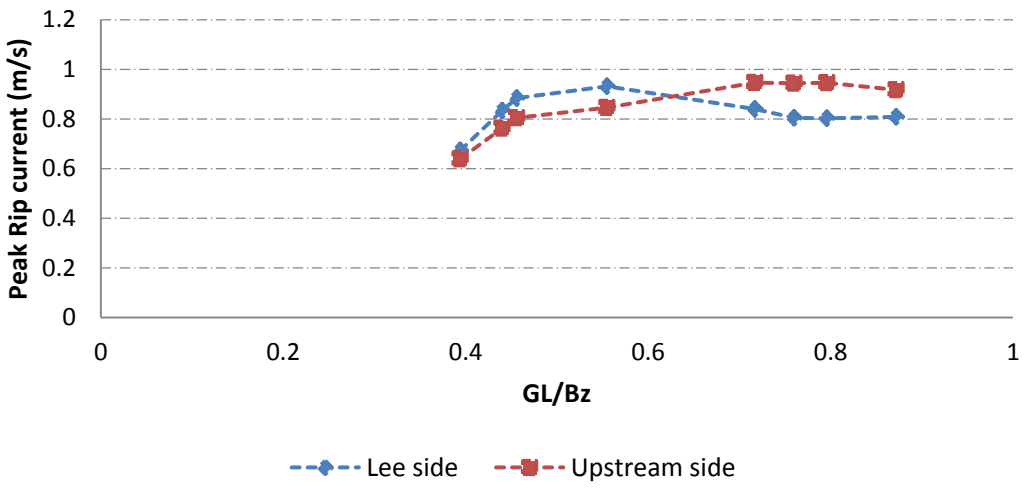

Figure 6-10: Graph of Peak rip currents vs. level of constriction for the (H_s = 2m; T_p = 14s; θ = 45°) wave conditions. Points are joined to lines for clarity.

Figure 6-10 shows that for a 2m significant wave height with a 45° incident angle as the G_L/B_z decreased from 0.8 to 0.55, the peak rip current on the upstream side of the groyne decreased while the peak rip current on the lee side increased. As G_L/B_z decreased from 0.55 to 0.4 both the peak rip currents on either side of the groyne trunk decreased. It can also be noted that for a G_L/B_z of 0.65 the location of the strongest peak rip current changes. The peak rip current on the lee side of the groyne trunk becomes stronger than the peak rip current on the upstream side of the groyne with a decrease in the level of constriction of cross-sectional flow.

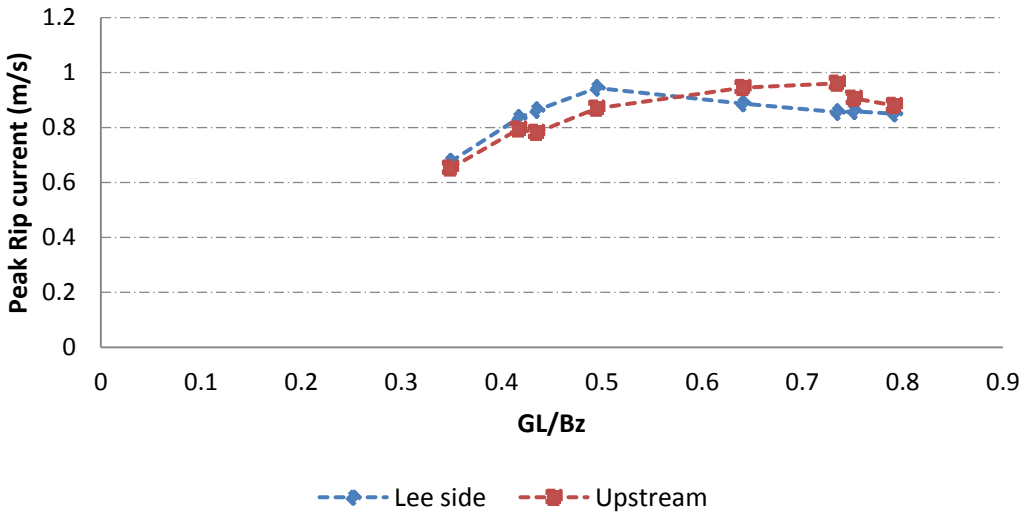

Figure 6-11: Graph of Peak rip currents vs. level of constriction for the (H_s = 2m; T_p = 14s; θ = 60°) wave conditions. Points are joined to lines for clarity.

Figure 6-11 shows that for a 2m significant wave height with a 60° incident angle as the G_L/B_z decreases from 0.74 to 0.5 the peak rip current in the upstream side of the groyne trunk decreased while the peak rip current on the lee side increased. As G_L/B_z decreased from 0.5 to 0.35 both the peak rip currents on either side of the groyne trunk decreased. It can also be noted that for a G_L/B_z of 0.58 the location of the strongest peak rip current changes. The peak rip current on the lee side of the groyne trunk becomes stronger than the peak rip current on the upstream side of the groyne with a decrease in the level of constriction of cross-sectional flow.

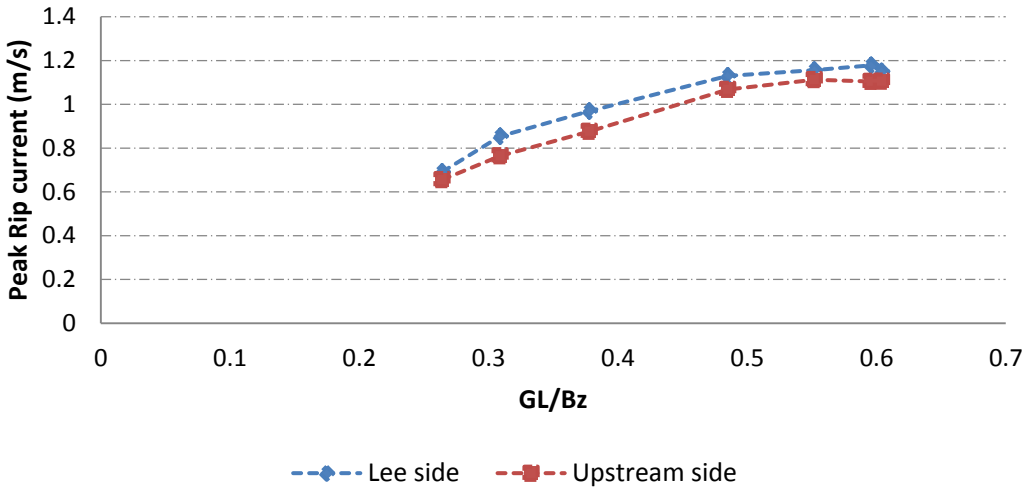

Figure 6-12: Graph of Peak rip currents vs. level of constriction for the (H_s = 3m; T_p = 14s; θ = 45°) wave conditions. Points are joined to lines for clarity.

Figure 6-12 shows that for a 3m significant wave height as the G_L/B_z decreased from 0.6 to 0.25 both the peak rip currents on either side of the groyne trunk decreased. The peak rip current on the lee side of the groyne trunk was stronger than the peak rip current on the upstream side of the groyne

From figures 6-9 to 6-12 it was apparent that as the G_L/B_z decreased from ±0.6, so too did the peak rip currents decrease in strength on the upstream and downstream side of the groyne.

A summary of the level of constriction of cross-sectional flow effects are listed in table 6-2:

Table 6-2: Effects of the level of constriction on the groyne rip-currents

G_L/B_z	Rip Current Extent Along Groyne Span from the Tip (%) in excess of 0.35m/s		Rip Current Magnitude	
	Upstream	Downstream	Upstream	Downstream
> 1.0	45-55	65-85	Higher	Lower
0.9	43-45	57-73	Higher	Lower
0.8	42-43	57-73	Higher	Lower
0.7	33-44	62-67	Higher	Lower
0.6	20-36	40-64	Lower	Higher
0.5	31-43	53-71	Lower	Higher
0.4	24-42	42-71	Lower	Higher
< 0.3	20-29	40-64	Lower	Higher

As shown in table 6-2 above, the rip current occurring along the trunk of the groyne in excess of 0.35 m/s has a greater length of action on the lee side (40-85%) than on the upstream side (20-55%). The largest length of action that occurred for the rip currents from the simulations was for a level of constriction of cross-sectional flow > 0.8. In general, as the level of constriction of cross-sectional flow decreased so too did the length of action of the rip current along the groyne trunk on the upstream side. This did however tend to fluctuate on the lee side trunk, as the greater length of action of the rip current on the lee side can be attributed to the eddy circulation. The strongest rip current velocity shifted from the upstream side to the lee side of the groyne trunk as the G_L/B_z decreased from ±0.6.

6.6 Alongshore Current

Cross-sections of the alongshore flow from the tip of the groyne for the model runs were taken to assess how the alongshore current changes with respect to the level of constriction of the cross-section flow. The sign orientation for the following results; positive flow values oppose the direction of the alongshore current, negative flow values are in the direction of the alongshore current. The results are as follows:

20mx200m Impermeable groynes

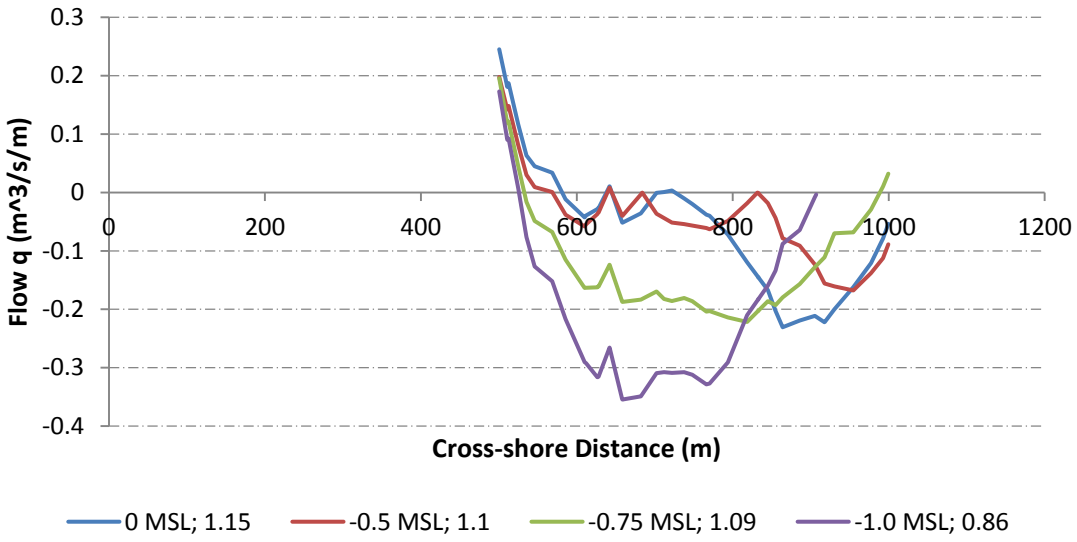

Figure 6-13: Graph of cross-section flow at the tip of the groyne for the different datums and G_L/B_z. For the (H_s = 1m; T_p = 14s; θ = 45°) wave conditions.

Figure 6-13 for the 20m wide groyne near the very tip of the groyne (500m along the cross-shore distance) showed that there were turbulent conditions leading to a reverse flow. The affect decreases as the current bends around the tip of the groyne and the reverse flow was only apparent for the 20m wide groyne.

For figure 6-13 as G_L/B_z decreased from 1.15 to 0.86, the width over which the alongshore current acted decreased and its peak flow increased. What was interesting to note is that for the -0.5 MSL the peak flow moved further offshore before the width of the alongshore current increased and it moved closer shoreward for the -0.75 MSL.

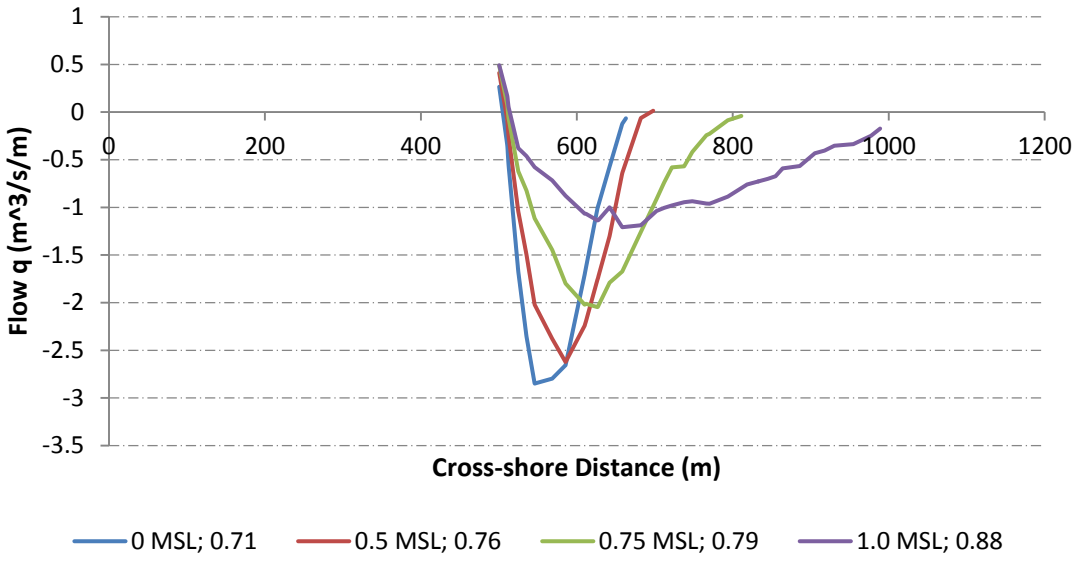

Figure 6-14: Graph of cross-section flow at the tip of the groyne for the different datums and G_L/B_z. For the (H_s = 2m; T_p = 14s; θ = 45°) wave conditions.

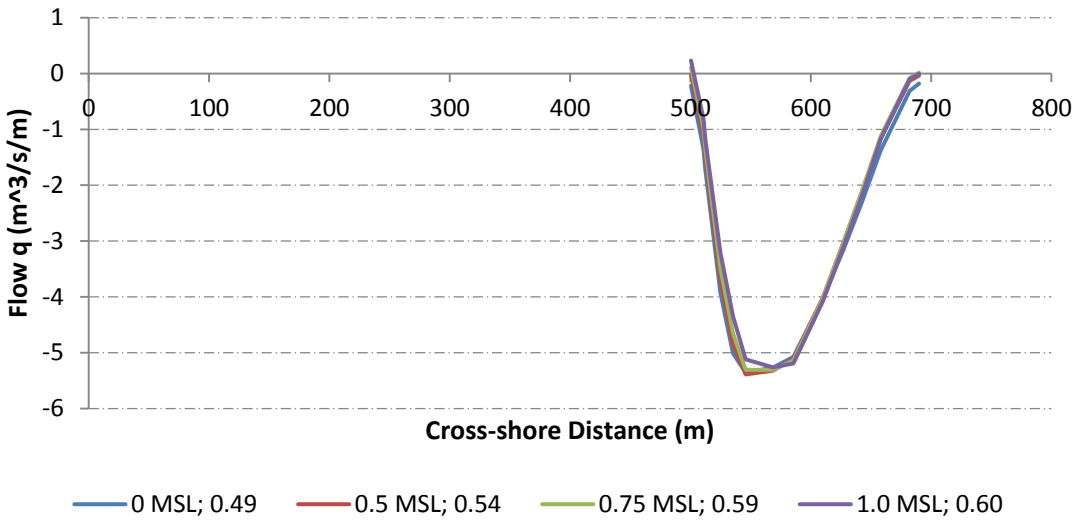

Figure 6-15: Graph of cross-section flow at the tip of the groyne for the different datums and G_L/B_z. For the (H_s = 3m; T_p = 14s; θ = 45°) wave conditions.

When comparing figures 6-13, 6-14 and 6-15, as the significant wave height increased so too did the peak flows. This is due to an increase in the radiation stresses because of the change in significant wave height; mainly S_{xy} as this plays a major role in the alongshore flow. As the significant wave height increases so too does the extent of the breaker zone width, this relates to a decrease in G_L/B_z. This will also cause the alongshore current width to decrease and the peak flow to increase.

There was a drastic change in figure 6-14 as the G_L/B_z decreased from 0.79-0.71. As the level of constriction decreased from 0.79, the peak alongshore flow began to occur within 100m of the groyne. Then as G_L/B_z decreased from 0.6, as shown in figure 6-15, there was little change in the location of the peak flow. The concern with high flow is that there are high velocities, especially if this is occurring at the tip of the groyne.

1x100m & 1x200m Impermeable groynes

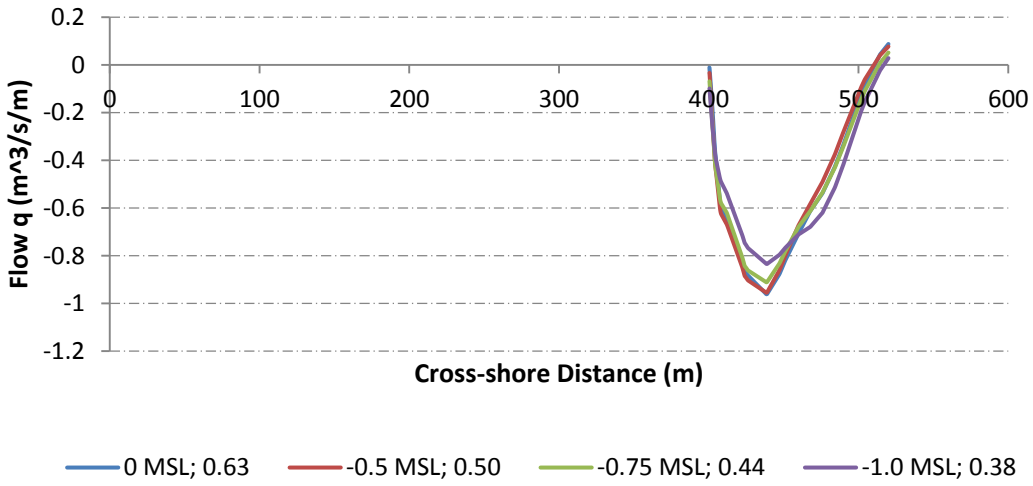

Figure 6-16: Graph of cross-section flow at the tip of the 100m groyne for the different datums and G_L/B_z. For the (H_s = 1m; T_p = 14s; θ = 45°) wave conditions.

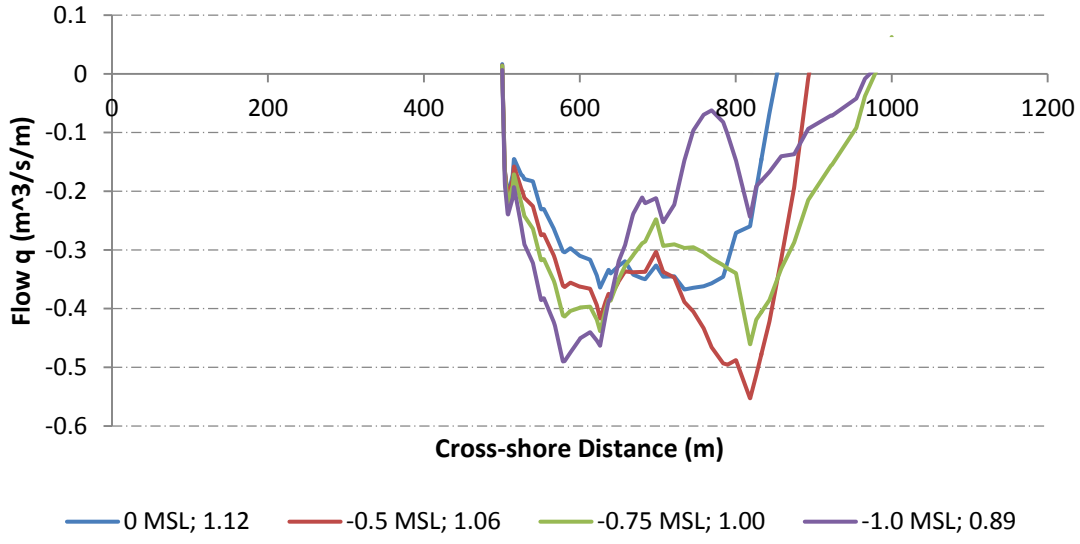

Figure 6-17: Graph of cross-section flow at the tip of the 200m groyne for the different datums and G_L/B_z. For the (H_s = 1m; T_p = 14s; θ = 45°) wave conditions.

In figure 6-16 the entire 100m groyne acts within the alongshore current width. This is visible on the graph by the large flow values and relatively small width over which the alongshore current acts. The alongshore current is concentrated within a 100m width beyond the tip of the groyne. If the groyne is now extended 100m to move this concentrated zone further offshore it would result in figure 6-17. The concentrated alongshore current decreased in flow strength and increased in width (in excess of a 250m width).

In figure 6-17 as the datum changed from 0 MSL to -0.75 MSL, the alongshore current increased in flow strength and cross-sectional width before the peak alongshore flow moved shoreward towards the groyne tip. This occurrence was only apparent for the 1m significant wave height simulations. This increase in the alongshore current cross-sectional width may be due to the change in the tip velocity angle (the angle decreases). The predominantly rip current flow starts to deviate, increasing the width of the alongshore current, before bringing the peak alongshore flow (core alongshore current) closer to the groyne.

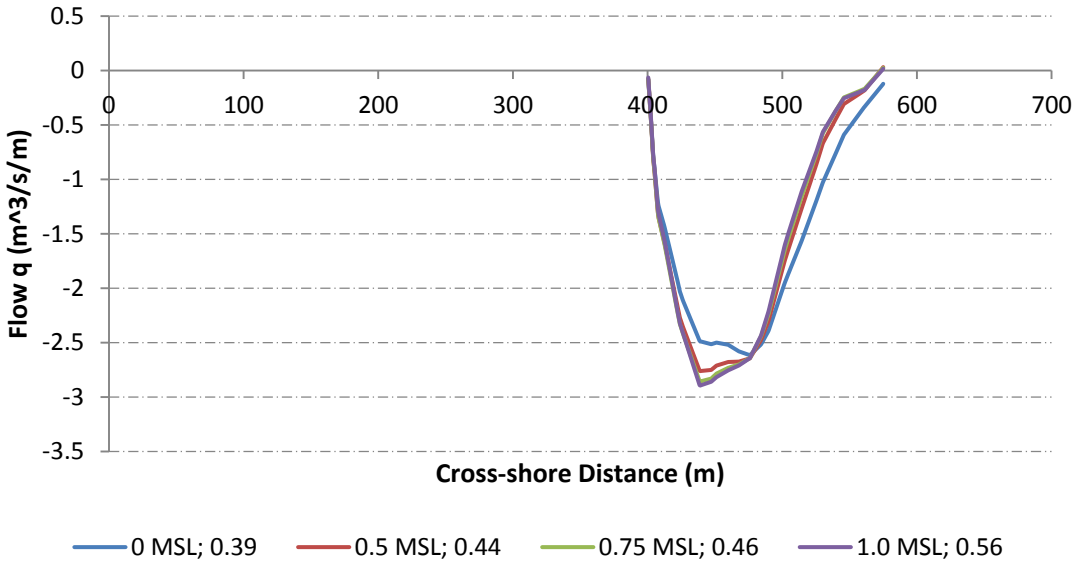

Figure 6-18: Graph of cross-section flow at the tip of the 100m groyne for the different datums and G_L/B_z. For the (H_s = 2m; T_p = 14s; θ = 45°) wave conditions.

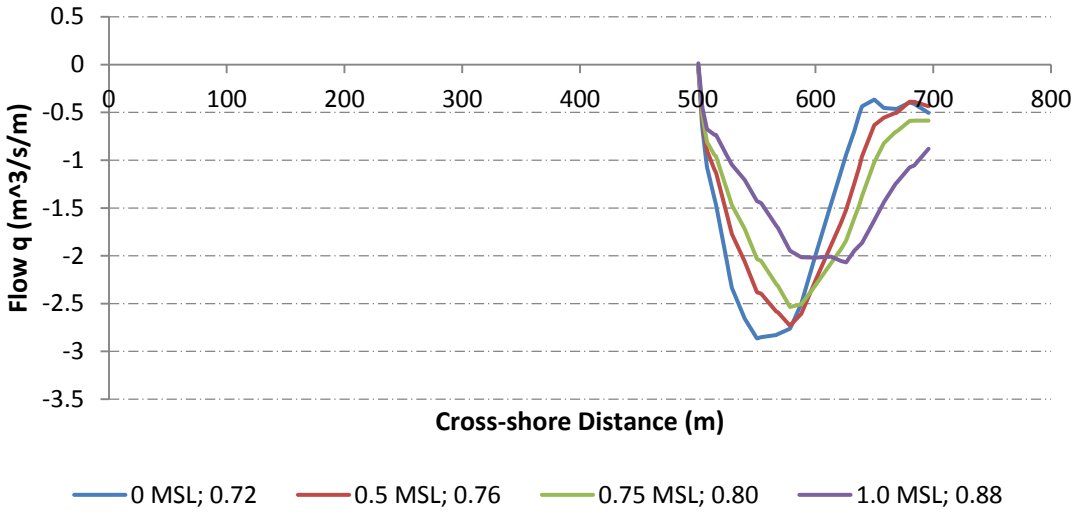

Figure 6-19: Graph of cross-section flow at the tip of the 200m groyne for the different datums and G_L/B_z. For the (H_s = 2m; T_p = 14s; θ = 45°) wave conditions.

In figure 6-14 and figure 6-19, there is quite a significant change between the 0.88-0.72 levels of constriction of cross-sectional flow. This will be discussed in more detail in section 6.7.

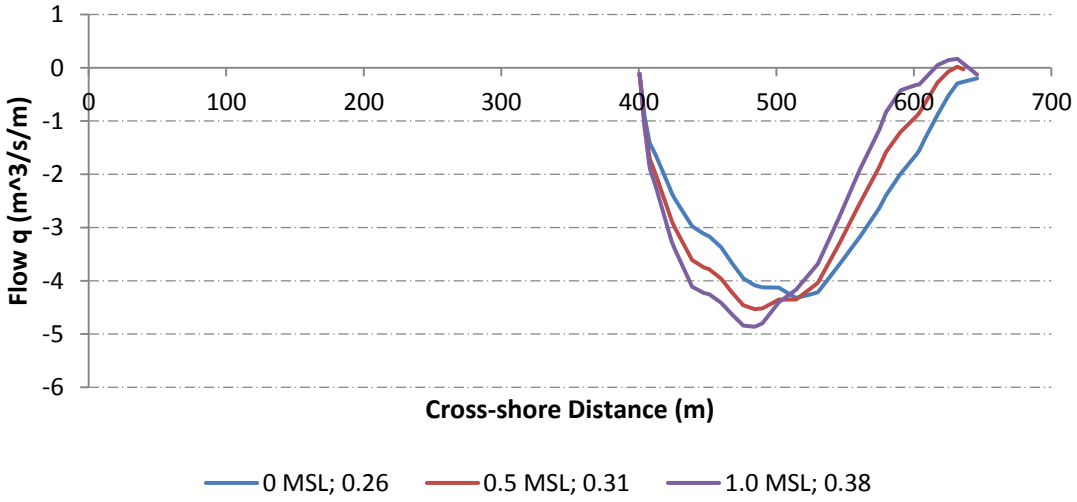

Figure 6-20: Graph of cross-section flow at the tip of the 100m groyne for the different datums and G_L/B_z. For the (H_s = 3m; T_p = 14s; θ = 45°) wave conditions.

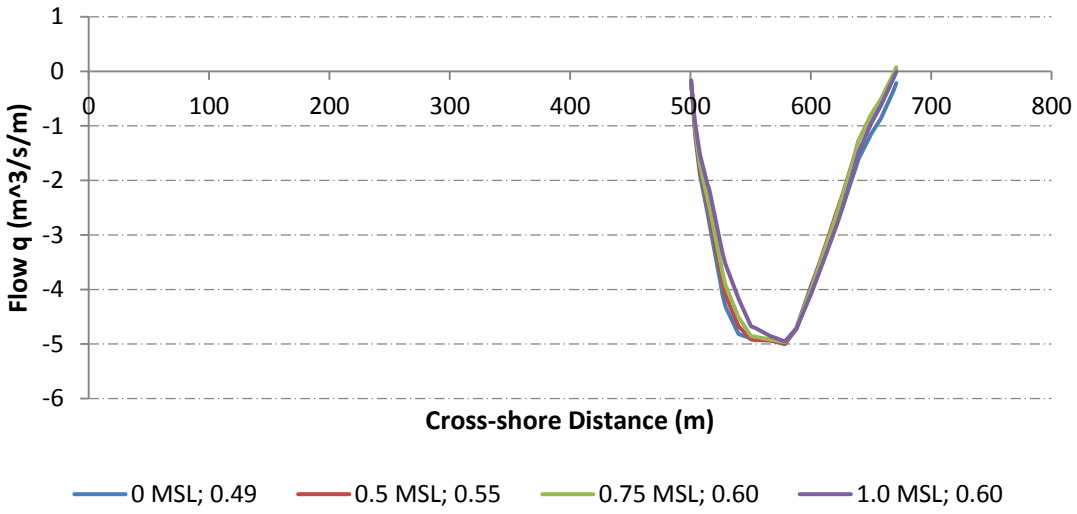

Figure 6-21: Graph of cross-section flow at the tip of the 200m groyne for the different datums and G_L/B_z. For the (H_s = 3m; T_p = 14s; θ = 45°) wave conditions.

When comparing figures 6-16, 6-18 and 6-20, as G_L/B_z decreases from 0.44, the alongshore flow begins to behave naturally, without any anthropogenic influence. When the level of constriction decreased from 0.4 the strength of the alongshore flow decreased and the cross-sectional width increased. When comparing figure 6-20 and 6-21 there was very little change with respect to the flow. It was therefore noted that for a G_L/B_z less than 0.6, the peak flow is relatively constant. This is visible in figure 6-15 - a dominant alongshore flow.

From figures 6-13 to 6-21, when G_L/B_z is greater than 0.88 the alongshore flow is relatively weak and acts over a large cross-sectional width. Between 0.88 and 0.71 the alongshore flow cross-sectional width decreases and the strength of the peak flow drastically increases. Between 0.88 and 0.44 the alongshore flow is strong in intensity and acts over a very small cross-sectional width. If it is less than 0.44 the alongshore flow cross-sectional width increases and the alongshore flow strength decreases.

6.7 Predominant flow pattern vs. level of constriction

It is apparent from section 6.6, that the most drastic changes in the alongshore flow occur between the 0.88 and 0.71 levels of constriction. To assess this in further detail the same cross section where the alongshore flow was taken, at the tip of the groyne, was now separated into the current vector velocity components. Where the cross-shore currents, u velocity, and the alongshore currents, v velocity, could be compared to evaluate the dominant flow directions.

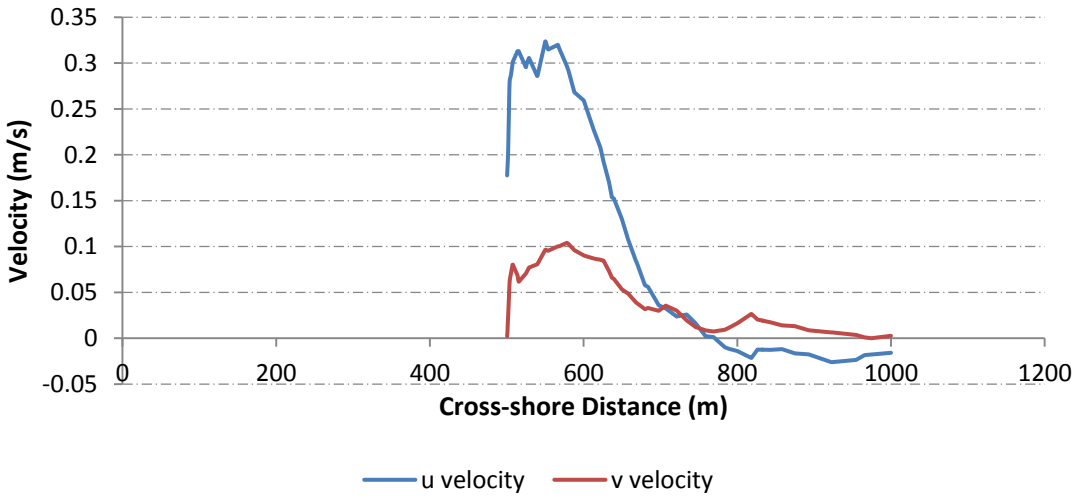

Figure 6-22: Graph of cross-section velocities at the tip of the groyne with a MSL = -1 and G_L/B_z = 0.89. For the (H_s = 1m; T_p = 14s; θ = 45°) wave conditions (Table A3.2.3, model run 2).

In figure 6-22 with a 0.89 G_L/B_z, the cross-shore velocity is greater than the alongshore velocity, the flow pattern is therefore rip current dominant. The alongshore velocity only becomes dominant 200m offshore from the groyne tip, at ±700m. As G_L/B_z continues to increase (refer to figure 6-23) so too does the cross-shore velocity component. The flow is directed far offshore from the trunk of the groyne, taking that much longer before the alongshore current becomes dominant. When comparing figure 6-22 and figure 6-23, the alongshore velocity component becomes dominant at ±700m cross-shore distance for 0.89 and ±950m for 1.12. This shows that with an increase in the level of constriction, there is an increase in the tip velocity angle; changing from an alongshore velocity component to a cross-shore velocity component.

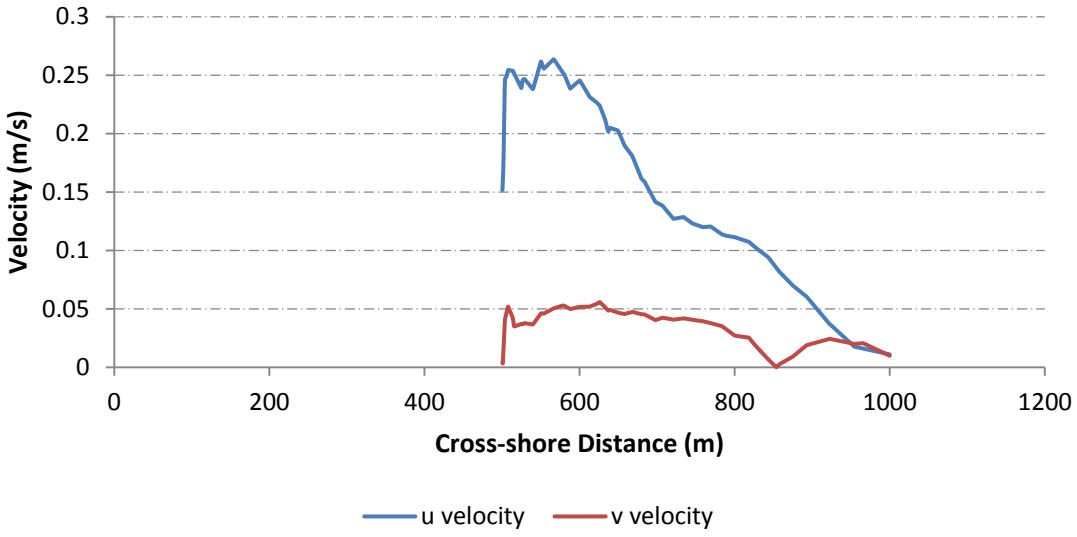

Figure 6-23: Graph of cross-section velocities at the tip of the groyne with a MSL = 0 and G_L/B_z = 1.12. For the (H_s = 1m; T_p = 14s; θ = 45°) wave conditions (Table A3.2.3, model run 1).

A decision was made to classify a transition state between the two dominant flow patterns (rip current dominant and alongshore dominant). The reason is that there is a point at which both the alongshore and cross-shore currents are high in magnitude in the vicinity of the groyne. Figure 6-24 showed a peak alongshore current occurring within 100m of the groyne tip, for a 0.8 G_L/B_z. The alongshore current also begins to dominate approximately 130m from the tip of the groyne, 630m offshore. The 0.8 G_L/B_z will be considered as the start of the transition state.

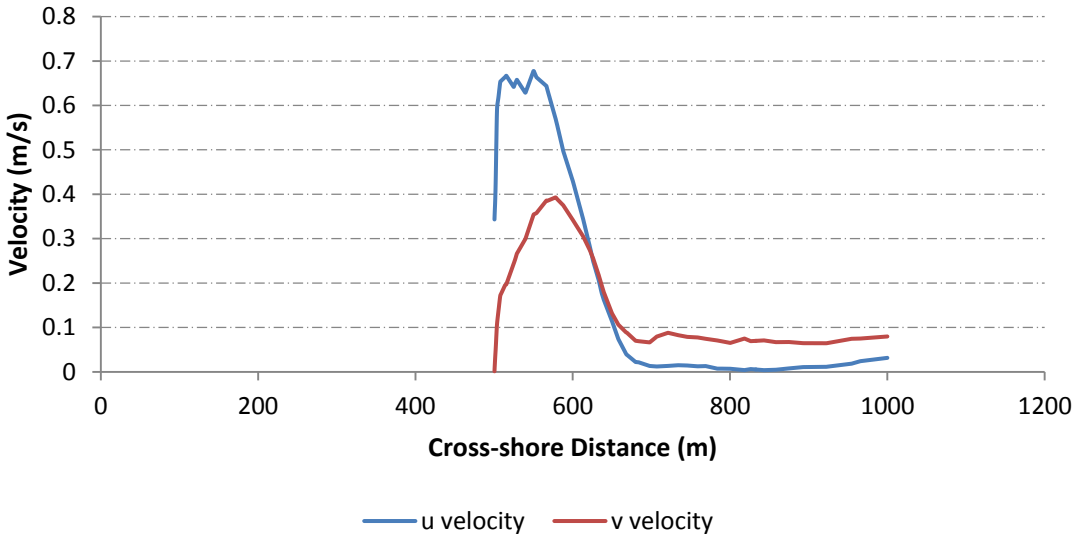

Figure 6-24: Graph of cross-section velocities at the tip of the groyne with a MSL = 0.75 and G_L/B_z = 0.80. For the (H_s = 2m; T_p = 14s; θ = 45°) wave conditions (Table A3.2.3, model run 11).

The different cross-section velocity plots were compared until such time a plot was found where the alongshore peak velocity value was on par with the cross-shore peak velocity value i.e. the u and v graph maximums were level. This was taken to be the end of the transition state between the two flow patterns. This state occurred between 0.6 - 0.55 G_L/B_z (refer to figure 6-25 and figure 6-26).

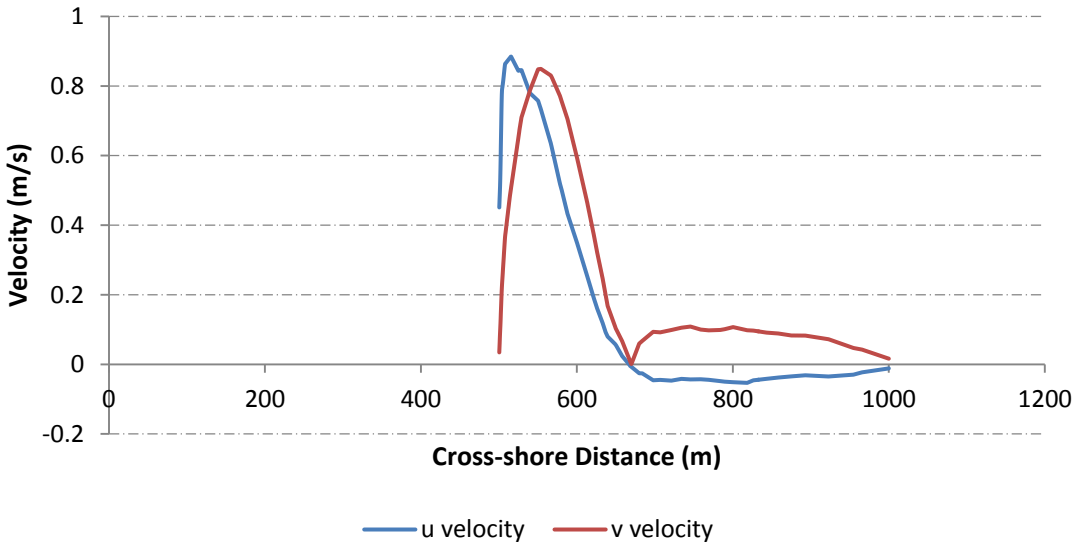

Figure 6-25: Graph of cross-section velocities at the tip of the groyne with a MSL = 0.75 and G_L/B_z = 0.60. For the (H_s = 3m; T_p = 14s; θ = 45°) wave conditions (Table A3.2.3, model run 19).

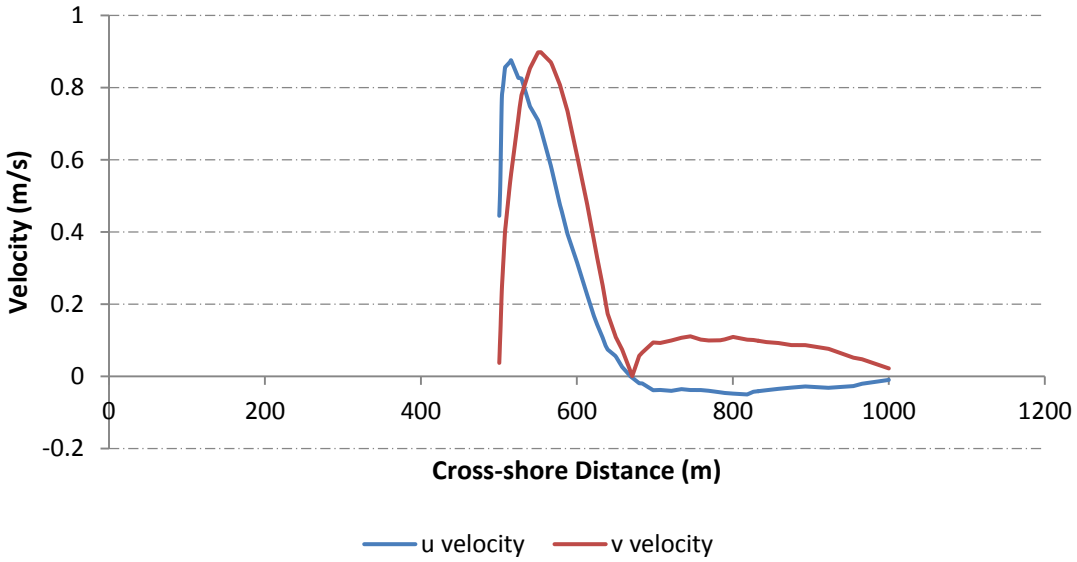

Figure 6-26: Graph of cross-section velocities at the tip of the groyne with a MSL = 0.5 and G_L/B_z = 0.55. For the (H_s = 3m; T_p = 14s; θ = 45°) wave conditions (Table A3.2.3, model run 20).

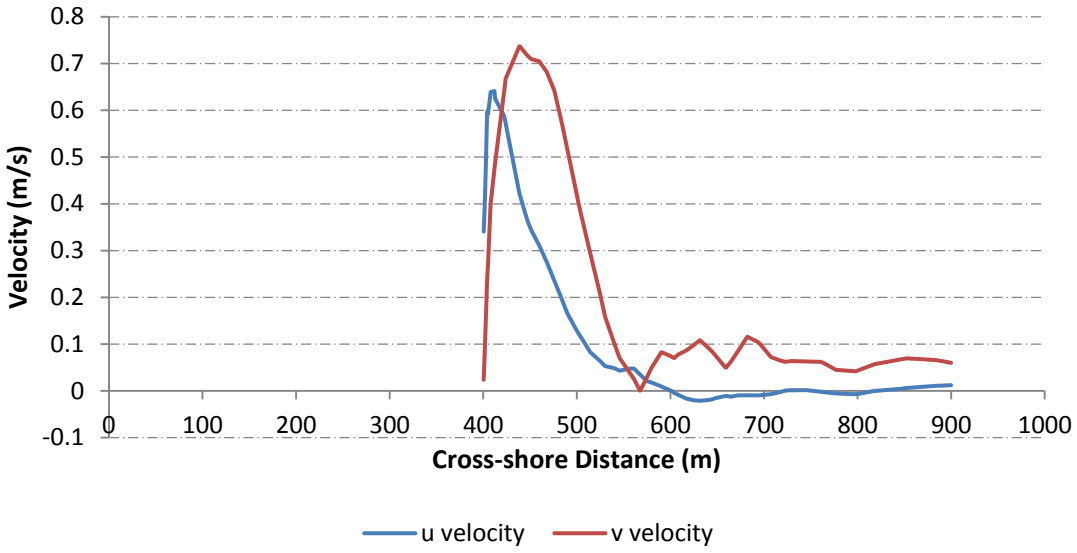

Figure 6-27: Graph of cross-section velocities at the tip of the groyne with a MSL = 1 and $G_L/B_z = 0.50$. For the (H_s = 2m; T_p = 14s; θ = 60°) wave conditions (Table A3.2.4, model run 14).

All graphs with levels of constriction of cross-sectional flow values less than 0.55, for e.g. figure 6-27, displayed an alongshore dominant flow pattern. The v velocity (alongshore direction) along the groyne tip cross-section (within 20m distance) was greater than the u velocity (cross-shore direction).

From figures 6-22 to 6-27, as the level of constriction decreased so too did the u velocity and the distance over which the peak u velocity acts. The distance over which the peak rip-currents act near the tip of the groyne decreased. As the level of constriction decreased, the v velocity increased and so too did the distance over which the peak v velocity acts. The alongshore current and area over which it acts increased.

6.8 Summary of Impermeable Groynes Parametric Study

There were several important discoveries found from this parametric study. The location where strong rip currents occurred, in excess of 0.35m/s, for all simulations was along the lee-side of the groyne. The high frequency of rip currents forming on the lee side of the groyne can be attributed to the eddy formation. The largest area, over which rip current conditions occurred, was in excess of the 0.8 level of constriction of cross-sectional flow. If the level of constriction of cross-sectional flow is greater than 0.8 it induces a rip current dominant system (refer to figure 6-28). When it is greater than 0.88 the alongshore flow is relatively weak and has a large area of action.

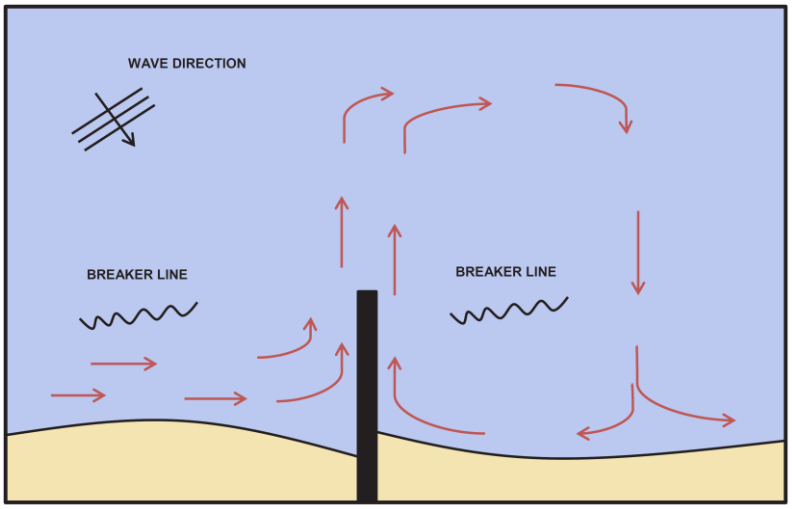

Figure 6-28: Schematic of rip current dominant flow pattern around an impermeable groyne

When G_L/B_z is between 0.8 and 0.55, it yields a transitional state where the peak alongshore current velocity and the peak cross-shore current velocity act within a 100m cross-shore distance of the groyne tip. As G_L/B_z decreases from 0.88 to 0.71, the cross-sectional area of action of the alongshore flow drastically decreases and the strength of the peak flow drastically increases near the tip of the groyne. In general as G_L/B_z decreases so too does the area of action of the rip current along the groyne on the upstream side trunk. The peak rip current velocity shifts location from the upstream side to the downstream side of the groyne when G_L/B_z is between 0.5-0.6.

The flow pattern is considered as alongshore dominant when G_L/B_z is less than 0.55 (refer to figure 6-29). The strongest alongshore currents occurred between 0.88 and 0.44, and had the smallest cross-sectional area of action. Anything less than 0.44 displayed minor rip currents

with stronger rip currents on the lee side trunk and weaker alongshore currents with a large area of action.

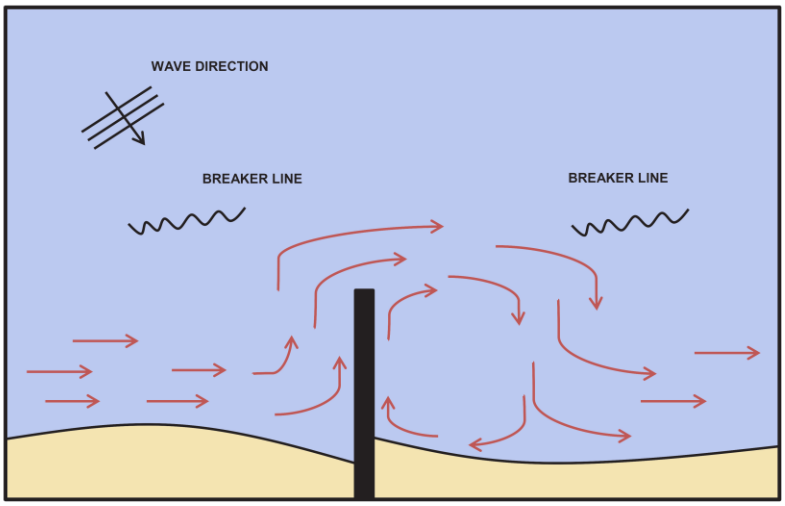

Figure 6-29: Schematic of alongshore current dominant flow pattern around an impermeable groyne

With respect to sediment transport, with a constriction greater than 0.8 there is likely to be either a channel forming on the upstream side and accretion at the tip of the groyne or accretion on the upstream side depending on how far shoreward the waves are breaking. Between 0.8 and 0.55 the latter half of the groyne will suffer scour, there are both strong alongshore currents near the groyne tip and strong rip currents along either trunk side. The stronger rip current is upstream. Persistence of this condition could lead to undermining of the upstream side at the tip with accretion downstream. Lastly, less than 0.55 is alongshore dominant there will be tip erosion with a stronger rip current is on the lee side tip of the trunk.

CHAPTER 7

RESULTS & DISCUSSION – FRICTION MANIPULATION

Chapter Seven comprises a detailed discussion of the friction manipulation simulation results. It is an evaluation of the strengths and weaknesses of the attempted methods to mimic semi-permeability by manipulating the drag terms in the numerical models. It also compares the friction manipulation methods with respect to the impermeable and permeable pile screen simulations.

7.1 Introduction to Study 3

This section of results comprises of the two methods, introduced in section 4.2.3, applied to the model runs in an attempt to mimic permeability through a water column over a given area. The results were separated into two sections and discussed. The sections are as follows:

- Alongshore current
- Permeability
- Impermeable groynes vs. Friction manipulation
- Permeable pile screens vs. Friction manipulation

When the C_f is manipulated the Manning's M value changes, this follows in accordance with equation A2-11. The C_f value is set in the SW model and the M value is set in the FM model. For simplicity, this chapter's results will be discussed with respect to the friction coefficient C_f values.

7.2 Alongshore current

Cross-sections of flow were taken along the length of the geometric area where the friction was manipulated. This was done to assess how the alongshore current changed with respect to the friction manipulation method. The sign orientation for the following results; positive flow

values oppose the direction of the alongshore current and negative flow values are in the direction of the alongshore current.

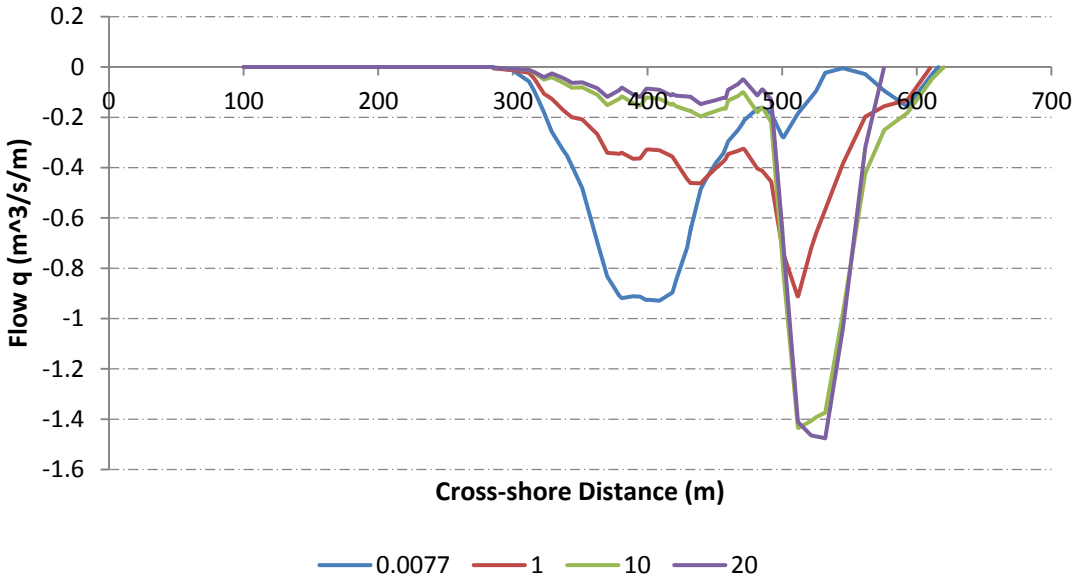

Figure 7-1: Graph of cross-section flow along the friction coefficient geometric area for different cases. This is for the (H_s = 2m; T_p = 14s; θ = 10°) wave conditions.

For Figure 7-1, as the friction coefficient C_f is increased from 0.0077 to 20 (between the 300 and 500m cross-shore distance) both the magnitude of the alongshore current peak flow and location of the alongshore current moved offshore. The 0.0077 friction coefficient value is the pre-set value for beaches (MIKE21, 2011a). The cross-section line for 0.0077 therefore shows where the alongshore current should be if there are no obstructions to the alongshore current. With the increase in the friction coefficient the alongshore current moves further offshore increasing in strength and decreasing in cross-sectional width. This method shows it is possible to impede the alongshore flow however it does not completely obstruct the flow like that of an impermeable groyne. It was found that for the modelling package used, increasing the friction coefficient beyond 10 had little effect in changing the flow structure any further.

It was observed that even though a constant friction coefficient was applied over a given width, as the depth increased so too did the flow. This was due to the 2D depth-average formulation i.e. when the momentum equation is integrated over the depth, the effect of bottom friction scales inversely with depth (refer to appendix A: section A2.1 and A2.3 for equations). In an attempt to further improve this method of impeding the flow the coefficient of friction was multiplied by the depth across the geometric area (refer to figure 7-2). This is equivalent to applying a uniform drag through the vertical extent of the water column.

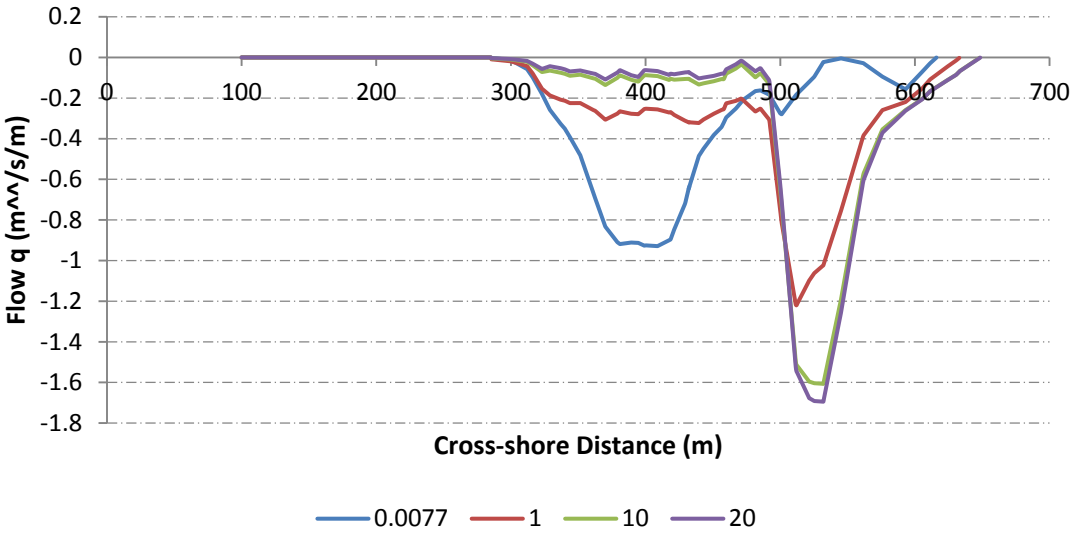

Figure 7-2: Graph of cross-section flow along the friction coefficient geometric area multiplied by the depth for different cases. This is for the (H_s = 2m; T_p = 14s; θ = 10°) wave conditions.

When comparing figures 7-1 and 7-2 it can be seen that by multiplying the friction coefficient by the depth improved the uniformity of the drag effect on the water column. The drag effect became more consistent over the geometric area (between 300 and 500m cross-shore distance). The methods did begin to display impermeable characteristics along the geometric area when the friction coefficient was increased. There was a sharp increase in the flow at the end tip of the affected area. This is characteristic of a redirected alongshore current.

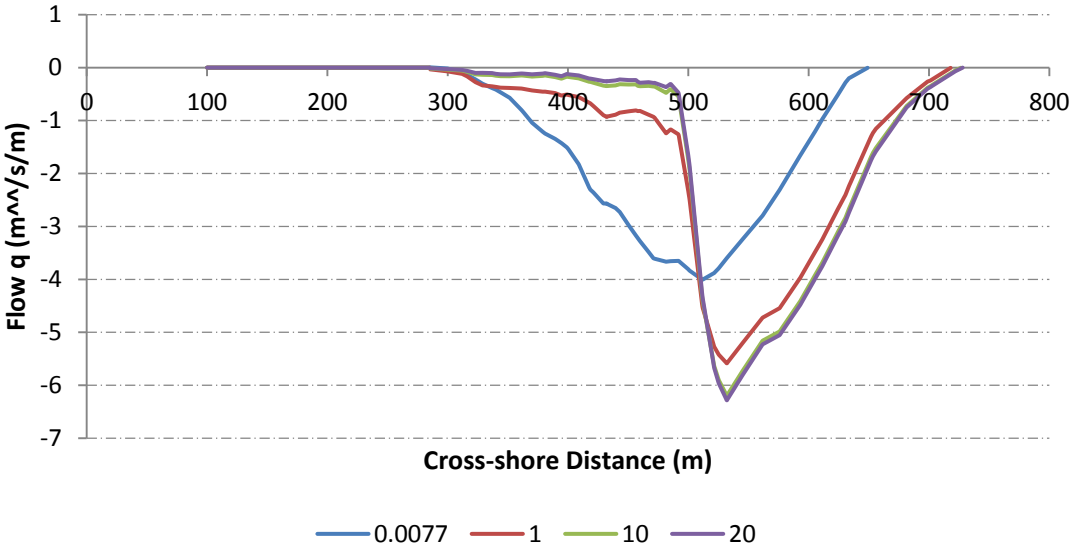

Figure 7-3: Graph of cross-section flow along the friction coefficient geometric area multiplied by depth for different cases. This is for the (H_s = 3m; T_p = 14s; θ = 45°) wave conditions.

The characteristics displayed in figures 7-1 and 7-2, where the alongshore current moved offshore decreasing in cross-sectional width and increasing in strength, were found for all model run wave conditions. The only difference was the relative strength and location, with an increase (refer to figure 7-3) or a decrease (refer to figure 7.4) in significant wave height.

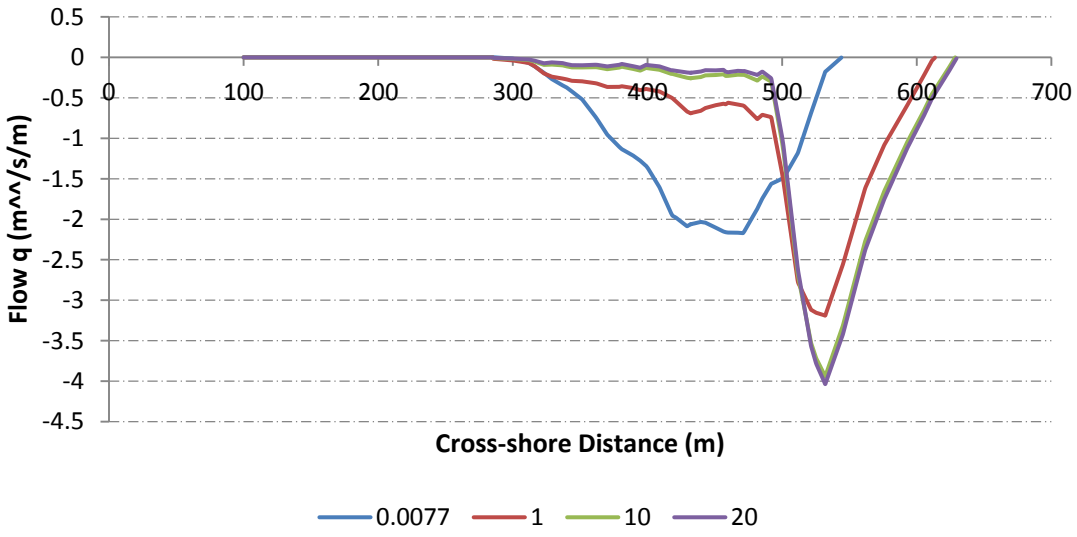

Figure 7-4: Graph of cross-section flow along the friction coefficient geometric area multiplied by depth for different cases. This is for the (H_s=2m; T_p=14s; θ=45°) wave conditions.

7.3 Permeability

The purpose of the two methods of drag manipulation was to investigate how well it impeded the flow over a given area. The results in figure 7-5 and 7-6 are summaries of the permeability reduction effects associated with the friction manipulations for a few cases:

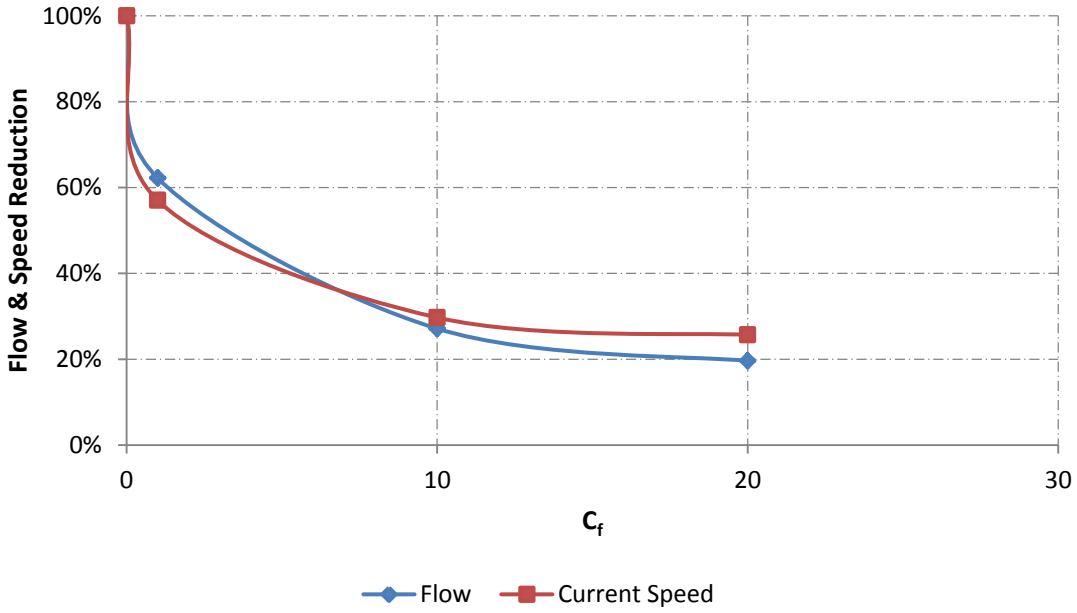

Figure 7-5: Graph of the flow & speed reduction for the friction coefficient manipulation. For the (H_s = 2m; T_p = 14s; θ = 10°) wave conditions.

Comparing figure 7-5 and figure 7-1 between 0.0077 and 8 the friction coefficient manipulation had a greater effect on the current speed reduction than on the flow reduction. As the friction coefficient increased beyond 8m/s, it had a greater effect on flow reduction. It is evident that most of the change in through flow occurs for a $C_f < 10$.

Comparing figure 7-6 and figure 7-2 the manipulation of the friction coefficient with the depth improved the reduction effects for both the current speed and the alongshore flow. This method showed was more effective than manipulating C_f alone.

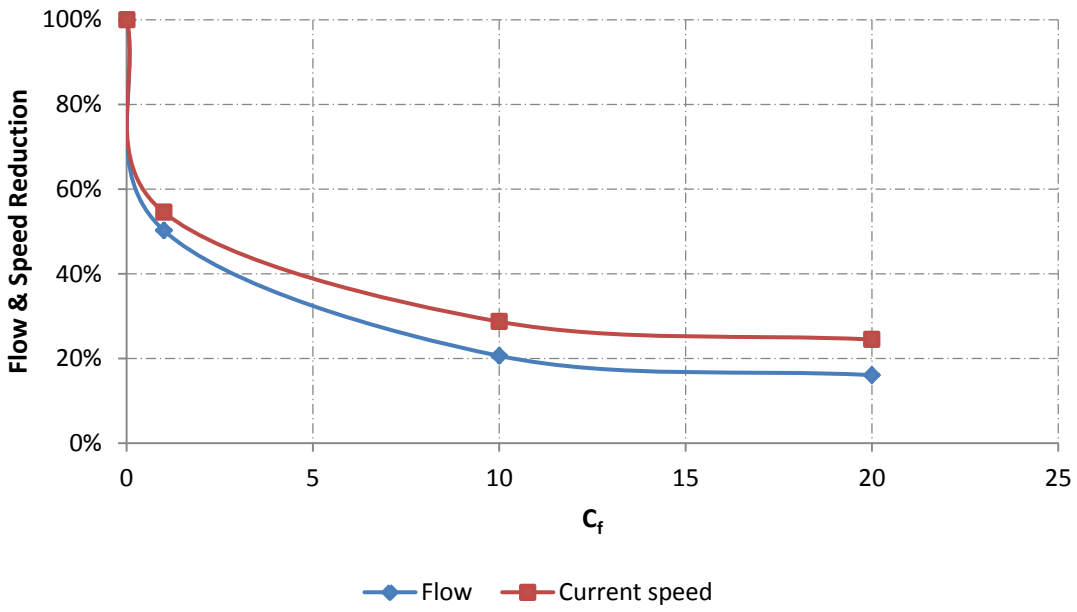

Figure 7-6: Graph of permeability reduction for friction coefficient multiplied by the depth. For the (H_s = 2m; T_p = 14s; θ = 10°) wave conditions.

This method displayed 90 per cent flow impedance which equates to a permeability of 10 per cent. This method was limited to a C_f value of 20m/s, anything greater than 20m/s yielded the same flow reduction as the 20m/s value i.e. 90 per cent. In accordance with literature (Trampenau, Oumeraci and Dette, 2004) a groyne with permeability less than or equal to 10 per cent behaves as an impermeable structure therefore the method is not required to reach 0 per cent permeability.

7.4 Impermeable Groyne vs. Friction Manipulation

A comparison was carried out between an impermeable groyne and the friction manipulation method. When comparing the results of the model runs it was found that the flow patterns varied. An example of this is given by figure 7-8 and figure 7-9. Figure 7-8 is an impermeable groyne, 1m wide at the 2000m mark on the y axis and figure 7-9 is the friction manipulated geometric area at the 2000m y axis mark with an approximate 10 per cent permeability (according to theory 10 per cent behaves as an impermeable structure).

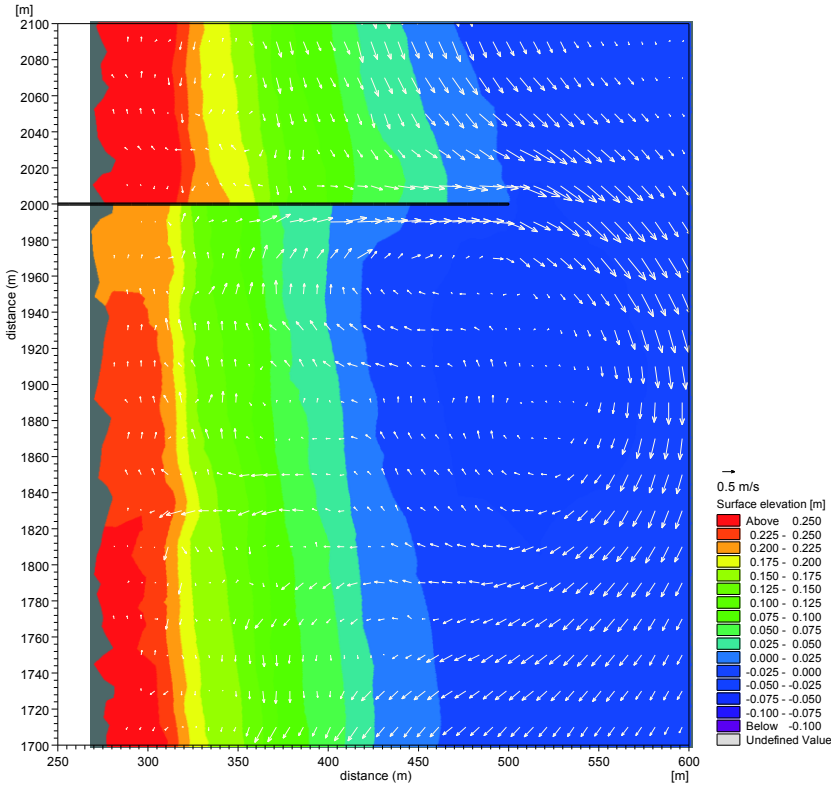

Figure 7-8: Impermeable groyne vector plot showing the predicted current vectors and the wave set-up for (H_s = 2m; T_p = 14s; θ = 45°) (Table A3.2.3, model run 9).

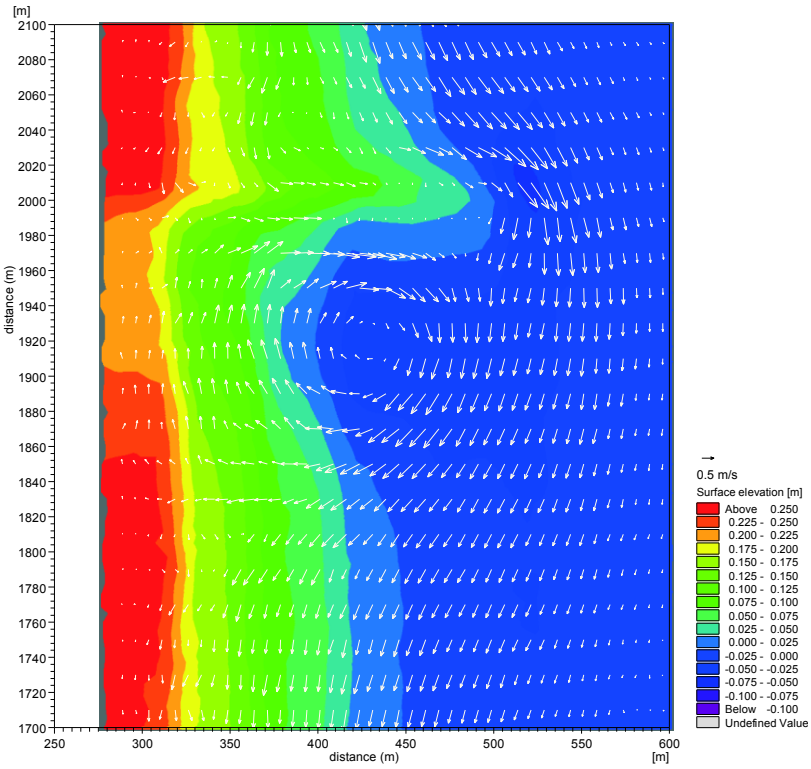

Figure 7-9: Vector plot showing the predicted current vectors and the wave set-up for (H_s = 2m; T_p = 14s; θ = 45°). For the C_f x h manipulation over a 20m width (Table A3.3.3, model run 9).

Both figures displayed higher surface elevations upstream of the obstruction with flow tending offshore. This was more dominant however with the impermeable groyne (refer to figure 7-8). The effect of the downstream rip current was greater for the impermeable groyne. This increased the tip velocity angle which also increased the size of the lee side eddy; forming an irregular eddy.

The friction manipulation method only impedes flow it does not stop flow because of this there was still flow over the manipulated area (refer to figure 7-9). This reduced the tip velocity angle which reduced the size of the eddy, making it more circular.

The lee side is completely sheltered in the case of the impermeable groyne but not for the friction manipulated case. It therefore stands to reason that friction manipulated case, even though it is only 10 per cent permeable, behaves as a semi-permeable structure and not as an impermeable structure.

For the permeable pile screen vs. friction manipulation discussion, please refer to chapter 8 section 8.7. It will be discussed after showing the data for the permeable pile screen.

7.6 Summary of Friction Manipulation

The purpose of this parametric study was to ascertain whether or not groyne permeability could be modelled by manipulating friction effects so as to mimic permeable structures in a numerical model. Ideally the friction manipulation would force the software package to impede the flow over an area. Of the two methods of friction manipulation that were attempted, the one that yielded the better results was that of the friction coefficient manipulation multiplied by the depth. This method improved the current speed and alongshore flow reduction effects to a greater degree than that of the first methods. It therefore showed a better trend for permeability manipulation.

Though the second method had a greater effect on flow reduction over a given area, this does not mean the initial method was a failure. Since the initial method only made use of a constant friction coefficient, the drag effect on the water column lessened with an increase in depth. This method behaved similarly to that of a low crested groyne as the structure induces drag on the water as it flows over. The drag effect decreases with depth due to the increase in water over head.

At most the permeability could be reduced to 10 per cent over a drag manipulated area. This approach of manipulating the friction to induce drag shows promise and could be implemented eventually to include sediment transport.

CHAPTER 8

RESULTS & DISCUSSION – PERMEABLE PILE SCREEN GROYNES

Chapter Eight comprises of a detailed discussion of the permeable pile screen groyne simulation results. It is an evaluation of the change in flow pattern due to the change in the breaker zone width using the level of constriction of cross-sectional flow.

8.1 Introduction to Study 4

This study will discuss the findings of the permeable pile screen model runs with a relative comparison of these findings against those of the friction manipulation and the impermeable groyne model runs. The model setup and configurations for the permeable pile screens, friction manipulation and the impermeable groynes were the same including the width and length of the overall structures (The only exception was the grid sizes between the piles). An assessment was undertaken to compare the observed flow patterns for the level of constriction of cross-sectional flow for different permeability's of pile screens. The chapter comprises of several sections:

- Eddy in the lee of the groyne
- Groyne length change
- Rip currents
- Alongshore current
- Predominant flow pattern vs. the level of constriction

8.2 Eddy circulations

With a high permeability there is a large flow through the pile spacing, this reduces the difference in the alongshore velocity gradient. The smaller the difference in the gradients the smaller the eddy circulations will be. As the permeability decreases the eddy circulation moves

closer toward the lee side trunk of the groyne in the alongshore direction. The eddy centre also moves further offshore in the cross shore direction. A decrease in the permeability will increase the area over which the eddy circulation pattern occurs.

- For a permeability of ±70 per cent the recirculation zone comprises of small eddies and has a smaller spatial extent for the separation length.
- For a permeability of ±50 per cent, there is a definite large eddy forming downstream of the groyne, as shown in figure 8-1.
- For a permeability of ±30 per cent, a large eddy forms with a greater intensity than that of a 50 per cent permeability, as shown in figure 8-2.

The level of constriction of cross-sectional flow changes the position of the eddy centre in the cross-shore direction. Between a G_L/B_z of 0.72-0.49, the location of the eddy centre shifts from near the permeable pile screen half way mark to the latter half of the permeable pile screen.

8.3 Groyne length change

Whether or not the permeability was kept constant, a reduction in permeable pile screen length reduces the level of constriction of cross-sectional flow. It will have the following affects:

- The permeable pile screen will at inside the alongshore current zone. The alongshore current will then cause a reduction in the groyne tip velocity, this then reduces the size and vorticity of the lee side eddy
- The recirculation zone decreases in size, therefore the separation length decreases.

Please note, with an increase in permeability there is a decrease in the downstream flow pattern effects; the recirculation zone (for more detail on the recirculation zone, refer back to figure 2-4).

The main effect that the change in groyne length has is the change in the level of constriction of cross-sectional flow. Irrespective of groyne length, for permeability $\geq$ 30 per cent it is an alongshore dominant flow pattern at the groyne tip. As shown in figure 8-1 and 8-2 for a 50 per cent and 33 per cent permeability.

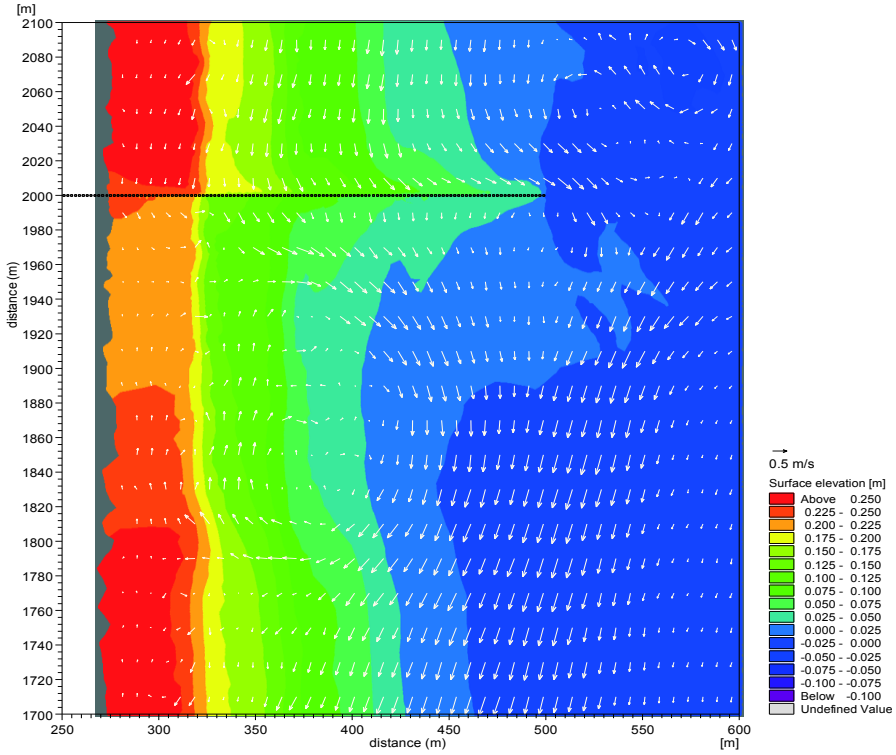

Figure 8-1: Vector plot of a 50.13 per cent permeable pile screen showing the predicted current vectors and the wave set-up for (H_s = 2m; T_p = 14s; θ = 45°) (Table A3.4.1, model run 5).

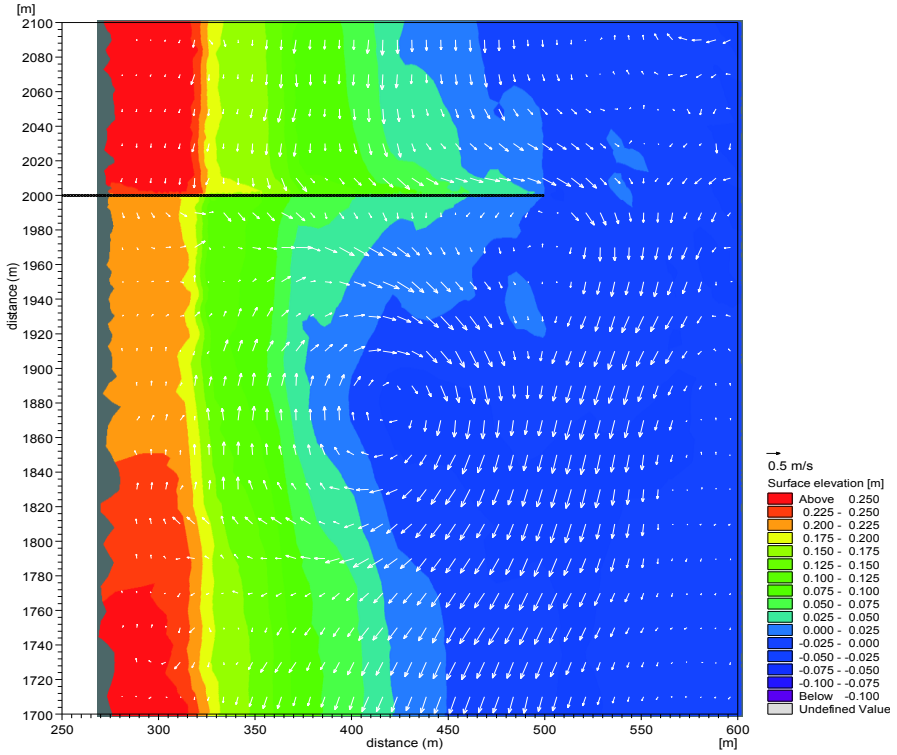

Figure 8-2: Vector plot of a 33.33 per cent permeable pile screen showing the predicted current vectors and the wave set-up for (H_s = 2m; T_p = 14s; θ = 45°) (Table A3.4.1, model run 6).

8.4 Rip currents

In the model runs, where the alongshore current acts within the permeable pile screen range ($G_L/B_z \geq 1$) it was found that shoreward rip-currents occurred along the trunk at the tip of the groyne. This occurred when the permeability was ≥ 30 per cent (refer to figure 8-3). This was due to there being insufficient resistance to flow; the offshore directed rip current dissipated through the pile screen gaps.

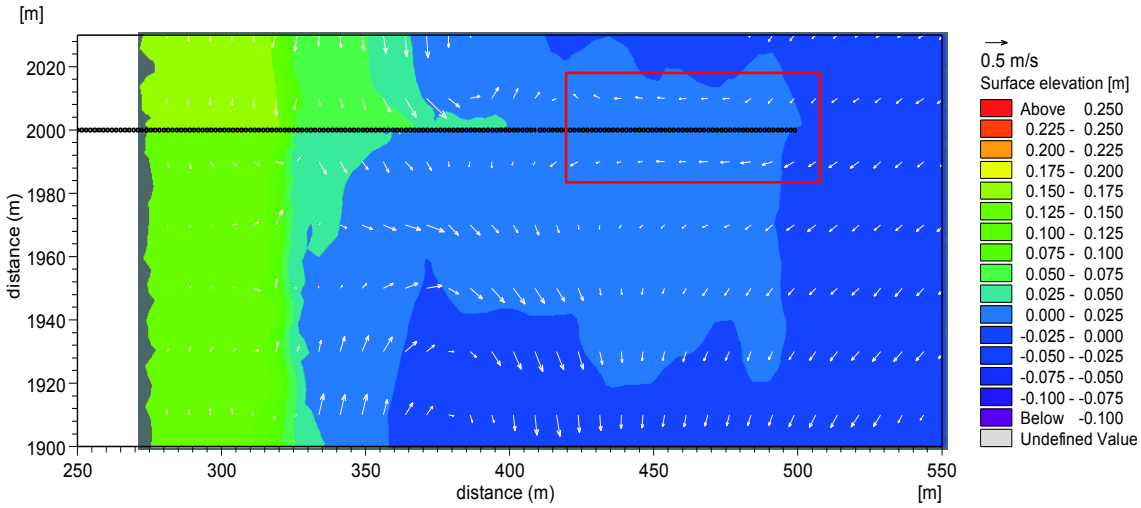

Figure 8-3: Vector plot of a 33.33 per cent permeable pile screen showing the predicted current vectors and the wave set-up for (H_s = 1m; T_p = 14s; θ = 45°) (Table A3.4.1, model run 3). Shoreward rip current highlighted in red.

For the groynes with a $G_L/B_z > 0.65$ and a permeability of 70 per cent, a shoreward rip current occurred at the tip of the permeable pile screen. This was visible on both the upstream and downstream sides of the trunk (refer to figure 8-4). This was only minor however in comparison to the permeable pile screens with a $G_L/B_z \geq 1$, and it only constituted one-tenth of the groyne length.

Pile screen groynes depending on permeability are known to display severe erosion due to rip currents, especially scour around the tip of the groyne. For more detail on how the currents affect the sediment transport around such groynes refer to section 9.2.

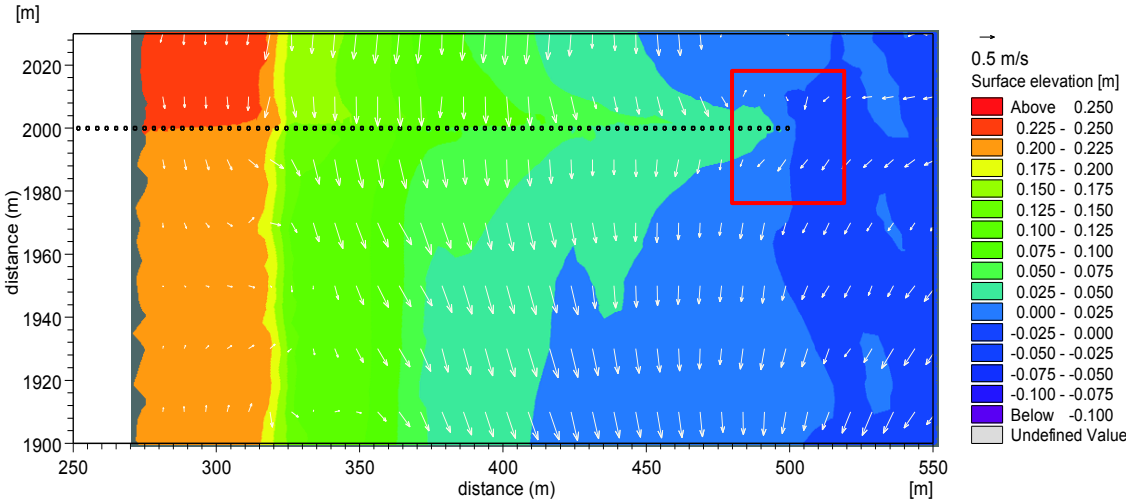

Figure 8-4: Vector plot of a 70.32 per cent permeable pile screen showing the predicted current vectors and the wave set-up (H_s = 2m; T_p = 14s; θ = 45°) (Table A3.4.1, model run 4). Location of shoreward rip current highlighted in red.

The following graphs display the change in the peak rip currents on the upstream and downstream sides of the permeable pile screens as the permeability decreases:

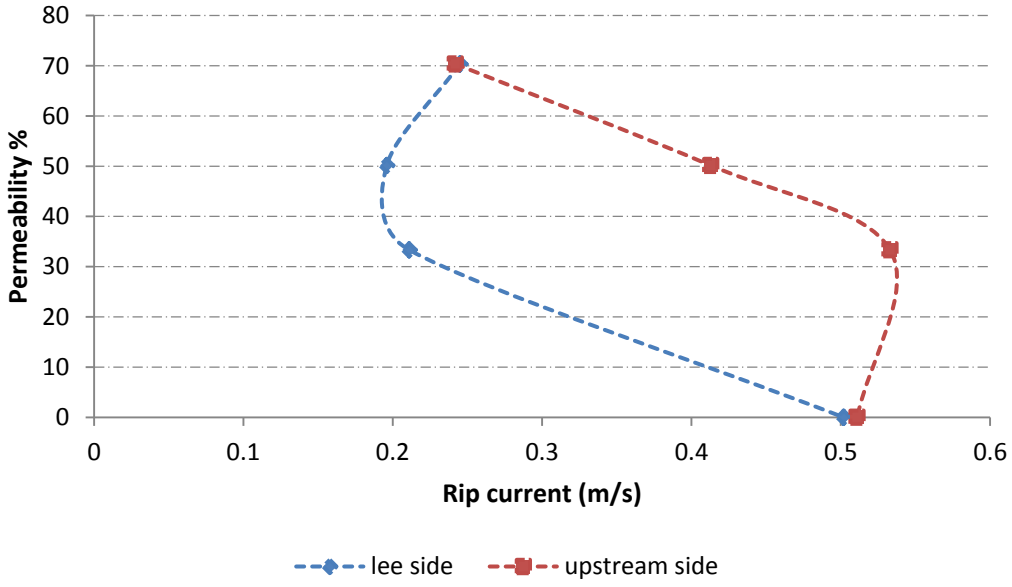

Figure 8-5: Graph of 200m pile screen permeability vs. peak rip currents for G_L/B_z=1.14 and (H_s = 1m; T_p = 14s; θ = 45°) wave conditions. Points are joined to lines for clarity.

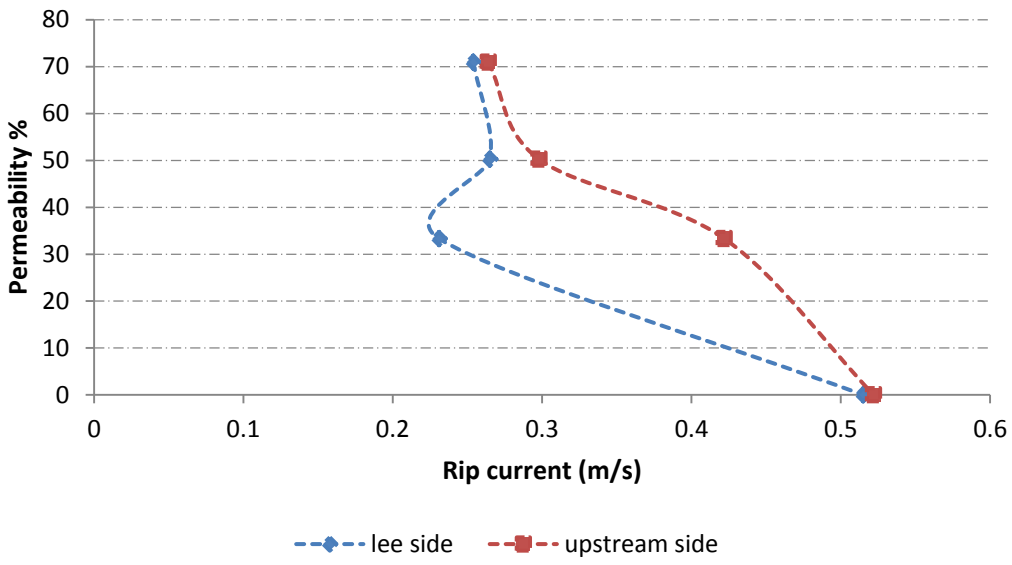

Figure 8-6: Graph of 100m Pile screen permeability vs. Peak rip currents for G_L/B_z=0.63 and (H_s = 1m; T_p = 14s; θ = 45°) wave conditions. Points are joined to lines for clarity.

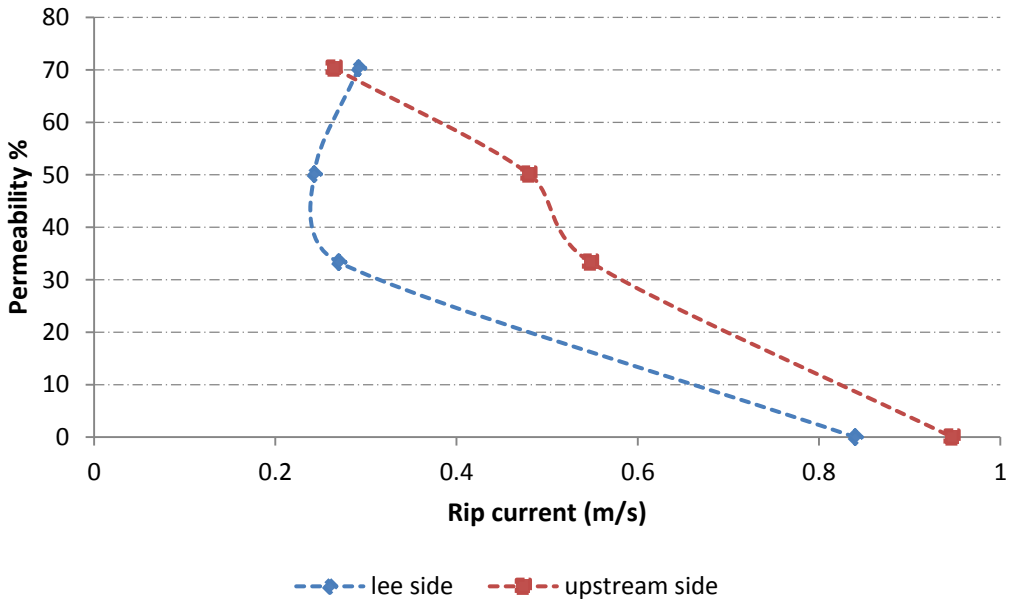

Figure 8-7: Graph of 200m Pile screen permeability vs. Peak rip currents for G_L/B_z=0.72 and (H_s = 2m; T_p = 14s; θ = 45°) wave conditions. Points are joined to lines for clarity.

For figures 8-5 and 8-7 where to $G_L/B_z \geq 0.72$, the lee side peak rip current was lowest when the permeability was 50 per cent.

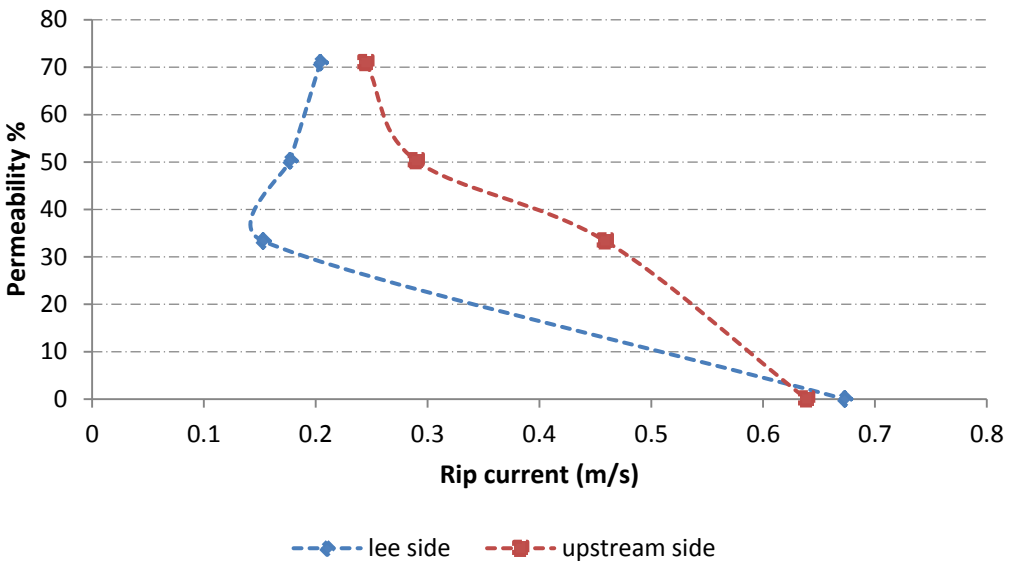

Figure 8-8: Graph of 100m Pile screen permeability vs. Peak rip currents for G_L/B_z=0.40 and (H_s = 2m; T_p = 14s; θ = 45°) wave conditions. Points are joined to lines for clarity.

For figures 8-6 and 8-8 where G_L/B_z was between 0.40-0.63, the lee side peak rip current was lowest when the permeability was 30 per cent.

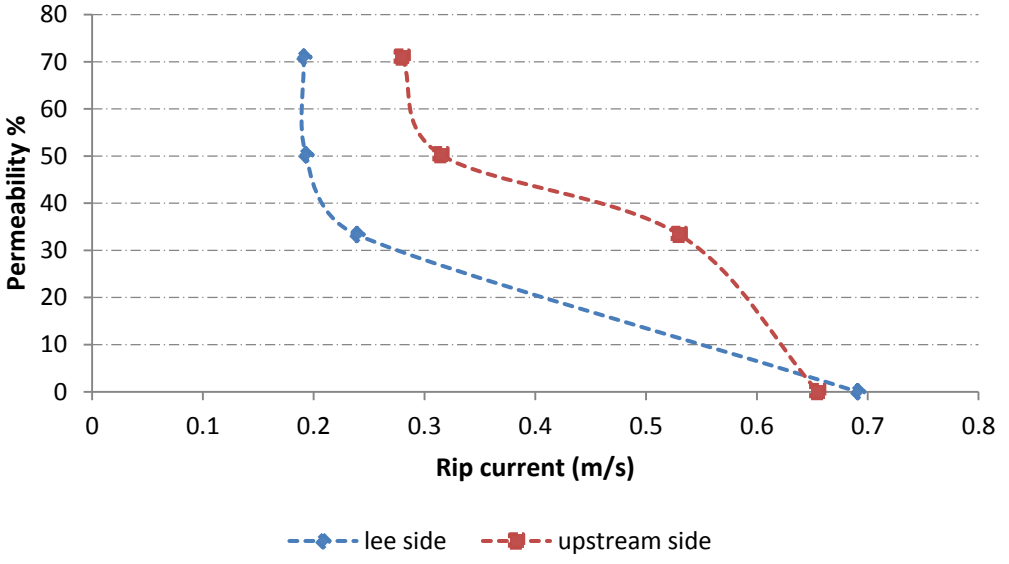

Figure 8-9: Graph of 100m Pile screen permeability vs. Peak rip currents for G_L/B_z=0.27 and (H_s = 3m; T_p = 14s; θ = 45°) wave conditions. Points are joined to lines for clarity.

As the permeability decreased the general trend was that the rip current magnitudes increased. For figures 8-6 to 8-9 where $G_L/B_z \leq 0.72$, as the permeability decreased the upstream peak rip

current increased. The reason why the lee side peak rip current decreases at some point before increasing is due to the interference that the through flow has on the velocity gradient on the lee side. The greatest change in peak rip current strength is between the 30 per cent and 0 per cent permeability. The lee side peak rip current shows the largest change as the permeability decreases.

From figures 8-5 to 8-9 for permeable groynes, the worst rip currents tended to occur on the upstream side of the groyne for all levels of constriction. The only exception was for a $G_L/B_z \geq 0.72$ with permeability greater than equal to 70 per cent.

Table 8-1 displays a summary of the position of the strongest rip current depending on the permeability and level of constriction of the particular system for the simulations run.

For more detail refer to Appendix D: Impermeable groynes, tables D1.2-D1.3 and appendix E: Permeable method and Permeable groynes, tables E1.1-E1.2 for rip current magnitude data.

Table 8-1: Summary of permeability effects on the groyne rip-currents

G_L/B_z	Permeability							
	70%		50%		33%		0%	
	Rip Current Magnitude							
	Up stream	Down stream	Up stream	Down stream	Up stream	Down stream	Up stream	Down stream
≥ 1.0	Lower	Higher	Higher	Lower	Higher	Lower	Higher	Lower
0.9	-	-	-	-	-	-	Higher	Lower
0.8	-	-	-	-	-	-	Higher	Lower
0.7	Lower	Higher	Higher	Lower	Higher	Lower	Higher	Lower
0.6	Higher	Lower	Higher	Lower	Higher	Lower	Lower	Higher
0.5	-	-	-	-	-	-	Lower	Higher
0.4	Higher	Lower	Higher	Lower	Lower	Higher	Lower	Higher
≤ 0.3	Higher	Lower	Higher	Lower	Lower	Higher	Lower	Higher

8.5 Alongshore currents

Cross-sections of the alongshore flow just downstream of the permeable pile screen groynes, for the model runs, were taken to assess how the alongshore current changes. This is with respect to a change in permeability for a specific level of constriction of cross-sectional flow. The sign orientation for the following results; positive flow values oppose the direction of the alongshore current, negative flow values are in the direction of the alongshore current. For figures 8-10 to 8-12 the groyne ends at 400m and for figures 8-13 to 8-15 the groyne ends at 500m. The results are as follows:

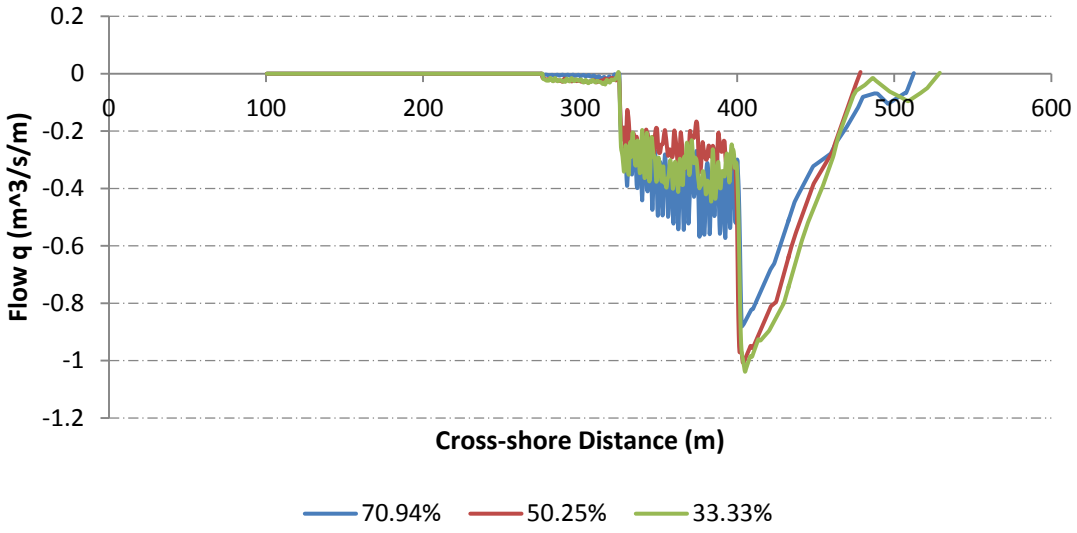

Figure 8-10: Graph of cross-section flow along 100m permeable pile screen groyne for a change in permeability and a $G_L/B_z = 0.63$. For the ($H_s = 1m$; $T_p = 14s$; $\theta = 45°$) wave conditions.

Due to the piles, for the flow to flow through the pile spacing the water has to accelerate (Raudkivi, 1996). The accelerated flow can be seen in figures 8-10 to 8-15, where the permeable pile screens act. As the permeability decreased, the spacing between piles decreased and the accelerated flow between the piles decreased as well (shown in figure 8-10). As the permeability decreases the resistance to through flow increases which causes the alongshore flow to increase in strength at the tip of the pile screen groyne. It has to increase as the flow is being directed around the trunk of the groyne to the tip of the groyne.

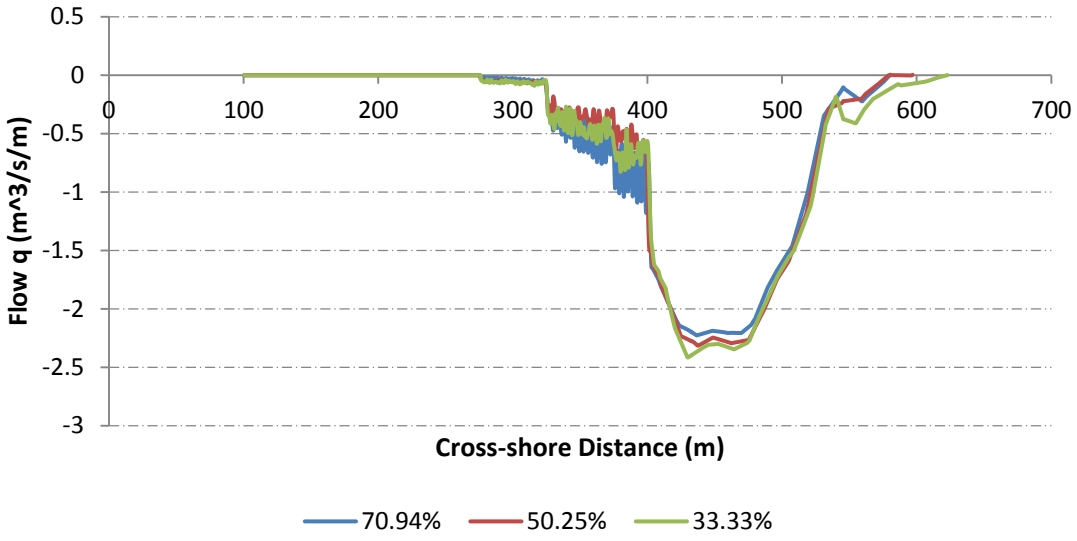

Figure 8-11: Graph of cross-section flow along 100m permeable pile screen groyne for a change in permeability and a $G_L/B_z = 0.40$. For the ($H_s = 2m$; $T_p = 14s$; $\theta = 45°$) wave conditions.

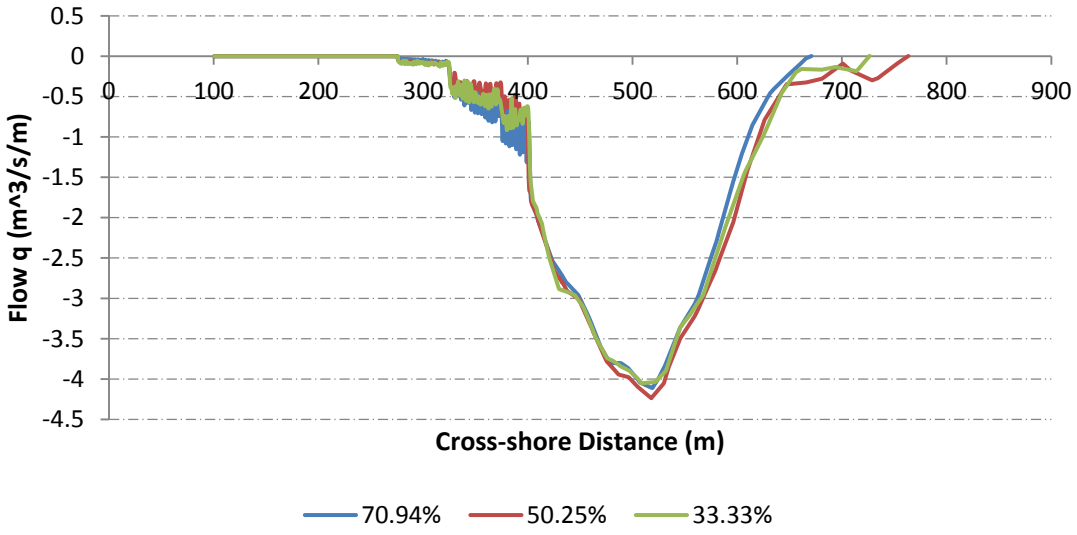

Figure 8-12: Graph of cross-section flow along 100m permeable pile screen groyne for a change in permeability and a $G_L/B_z = 0.27$. For the ($H_s = 3m$; $T_p = 14s$; $\theta = 45°$) wave conditions.

When comparing figures 8-10, 8-11 and 8-12, the permeability has very little effect on the area of action of the alongshore current. As G_L/B_z decreases from 0.63 to 0.27, the permeable pile screen has less of an effect on the alongshore flow at the tip of the groyne. It is already apparent that at this point the flow pattern is alongshore dominant. Regardless of the permeability change the shape of the cross-sectional flows for each figure are relatively the same, this is due to the fact that the level of constriction has not changed.

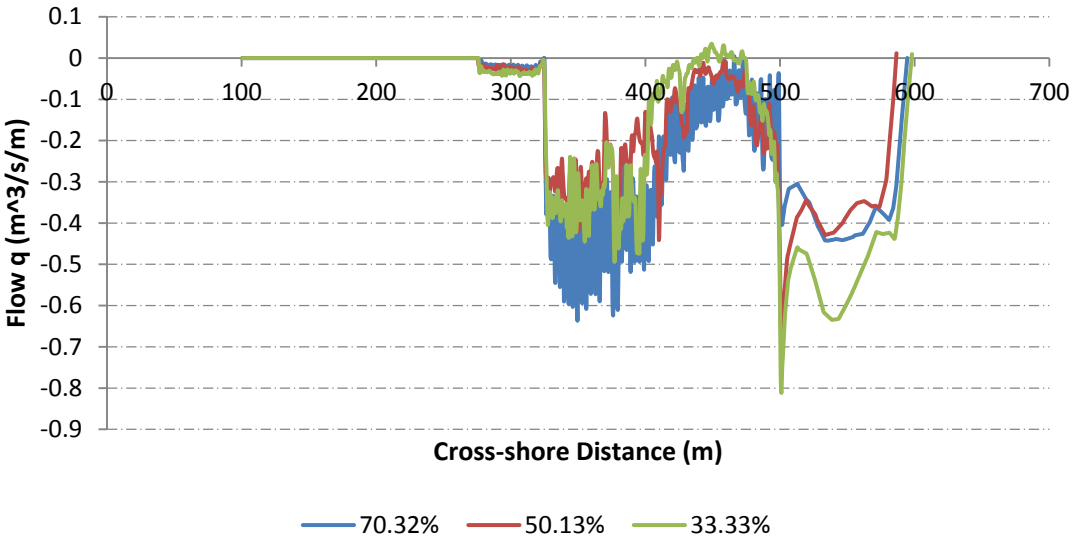

Figure 8-13: Graph of cross-section flow along 200m permeable pile screen groyne for a change in permeability and a $G_L/B_z = 1.14$. For the ($H_s = 1m$; $T_p = 14s$; $\theta = 45°$) wave conditions.

When comparing figure 8-10 and 8-13, the 1.14 level of constriction of cross-sectional flow had a weaker flow than that of 0.63.

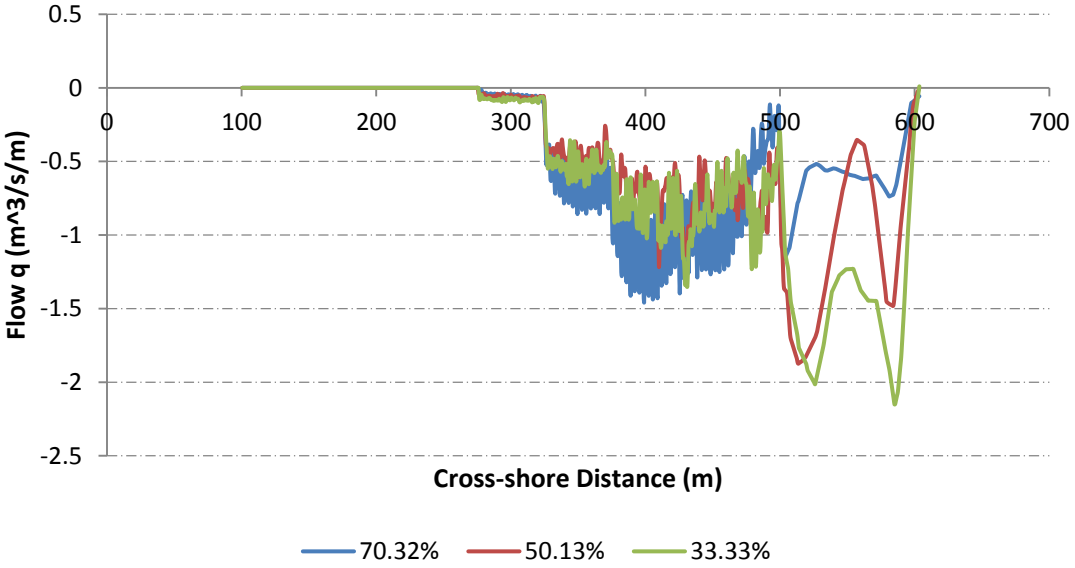

Figure 8-14: Graph of cross-section flow along 200m permeable pile screen groyne for a change in permeability and a $G_L/B_z = 0.72$. For the ($H_s = 2m$; $T_p = 14s$; $\theta = 45°$) wave conditions.

In figure 8-13 between the 400m and 500m cross-shore distance, regardless of permeability there was a change in the flow trend. This decrease in negative flow was actually the location of onshore rip currents (as discussed in section 8.4). This change in the flow trend was also

apparent in figure 8-14 but only for permeability ≥ 70 per cent. As G_L/B_z increases from 0.72 to 1.14, the breaker zone begins to act within the length of the permeable pile screen. At this point, onshore rip current becomes more apparent regardless of permeability. This change in the flow trend at the tip of the permeable pile screen is followed by a peak in the alongshore flow at the tip of the groyne.

When comparing figure 8-11 and 8-14, the 0.72 level of constriction of cross-sectional flow had a weaker flow than that of 0.4.

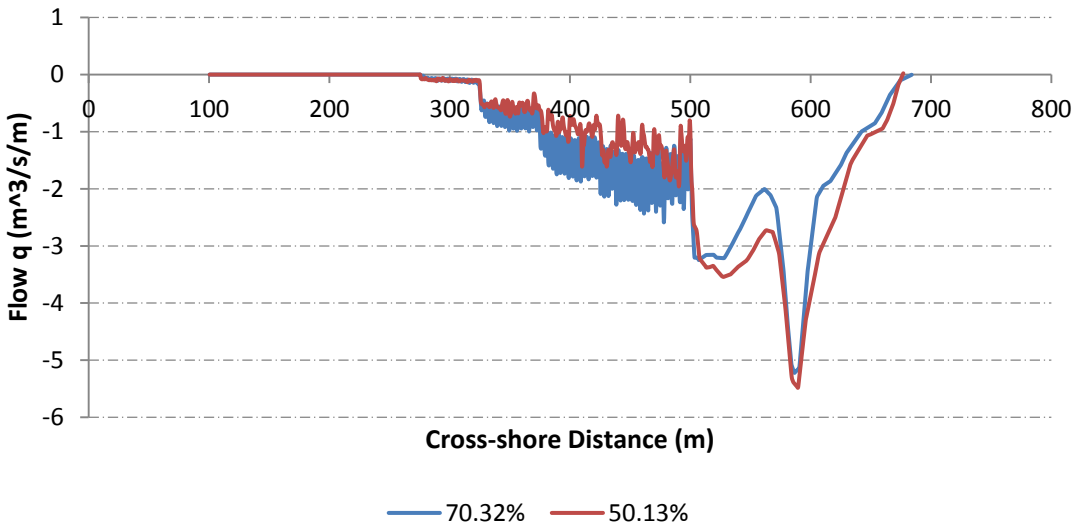

Figure 8-15: Graph of cross-section flow along 200m permeable pile screen groyne for a change in permeability and a $G_L/B_z = 0.49$. For the ($H_s = 3m$; $T_p = 14s$; $\theta = 45°$) wave conditions.

When comparing figure 8-12 and 8-15, the 0.49 level of constriction of cross-sectional flow had a stronger flow than that of 0.27.

From figures 8-10 to 8-15, as mentioned previously the area of action of the alongshore flow shows little change when changing the permeability. The flow strength or peak flow showed only noticeable changes for permeability changes when $G_L/B_z > 0.49$; where a decrease in permeability increased the peak alongshore flows.

For the cases where $G_L/B_z < 0.49$, the breaker zone width was double the size of the groyne length. The core alongshore current then acts outside of the groyne length and a change in permeability will have a negligible effect on the alongshore current strength.

8.6 Predominant flow pattern vs. the level of constriction

It is apparent from section 8.4 and 8.5 that the predominant flow pattern for the permeable pile screen simulations was an alongshore flow pattern, regardless of the level of constriction of cross-sectional flow. There was however onshore rip currents occurring along the latter trunk section of the permeable pile screens for $G_L/B_z \geq 0.72$. To assess this in further detail, cross sections were taken at the permeable pile screen groyne tip for the onshore rip current cases.

The cross-section was separated into the current vector velocity components. The cross-shore current, u velocity, and the alongshore current, v velocity, were compared to determine the dominant directions at the tip of the permeable pile screen groynes. The results for the different permeable cases for the specific levels of constriction of cross-sectional flows are as follows:

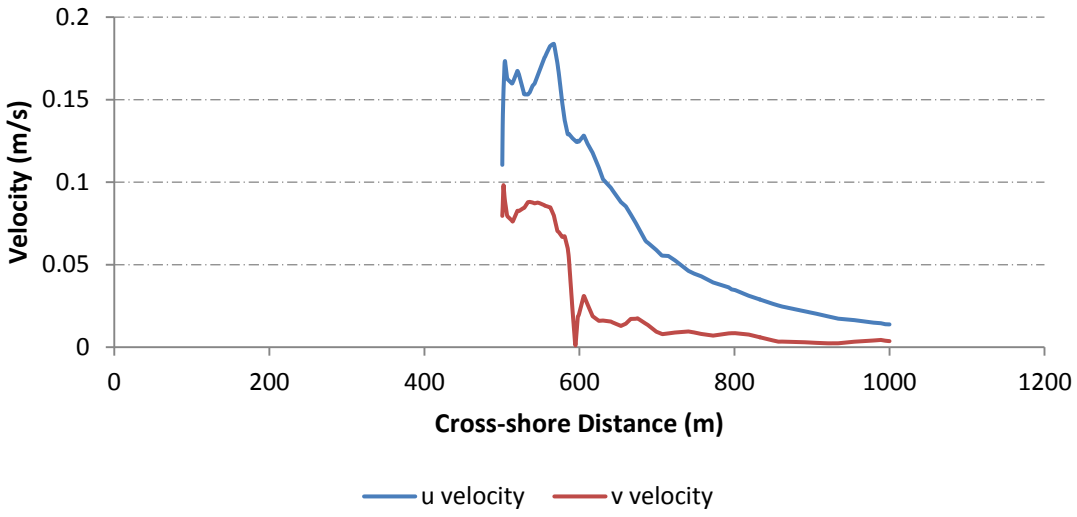

Figure 8-16: Graph of cross-section velocities at the tip of the permeable pile screen for a permeability of 70.32% and a $G_L/B_z = 1.14$. For the ($H_s = 1$m; $T_p = 14$s; $\theta = 45°$) wave conditions (Table A3.4.1, model run 1).

When comparing figures 8-16, 8-17 and 8-18, it can be seen that the dominant velocity is the u velocity at the tip of the groyne; the cross-shore current dominates the alongshore current. The cross-shore current is directed onshore and it increases in strength as it moves shoreward toward the permeable pile screen. As the permeability decreases the cross-shore current, u velocity, begins to decrease and the alongshore current, v velocity, begins to increase.

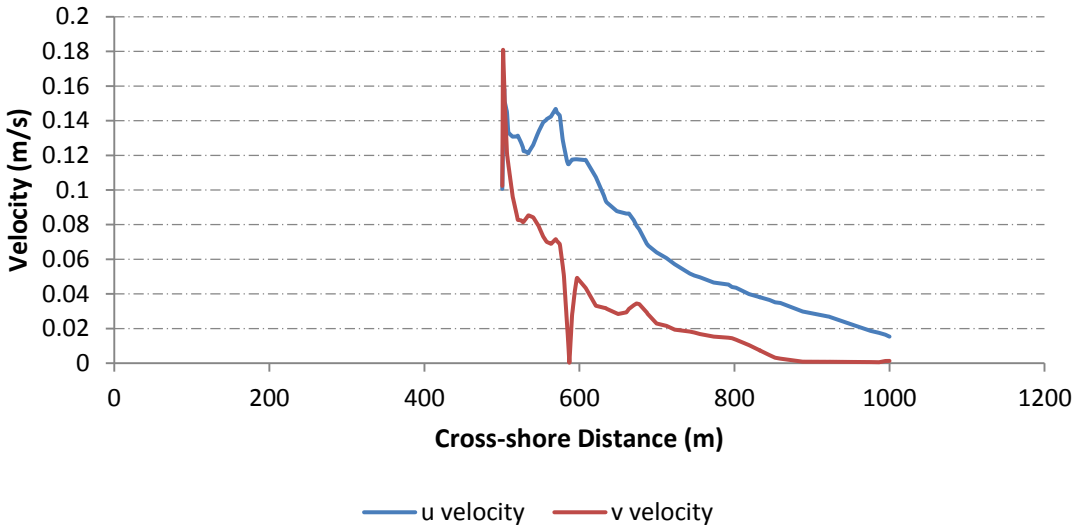

Figure 8-17: Graph of cross-section velocities at the tip of the permeable pile screen for a permeability of 50.13% and a $G_L/B_z = 1.14$. For the ($H_s = 1m$; $T_p = 14s$; $\theta = 45°$) wave conditions (Table A3.4.1, model run 2).

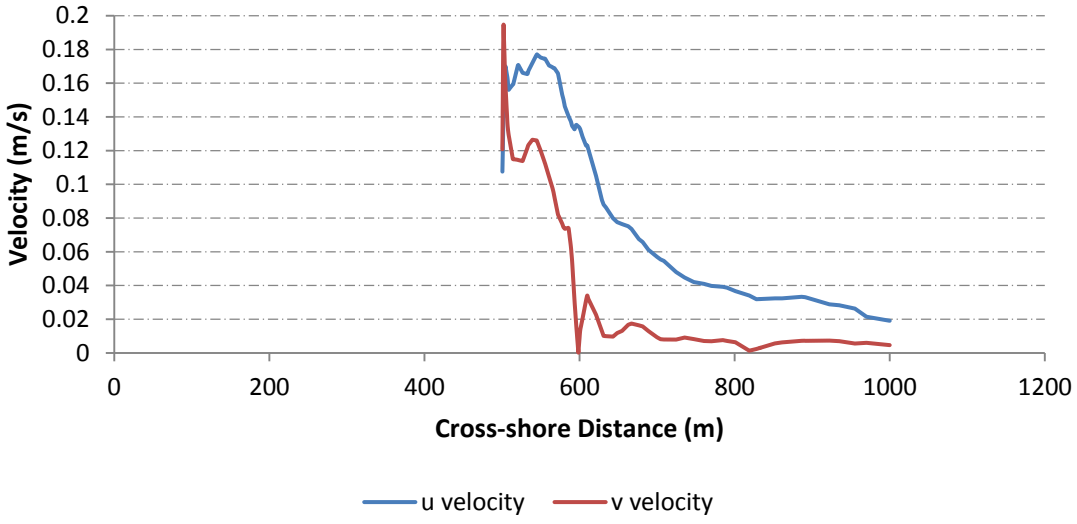

Figure 8-18: Graph of cross-section velocities at the tip of the permeable pile screen for a permeability of 33.33% and a $G_L/B_z = 1.14$. For the ($H_s = 1m$; $T_p = 14s$; $\theta = 45°$) wave conditions (Table A3.4.1, model run 3).

In figure 8-19 there was a strong cross-shore current moving towards the permeable pile screen tip; however near the tip the alongshore current was greater in magnitude. This model run still displayed an onshore rip current as per the model runs for figures 8-16, 8-17 and 8-18. The only characteristic that figures 8-16 to 8-19 had in common was that no other permeable pile screen cross-section velocity plots had u velocities greater than v velocities along the tip cross section. Figure 8-20 is an example of this, where the alongshore current was greater in magnitude; v

velocity greater than the u velocity. This was the same trend for all other permeable pile screen cross-section velocity plots.

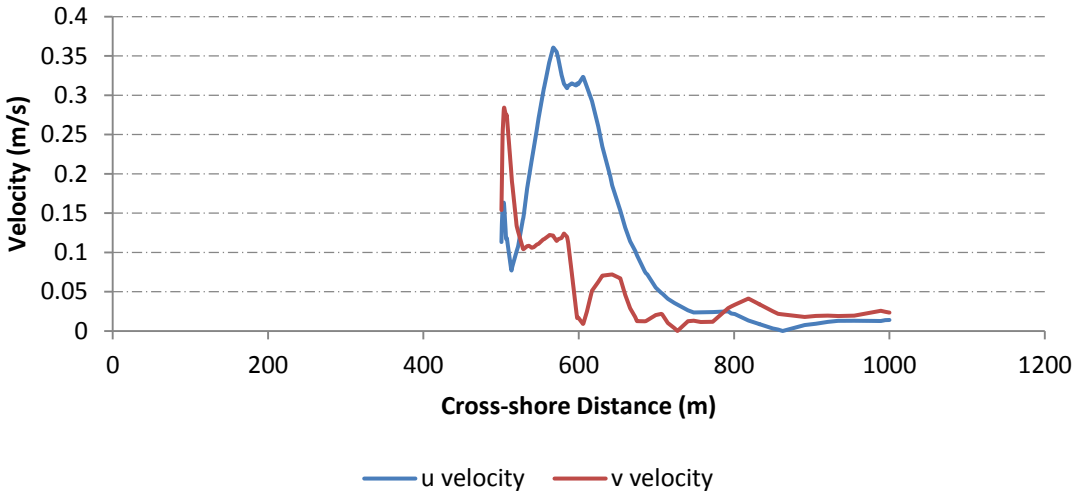

Figure 8-19: Graph of cross-section velocities at the tip of the permeable pile screen for a permeability of 70.32% and a $G_L/B_z = 0.72$. For the ($H_s = 2m$; $T_p = 14s$; $\theta = 45°$) wave conditions (Table A3.4.1, model run 4).

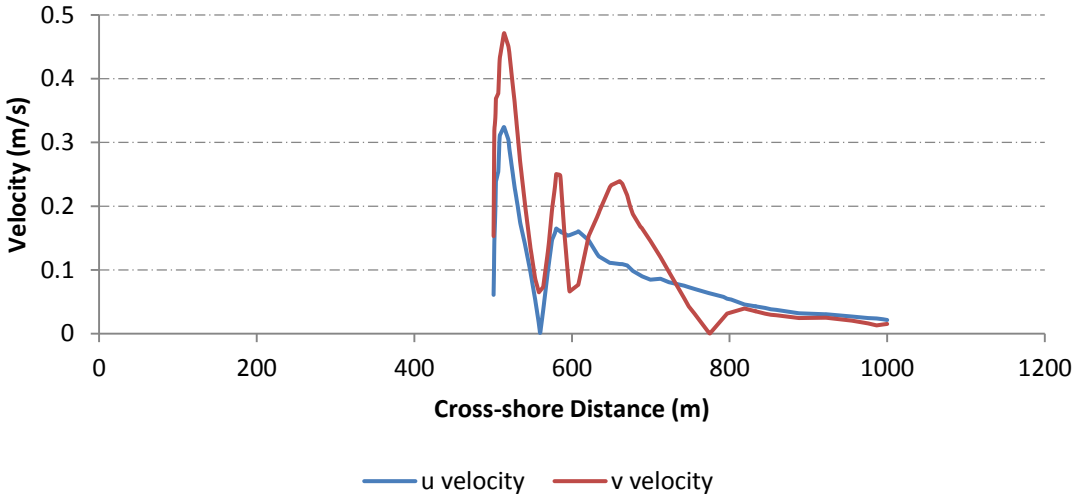

Figure 8-20: Graph of cross-section velocities at the tip of the permeable pile screen for a permeability of 50.13% and a $G_L/B_z = 0.72$. For the ($H_s = 2m$; $T_p = 14s$; $\theta = 45°$) wave conditions (Table A3.4.1, model run 5).

Figure 8-16 and 8-19 were the only plots to display a greater cross-shore current. As the level of constriction increased from 0.72, the permeability had less of an effect on the driving current along the permeable pile screen. The majority of the alongshore current had already migrated through the permeable pile screen or was insufficient in strength to dominate the onshore rip current. This was due to the breaker zone width deviating inside of the groyne length.

8.7 Permeable pile screens vs. Friction manipulation

A comparison was carried out between a permeable pile screen and the friction manipulation method. When comparing the results of the simulations, it was found that if the friction manipulation method was used on the same size geometric area as a permeable pile screen it did not have the same effect. This can clearly be seen when comparing figure 8-21 with figure 8-22. Figure 8-21 displays a 1m wide permeable pile screen with 33 per cent permeability at the 2000m mark on the y axis. Figure 8-22 is a 1m wide friction manipulated area with at the 2000m y axis mark.

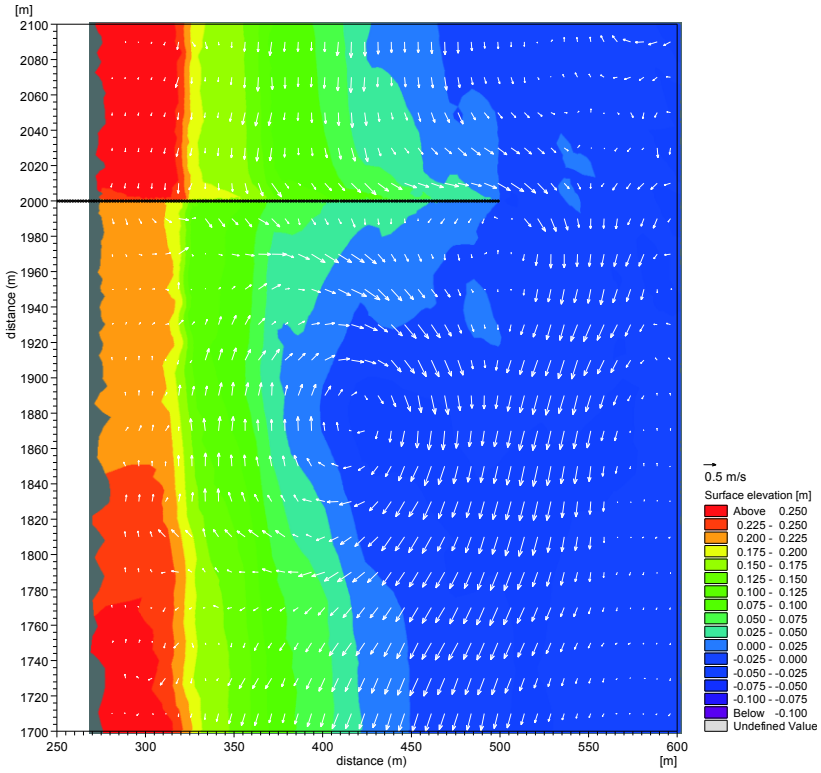

Figure 8-21: Vector plot showing a 33.33 per cent permeable pile screen with the predicted current vectors and the wave set-up for (H_s = 2m; T_p = 14s; θ = 45°) (Table A3.4.1, model run 6).

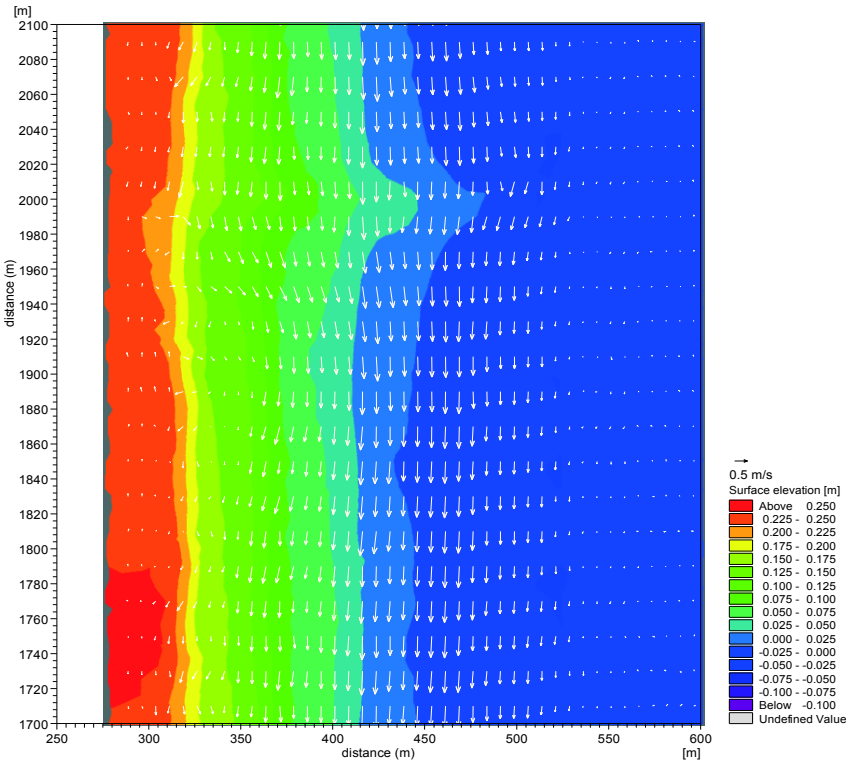

Figure 8-22: Vector plot showing the predicted current vectors and the wave set-up for (H_s = 2m; T_p = 14s; θ = 45°). For the C_f x h manipulation over a 1m width (Table A3.3.3, model run 13).

It was found that the permeability varied, for the friction manipulation method, depending on the width over which it was applied. This was thought to be a mesh problem; if the mesh is too large in the vicinity of the friction manipulated area it is possible that it is not being resolved correctly. In an attempt to evaluate this, a larger area was manipulated. This corrected the issue and yielded a similar permeability to that of the permeable pile screen with a ±3 per cent permeability difference (refer to figure 8-23).

This yielded similar flow reductions and flow patterns (comparing figure 8-23 with figure 8-21). The concern with this however is that it required a 20m x 200m long friction manipulated area to yield similar results to that of a 1m x 200m long permeable groyne. This is possibly due to the friction simulations not being implemented correctly. The resolution is perhaps too coarse over the area that is manipulated, so the simulation is not resolving the high friction effects properly. More gridlines will need to be implemented over the manipulated area to reduce computational errors.

Though the two figures display similar patterns they are still different, the friction manipulation method applied only impedes flow it does not obstruct it like that of a permeable pile screen where the flow is forced around the piles.

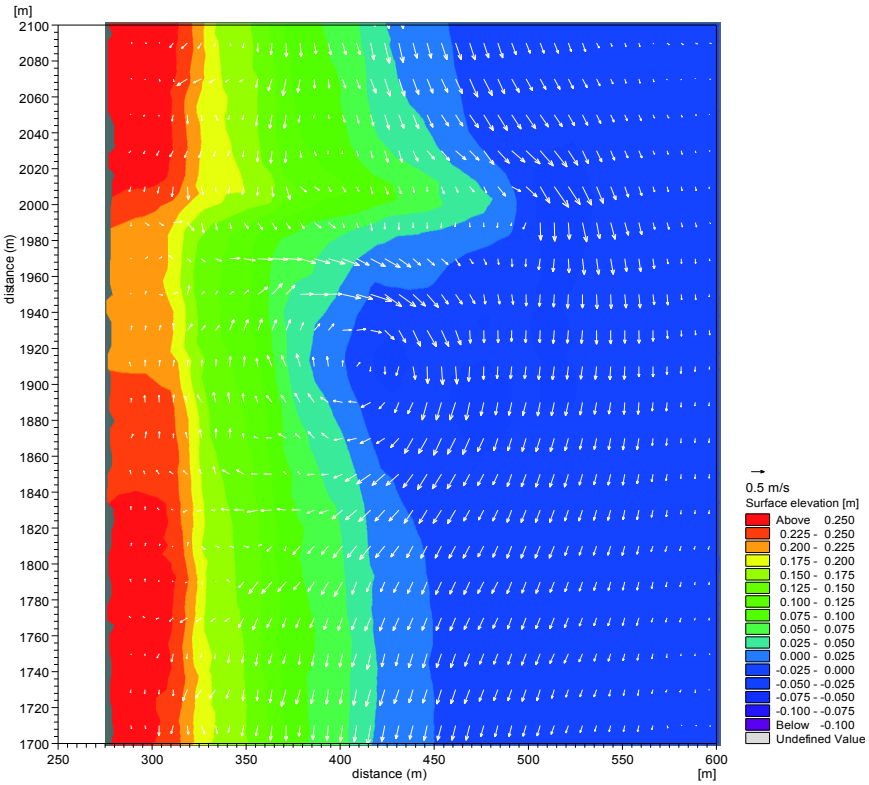

Figure 8-23: Vector plot showing the predicted current vectors and the wave set-up for (H_s = 2m; T_p = 14s; θ = 45°). For the C_f x h manipulation over a 20m width (Table A3.3.3, model run 7).

8.8 Summary of Permeable Pile Groynes

When comparing this parametric study against that of the impermeable groyne study, there were some noticeable differences. The most apparent difference was that the velocity gradient, normal to the groyne, was smaller on the lee side of the permeable pile screen than on an impermeable groyne due to through flow. The greater the permeability was the smaller the velocity gradient was and the less likely that a recirculating lee eddy would form.

A change in the permeable pile screen groyne length has little effect on the tip velocity angle because of through flow between the piles. The impermeable groyne impedes the alongshore flow and deviates it around the groyne tip. The affect that the impermeable groyne length has on the tip velocity angle is greater than that of a permeable pile screen. If the permeability of a pile screen groyne is greater than 30 per cent, it will have minimal effect on the tip velocity angle. It cannot therefore produce a strong enough rip current, i.e. dominant rip current pattern.

The permeable pile screens did display an onshore rip current around the groyne tip for a $G_L/B_z \geq 0.72$. In comparison the impermeable groyne displayed an offshore rip current for a $G_L/B_z \geq 0.80$. The peak rip current along the trunk of the groyne can either be on the upstream side or downstream side of the groyne, depending on both the permeability and the level of constriction of cross-sectional flow. The simulations indicated that an impermeable groyne generates the stronger rip currents in all cases.

The tip velocity plots for the permeable pile screens did display a state of transition. The u and v velocities at the tip of the groyne were similar in magnitudes between the 0.72 and 0.48 level of constriction of cross-sectional flow, whereas for an impermeable groyne the range was between 0.8 and 0.55.

With respect to the alongshore current, the area of action and flow strength at the tip of the impermeable groyne is far greater than that of the permeable pile screen for the same level of constriction of cross-sectional flow. For both types of groynes, the v velocity becomes much larger than the u velocity at the groyne tip when $G_L/B_z < 0.48$. It was noted that for both impermeable and permeable groynes, as the level of constriction of cross-sectional flow decreased from 0.44 to 0.4 the flow increased in strength and the area over which the alongshore current acts decreased. Anything less than a G_L/B_z of 0.4, and the flow strength decreased while the area over which the alongshore current acts increased; tending towards a normal unhindered alongshore current state.

CHAPTER 9

RESULTS & DISCUSSION – FIELD INVESTIGATION

Chapter Nine is the final results chapter where field measurements from the case study site were presented and evaluated. The observations are discussed in the context of the results from the numerical simulations that have been described in the foregoing chapters.

9.1 Introduction to Study 5

Eularian measurements of the water flow around the Bay of Plenty Pier were conducted on 06/11/2012. Custom made current meters (refer to chapter 4, section 4.1.1 for details) were programmed to sample the current speeds at a rate of 0.5Hz and twenty-five were placed both inside and outside of the surf zone depending on high and low tide; the water depth for placement ranged from 1.9m – 9.5m. The current meters were used to obtain comparative Eularian measurements of the rip-current flow and alongshore current flow.

9.1.1 Durban Conditions

The wave data for the day was compiled from Transnet Port authority's wave buoy to yield a day average wave rose, figure 9-1 for the 6 November 2012. The wave buoy records every three hours, the data set range was taken from 2012/11/06 00:00 to 2012/11/07 00:00.

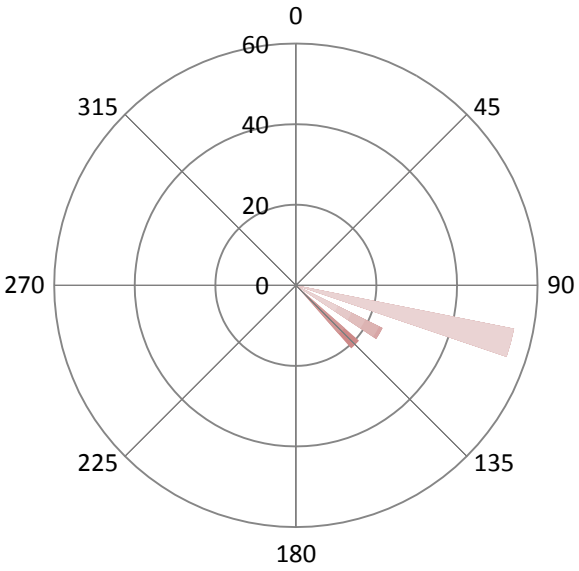

Figure 9-1: Wave Rose for Durban central beach front, 6 November 2013

The average significant wave height for the day was 1.4m with a period of 9.05 seconds and an average angle of incidence of 116 degrees. These are relatively minor swell conditions from the East South East and so the waves were propagating towards the South side trunk face of the Bay of Plenty Pier.

The tidal range for the 6 November 2012 was 0.6m, with peak high tide at 1.5m CD (Chart Datum) and peak low tide at 0.9m CD.

9.1.2 Current Meter Measurements

(*For the detailed current roses, displaying the current meter data for both direction, frequency of occurrence and magnitude, please refer to appendix B, section B2)*

To evaluate the main current directions for the day, the current meter data was averaged over 10 minutes (refer to figure 9-2). This removed the wave interference due to the orbital wave motions, the slow and diffusive onshore flow that results from the Stokes' drift and the mass transport of breaking waves.

Figure 9-2: Current roses with 10 minute averaging, displaying the most frequent current direction for the current meters (background image from Google, 2012).

Figure 9-2 displays the current roses for the 10 minute averaging, at the current meter locations. The current roses show the direction of the most frequently occurring currents. If the current rose exceeded the circle surrounding it, then the frequency of occurrence was greater than 50 per cent. The most prominent occurrences were around the groyne. This was particularly the case on the South side, the direction from where the waves were propagating.

The number 18 and number 22 current meter roses, on the Southside near the shore, showed that the dominant direction of the currents tended towards the groyne. The current roses on the Southside trunk of the groyne display a rip current with some through flow near the tip of the groyne, due to the permeable piles. Just off the tip of the groyne, where the number 16 current meter was, the current rose showed a primary current direction tending offshore.

When looking at the current roses on the North side of the groyne the number 7 current meter, just north of the number 11 current meter, displayed two dominant current directions; due to the changing tide.

To give a general picture of the flow around the groyne the total current meter data sets, for the field test, were vector averaged. This generated vectors of the average currents for the day, as shown in figure 9-3.

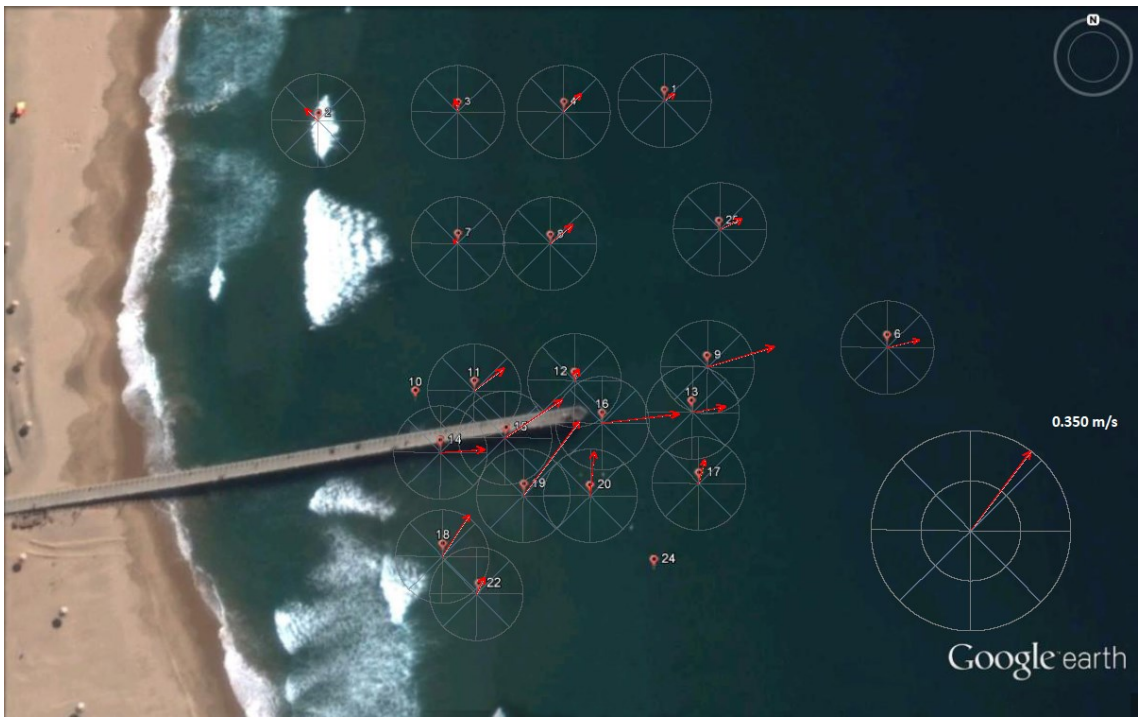

Figure 9-3: Current meter average vector plot (background image from Google, 2012).

According to the average current vectors for the day, the dominant currents occurred within the vicinity of the groyne. This showed strong rip currents along the South side trunk tending offshore from the tip of the groyne, as seen by current meter 16, 13 and 9 in an East-North-East direction. This accounted for approximately 90, 50, and 50 per cent of the currents measured at current meter 16, 13 and 9. This offshore current can be seen as far out as current meter 6. At current meter 6, the East-North-East directed currents accounted for more than 30 per cent of the currents measured at the ADCP that was positioned there.

The strongest day average for any current meter was 0.35m/s and this occurred at current meter 19. The current tended towards the tip of the groyne in a North Easterly direction. From previous years, the bathymetry surveys show a natural channel formation on the sea bed near the South side tip (refer back to figure 1-4 and 1-5) following a similar path to that of the current meter 19 current vector. This strong flow may be the driving force behind the channel formation.

For the combined current meter data sets, on average 52.5 per cent of the current speeds were < 0.2 m/s. Current meter 15 and 19 however were exceptions with more than 70 per cent of their recorded speeds being > 0.3 m/s.

9.1.2.1 Tide

To evaluate how the flow pattern changes with the tide, the current meter results were separated into high and low tide. Where the data set within 1 hour of the peak high, shown in figure 9-4, and peak low, shown in figure 9-5, were averaged to generate the current vectors at the current meter locations.

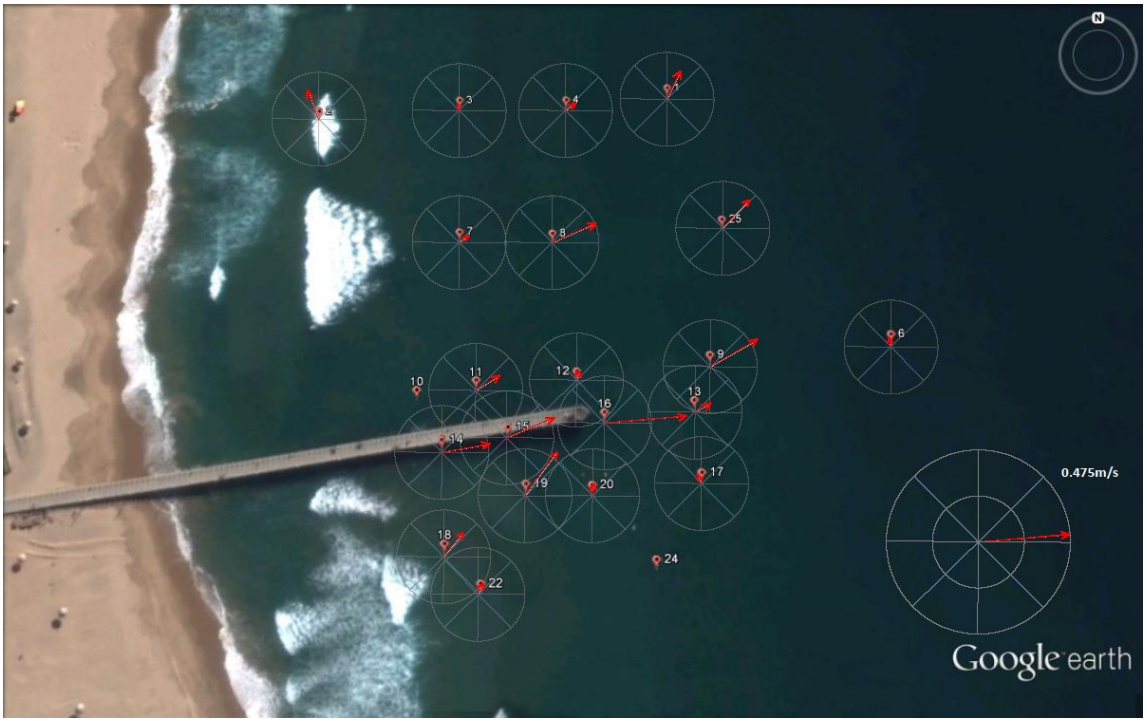

Figure 9-4: High tide current meter vector plot (background image from Google, 2012).

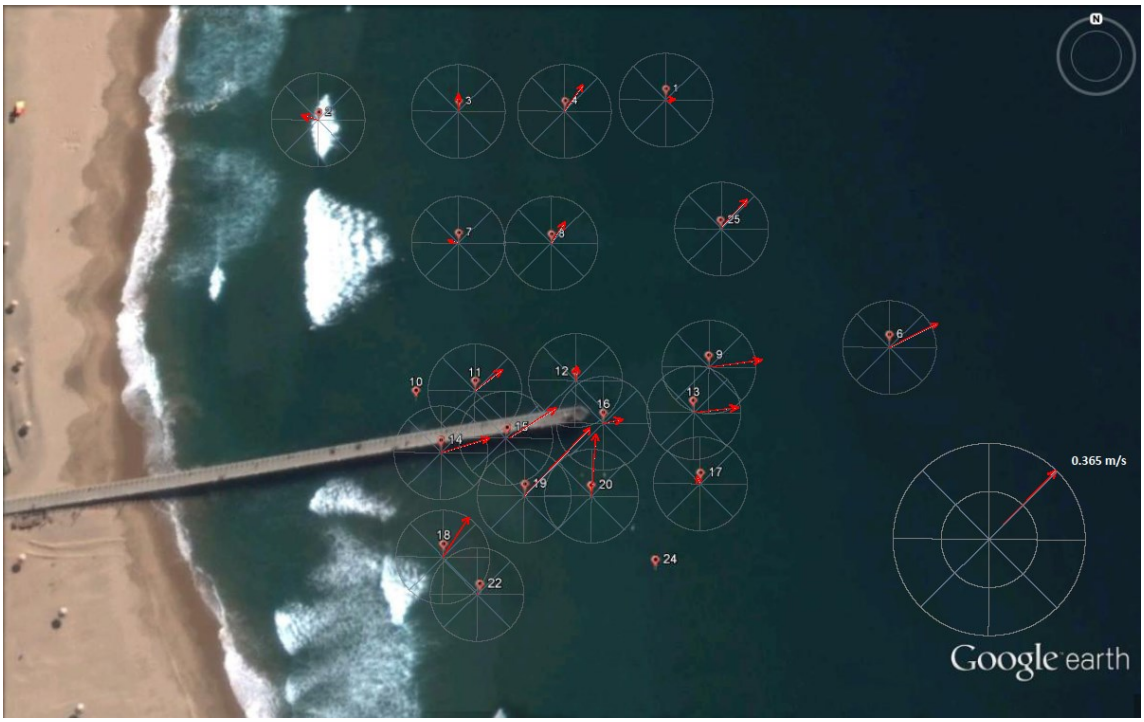

Figure 9-5: Low tide current meter vector plot (background image from Google, 2012).

During high tide (refer to figure 9-4) when the water level was at 1.5m CD, the strongest currents in order of strength were at current meter 16, 15, 9, 14 and 19. At current meter 16 the average current was 0.475 m/s and the current was directed offshore. High tide showed a relatively strong rip current occurring along the South side trunk at current meter 14 and 15, with 0.288 m/s and 0.349 m/s. Current meter 15 showed that some of the rip current deviated through the groyne piles. This did however seem to affect the direction of the rip current at the tip of the groyne.

The highest recorded speed, from the current meter data sets for the day was 2.07 m/s, at current meter 14. This speed was found to be within 40 minutes of the morning peak high tide. When looking at the data set for this current meter, all the readings where the speeds were > 1m/s occurred within 90 minutes of the peak high tide. This current meter also produced the highest set of current speeds for the day. This midway location along the groyne seems to be a critical point with respect to the frequency of high speed currents occurring there.

During low tide (refer to figure 9-5) when the water level was at 0.9m CD, the strongest currents in order of strength were at current meter 19, 15, 20, 6, 9 and 14. At current meter 19 the average low tide current was 0.365 m/s and the current was directed towards the groyne tip. Low tide also showed a relatively strong rip current along the South side trunk at current meter

14 and 15, with 0.206 m/s and 0.244 m/s. The relative strength however of these South side rip currents was less than that of their high tide counterparts. Current meter number 16 had a relatively small vector average for low tide in comparison to its high tide counterpart.

The current meter that produced the second highest set of current speeds for the day was current meter 17. The peak speed recorded was 1.79 m/s and this occurred within 20 minutes of the peak low tide.

When comparing figures 9-4 and 9-5, though high tide had a stronger offshore current just off the tip of the groyne (at current meter 16) deviating to the North East (as seen at current meter 9), low tide showed a more lasting offshore current. This was visible from current meter 9 and 13, where the current deviates to the North East at the ADCP located at current meter 6.

The current meters' data revealed that offshore currents, parallel to the groyne, were dominant upstream of the groyne (Southside) for incident swell from the South-East.

9.1.3 Level of Constriction

The level of constriction of cross-sectional flow was calculated, for the day, for high and low tide. This was done for the 1.5m CD and 0.9m CD to coincide with the tide peaks, while using the average significant wave height of 1.4m. The calculation was carried out using three different bathymetric surveys that were taken on separate occasions, in the last two years, in the vicinity of the Bay of Plenty Pier. This would yield approximate levels of constriction of cross-sectional flow values. The yielded values were; a $G_L/B_z = 1.0$ for high tide and a $G_L/B_z = 0.9$ for low tide. To better explain the results the levels of constriction of cross-sectional flow were placed on figure 9-6, with the 0.8 wave breaker indices for high and low tide. The reference lines are positioned according to their actual locations along the groyne length.

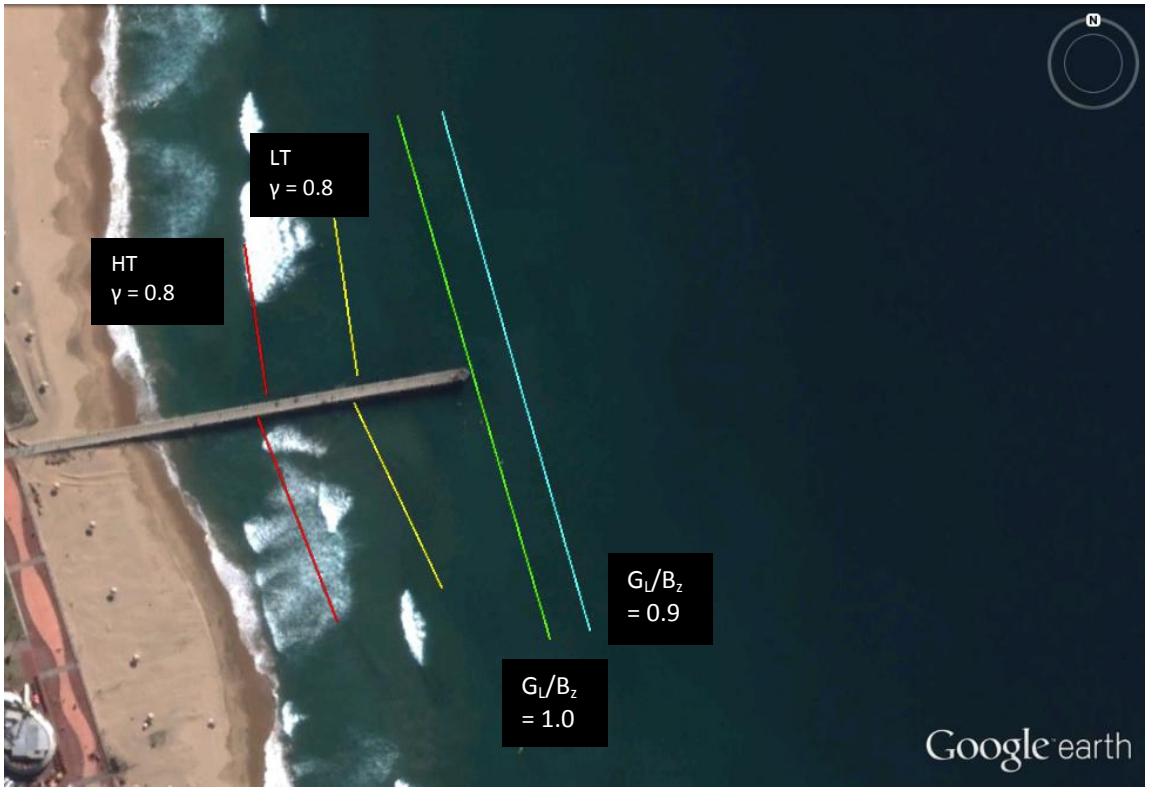

Figure 9-6: Wave breaking conditions around the Bay of Plenty Pier (background image from Google, 2012).

The 0.8 breaker indices for high and low tide were positioned on figure 9-6 for the purpose of discussing the current strength. This will take into consideration the level of constriction of cross-sectional flow with the breaker indices to make use of previous results on groyne rip currents (refer back to section 6.5 and section 8.4). The first observation is that the strongest currents along the groyne trunk will occur behind the 0.8 breaker index. As the water level drops, the 0.8 line moves further offshore from high tide (HT) to low tide (LT). In short there will be strong rip currents along the latter half of the groyne. The G_L/B_z are relatively high due to the small swell. The strongest rip currents will occur on the upstream side, or in this instance along the Southside trunk of the groyne.

If the theory holds true from the parametric study results on groynes, then the magnitude of the rip currents will be greater for the high tide than the low tide due to the higher level of constriction of cross-sectional flow. As the level of constriction of cross-sectional flow decreases, so too does the rip current magnitude. Referring back to figure 9-4 and 9-5, for high tide current meter 14 and 15 were 0.288 and 0.349 m/s, and for low tide they were 0.206 and 0.244 m/s.

When comparing the day averages with the high tide and low tide (refer to figures 9-3, 9-4 and 9-5) it can be seen that the rip current is directed offshore from the tip of the groyne. Considering the fact that this is a semi permeable groyne, it is interesting to note that it has a predominant rip current effect. It is as if this permeable structure is behaving as an impermeable structure; impermeable structures with a $G_L/B_z \geq 0.8$ display a strong rip current tending offshore from the tip of the groyne. If it were behaving ideally as a permeable groyne then the alongshore current would be more predominant and the offshore rip current at the tip of the groyne tending out to sea would be almost existent.

9.2 Results for Bedload transport assessment

Sediment samples were collected and graded and in conjunction with bathymetry and Eularian measurements of current speed around the Bay of Plenty Pier, a bedload transport assessment was carried out. The assessment was broken up into two sections:

- The evaluation of the threshold velocities
- Estimated bedload transport due to waves and currents

The purpose behind this discussion is to ascertain the required conditions that would affect the sea bed around the semi-permeable groyne (Bay of Plenty Pier), inducing sediment motion. This is in an attempt to understand the cause of scour at the groyne tip.

Only the results for the Soulsby and Clarke (2005) method (from appendix F, section F2) will be listed for section 9.2.2 under bedload transport, due to waves and currents. The reason is that it is the revised method for the determination of bed shear stresses under the action of both waves and currents. Soulsby and Clarke (2005) better fits previous models and therefore the results of Soulsby and Clarke (1997) shall not be listed.

For all figures to follow (figures 9-7 to 9-12), in the legend titles, the “S” denotes “Shallow” and the “D” denotes “Deep”. This was for the different depths at the specific locations for the bathymetric surveys. Sometimes the location was shallow or deep, depending when the survey was taken. The data for figures 9-7 to 9-12 can be found in appendix F at the end of section F2.4 in tables F2-1 to F2-6.

For in depth detail on the different methods and models that were approached refer to appendix F: F2 Sediment Transport Model.

9.2.1 Threshold velocities

Using the graded sediment samples collected on both the North and South side of the Bay of Plenty Pier, threshold velocity plots were generated (refer to figure 9-7 and 9-8, the tip of the groyne is ±133m on the cross-shore distance.). There were two current velocity threshold methods applied and one orbital wave velocity threshold method. This section was dependant mainly on the recorded depths around the Bay of Plenty Pier from past bathymetry surveys. It is therefore independent of the Eularian results recorded from the field test.

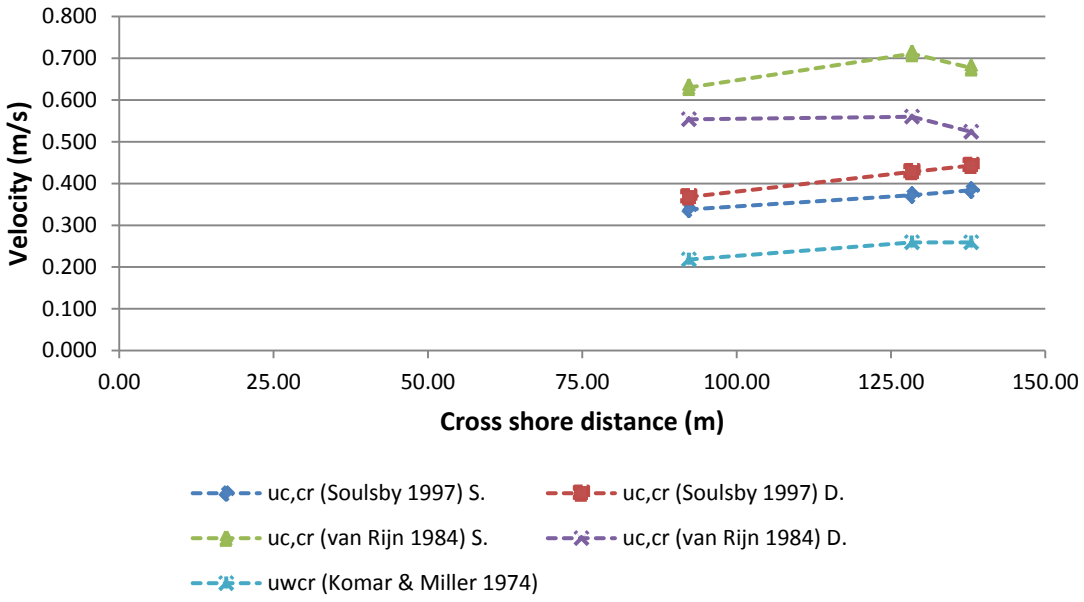

Figure 9-7: Average threshold velocities for the North side of the Bay of Plenty Pier. Points are joined to lines for clarity.

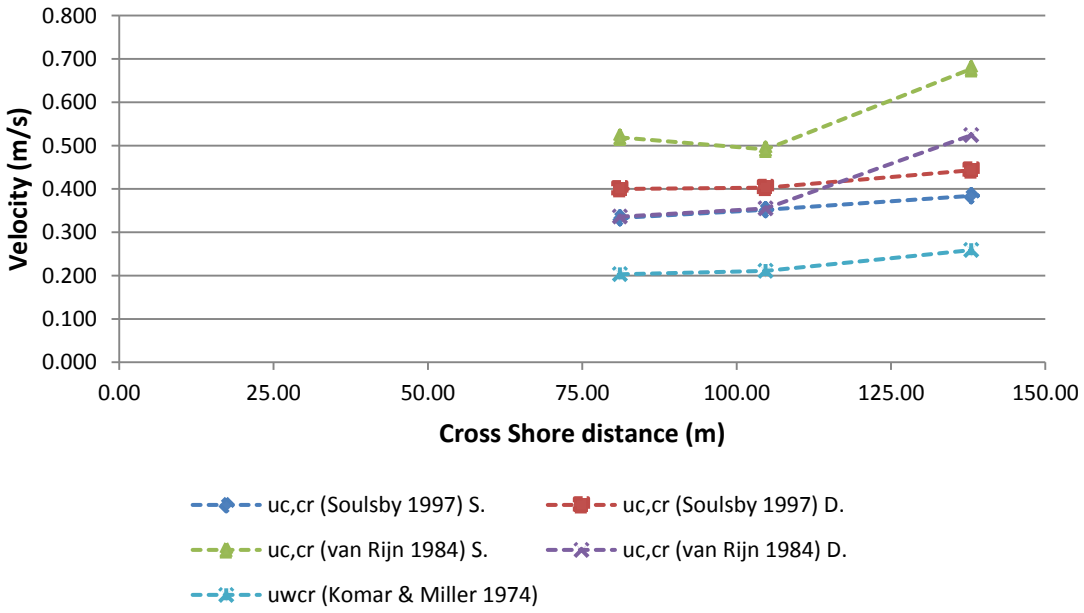

Figure 9-8: Average threshold velocities for the South side of the Bay of Plenty Pier. Points are joined to lines for clarity.

There is a large variation in the yielded current threshold velocities between the Soulsby (1997) and the van Rijn (1984) method. The van Rijn (1984) method has higher threshold velocities than that of the Soulsby (1997) method. The reason is because the van Rijn (1984) method is a function of not only the median grain d_{50} but the d_{90} grain as well. Since this factors in the larger grain size with the median grain size it requires a larger velocity to initiate motion of the grains at rest on the seabed. The van Rijn (1984) method will be considered, as it is the more conservative method.

For both figure 9-7 and figure 9-8 the required threshold velocities, for the van Rijn (1984) method, to induce motion were less in deeper water than in shallow water due to the uplift forces occurring on the grains. In short the current velocity required in deeper water to move sediment is less (for van Rijn (1984) method).

The relative depth on the South side tip of the Pier was greater than that of the North side, from the bathymetric surveys. As seen in chapter 9.1, the upstream side of the groyne had greater current speeds on the latter half of the groyne trunk. The South side is generally deeper than the North side of the Pier, due to the Durban net sediment transport being directed north (Schoonees, 2000). The large current speeds on the South side, recorded via Eularian measurement, only lead to further aggravate the situation.

Both figure 9-7 and figure 9-8 showed that the most sensitive parameter for inducing bedload motion was the orbital wave threshold velocity, u_{wcr}. It only required between 0.2 - 0.3m/s to induce bedload motion. The KwaZulu-Natal coastline has an average significant wave height of 1.65m, an average peak period of 10s and an average incident angle of 130 degrees (Corbella and Stretch, 2012c). The orbital wave velocities calculated from the field test were higher than 0.2m/s and this only used the wave buoy data (H_{savg}=1.4m and T_{pavg}=9.05s). The field test wave data was less than the average wave values for the KwaZulu-Natal coastline and they still yielded higher orbital wave velocities than that of the orbital wave threshold values.

The average incident angle of 130 degrees implied that on average the waves are coming from the South-East. This means that the South side of the Bay of Plenty Pier will receive the most wave action. The South side is more likely to erode or scour than that of the North side.

9.2.2 Bedload transport due to currents and waves

In accordance with appendix F: F2 Sediment Transport Model, the bedload transport was estimated around the Bay of Plenty Pier. The section comprised of three parts, the initial two parts were to evaluate which played the major role in bedload transport; whether it was the transport due to currents or the transport due to waves.

It is incorrect to solve the transport processes separately, as it is the waves that generate the currents and so they work in unison. Their component shear stresses are however solved separately, prior to calculating their non-linear interaction resultant bed shear stress τ_{max}.

In figure 9-9 and 9-10 you can see that the bed shear stress component induced by waves τ_w is greater than that for the bed shear stress component induced by currents τ_c. The major cause for transport is therefore waves, this coincides with the South African coastline being a wave energetic climate (Mather and Stretch, 2011), not a tide dominated climate. The results listed are for bedload transport due to the combination of currents and waves:

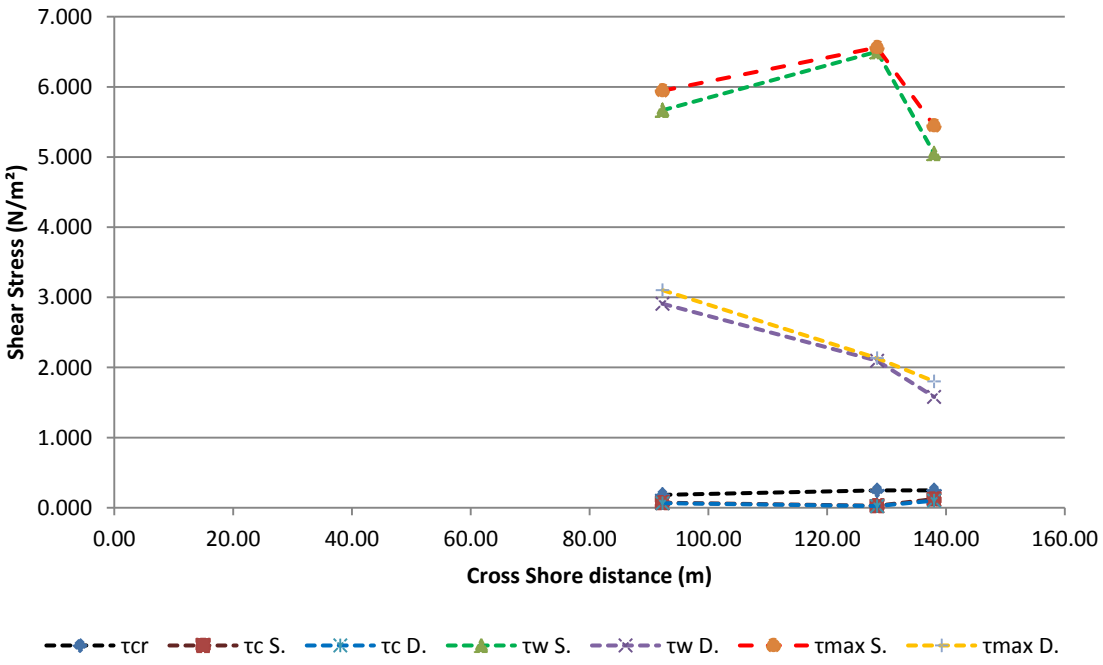

Figure 9-9: Average bed shear stresses for the North side of the Bay of Plenty Pier using the Soulsby and Clarke (2005) method. Points are joined to lines for clarity.

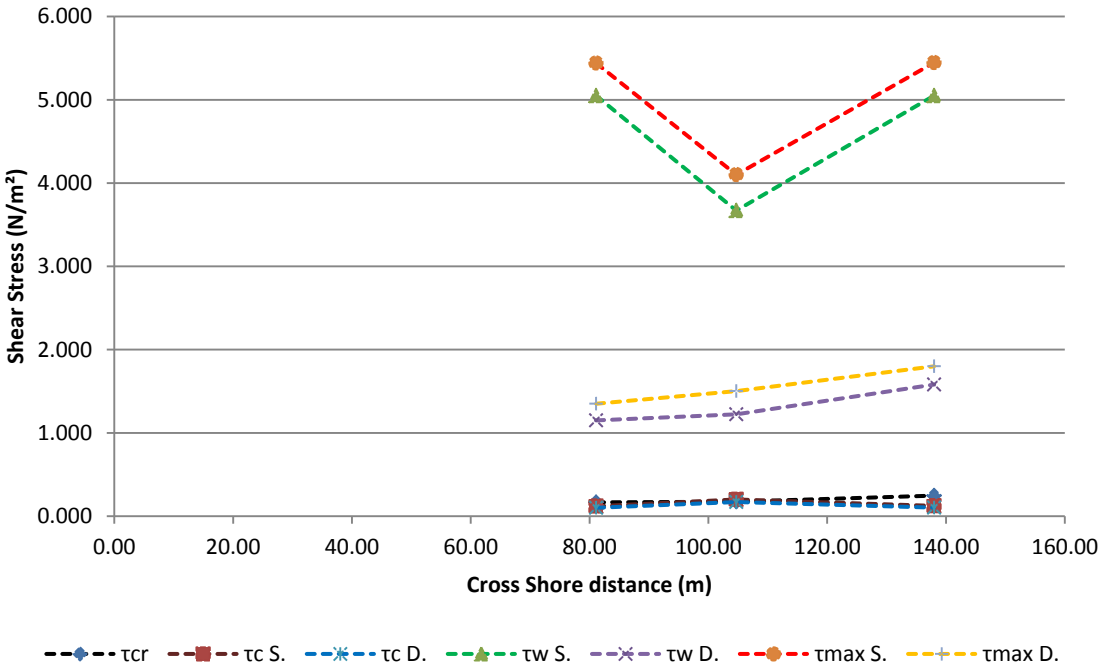

Figure 9-10: Average bed shear stresses for the South side of the Bay of Plenty Pier using the Soulsby and Clarke (2005) method. Points are joined to lines for clarity.

Figure 9-9 and 9-10 display the bed shear stresses along the North and South side of the Bay of Plenty Pier. The critical shear stress τ_{cr} is calculated by use of the critical entrainment function, also known as the critical shields parameter. If the bed shear stress is greater than τ_{cr} it will induce bedload transport. The bed shear stresses were calculated using the average current speeds from the Eularian measurements recorded from the field test. As you can see in both figures, irrespective of whether or not the conditions are shallow or deep, sediment transport is occurring since τ_{max} is greater than τ_{cr}. It is also important to note that the critical shear stress was exceeded by quite a large margin, and this was using data from the field test when there were only minor swell conditions.

The bed shear stresses will be higher for shallow water due to the boundary conditions, between the water and the surface of the seabed. If you compare the figures for shallow conditions, in figure 9-9, from 80m to 140m it is a decreasing trend. For figure 9-10 however, from 80m to 140m the trend decreases then increases. This change in trend leads to an increase in sediment transport along the tip of the South Side of the Bay of Plenty Pier. This behaviour will tend to generate scour along the latter half of the South side near the groyne tip, as the bed shear stress gradient infers the sediment transport rate. If you then compare figure 9-10 for deep conditions, the bed shear stresses are far less along the latter half of the groyne and so is the gradient change. The gradient change implies that the sediment transport rate is less.

Figure 9-11 and 9-12 display the calculated volumetric bedload transport rates per unit width, along the cross section lengths for the North and South side of the Bay of Plenty Pier. The bedload transport rates could only be calculated at the locations where current meters were positioned. These were calculated by use of the field test data from the eularian measurements and the sediment gradings. There were two methods implemented, Meyer-Peter and Muller (1948) method, qb_1 and Neilsen (1992) method qb_2. Both methods are widely used to date however under high stresses the Meyer-Peter and Muller (1948) method deviates. Both were therefore used for the estimation of bedload transport rates for waves and currents in combination. These methods used the bed shear stress results from the Soulsby and Clarke (2005) method. For both figures 9-11 and 9-12, the Nielsen (1992) method qb_2 generated larger bedload transport rates.

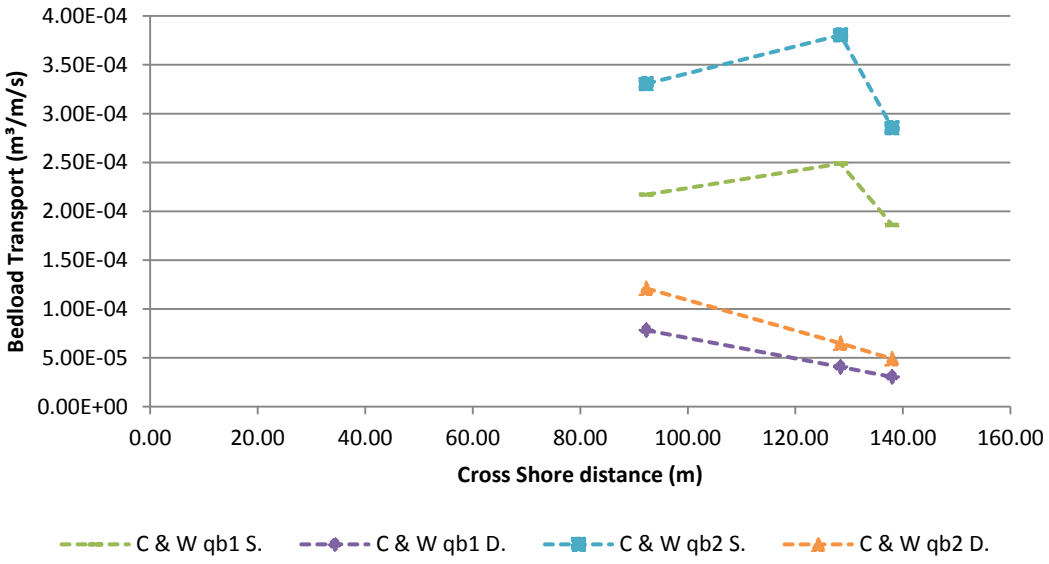

Figure 9-11: Average bedload transport rate for the North side of the Bay of Plenty Pier using the Soulsby and Clarke (2005) method with the Neilsen (1992) method. Points are joined to lines for clarity.

The average bedload transport rates are higher for the North side (refer to figure 9-11) of the Bay of Plenty Pier then they are for the South Side (Figure 9-12). This is due to the North side being naturally shallower (due to sheltering); so the bed stresses are higher and therefore the bedload transport rate is higher. The bedload transport rate is quite sensitive to depth change, so when the water depth is relatively shallow the bedload transport rate has a larger rate of change than when the water depth is large.

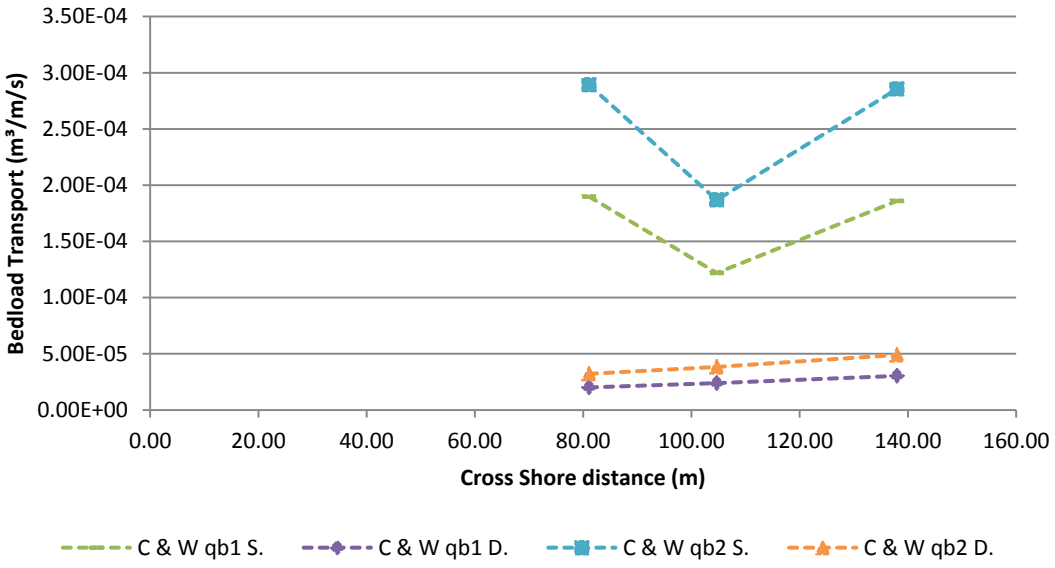

Figure 9-12: Average bedload transport rate for the South side of the Bay of Plenty Pier using the Soulsby and Clarke (2005) method with the Neilsen (1992) method. Points are joined to lines for clarity.

The average bedload transport rates show that the North side (refer to figure 9-11) transports sediment faster than that of the South side (refer to figure 9-12). This does not however account for the high current velocities that are prone to occur along the trunk of the groyne on the South side. The sediment transport models used to generate the approximate bedload rates are only calculated using the average current speeds for the day the Eularian measurements were taken. This does not however account for the maximum currents that occurred infrequently on that day. Lastly it must be noted that the Southside of the groyne is in direct contact with the propagating waves, whereas the North side is sheltered and only undergoes a fraction of the propagating wave's energy.

9.3 Summary for Field Study

The Eularian measurements from the field study showed that the semi-permeable groyne (Bay of Plenty Pier) had a strong rip-current tending offshore from the tip of the groyne. This dominant rip current phenomenon was not apparent for the permeable groyne simulations, only the impermeable groyne simulations. It is evident that the semi-permeable groyne behaves more impermeable than permeable.

From the literature Kolp (1970) did indicate that reduced permeability near the shore, barring parallel movement in the swash zone, would result in the occurrence of rip currents. The Bay of Plenty Pier is near impermeable at the shoreline due to the sloping groyne inside the piles; this may be the major cause behind the impermeable behaviour. The Eularian measurements did note some through flow at the tip of the groyne where the semi-permeable groyne was at its most permeable. The groyne however still displayed a strong resemblance to that of an impermeable groyne regardless of the through flow.

The levels of constriction of cross-sectional flow for the case study site were determined for the day that the measurements were taken. As the semi-permeable groyne was observed, from the Eularian measurements, to behave more impermeable than permeable, it was therefore compared against the findings of the impermeable groyne parametric study. The levels of constriction of cross-sectional flow for high tide and low tide were 1.0 and 0.8; both displayed an offshore rip current from the tip of the groyne. The levels of constriction of cross-sectional flow for the case study site coincided with those for the classification of flow patterns around an impermeable groyne.

With respect to the sediment transport results estimated at the case study site; the coastal methods to date are far from accurate and are only used as a guideline for engineering applications. In stating this, the sediment model was developed using as much available literature (refer to section F2 for details) as possible in an attempt to reduce the discrepancies.

The threshold velocities were calculated from collected sediment samples. There was quite a large variation between the different methods however the most important threshold velocity was that of the wave velocity. The results showed that even mild swell conditions along the case study site induced motion of sediment along the seabed. The findings that were displayed in this chapter for the sediment transport models were calculated using only the average current speeds from the Eularian measurements. This led therefore to some inconsistencies, such as the results displaying that the bedload transport rate was higher on the lee side. This is not an accurate reflection as the maximum current speeds were not considered.

CHAPTER 10

SUMMARY & CONCLUSIONS

Chapter Ten presents a summary of the research outcomes and the key conclusions. The objectives presented in Chapter 1 of the report are revisited. Recommendations for future research are provided.

10.1 Comparison with previous modelling work

To meet the initial objectives, modelling comparisons were carried out using previous work by Pattiaratchi et al (2009) in conjunction with literature on the expected hydraulic responses of a groyne as a structure. When using Pattiaratchi et al (2009) model descriptions and configurations a number of discrepancies were found;

- Their simulation results displayed boundary conditions and current vectors that did not match the configurations that were listed in their paper. At the groyne boundary their simulated results showed undefined patches where the model could not resolve the flow. The current vectors displayed on the simulated results were larger spatially than what the configuration should yield. The size of their model mesh was larger than stated in the configurations of their paper. Also a structured vector solving was applied to an unstructured file: this is where the current vectors are averaged over a certain area of the model, changing the displayed flow pattern.
- Pattiaratchi et al (2009) discussed and displayed a convergence point along the trunk of the groyne on the lee side where an onshore rip current was present (refer back to figures 5-5, 5-7, 5-9 and 5-11). This occurrence was not found when running numerical models using the same model descriptions and configurations, nor was this occurrence found in any existing literature on circulation patterns surrounding groynes. This is perhaps due to Pattiaratchi et al (2009) applying a structured vector solving that the discrepancies occurred.

The models that were generated using Pattiaratchi et al (2009) model configurations for the purpose of comparison followed existing literature relatively well. The geometric parameters of

the groyne generated alongshore variations in the significant wave height, on the lee side of the groyne. The variations changed the wave radiation stress conditions in the vicinity of the groyne affecting the surrounding circulation patterns. The generated alongshore current flowed towards the groyne and was then directed offshore due to the presence of the groyne, forming a rip current adjacent to the groyne. At the tip of the groyne the rip current was deflected around the groyne due to the alongshore current. A large velocity gradient on the lee side of the groyne would then generate a separation layer that induced a recirculation zone.

10.2 Level of Constriction

In an attempt to evaluate how flow patterns change around a groyne, various characteristics were changed during modelling; groyne length, water level, wave conditions etc. To classify the patterns, a parameter defined by Taranowska (1985) as the ratio of groyne length to the width of breaker zone (G_L/B_z), representing the level of constriction of the cross-sectional flow was used. The level of constriction helped not only to classify different flow patterns around the groyne, depending on the ratio, but also to determine that the main factor behind flow pattern formations is the extent over which the breaker zone occurs. Through the use of numerical modelling, parametric studies allowed for the characterisation of flow pattern classes around groynes.

There were three main flow pattern classes determined that occur around a groyne;

- Rip current dominant (Figure 10-1): where the cross-shore current magnitude tending offshore is greater than the alongshore current magnitude at the tip of the groyne. This causes the rip current to move offshore a distance before deviating back into the alongshore current direction. The alongshore current flow is relatively weak and acts over a large cross-sectional area. This occurred for scenarios where the breaker zone width was either just outside or within the groyne extent; where $G_L/B_z > 0.8$. This pattern would put strain on the sea bed along the trunk of the groyne with stronger rip currents occurring on the upstream side of the groyne. There would either be accretion on the upstream trunk side or downstream trunk side depending on how much greater than 0.8 the G_L/B_z was.
- Alongshore dominant (Figure 10-2): where the alongshore current magnitude was greater than the rip current magnitude at the tip of the groyne. The alongshore current flow is strong and it acts over a large cross-sectional area. This occurred for scenarios where the breaker zone width was far greater than the length of the groyne. The alongshore current showed little deviation around the groyne as the majority of this

current occurred outside the extent of the groyne; where $G_L/B_z < 0.55$. This pattern would put strain on the sea bed along the latter half of the groyne with stronger rip currents occurring on the lee side of the groyne. There would be erosion around the groyne with accretion occurring downstream of the groyne's location.

- Transitional: this is an intermediary stage where either the cross-shore or alongshore current magnitudes can be larger, however neither one dominates the other. Such that their peak velocities are within 100m of the groyne tip. The alongshore current flow is strong and it acts over a small cross-sectional area. The G_L/B_z is between 0.55 and 0.8. This pattern would put strain on the latter half of the groyne similar to that of the alongshore dominant pattern.

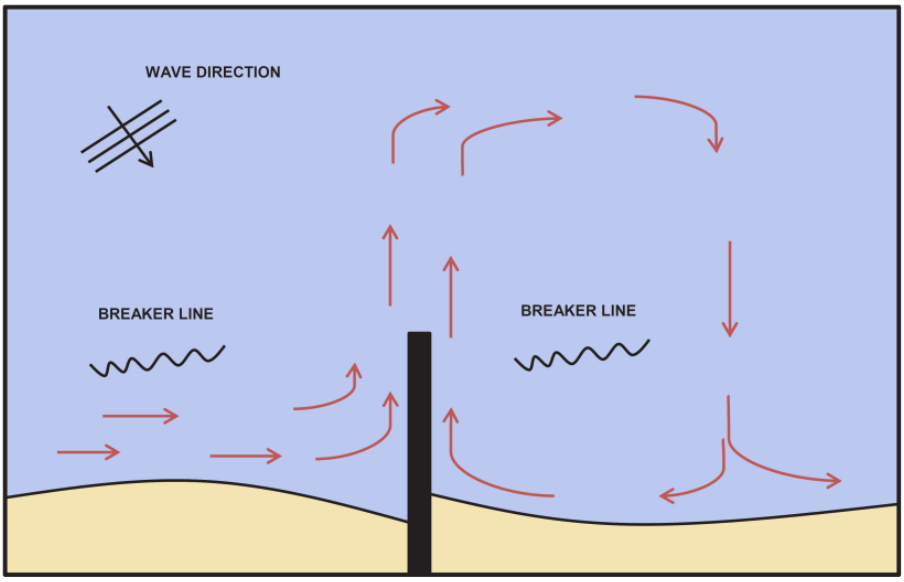

Figure 10-1: Schematic of rip current dominant flow pattern around an impermeable groyne

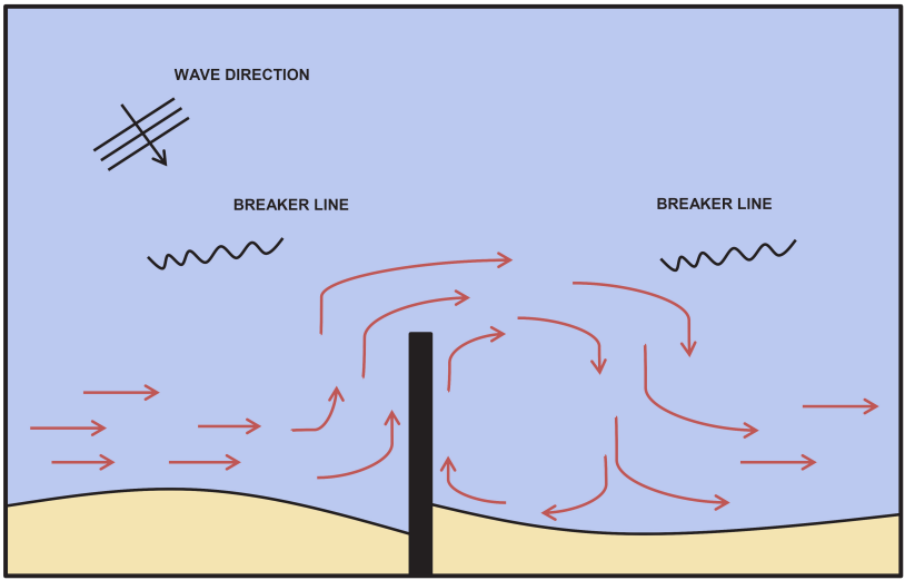

Figure 10-2: Schematic of alongshore current dominant flow pattern around an impermeable groyne

The relevance of the level of constriction of cross-sectional flow on the flow pattern decreases as the permeability of the groyne increases. The three flow pattern characteristics above apply to groynes with permeability less than equal to 33 per cent. For all permeable groynes greater than 33 per cent permeability the flow pattern was alongshore dominant. The cross-sectional area and flow strength along the tips of the permeable groynes was reduced in comparison to the impermeable groynes for the same levels of constriction of cross-sectional flow. There was however still traits of the previous flow classifications when comparing the occurrences along the tip of the permeable groyne. When the permeability increased from 33 per cent the following changes were noted in the flow pattern classes:

- Rip current dominant: for the permeable pile screens an onshore directed rip current occurred around the groyne tip when $G_L/B_z > 0.72$. Whereas an offshore directed rip current occurred for the impermeable groyne when $G_L/B_z > 0.80$.
- Alongshore dominant: the alongshore current velocity is much larger than the cross-shore velocity at the tip of the permeable groyne when $G_L/B_z < 0.48$.
- Transitional: for the permeable pile screen groynes there was also an intermediary stage where the cross-shore and alongshore current magnitudes were both similar in magnitudes at the tip of the groyne. The G_L/B_z was between 0.72 and 0.48.

10.3 Modelling groynes with varying permeability

Numerical models are far from ideal when modelling coastal structures, simpler methods to mimic rocks, boulders and concrete structures would be useful for simulations. In an attempt to simplify permeable groyne numerical modelling, the friction source terms were manipulated in the models.

Two different methods were applied, both of which had varied effects on flow impedance. The initial method applied a constant friction manipulation over a given area. This method behaved similarly to that of a low crested groyne, i.e. as the depth increased the drag effect on the water column decreased. It became more permeable the deeper it got.

The second method applied a friction manipulation over a given area that was dependant on depth. The friction increased with depth such that a uniform drag was applied throughout the water column. This method reduced the flow over the area considerably, such that only 10 per cent could filter through. Though the second method had a better effect on varying permeability, the two methods were flawed as it was impossible to create an impermeable structure with friction manipulation alone.

The two applied methods were able to generate similar flow patterns to that of observed impermeable and permeable groynes. However the proposed methods are far from ideal, they require larger areas of friction manipulation to generate the same flow pattern as a smaller permeable structure. This was possibly due to the friction simulations not being implemented correctly. The resolution was perhaps too coarse over the area that was manipulated. The methods would therefore require further work, implementing more gridlines and a finer resolution over the manipulated area, if they are to be used for modelling coastal structures.

10.4 Bay of Plenty Pier

Data obtained from twenty-two current meters and an ADCP deployed at Durban's central beach front revealed the flow patterns around the Bay of Plenty Pier, semi-permeable groyne. The swell conditions were relatively minor, of which the swell direction and the significant wave height did not vary much for the day of the test. The general flow pattern around the Pier stayed the same with only minor differences due to the change in tide.

The offshore extent of the currents at the tip of the Pier increased with a decrease in tide, as the strength of the current is dependent on where the majority of the breaking waves are. An increase in tide shifts the breaker zone shoreward and a decrease in tide shifts the breaker zone seaward.

The flow pattern garnered from the Eularian measurements around the Bay of Plenty Pier, during both high and low tide displayed rip currents directed offshore from the tip of the pier. By observational definition, the flow around the semi-permeable groyne was rip current dominant during the day of the field test. Though the flow pattern showed currents tending North-East toward the South side tip with some through flow at the tip of the pier, there was still a strong current tending offshore from the tip of the Pier. The level of constriction of cross-sectional flow was then calculated, it ranged between 0.8 – 1.0 from low to high tide; this falls within the rip current dominant flow pattern class.

The pier is semi-permeable however the flow pattern shows characteristics of an impermeable groyne. This could be due to two possible reasons, the first being the fact that the Bay of Plenty Pier may be sheltered by the two Piers South of its location. As both of those piers are semi-permeable, resisting the alongshore current and reducing its effects around the Bay of Plenty Pier. The second possible reason is that the Bay of Plenty Pier does not have a set permeability; it is semi-permeable, so the permeability varies due to the large rocks inside the Pier. On the shore the rocks are visible and so it is near impermeable in the swash zone. This factor in conjunction with the large amount of vegetation (e.g. mussels) on the piles further reduces the permeability due to drag.

In previous bathymetric surveys (for e.g. refer back to figure 1-4 and 1-5) scour occurred predominantly along the south side tip of the semi-permeable groyne. When considering the groyne has a rip current dominant pattern, and due to a level of constriction of 0.8 - 1.0, it will also have a stronger rip current on the upstream side of the groyne. The threshold velocities determined using sediment samples displayed that it did not require currents or waves of large magnitude to induce sediment motion, even in the deeper regions around the groyne.

Though the most frequent currents recorded by the current meters were small with 52.5 per cent having average currents < 0.2 m/s, there were still some infrequent rip currents along the South side of the groyne that were as large as 2.07 m/s during high tide. It would seem quite reasonable therefore that the latter half of the trunk on the South side would undergo erosion, more so than that of the North side trunk. Now if we consider this and the strong North-Easterly currents tending towards the South side of the groyne, with average currents > 0.3 m/s, this could explain the formation of a scour hole on the South side of the groyne. The currents

generated were only for Durban's average swell conditions, the concern therefore is the development of rip currents that would occur under larger swell conditions. Under large swell conditions there would likely be an alongshore dominant flow, putting the seabed on the latter half of the groyne under severe stress.

10.5 Summation

Groynes are commonly used for Coastal protection against erosion with varying degrees of success. Trampenau, Oumeraci and Dette (2004) and Komar (1998) state that one of the reasons for failure is attributed to the influence of rip currents along the trunk of a groyne. This results in the deflection of the alongshore current by the structure, from the upstream side of the groyne. The results of this study indicate however that the failure of the groyne is not due to one factor, such as rip currents, but due to the interaction between the groyne and the wave breaking zone. The change in the interaction will affect the strength of both the cross-shore and alongshore currents around the groyne changing flow patterns, irrespective of permeability. A change in the flow pattern also changes the location where sediment transport is more likely to occur.

The flow pattern around the groyne was classified categorically into three classes; simply by considering the length of the groyne and the length of the breaker zone. This will allow for a better understanding of the mechanisms behind groyne erosion due to rip current and alongshore current interaction as detailed in this study.

10.6 Recommendations

It would be recommended to carry out the same Eularian experiment around the Bay of Plenty Pier over several different days with varying swell conditions. This would yield additional flow patterns with their corresponding levels of constriction to improve and further verify the level of constriction of cross-sectional flow for flow pattern classifications around groynes.

A major limitation of this research is that it does not consider the level of constriction of cross-sectional flow with respect to groyne arrays. The Bay of Plenty Pier may be sheltered by the two Piers South of its location. In order to improve the classification of flow patterns using the level of constriction of cross-sectional flow it would be suggested that both numerical models and Eularian measurements be carried out with respect to groyne arrays.

Considering that a change in water level, due to the tide, affects the location of the breaker zone so too does beach nourishment. The expansion of the beach may shift the breaker zone seaward of the groyne. This could change the natural flow patterns around the groyne depending on the quantity of nourishment and the change in the beach profile due to nourishment. A groyne that naturally has a rip current dominant flow pattern may change to that of a transition pattern, putting more strain on the latter half of the groyne. This is something worth investigating as nourishment may inadvertently have a negative effect.

Lastly it would be recommended to use the level of constriction of cross-sectional flow, not only to classify and evaluate flow patterns but to classify morphological changes due to the flow patterns as well. This could be tied into and further expanded on work done by (Walker, Dong and Anastasiou, 1991), this work only made use of numerical modelling. Verifying the work, using a case study site and physical models would be beneficial. One possible approach would be to carry out bathymetric surveys in combination with current and wave readings over several weeks around a groyne. The other approach would be to carry out physical models in the laboratory and verify these using numerical modelling.

REFERENCES

Bakker, W.T., Hulsbergen, C.H., Roelse, P., de Smit, C. and Svasek, J.N. (1984) 'Permeable Groynes: Experiments and Practice in the Netherlands', Proceedings of the 19th International Conference on Coastal Engineering, Houston, 2026-2041.

Barnett, K.A. (1982) 'Durban Beaches Reclamation: Practical Aspects', Proceedings of the 18th International Conference on Coastal Engineering, Cape Town, South Africa, 1970-1991.

Barnett, K.A. (1999) 'The Management of Durban's Beaches: An Historical Perspective', Fifth International Conference of Coastal and Port Engineering in Developing Countries, COPEDEC V, Cape Town, 19-25.

Battjes, J.A. (1974) 'Surf Similarity', Proceedings of the 14th International Conference on Coastal Engineering, New York, 466-479.

Battjes, J.A. (1988) 'Surf-Zone Dynamics', *Annual Review Fluid Mechanics*, vol. 20, no. 1, pp. 257-93.

Battjes, J.A. and Janssen, J.P.F.M. (1978) 'Energy loss and set-up due to breaking of random waves', Proceedings of the 16th Conference on Coastal Engineering, Hamburg, Germany, 569-587.

Battjes, J.A. and Stive, M.J.F. (1985) 'Calibration and verification of a dissipation model for random breaking waves', *Journal of Geophysical Research*, vol. 90, no. C5, September, pp. 9159-9167.

Beach, R.A. and Sternberg, R.W. (1996) 'Suspended-sediment transport in the surf zone: response to breaking waves', *Journal of Continental Shelf Research*, vol. 16, no. 15, pp. 1989-2003.

Bell, R.G., Goring, D.G. and de Lange, W.P. (2000) 'Sea-level change and storm surges in the context of climate change', *IPENZ transactions*, vol. 27, no. 1, pp. 1-10.

Bird, E.C.F. (1985) *Coastline Changes - A Global Review*, Chichester: John Wiley-Interscience.

Brander, R.W. (1999) 'Sediment Transport in Low-Energy Rip', *Journal of Coastal Research*, vol. 15, no. 3, pp. 839-849.

Bronsvoort, K., Radermacher, M., van der Spek, B.J., Spruit, R. and van Tongeren, B. (2011) *Modelling nourishments through the Durban piers*, Durban: Delft University of Technology.

Brooke, J. (2003) *Wave Energy Conversion*, 6th edition, Kidlington, Oxford: Elsevier Science Ltd.

Bruun, P., Mehta, A.J. and Johnson, I.G. (1978) 'Stability of tidal inlets: Theory and Engineering', in *Developments in Geotechnical Engineering*, 23rd edition, Amsterdam: Elsevier Scientific Publishing Company.

Corbella, S. (2010) 'A review of Durban's wave climate and storm induced changes', M.Sc, University of KwaZulu-Natal, Durban, 308 pp.

Corbella, S. and Stretch, D.D. (2012a) 'Coastal defences on the KwaZulu-Natal coast of South Africa: a review with particular reference to geotextiles', *South African Institution of Civil Engineering*, vol. 54, no. 2, October, pp. 55-64.

Corbella, S. and Stretch, D.D. (2012b) 'Shoreline recovery from storms on the east coast of Southern Africa', *Natural Hazards and Earth System Science*, vol. 12, no. 1, pp. 11-22.

Corbella, S. and Stretch, D.D. (2012c) 'The wave cimate on the KwaZulu-Natal coast of South Africa', *South African Institution of Civil Engineering*, vol. 54, no. 2, October, pp. 45-54.

Corne, N.P. (2009) 'The Implications of Coastal Protection and Development on Surfing', *Journal of Coastal research*, vol. 25, no. 2, pp. 427-434.

Davis, R. and Hayes, M.O. (1984) 'What is a wave-dominated coast?', *Marine Geology*, vol. 60, no. 1-4, pp. 313-329.

Dean, R.G. (1978) 'Diffraction Calculation of Shoreline Planforms', Proceedings of the 15th International Conference on Coastal Engineering, Honolulu, 1903-1917.

Dette, H.H., Raudkivi, A.J. and Oumeraci, H. (2004) 'Permeable Pile Groin Fields', *Journal of Coastal Research*, no. (SI) 33, pp. 145-159.

Dolan, T.J., Castens, P.G., J, S.C. and Egense, A.K. (1987) 'Review of sediment budget methodology: Oceanside littoral cell', *Coastal Sediments*, vol. 2, pp. 1289-1304.

Dong, P. (2004) 'An Assessment of Groyne Performance in the United Kingdom', *Coastal Management*, vol. 32, no. 2, pp. 203-213.

EMS (2013) *Environmental Mapping & Surveying*, [Online], Available: http://www.enviromap.co.za/ [15 Oct 2013].

eThekwini Municipality (2011) *Durban Lower Level Groynes Project*, [Online], Available: http://www.durban.gov.za/City_Services/engineering%20unit/Coastal_Engineering_Stormwater_Catchment_Management/Coastal_Engineering/Pages/Durban_Lower_Level_Groynes_Project.aspx [12 March 2013].

Fleming, C.A. (1990) *Guides on the Uses of Groynes in Coastal Engineering*, London, England: CIRIA.

Fulford, E.T. and Grosskopf, W.G. (1989) 'Storm Protection Project Design - Ocean City Maryland', *Beach Preservation Technology '89*, pp. 239-248.

Galvin, C.J. (1972) 'Wave breaking in shallow water', in Meyer, R.E. (ed.) *Waves on Beaches*, New York: Academic Press.

Goda, Y. (1970) 'A synthesis of breaking indices', *Translation, Japan Society of Civil Engineering*, vol. 2, no. 2, pp. 227-230.

Goda, Y. (2000) 'Transformation and Deformation of Random Sea Waves', in Goda, Y. *Random Seas and Design of Maritime Strucutures*, 2nd edition, Singapore: World Scientific.

Hansen, J.B. (1990) 'Periodic waves in the surf zone: Analysis of experimental data', *Coastal Engineering*, vol. 14, no. 1, pp. 19-41.

Hanson, H. and Larson, M. (2004) 'Wave Directional Characteristics as a Design Parameter for Groin Performance', *Journal of Coastal Research*, no. (SI) 33, pp. 188-197.

Herbert, B. (2007) 'Climate Change 2007: Physical Science Basis', IPCC WGI Fourth Assessment Report, Geneva, 1-18.

Holthuijsen, L.H., Booij, N. and Herbers, T.H.C. (1989) 'A prediction model for stationary, short-crested waves in shallow water with ambient currents', *Coastal Engineering*, vol. 13, no. 1, May, pp. 23-54.

Holthuijsen, L.H., Herman, A. and Booij, N. (2003) 'Phase-decoupled refraction-diffraction for spectral wave models', *Coastal Engineering*, vol. 49, no. 4, October, pp. 291-305.

Hulsbergen, C.H., Bakker, W.T. and van Bochove, G. (1976) 'Experimental Verification of Groyne Theory', Proceedings of the 15th Coastal Engineering Conference, 1439-1458.

IPCC (1990) *Strategies for Adaption to Sea Level Rise*, Rijkswaterstaat: Response Strategies Working Group, Intergovernmental Panel on Climate Change.

Johnson, H.K., Karambas, T.V.A.I., Zanuttigh, B., Gonzalez-Marco, D. and Caceres, I. (2005) 'Modelling of waves and currents around submerged breakwaters', *Coastal Engineering*, vol. 52, no. 10-11, pp. 949-969.

Jordan, J.M.J. (1970) 'Study of Durban Harbour Silting and Beach Erosion', Proceedings of the 12th International Conference on Coastal Engineering, Washington D C, 1097-1116.

Kaminsky, G.M. and Kraus, N.C. (1993) 'Evaluation of depth-limited wave breaking criteria', *ASCE - Ocean Wave Measurement and Analysis*, pp. 180-193.

Kang, J., Yeo, H., Kim, S. and Ji, U. (2011) 'Experimental investigation on the local scour characteristics around groynes using a hydraulic model', *Water and Environmental Journal*, vol. 25, no. 2, pp. 181-191.

Kolp, O. (1970) 'Farbsandversuche mit lumineszenten Sanden in Buhnenfeldern: Ein Beitrag zur Hydrographie der Ufernahen Meereszone "Trying with luminescent coloured sands in the Buhnen fields: A contribution to the hydrography of the near-shore marine zone"', *Petermanns Geographischen Mitteilungen*, vol. 114, no. 2, (In German).

Komar, P.D. (1996) 'The budget of littoral sediments: concepts and applications', *Journal of Shore and Beach*, vol. 64, pp. 18-26.

Komar, P.D. (1998) *Beach Processes and Sedimentation*, 2nd edition, Upper Saddle River: Prentice Hall.

Komen, G.J., Cavaleri, L., Donelan, M., Hasselmann, K., Hasselmann, S. and Janssen, P.A.E.M. (1994), in *Dynamics and Modelling of Ocean Waves*, New York: Cambridge University Press.

Kraus, N.C., Hanson, H. and Blomgren, S.H. (1994) 'Modern Functional Design of Groin Systems', Proceedings of the 24th International Conference on Coastal Engineering, Orlando, USA, 1327-1342.

Kuriyama, Y. (1996) 'Models of Wave Height and Fraction of Breaking Waves on a Barred Beach', Proceedings of the 25th International Conference on Coastal Engineering, Orlando, Florida, 247-260.

Lamberti, A. and Zanuttigh, B. (2010) 'Low Crested Breakwaters', in Kim, Y.C. (ed.) *Handbook of Coastal and Ocean Engineering*, 1st edition, Singapore: World Scientific Publishing.

Laubscher, W.I., Coppoolse, R.C., Schoonees, J.S., Pfaff, W.M. and Davis, A.B. (1990) 'The Durban beach restoration scheme after 30 years', Proceedings of the 22nd International Conference on Coastal Engineering, Delft, 3227-3238.

Longuet_Higgins, M.S. and Stewart, R.W. (1962) 'Radiation stress and mass transport in gravity waves', *Journal of Fluid Mechanics*, vol. 13, no. 4, pp. 481-504.

Longuet-Higginds, M.S. and Stewart, R.W. (1963) 'A note on wave set-up', *Journal of Marine Research*, vol. 21, pp. 4-10.

Longuet-Higgins, M.S. (1970) 'Longshore Currents Generated by Obliquely Incident Sea Waves, 1', *Journal of Geophysical Research*, vol. 75, no. 33, pp. 6778-6789.

Longuet-Higgins, M.S. and Stewart, R.W. (1960) 'Changes in the Form of Short Gravity Waves on Long Waves and Tidal Currents', *Journal of Fluid Mechanics*, vol. 8, no. 4, pp. 565-583.

Longuet-Higgins, M.S. and Stewart, R.W. (1964) 'Radiation stresses in water waves; a physical discussion, with applications', *Deep-Sea Research*, vol. 11, no. 4, pp. 529-562.

MacMahan, J.H., Reniers, A.J.H.M., Thornton, E.B. and Stanton, T.P. (2004) 'Surf zone eddies coupled with rip current morphology', *Journal of Geophysical Research-Oceans*, vol. 109 , no. C7, pp. 1-15.

MacMahan, J.H., Thornton, E.B. and Reniers, A.J.H.M. (2006) 'Rip Current Review', *Journal Of Coastal Engineering*, vol. 53, no. 2-3, pp. 191-208.

Marchand, M. (ed.) (2010) *Concepts and Science for Coastal Erosion Management: Concise report for policy makers*, Delft: Deltares.

Mather, A., Kasserchun, R. and Wenlock, H. (2003) 'City of Durban sand bypass scheme: 20 year performance evaluation', COPEDEC VI, Colombo, 401-402.

Mather, A. and Stretch, D.D. (2011) 'Predicting extreme wave run-up on natural beaches for coastal planning and management', *Coastal Engineering Journal*, vol. 53, no. 2, March, pp. 87-109.

McCowen, J. (1894) 'On the highest wave of permanent type', *Philosophical Magazine*, vol. 5, no. 38, pp. 351-357.

Meyer-Peter, E. and Muller, R. (1948) 'Formulas for bedload transport', Report of Second Meeting of the International Association of Hydraulic and Structural Research, Stockholm, 39-64.

MIKE21 (2011a) *Spectral Wave Module Scientific Documentation*, 2011th edition, Denmark: DHI.

MIKE21 (2011b) *Hydrodynamic and Transport Module Scientific Documentation*, 2011th edition, Denmark: DHI.

Myrhaug, D. (1989) 'A rational approach to wave friction coefficients for rough, smooth and transitional turbulent flow', *Journal of Coastal Engineering*, vol. 13, no. 1, May, pp. 11-21.

Nam, P.T., Larson, M., Hanson, H. and Hoan, L.X. (2011) 'A numerical model of beach morphological evolution due to waves and currents in the vicinity of coastal structures', *Journal of Coastal Engineering*, vol. 58, no. 9, May, pp. 863-876.

Neilsen, P. (1992) *Coastal Bottom Boundary Layers and Sediment Transport*, Singapore: World Scientific Publishing.

Nielsen, C. and Apelt, C. (2003) 'The application of wave induced forces to a two-dimensional finite element long wave hydrodynamic model', *Journal of Ocean Engineering*, vol. 30, no. 10, August, pp. 1233-1251.

Patsch, K. and Griggs, G. (2006) *Littoral cells, sand budgets, and beaches: Understanding California's Shoreline*, California, Santa Cruz: Institute of Marine Sciences.

Pattiaratchi, C., Olsson, D., Hetzel, Y. and Lowe, R. (2009) 'Wave-driven circulation patterns in the lee of groynes', *Continental Shelf Research*, vol. 29, no. 16, pp. 1961-1974.

Preston-Whyte, R. (2002) 'Constructions of surfing space at Durban, South Africa', *Tourism Geographies: An International Journal of Tourism Space, Place and Environment*, vol. 4, no. 3, pp. 307-328.

Rajaratnam, N. and Nwachukwu, B.A. (1983) 'Flow near groin-like structures', *Journal of Hydraulic Engineering*, vol. 109, no. 3, March, pp. 463-480.

Rattanapitikon, W. and Shibayama, T. (1998) 'Energy Dissipation Model for Irregular Breaking Waves', Proceedings of 26th International Conference on Coastal Engineering, Copenhagen, Denmark, 112-125.

Raudkivi, A.J. (1996) 'Permeable Pile Groins', *Journal of Waterway, Port, Coastal, and Ocean Engineering*, vol. 122, no. 6, November/December, pp. 267-272.

Reeve, D., Chadwick, A. and Fleming, C. (2004a) 'Wave Theory', in Reeve, D., Chadwick, A. and Fleming, C. *Coastal Engineering: Processes, theory and design practice*, Oxford: Spon Press.

Reeve, D., Chadwick, A. and Fleming, C. (2004b) 'Wave Breaking', in Reeve, D., Chadwick, A. and Fleming, C. *Coastal Engineering: Processes, theory and design practice*, Oxford: Spon Press.

Reeve, D., Chadwick, A. and Fleming, C. (2004c) 'Coastal transport porcesses', in Reeve, D., Chadwick, A. and Fleming, C. *Coastal Engineering: Processes, theory and design practice*, Oxford: Spon Press.

Roelvink, J.A. (1993) 'Dissipation in random wave groups incident on a beach', *Journal of Coastal Engineering*, vol. 19, no. 1-2, February, pp. 127-150.

Saxena, P.S., Vaidyaraman, P. and Srinivasan, R. (1976) 'Design and behaviour of sand traps in regions of high littoral drift', Proceedings of the 15th International Conference on Coastal Engineering, New York, 1377-1393.

Schoonees, J.S. (2000) 'Annual variation in the net longshore sediment transport rate', *Journal of Coastal Engineering*, vol. 40, no. 2, pp. 141-160.

Schoonees, J.S. and Theron, A.K. (2002) 'Development of an accurate longshore sediment transport model', *Journal of the South African Institution of Civil Engineering*, vol. 44, no. 3, pp. 12-17.

Shepard, F.P., Emery, K.O. and La Fond, E.C. (1941) 'Rip currents: A process of geological importance', *Journal of Geology*, vol. 49, no. 4, May-June, pp. 337-369.

Shields, A. (1936) 'Anwendung der Ähnlichkeitsmechanik und der Turbulenzforschung auf die Geschiebebewegung,"Application of similarity mechanics and turbulence research to bedload movement"', *Mitteilungen der Preussischen Versuchsanstaltung für Wasserbau und Schiffbau*, vol. 26, (In German), pp. 5-24.

Shiereck, G.J. (2004) *Introduction to Bed, Bank and Shore Protection*, London: Taylor & Francis.

Smagorinsky, J. (1963) 'General circulation experiments with the primitive equations: 1. The basic experiment', *Monthly Weather Review*, vol. 91, no. 3, pp. 99-164.

Sorenson, T. (1960) 'The Development of Coast Profiles on a Receding Coast Protected by Groynes', Proceedings of the 7th International Conference on Coastal Engineering, Hague, 836-846.

Sorenson, O.R., Kofoed-Hansen, H., Rugbjerg, M. and Sorenson, L.S. (2004) 'A third generation spectral wave model using an unstructured finite volume technique', Proceedings of the 29th International Conference on Coastal Engineering, Lisbon, 894-906.

Soulsby, R.L. (1995) 'Bed shear stresses due to combined waves and currents', in Stive, M.J.F., de Vriend, H.J., Fredsoe, J., Hamm, L. and Soulsby, R.L. (ed.) *Advances in Coastal Morphodynamics*, Netherlands: Delft Hydraulics.

Soulsby, R. (1997) *Dynamics of Marine Sands*, London: Thomas Telford Publications.

Soulsby, R.L. and Clarke, S. (2005) *Bed Shear-stresses Under Combined Waves and Currents on Smooth and Rough Beds*, Report TR 137: HR Wallingford.

Soulsby, R.L. and Whitehouse, R.J.S.W. (1997) 'Threshold of sediment motion in coastal environments', Proceedings of the 13th Australian Coastal and Engineering Conference, Christchurch, New Zealand, 149-154.

South African Tourism (2013) *Durban's Beaches*, [Online], Available: http://www.vayamzansi.co.za/za/en/articles/entry/article-southafrica.net-durbans-beaches [14 March 2013].

Southgate, H.N. and Nairn, R.B. (1993) 'Deterministic profile modelling of nearshore processes. Part 1. Waves and currents', *Journal of Coastal Engineering*, vol. 19, no. 1-2, February, pp. 27-56.

Stive, M.J.F., Aarninkhof, S.G.J., Hamm, L., Hanson, H., larson, M., Wijnberg, K.M., Nicholls, R.J. and Capobianco, M. (2002) 'Variability of shore and shoreline evolution', *Journal of Coastal Engineering*, vol. 47, no. 2, pp. 211-235.

Stive, M.J.F., Ranasinghe, R. and Cowell, P.J. (2010) 'Sea Level Rise and Coastal Erosion', in Kim, Y.C. (ed.) *Handbook of Coastal and Ocean Engineering*, Singapore: World Scientific Publishing Co.

Stive, M.J.F., Roelvink, J.A. and De Vriend, H. (1990) 'Large scale coastal evolution concept', Proceedings of the 22nd International Conference on Coastal Engineering, New York, 1962-1974.

Taranowska, M. (1985) 'Wplyw dlugosci ostrogi na zmiany batymetryczne strefy brzegowej, "Effect of length of spurs on the coastal bathymetric changes"', *Inzynieria Morska*, vol. 1, (In Polish).

Teraguchi, H., Nakagawa, H., Muto, Y., Baba, Y. and Zhang, H. (2008) 'Flow and Sediment Transport around Impermeable or Permeable Groins', *Annual Journal of Hydraulic Engineering*, vol. 52, February, pp. 175-180.

Trampenau, T., Oumeraci, H. and Dette, H.H. (2004) 'Hydraulic functioning of permeable groins', *Journal of Coastal Research*, no. (SI) 33, pp. 160-187.

Trampenau, T., Oumeraci, H. and Dette, H.H. (2004) 'Hydraulic Functioning of Permeable Pile Groins', *Journal of Coastal Research*, no. (SI) 33, pp. 160-187.

UCAR (2012a) *Meteorology Education and Training: University Corporation for Atmospheric Research*, [Online], Available: http://www.meted.ucar.edu/marine/ripcurrents/NSF/navmenu.php?tab=1&page=2.3.1&type=text [15 May 2012].

Uijttewaal, W.S.J. (2005) 'Effects of Groyne Layout on the Flow in Groyne Fields:Laboratory Experiments', *Journal of Hydraulic Engineering*, vol. 131, no. 9, September, pp. 782-791.

van Rijn, L.C. (1984) 'Sediment Transport, Part 1: Bed Load Transport. ', *Journal of Hydraulic Engineering*, vol. 110, no. 10, pp. 1431-1456.

van Rijn, L.C. (2011) 'Coastal erosion and control', *Ocean & Coastal Management*, vol. 54, no. 12, pp. 867-887.

Vilsmeier, R. and Hanel, D. (1996) 'Adaptive solutions for unsteady laminar flows on unstructured grids', *International Journal for numerical methods in fluids*, vol. 22, no. 2, pp. 85-101.

Visser, R. (2002) *Morphological modelling in the vicinity of groynes*, Delft: TUDelft.

Walker, D.J., Dong, P. and Anastasiou, K. (1991) 'Sediment transport near Groynes in the Neashore Zone', *Journal of Coastal Research*, vol. 7, no. 4, pp. 1003-1011.

Warwick, R.A., Le Provost, C., Meier, M.F., oerlemans, J. and Woodworth, P.L. (1996) 'Changes in sea level', in Houghton, J.T., Meira Filho, L.G., Callander, B.A., Harris, N., Kattenberg, A. and Maskell, K. *Climate change 1995: The Science of climate change*, Cambridge: Cambridge University Press.

Weber, S.L. (1991) 'Eddy-viscosity and drag-law models for random ocean wave dissipation.', *Journal of Fluid Mechanics*, vol. 232, no. 1, pp. 73-98.

Weggel, R.J. (1972) 'Maximum breaker height', *Journal of Waterways, Harbors, and Coastal Engineering Division*, vol. 98, no. 4, pp. 529-548.

Wright, L.D. and Short, A.D. (1984) 'Morphodynamic variability of surf zones and beaches: a synthesis', *Marine Geology*, vol. 56, no. 1, pp. 93-118.

APPENDIX A

MIKE 21 – NUMERICAL MODELLING

A1. Spectral Wave Governing Equations

A1.1 Radiation stress

The basic principle behind the theory of radiation stresses (Longuet-Higgins and Stewart, 1962, 1963, 1964) is that waves exert a force on vertical surfaces; this provided a means to explain the set-up/set-down and the generation of currents due to the presence of waves. This force is due to the wave's innate nature to carry momentum and the rate of change of the momentum when a wave is reflected off a vertical surface, is what results in this force. In accordance with Longuet-Higgins and Stewart (1964) radiation stress, or wave thrust, was defined as the excess flow of momentum due to the presence of waves acting in the onshore offshore (xx), alongshore (yy) and oblique (xy) directions.

This radiation stress analysis established a relationship between the radiation stresses gradient for waves propagating towards a beach at an oblique angle and the resulting alongshore current.

S_{xx} is the principle radiation stress component that acts on a vertical plane that is perpendicular to the wave propagation direction. By integrating the momentum flux over the depth in a plane, perpendicular to the wave propagation direction, the radiation stress is defined as

$$S_{xx} = (2n - \frac{1}{2})E \qquad \text{(A1-1)}$$

Similarly S_{yy} is the principle radiation stress component that acts on a vertical plane that is parallel to the wave propagation direction. The radiation stress is defined as

$$S_{yy} = (2n - \frac{1}{2})E \qquad \text{(A1-2)}$$

The wave group velocity to wave celerity ratio (n) and the mean wave energy (E) variables from equation A1-1 and A1-2 are given by

$$n = \frac{1}{2}\left(1 + \frac{2kd}{\sinh(2kd)}\right) = \frac{c_g}{c} \qquad \text{(A1-3)}$$

- d is the water depth
- k is the wave number, $=2\pi/\lambda$, λ the wave length
- c_g the wave group celerity
- c the wave celerity

and

$$E = \frac{1}{8}(\rho g {H_{rms}}^2) \quad \text{(A1-4)}$$

- g is the gravitational acceleration
- H_{rms} is the RMS wave height
- ρ is the density of the fluid

Figure A1-1 shows the different tensors of radiation stress under conditions where waves propagate towards the coastline at an angle. The figure shows how the principle components that act in the direction of wave propagation are translated into shear stresses (S_{xy}) and normal stresses (S_{xx} and S_{yy}).

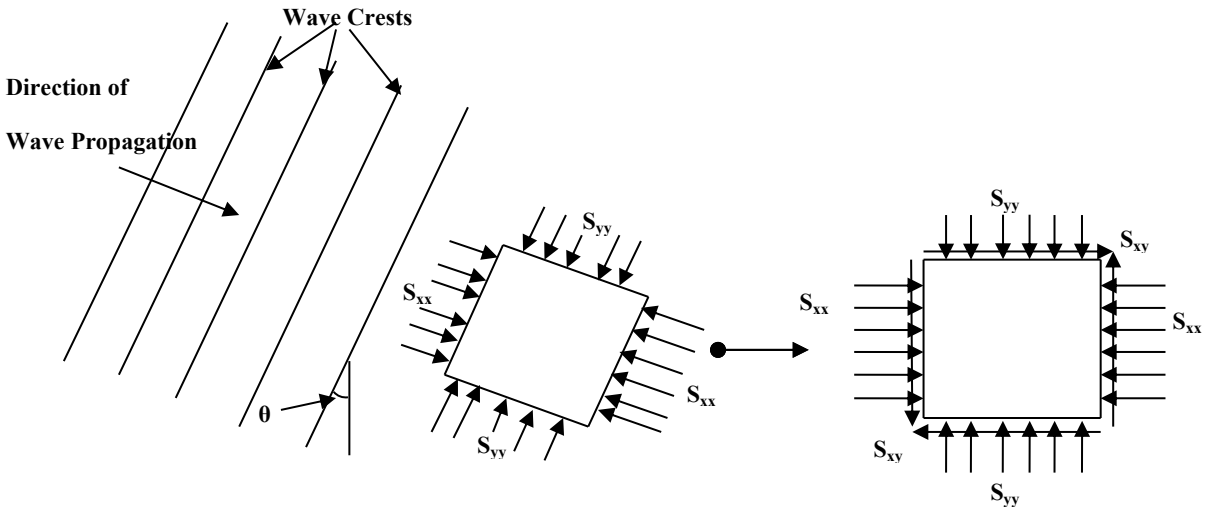

Figure A1-1: Translation description of radiation stresses (Nielsen and Apelt, 2003).

Using stress transformation techniques, the resultant transformed stresses that apply to a plane that is aligned to the principal direction at an angle θ are

$$S_{xx} = E(n\cos^2\theta + n - \frac{1}{2}) \quad \text{(A1-5)}$$

$$S_{yy} = E(n\sin^2\theta + n - \frac{1}{2}) \quad \text{(A1-6)}$$

$$S_{xy} = E(n \sin\theta \cos\theta) \quad \text{(A1-7)}$$

A1.1.1 Radiation stress induced forces

The above equations describe the action of wave radiation stresses on a vertical plane of water. It is the variations in these radiation stresses that result in a net force that acts in a specific direction, defined by the following wave force equations;

$$\tau_x = -\left(\frac{\partial S_{xx}}{\partial x} + \frac{\partial S_{xy}}{\partial y}\right) \quad \text{(A1-8)}$$

$$\tau_y = -\left(\frac{\partial S_{yy}}{\partial y} + \frac{\partial S_{xy}}{\partial x}\right) \quad \text{(A1-9)}$$

The changes in radiation normal stress ($\partial S_{xx}/\partial x$ and $\partial S_{yy}/\partial y$) are irrotational and will therefore induce the wave setup and set-down. The changes in the radiation shear stress ($\partial S_{xy}/\partial y$ and $\partial S_{xy}/\partial x$) are rotational and will therefore induce the currents. The wave setup and set-down cause water level variations which can induce lateral expansion currents or secondary currents; it can therefore be seen that the components all contribute to the development of currents.

The above equations are based on the water body's vertically integrated accelerations; this implies a solution in a two dimensional view (in plan). To determine the radiation stress calculations the wave conditions are used and the wave induced forces vary in accordance to the changes in the conditions of the waves.

A1.2 Bottom Friction

As discussed in section 2.2.1, the orbital motion of the wave begins to interact with the seabed as the water depth decreases the dissipation rate due to bottom friction interaction source term is given by

$$S_{bot}(f,\theta) = -\left(C_f + f_c\left(\bar{u}\cdot\bar{k}\right)/k\right)\frac{k}{\sinh(2kd)}E(f,\theta) \quad \text{(A1-10)}$$

where

- C_f is a drag coefficient, according to Komen et al., (1994) this value depends on the bed and flow conditions and can range typically between 0.001-0.01m/s.
- k is the wave number
- d is the water depth (m)

- f_c is the friction coefficient for the current, the default value in MIKE is 0, this corresponds to excluding the current effect on the bottom friction.
- u is the current velocity (m/s)

There are four different models for the determination of the dissipation coefficient. For all simulations the same model was used to standardize the modelling; a constant friction coefficient C_f.

A1.3 Wave Breaking

Depth-induced breaking occurs when waves propagate into very shallow water. The wave height can no longer be supported by the water depth as discussed in section 2.2.1.1. The formulation used is of wave breaking derived by Battjes and Janssen (1978). Following Eldeberky and Battjes (1996) the numerical modelling source term is written as:

$$S_{surf} = -\frac{2\alpha_{BJ} Q_b \bar{f}}{X} E(f,\theta) \qquad \text{(A1-11)}$$

where

- $\alpha_{BJ} \approx 1.0$, a calibration constant
- $\bar{f}$ is the mean frequency

X in equation A1-11 is the ratio of the total energy in the random wave train to the energy in a wave train with the maximum possible wave height and is given by

$$X = \frac{E_{tot}}{(H_m{}^2/8)} = \left(\frac{H_{rms}}{H_m}\right)^2 \qquad \text{(A1-12)}$$

where

- E_{tot} is the total wave energy
- H_m is the maximum wave height, it equals γd, where γ is the breaker parameter (Depending on the wave slope and wave parameters, γ varies from 0.5 to 1.0)
- H_{rms} is the root mean square wave height, it equals $\sqrt{8E_{tot}}$

Q_b is the fraction of breaking waves (Refer to equation 2-4 from Chapter 2 Literature Review) it is solved using Newton-Raphson iteration. The fraction is strongly dependant on the breaker index γ; the bathymetry is important with respect to this aspect of the solving.

A2. Flow Model Governing Equations

A2.1 Flow

The flow model is based on and solves the numerical solution of the two dimensional incompressible Reynolds averaged Navier-Stokes equations by using the assumptions of hydrostatic pressure and Boussinesq. The model consists thusly of, density, salinity, momentum, temperature and continuity equations and makes use of a turbulent closure scheme.

By assuming the vertical accelerations to be small compared to the gravitational equations, the vertical accelerations can be neglected; thus reducing the vertical momentum equation to that of the hydrostatic pressure equation. The main system equations therefore consist of:

- The continuity equation
- The horizontal equation of motion

Continuity equation;

$$\frac{\partial h}{\partial t} + \frac{\partial h\bar{u}}{\partial x} + \frac{\partial h\bar{v}}{\partial y} = hS \tag{A2-1}$$

x-component momentum for the horizontal equation of motion

$$\frac{\partial h\bar{u}}{\partial t} + \frac{\partial h\bar{u}^2}{\partial x} + \frac{\partial h\overline{vu}}{\partial y} = f\bar{v}h - gh\frac{\partial \eta}{\partial x} - \frac{h}{\rho_0}\frac{\partial p_a}{\partial x} - \frac{gh^2}{2\rho_0}\frac{\partial \rho}{\partial x} + \frac{\tau_{sx}}{\rho_0} - \frac{\tau_{bx}}{\rho_0} - \frac{1}{\rho_0}\left(\frac{\partial s_{xx}}{\partial x} + \frac{\partial s_{xy}}{\partial y}\right) + \frac{\partial}{\partial x}(hT_{xx}) + \frac{\partial}{\partial y}(hT_{xy}) + hu_sS \tag{A2-2}$$

y-component momentum for the horizontal equation of motion

$$\frac{\partial h\bar{v}}{\partial t} + \frac{\partial h\overline{uv}}{\partial x} + \frac{\partial h\bar{v}^2}{\partial y} = f\bar{u}h - gh\frac{\partial \eta}{\partial y} - \frac{h}{\rho_0}\frac{\partial p_a}{\partial y} - \frac{gh^2}{2\rho_0}\frac{\partial \rho}{\partial y} + \frac{\tau_{sy}}{\rho_0} - \frac{\tau_{by}}{\rho_0} - \frac{1}{\rho_0}\left(\frac{\partial s_{yx}}{\partial x} + \frac{\partial s_{yy}}{\partial y}\right) + \frac{\partial}{\partial x}(hT_{xy}) + \frac{\partial}{\partial y}(hT_{yy}) + hv_sS \tag{A2-3}$$

- h is the water depth in (m) for A2-1,A2-2 and A2-3

To determine the 2D shallow water equations, integration of the continuity equation (A2-1) and the momentum equations (A2-2; A2-3) are carried out over a depth h = η + d. For the 2D equations the velocities are depth averaged.

Below are the lateral stresses (including viscous friction, turbulent friction and differential advection), estimated using an eddy viscosity formulation that is based on the depth average velocity gradients;

$$T_{xx} = 2A\frac{\partial \bar{u}}{\partial x} \quad \text{(A2-4)}$$

$$T_{xy} = \left(\frac{\partial \bar{u}}{\partial y} + \frac{\partial \bar{v}}{\partial x}\right) \quad \text{(A2-5)}$$

$$T_{yy} = 2A\frac{\partial \bar{v}}{\partial y} \quad \text{(A2-6)}$$

- A is the sub-grid scale eddy viscosity, refer to section A2.2

A2.2 Horizontal eddy viscosity

For all simulations a constant eddy viscosity was used for the horizontal eddy viscosity. This made use of Smagorinsky (1963) expression of sub-grid scale transports by an effective eddy viscosity which is related to a characteristic length scale. This expression for the sub-grid scale eddy viscosity given by

$$A = {c_s}^2 l^2 \sqrt{2S_{ij}S_{ij}} \tag{A2-7}$$

where

- c_s is a constant
- l is the characteristic length relating to the eddy viscosity

The deformation rate is given by

$$S_{ij} = \frac{1}{2}\left(\frac{\partial u_i}{\partial x_j} + \frac{\partial u_j}{\partial x_i}\right) \quad (i,j = 1,2) \tag{A2-8}$$

A2.3 Bottom Stress

Bottom stress $\overrightarrow{\tau_b} = (\tau_{bx}, \tau_{by})$ is determined by the quadratic friction given by

$$\frac{\overrightarrow{\tau_b}}{\rho_0} = c_f \overrightarrow{u_b}|\overrightarrow{u_b}| \tag{A2-9}$$

where

- c_f is the dimensionless drag coefficient
- $\overrightarrow{u_b} = (u_b, v_b)$ is the flow velocity above the bottom of the sea bed

The friction velocity that is associated with the bottom stress is determined by

$$U_{\tau b} = \sqrt{c_f |u_b|^2} \tag{A2-10}$$

For the determination of the 2D calculations, the flow velocity above the bottom of the sea bed $\overrightarrow{u_b}$ is taken as a depth-averaged velocity. The drag coefficient C_f for all simulations was determined using the Manning number M (M is the reciprocal of Manning n) given by

$$C_f = \frac{g}{\left(Mh^{\frac{1}{6}}\right)^2} \quad \text{(A2-11)}$$

where

- g is gravitational acceleration (m/s^2)
- M is the Mannings number (m$^{1/3}$/s)
- h is the depth (m)

A2.4 Radiation Stress

For the simulations the spectral wave radiation stress outputs were included in the flow module. The radiation stresses are the driving force behind the mean flow and were used to calculate the wave induced flow in accordance with Longuet-Higgins and Stewart (1964) and Longuet-Higgins (1970).

A3. MIKE 21 Model Runs

A3.1 Part 1 – Comparison of Pattiaratchi Impermeable Groynes

Table A3-1-1: Model run impermeable groyne incident wave conditions (after Pattiaratchi et al., 2009)

Model Run	Wave height (H_s) (m)	Wave Direction (θ_m)	Wave period (T_p) (s)
1	1	45	14
2	1	45	8
3	1.5	45	14
4	1.5	45	8
5	2	60	8
6	2	45	8
7	2	30	8
8	2	10	8
9	2	60	10
10	2	45	10
11	2	30	10
12	2	10	10
13	2	60	14
14	2	45	14
15	2	30	14
16	2	10	14
17	2.5	45	14
18	2.5	45	8
19	3	45	14
20	3	45	8

A3.2 Part 2 – Impermeable Groynes

Table A3-2-1: Model run planar beach conditions

Model Run	Wave height (H_s) (m)	Wave Direction (θ_m)	Wave period (T_p) (s)	Datum shift (m)	Friction coefficient (m/s)
1	1	45	14	0	0.0077
2	2	10	14	0	0.0077
3	2	45	14	0	0.0077
4	2	60	14	0	0.0077
5	3	45	14	0	0.0077

Table A3-2-2: Model run impermeable groyne incident wave conditions & datum shift conditions

20m width x 200m length				
Model Run	Wave height (H_s) (m)	Wave Direction (θ_m)	Wave period (T_p) (s)	Datum shift (m)
1	1	45	14	0
2	1	45	14	-1
3	1	45	14	-0.75
4	1	45	14	-0.5
5	2	10	14	0
6	2	10	14	1
7	2	10	14	0.75
8	2	10	14	0.5
9	2	45	14	0
10	2	45	14	1
11	2	45	14	0.75
12	2	45	14	0.5
13	2	60	14	0
14	2	60	14	1
15	2	60	14	0.75
16	2	60	14	0.5
17	3	45	14	0
18	3	45	14	1
19	3	45	14	0.75
20	3	45	14	0.5

Table A3-2-3: Model run 200m impermeable groyne incident wave conditions & datum shift conditions

1m width x 200m length				
Model Run	Wave height (H_s) (m)	Wave Direction (θ_m)	Wave period (T_p) (s)	Datum shift (m)
1	1	45	14	0
2	1	45	14	-1
3	1	45	14	-0.75
4	1	45	14	-0.5
5	2	10	14	0
6	2	10	14	1
7	2	10	14	0.75
8	2	10	14	0.5
9	2	45	14	0
10	2	45	14	1
11	2	45	14	0.75
12	2	45	14	0.5
13	2	60	14	0
14	2	60	14	1
15	2	60	14	0.75
16	2	60	14	0.5
17	3	45	14	0
18	3	45	14	1
19	3	45	14	0.75
20	3	45	14	0.5

Table A3-2-4: Model run 100m impermeable groyne incident wave conditions & datum shift conditions

1m width x 100m length				
Model Run	Wave height (H_s) (m)	Wave Direction (θ_m)	Wave period (T_p) (s)	Datum shift (m)
1	1	45	14	0
2	1	45	14	-1
3	1	45	14	-0.75
4	1	45	14	-0.5
5	2	10	14	0
6	2	10	14	1
7	2	10	14	0.75
8	2	10	14	0.5
9	2	45	14	0
10	2	45	14	1
11	2	45	14	0.75
12	2	45	14	0.5
13	2	60	14	0
14	2	60	14	1
15	2	60	14	0.75
16	2	60	14	0.5
17	3	45	14	0
18	3	45	14	1
19	3	45	14	0.5

A3.3 Part 3 – Friction Manipulation

Table A3-3-1: Model run friction coefficient conditions

20m width x 200m length				
Model Run	Wave height (H_s) (m)	Wave Direction (θ_m)	Wave period (T_p) (s)	Friction coefficient (m/s)
1	1	45	14	1
2	1	45	14	10
3	1	45	14	20
4	1	45	14	40
5	1	45	14	100
6	1.25	45	14	20
7	1.5	45	14	20
8	2	10	14	1
9	2	10	14	10
10	2	10	14	20
11	2	45	14	1
12	2	45	14	10
13	2	45	14	20
14	3	45	14	1
15	3	45	14	10
16	3	45	14	20

Table A3-3-2: Model run datum shift & friction coefficient conditions

20m width x 200m length					
Model Run	Wave height (H_s) (m)	Wave Direction (θ_m)	Wave period (T_p) (s)	Friction coefficient (m/s)	Datum shift (m)
1	1	45	14	1	-1
2	1	45	14	10	-1
3	1	45	14	20	-1
4	2	10	14	1	1
5	2	10	14	10	1
6	2	10	14	20	1
7	2	45	14	1	1
8	2	45	14	10	1
9	2	45	14	20	1
10	3	45	14	1	1
11	3	45	14	10	1
12	3	45	14	20	1

Table A3-3-3: Model run friction coefficient multiplied by varied depth conditions

20m width x 200m length				
Model Run	Wave height (H_s) (m)	Wave Direction (θ_m)	Wave period (T_p) (s)	Friction coefficient (m/s)
1	1	45	14	1
2	1	45	14	10
3	1	45	14	20
4	2	10	14	1
5	2	10	14	10
6	2	10	14	20
7	2	45	14	1
8	2	45	14	10
9	2	45	14	20
10	3	45	14	1
11	3	45	14	10
12	3	45	14	20
1m width x 200m length				
13	2	45	14	1

NB: Depth change

For the Impermeable groyne sections and the friction manipulation sections only the model runs with 1m significant wave heights had negative datum shifts, the reasoning behind this is that the 1m significant model run at 0 MSL had a breaker zone predominantly within the groyne length, therefore to assess what would happen when the water level drops on a tidal low negative datum shifts were required. Similarly the 2m and 3m significant wave heights had a positive datum shift as their breaker zones exceeded the groyne length; this was done to assess what would happen during water level increases on tidal highs.

A3.4 Part 4 – Permeable Pile Groynes

Table A3-4-1: Model run 200m permeable pile conditions

1m width x 200m length						
Model Run	Wave height (H_s) (m)	Wave Direction (θ_m)	Wave period (T_p) (s)	Piles	Pile Spacing (m)	Permeability (%)
1	1	45	14	152	2.3	70.32
2	1	45	14	250	1.0	50.13
3	1	45	14	333	0.5	33.33
4	2	45	14	152	2.3	70.32
5	2	45	14	250	1.0	50.13
6	2	45	14	333	0.5	33.33
7	2	60	14	152	2.3	70.32
8	2	60	14	250	1.0	50.13
9	3	45	14	152	0.5	70.32
10	3	45	14	250	1.0	50.13

Table A3-4-2: Model run 100m permeable pile conditions

1m width x 100m length						
Model Run	Wave height (H_s) (m)	Wave Direction (θ_m)	Wave period (T_p) (s)	Piles	Pile Spacing (m)	Permeability (%)
1	1	45	14	122	2.3	70.94
2	1	45	14	200	1.0	50.25
3	1	45	14	267	0.5	33.33
4	2	45	14	122	2.3	70.94
5	2	45	14	200	1.0	50.25
6	2	45	14	267	0.5	33.33
7	2	60	14	122	2.3	70.94
8	2	60	14	200	1.0	50.25
9	2	60	14	267	0.5	33.33
10	3	45	14	122	2.3	70.94
11	3	45	14	200	1.0	50.25
12	3	45	14	267	0.5	33.33

APPENDIX B

CURRENT METERS & ADCP

B1. Current Meter Analysis

Table B1-1: Current meter calibration data

Prop	Counts			Count Average	Error			Count/ metre	Count/ Rotation	Rotations/metre	Pitch (cm/rotation)
	Slow	Medium	Fast		Slow	Medium	Fast				
1	295	304	314	304.33	3.07	0.11	3.18	15.22	4	3.80	26.29
2	290	296	327	304.33	4.71	2.74	7.45	15.22	4	3.80	26.29
3	311	318	327	318.67	2.41	0.21	2.62	15.93	4	3.98	25.10
4	492	522	524	512.67	4.03	1.82	2.21	25.63	4	4.01	24.97
4 test 2	320	322	328	323.33	1.03	0.41	1.44	16.17	4	4.04	24.74
5	405	409	438	417.33	2.96	2.00	4.95	20.87	4	3.73	26.84
5 test 2	308	318	328	318.00	3.14	0.00	3.14	15.90	4	3.98	25.16

The average count per metre for all propellers is: 17.85

The test for propeller 4 and 5 were carried out twice due to the abnormally high values recorded for their initial tests.

B2. Current Rose Plots

The current meters that were lost do not have current roses; 5, 21, 23.

B2.1 Current meters 1 second intervals

(All legend series units, m/s)

For the current meters where the propellers were lost, only the current directions could be displayed. This could only be done for the raw data sets; not for the 10 minute averaging of section A2.2.

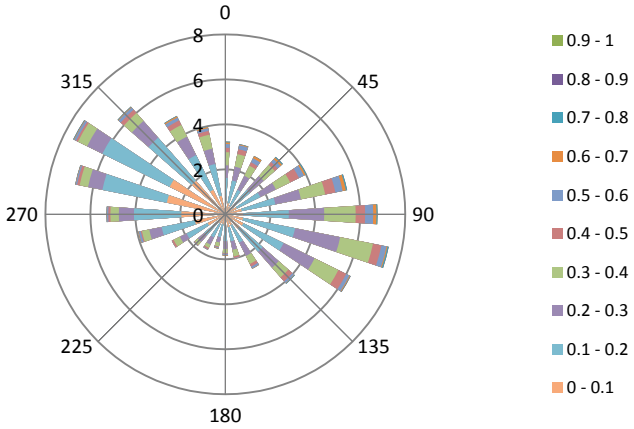

Figure B2-1: Current rose (m/s) for current meter no.1

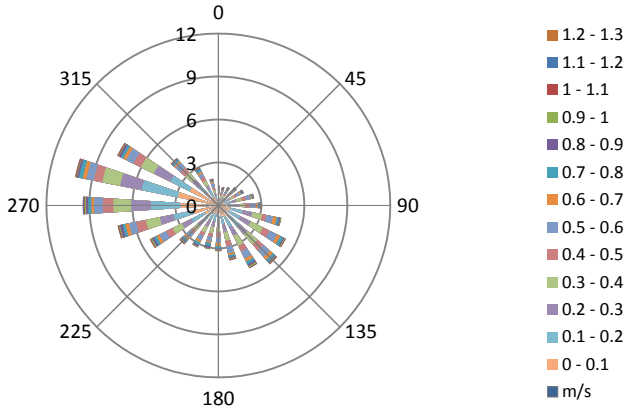

Figure B2-2: Current rose (m/s) for current meter no.2

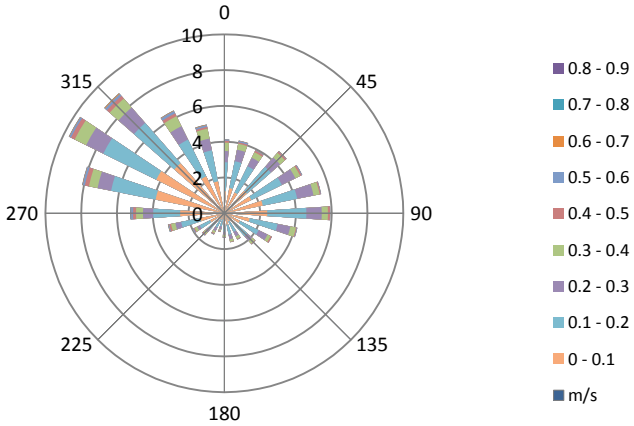

Figure B2-3: Current rose (m/s) for current meter no.3

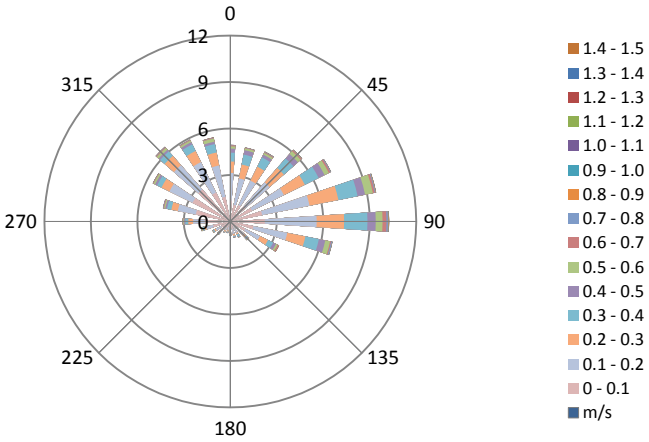

Figure B2-4: Current rose (m/s) for current meter no.4

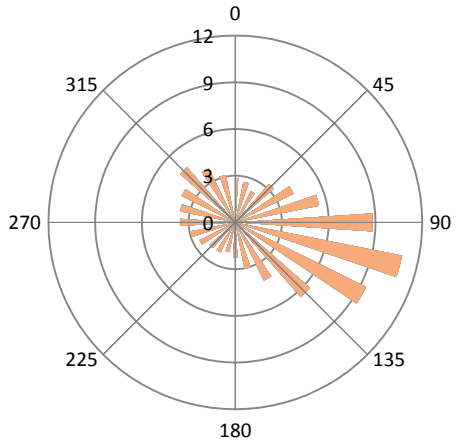

Figure B2-5: Current rose (Direction only) for current meter no.6

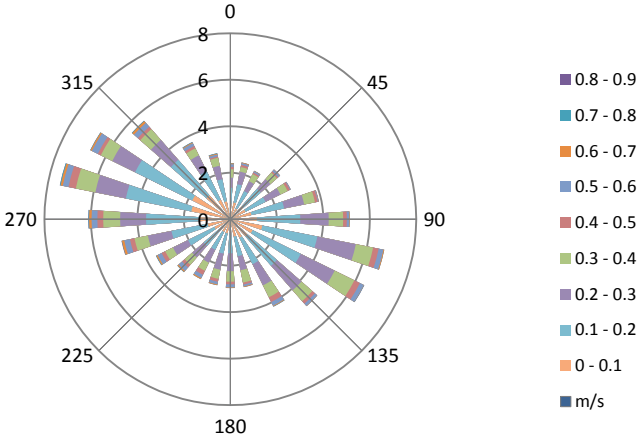

Figure B2-6: Current rose (m/s) for current meter no.7

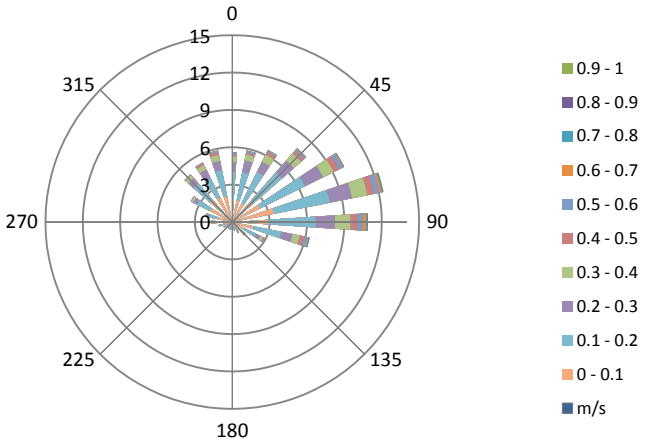

Figure B2-7: Current rose (m/s) for current meter no.8

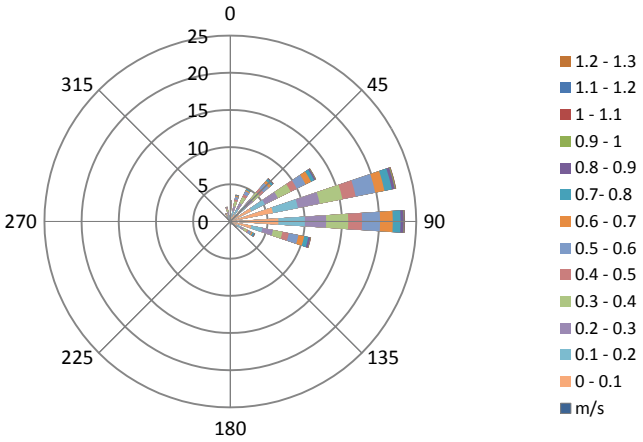

Figure B2-8: Current rose (m/s) for current meter no.9

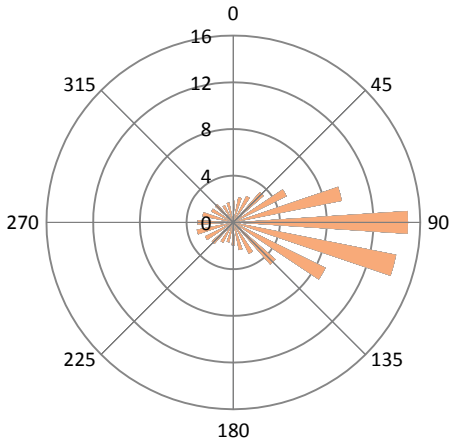

Figure B2-9: Current rose (Direction only) for current meter no.10

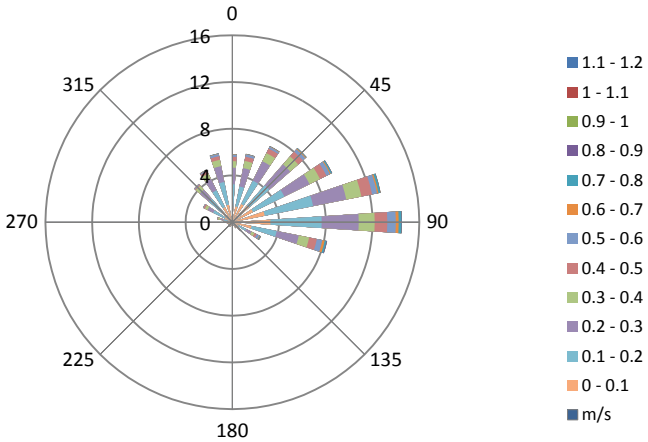

Figure B2-10: Current rose (m/s) for current meter no.11

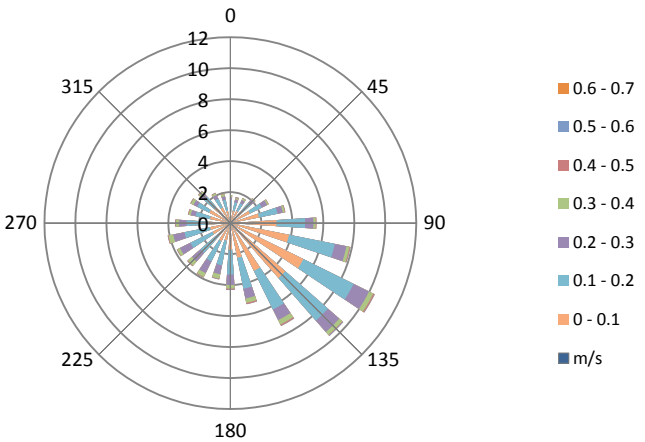

Figure B2-11: Current rose (m/s) for current meter no.12

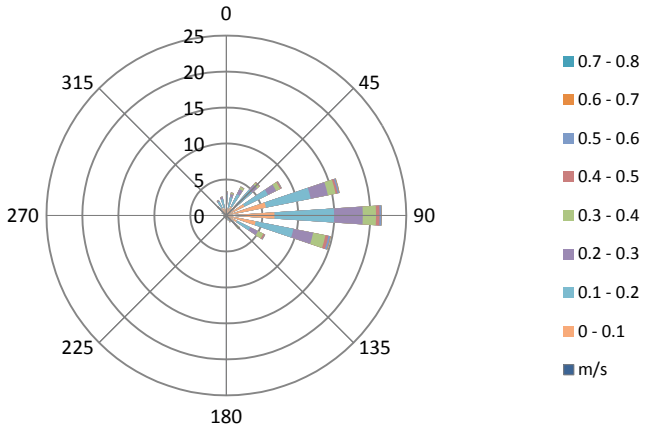

Figure B2-12: Current rose (m/s) for current meter no.13

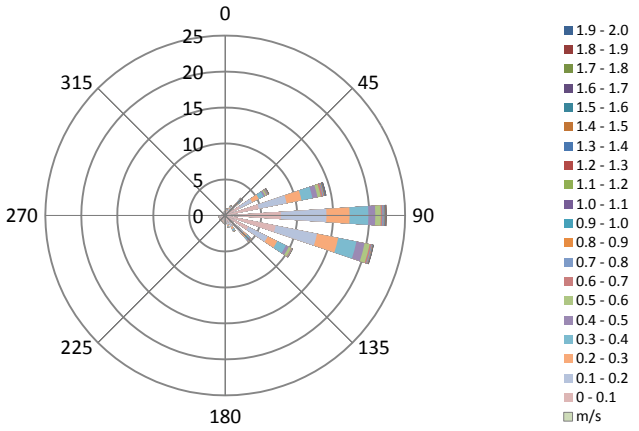

Figure B2-13: Current rose (m/s) for current meter no.14

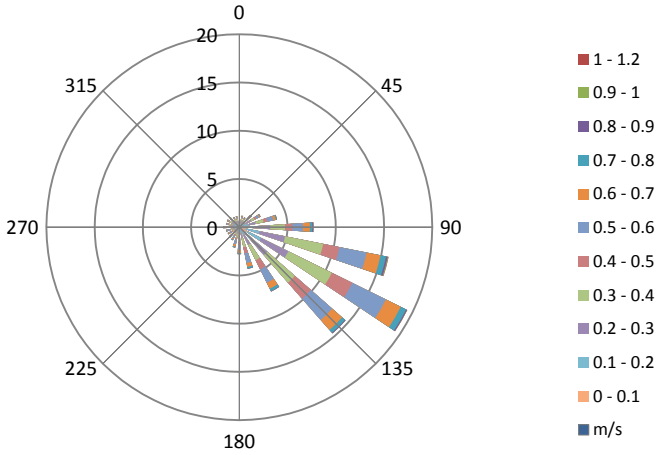

Figure B2-14: Current rose (m/s) for current meter no.15

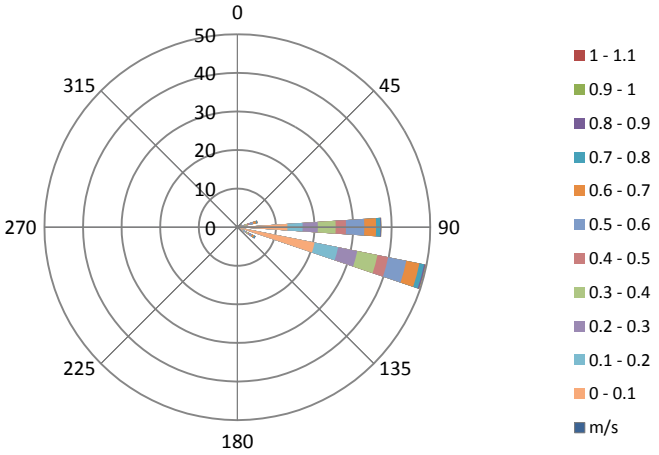

Figure B2-15: Current rose (m/s) for current meter no.16

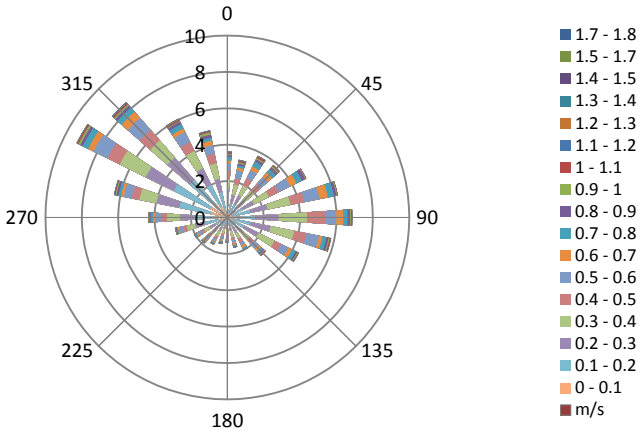

Figure B2-16: Current rose (m/s) for current meter no.17

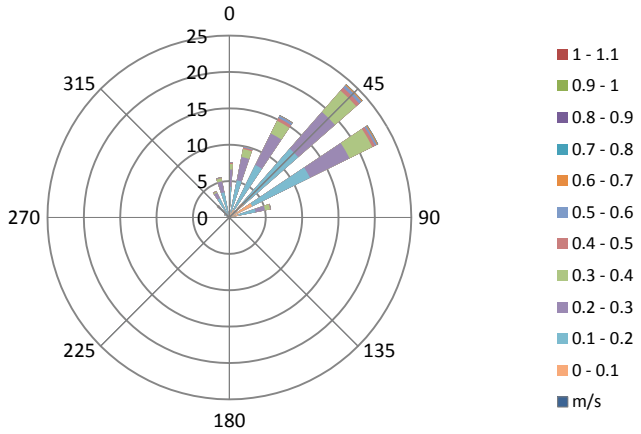

Figure B2-17: Current rose (m/s) for current meter no.18

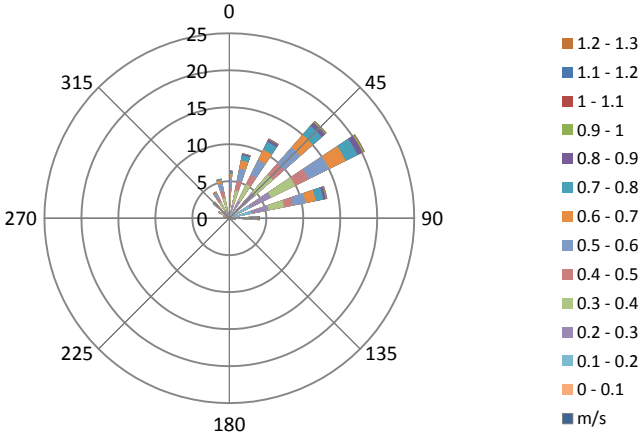

Figure B2-18: Current rose (m/s) for current meter no.19

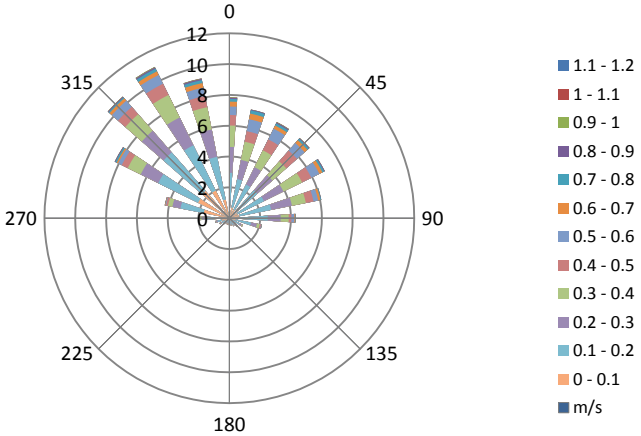

Figure B2-19: Current rose (m/s) for current meter no.20

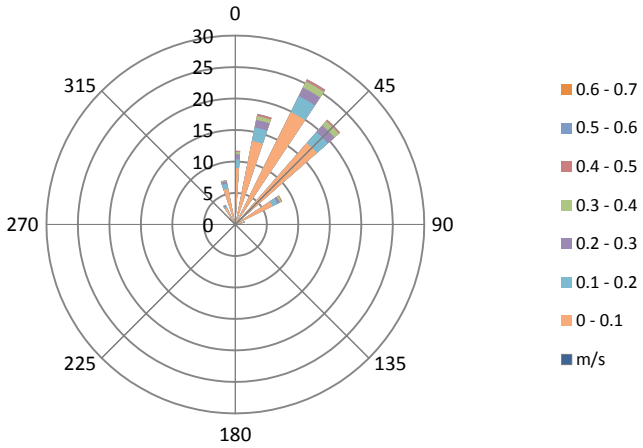

Figure B2-20: Current rose (m/s) for current meter no.22

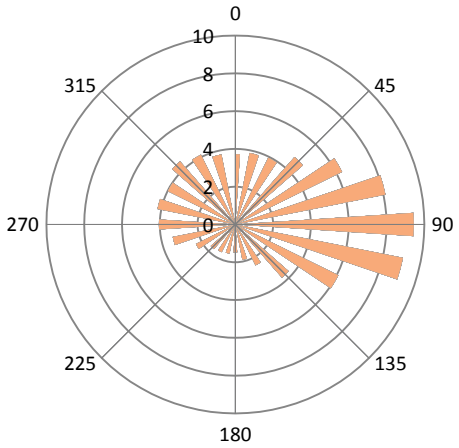

Figure B2-21: Current rose (Direction only) for current meter no.24

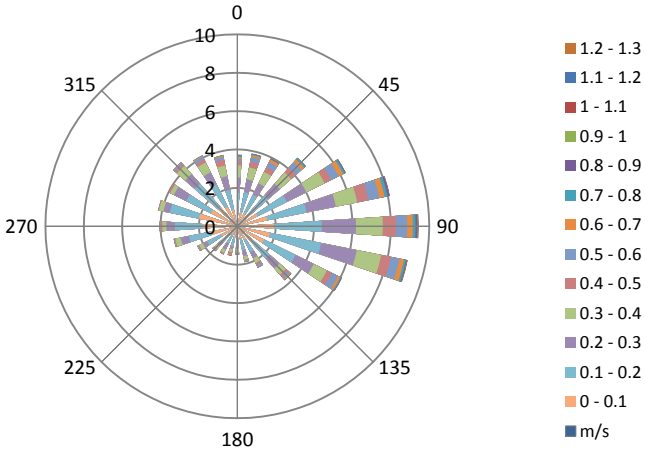

Figure B2-22: Current rose (m/s) for current meter no.25

B2.2 Current meters 10 minute averaging

(All legend series units, m/s)

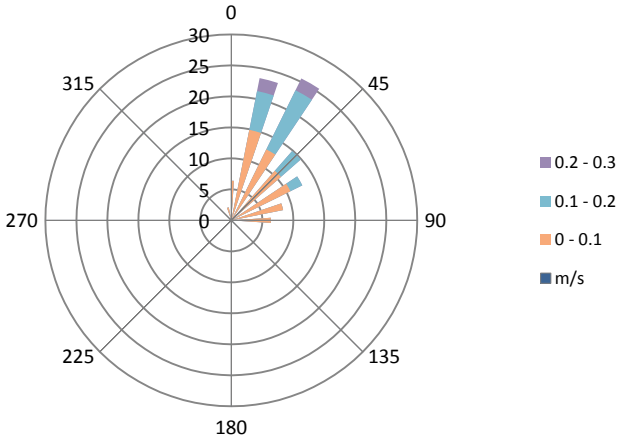

Figure B2-23: Current rose (m/s) for current meter no.1

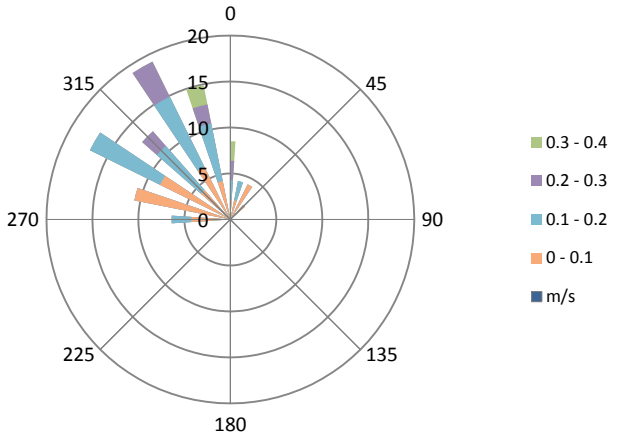

Figure B2-24: Current rose (m/s) for current meter no.2

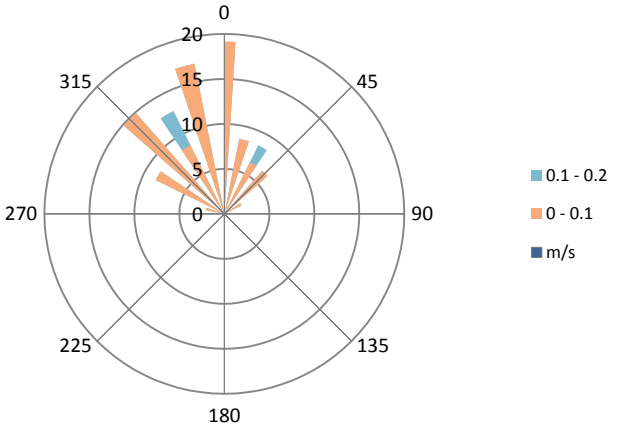

Figure B2-25: Current rose (m/s) for current meter no.3

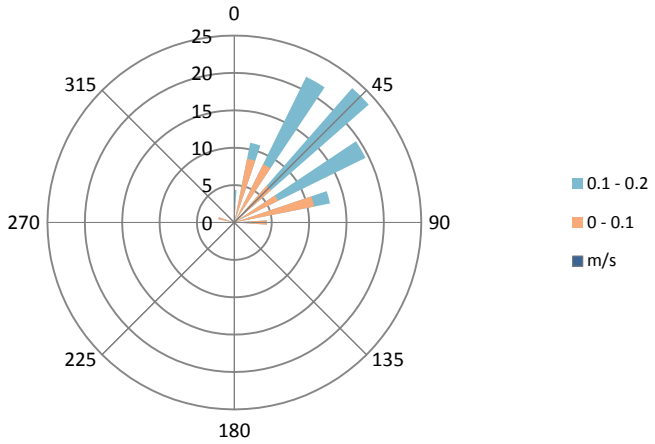

Figure B2-26: Current rose (m/s) for current meter no.4

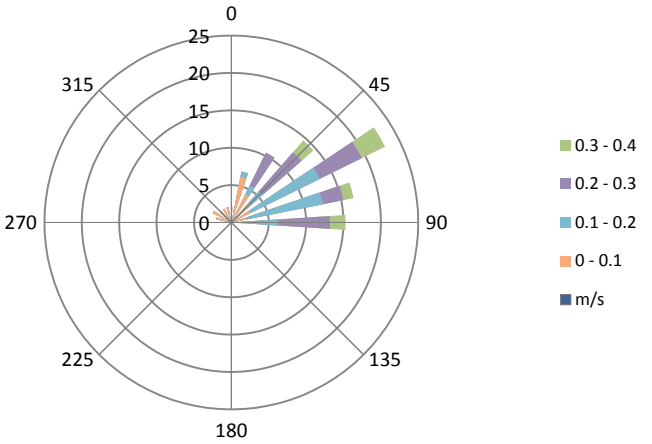

Figure B2-27: Current rose (m/s) for ADCP at current meter no.6 location

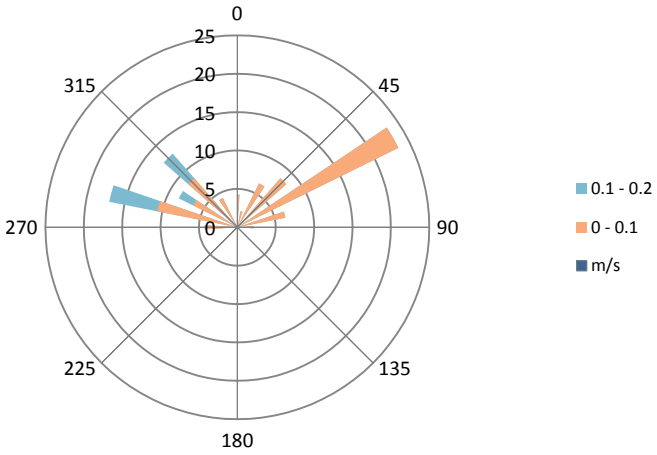

Figure B2-28: Current rose (m/s) for current meter no.7

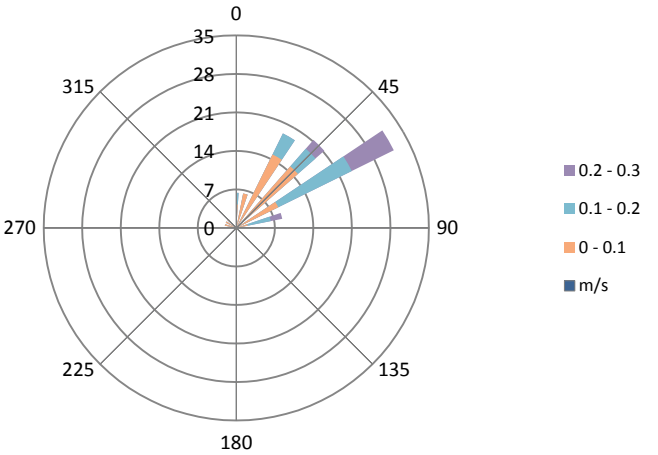

Figure B2-29: Current rose (m/s) for current meter no.8

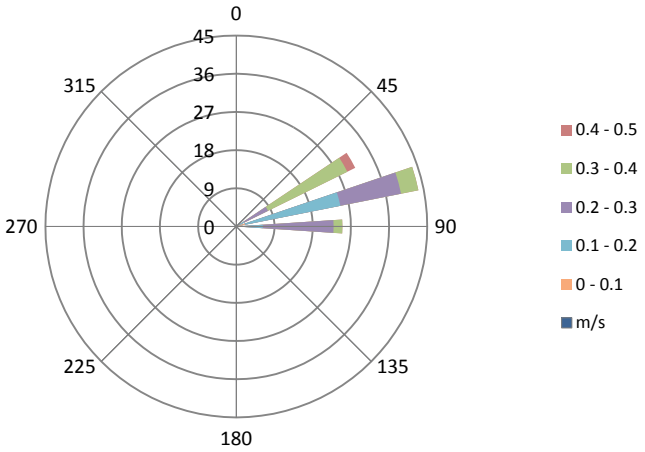

Figure B2-30: Current rose (m/s) for current meter no.9

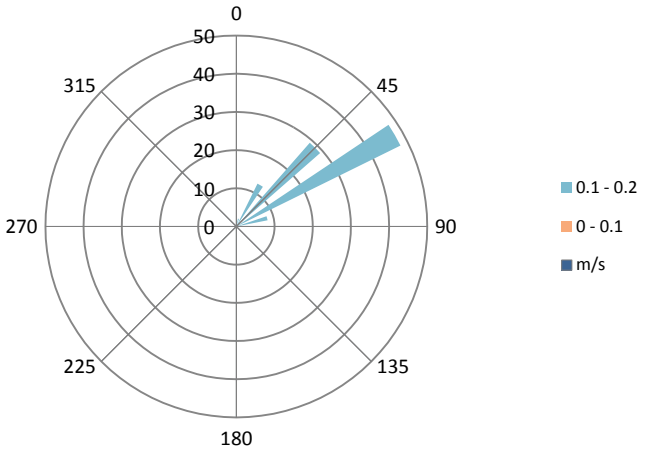

Figure B2-31: Current rose (m/s) for current meter no.11

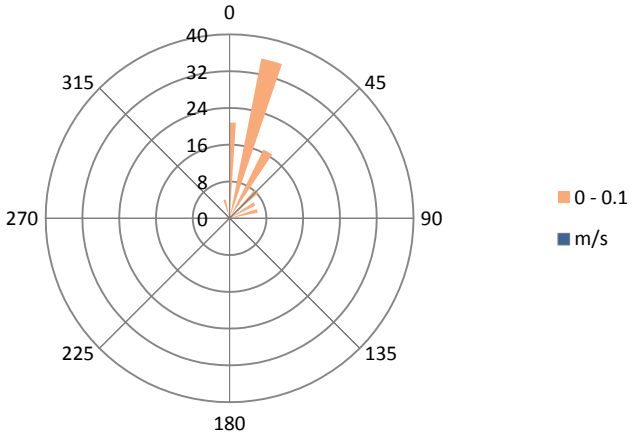

Figure B2-32: Current rose (m/s) for current meter no.12

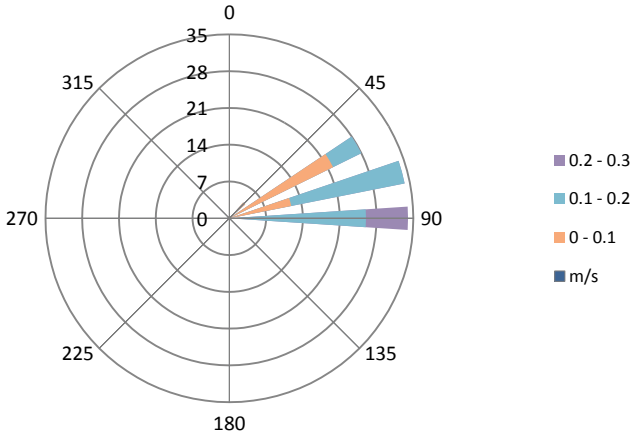

Figure B2-33: Current rose (m/s) for current meter no.13

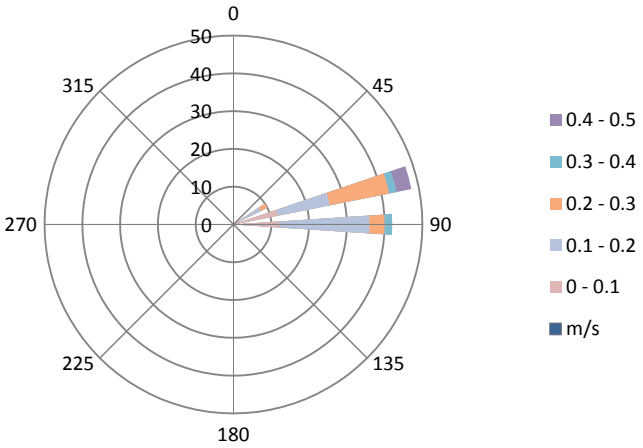

Figure B2-34: Current rose (m/s) for current meter no.14

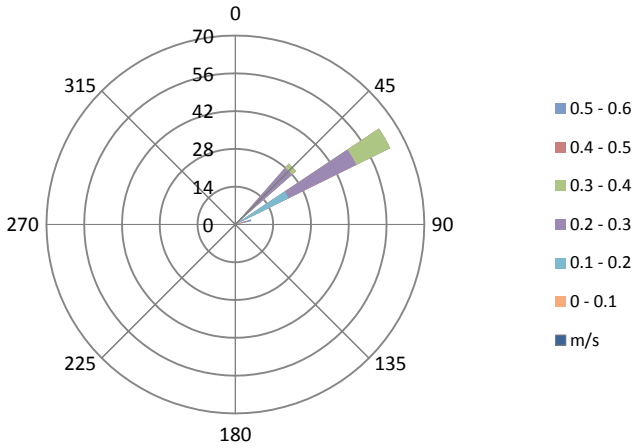

Figure B2-35: Current rose (m/s) for current meter no.15

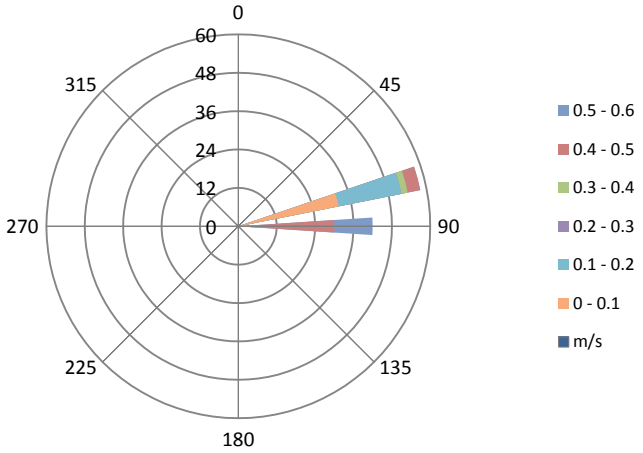

Figure B2-36: Current rose (m/s) for current meter no.16

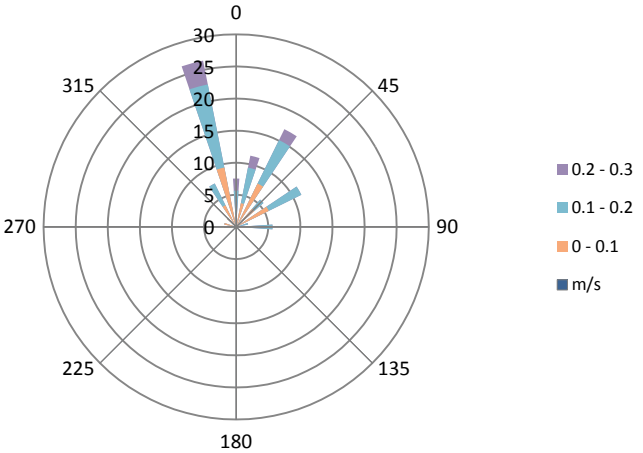

Figure B2-37: Current rose (m/s) for current meter no.17

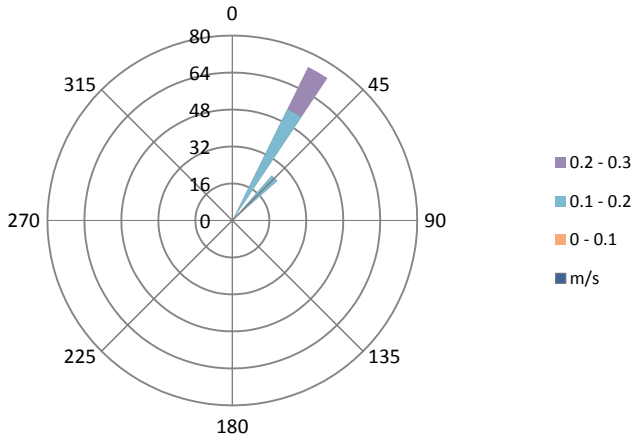

Figure B2-38: Current rose (m/s) for current meter no.18

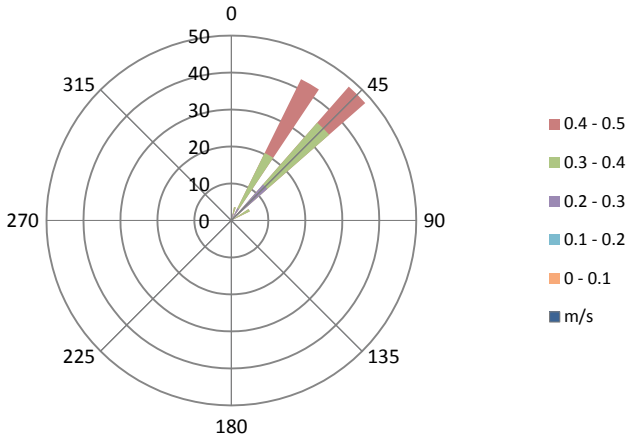

Figure B2-39: Current rose (m/s) for current meter no.19

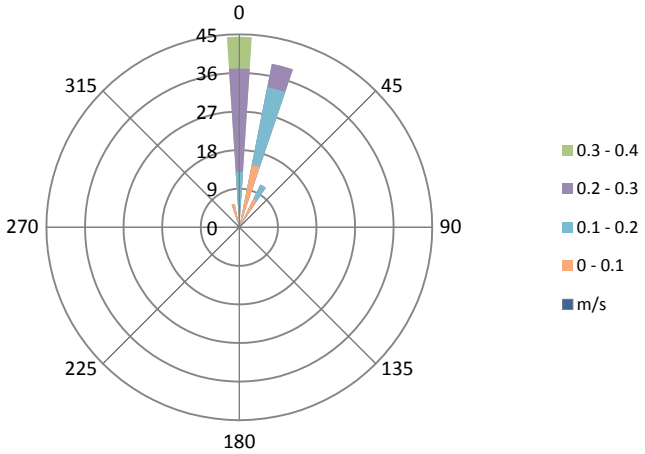

Figure B2-40: Current rose (m/s) for current meter no.20

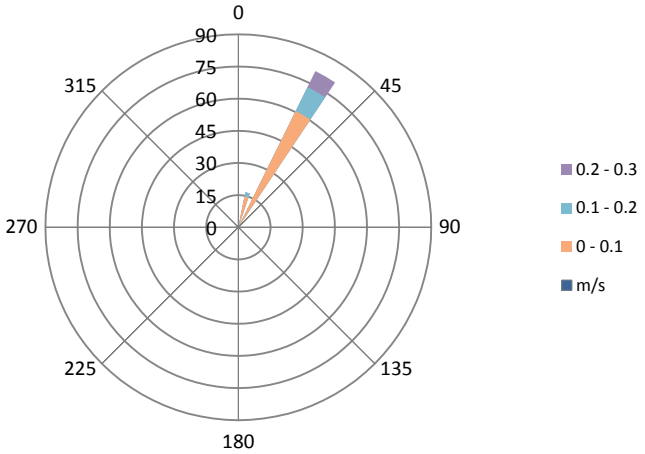

Figure B2-41: Current rose (m/s) for current meter no.22

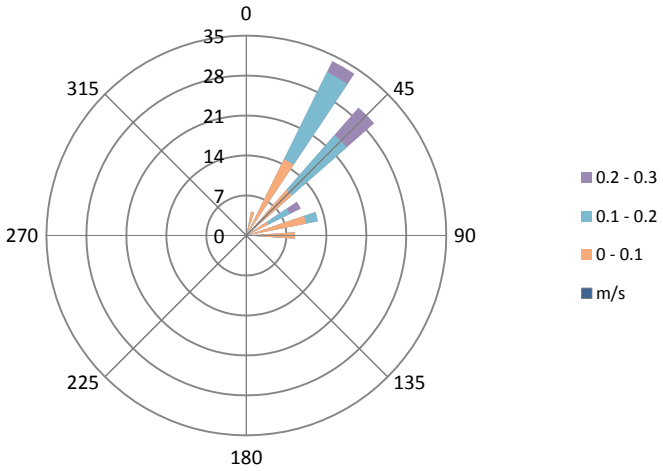

Figure B2-42: Current rose (m/s) for current meter no.25

APPENDIX C

Pattiarachi Comparison

C1. Model Run Results

Table C1-1: Summary of Pattiaratchi Results vs. Study Results

	Model Run	Wave height (H_s) (m)	Wave Direction (θ_m)	Wave period (T_p) (s)	Maximum rip current speed in lee of groyne (m/s)	Divergence location (m)
Pattiaratchi	1	1	45	14	0.44	140
Compared	1	1	45	14	0.33	135
Pattiaratchi	2	1	45	8	0.29	-
Compared	2	1	45	8	0.27	135
Pattiaratchi	3	1.5	45	14	0.59	-
Compared	3	1.5	45	14	0.53	188
Pattiaratchi	4	1.5	45	8	0.42	-
Compared	4	1.5	45	8	0.43	160
Pattiaratchi	5	2	60	8	0.63	-
Compared	5	2	60	8	0.48	244
Pattiaratchi	6	2	45	8	0.58	-
Compared	6	2	45	8	0.55	240
Pattiaratchi	7	2	30	8	0.5	-
Compared	7	2	30	8	0.55	195
Pattiaratchi	8	2	10	8	0.39	-
Compared	8	2	10	8	0.46	170
Pattiaratchi	9	2	60	10	0.72	-
Compared	9	2	60	10	0.54	238
Pattiaratchi	10	2	45	10	0.64	-
Compared	10	2	45	10	0.61	190
Pattiaratchi	11	2	30	10	0.56	-
Compared	11	2	30	10	0.61	180
Pattiaratchi	12	2	10	10	0.43	-
Compared	12	2	10	10	0.5	166
Pattiaratchi	13	2	60	14	0.83	-
Compared	13	2	60	14	0.59	236
Pattiaratchi	14	2	45	14	0.74	140
Compared	14	2	45	14	0.66	230
Pattiaratchi	15	2	30	14	0.67	-
Compared	15	2	30	14	0.66	204
Pattiaratchi	16	2	10	14	0.47	140
Compared	16	2	10	14	0.56	174
Pattiaratchi	17	2.5	45	14	0.86	-
Compared	17	2.5	45	14	0.83	230
Pattiaratchi	18	2.5	45	8	0.75	-
Compared	18	2.5	45	8	0.7	230
Pattiaratchi	19	3	45	14	1.01	160
Compared	19	3	45	14	0.93	370
Pattiaratchi	20	3	45	8	0.8	-
Compared	20	3	45	8	0.76	370

APPENDIX D

IMPERMEABLE GROYNES

D1. Model Run Results

Table D1-1: Level of constriction of cross-shore flow for depth changes for 20m x 200m groyne

20m width x 200m length											
Model Run	Wave height (H_s) (m)	Wave Direction (θ_m)	Wave period (T_p) (s)	Datum shift (m)	G_L (m) [In water]	B_z (m)	G_L/B_z	Lee side		Upstream side	
								Rip current (m/s)	Distance from shore (m)	Rip current (m/s)	Distance from shore (m)
1	1	45	14	0.00	220	191	1.152	0.433	130	0.502	175
2	1	45	14	-1.00	170	198	0.856	0.461	125	0.473	136
3	1	45	14	-0.75	170	157	1.086	0.434	122	0.482	136
4	1	45	14	-0.50	180	164	1.101	0.424	103	0.487	145
5	2	10	14	0.00	224	206	1.088	0.496	130	0.597	174
6	2	10	14	1.00	270	198	1.364	0.501	130	0.571	181
7	2	10	14	0.75	236	174	1.356	0.48	95	0.620	150
8	2	10	14	0.50	234	202	1.158	0.507	86	0.597	180
9	2	45	14	0.00	224	316	0.709	0.705	184	0.802	209
10	2	45	14	1.00	270	308	0.877	0.690	182	0.813	258
11	2	45	14	0.75	236	300	0.787	0.654	145	0.818	224
12	2	45	14	0.50	233	305	0.764	0.670	175	0.829	209
13	2	60	14	0.00	223	350	0.637	0.729	186	0.775	209
14	2	60	14	1.00	269.7	340	0.794	0.706	225	0.804	259
15	2	60	14	0.75	235.9	315	0.749	0.685	194	0.812	224
16	2	60	14	0.50	235.7	326	0.724	0.696	197	0.805	224
17	3	45	14	0.00	223	451	0.494	0.946	186	0.876	210
18	3	45	14	1.00	270	447	0.604	0.977	234	1.000	259
19	3	45	14	0.75	270	456	0.592	0.988	236	0.982	260
20	3	45	14	0.50	236	437	0.541	0.988	200	0.950	200

Table D1-2: Level of constriction of cross-shore flow for depth changes for 1m x 200m groyne

1m width x 200m length											
Model Run	Wave height (H_s) (m)	Wave Direction (θ_m)	Wave period (T_p) (s)	Datum shift (m)	G_L (m) [In water]	B_z (m)	G_L/B_z	Lee side		Upstream side	
								Rip current (m/s)	Distance from shore (m)	Rip current (m/s)	Distance from shore (m)
1	1	45	14	0.00	223	200	1.117	0.502	90	0.511	175
2	1	45	14	-1.00	178	200	0.890	0.441	114	0.537	142
3	1	45	14	-0.75	178	177	1.003	0.460	85	0.550	137
4	1	45	14	-0.50	187	176	1.065	0.481	89	0.531	144
5	2	10	14	0.00	223	212	1.053	0.515	127	0.595	185
6	2	10	14	1.00	270	201	1.346	0.519	131	0.589	178
7	2	10	14	0.75	236	190	1.241	0.521	91	0.535	139
8	2	10	14	0.50	236	213	1.109	0.532	91	0.562	186
9	2	45	14	0.00	223	311	0.717	0.840	194	0.947	214
10	2	45	14	1.00	270	310	0.872	0.809	178	0.918	264
11	2	45	14	0.75	236	297	0.796	0.803	149	0.946	234
12	2	45	14	0.50	236	310	0.760	0.805	204	0.944	234
13	2	60	14	0.00	223	348	0.641	0.887	185	0.945	214
14	2	60	14	1.00	270	341	0.792	0.850	179	0.880	265
15	2	60	14	0.75	236	314	0.752	0.859	205	0.906	234
16	2	60	14	0.50	236	321	0.735	0.856	204	0.961	236
17	3	45	14	0.00	223	459	0.485	1.130	185	1.068	214
18	3	45	14	1.00	270	447	0.604	1.150	235	1.105	264
19	3	45	14	0.75	270	453	0.596	1.178	235	1.104	267
20	3	45	14	0.50	236	428	0.552	1.156	205	1.112	236

Table D1-3: Level of constriction of cross-shore flow for depth changes for 1m x 100m groyne

1m width x 100m length											
Model Run	Wave height (H_s) (m)	Wave Direction (θ_m)	Wave period (T_p) (s)	Datum shift (m)	G_L (m) [In water]	B_z (m)	G_L/B_z	Lee side		Upstream side	
								Rip current (m/s)	Distance from shore (m)	Rip current (m/s)	Distance from shore (m)
1	1	45	14	0.00	120	191	0.630	0.515	88	0.522	116
2	1	45	14	-1.00	72	192	0.375	0.190	58	0.317	71
3	1	45	14	-0.75	72	162	0.444	0.401	42	0.424	71
4	1	45	14	-0.50	86	172	0.500	0.462	53	0.482	81
5	2	10	14	0.00	120	204	0.587	0.580	93	0.586	121
6	2	10	14	1.00	168	207	0.810	0.590	131	0.666	165
7	2	10	14	0.75	136	182	0.748	0.605	106	0.657	135
8	2	10	14	0.50	136	209	0.650	0.625	103	0.643	130
9	2	45	14	0.00	120	305	0.394	0.673	88	0.639	116
10	2	45	14	1.00	168	303	0.555	0.932	137	0.846	165
11	2	45	14	0.75	136	298	0.456	0.884	102	0.805	130
12	2	45	14	0.50	136	309	0.440	0.834	102	0.763	130
13	2	60	14	0.00	120	344	0.349	0.676	88	0.652	116
14	2	60	14	1.00	168	339	0.495	0.944	138	0.870	166
15	2	60	14	0.75	136	313	0.435	0.863	103	0.782	103
16	2	60	14	0.50	136	326	0.417	0.835	103	0.794	130
17	3	45	14	0.00	120	455	0.264	0.691	88	0.655	116
18	3	45	14	1.00	168	445	0.378	0.969	138	0.876	166
19	3	45	14	0.75	136	440	0.309	0.854	103	0.764	130

APPENDIX E

PERMEABLE GROYNES

E1. Model Run Results

Table E1-1: Model run permeable pile conditions for 1m x 200m groyne

1m width x 200m length											
Model Run	Wave height (H_s) (m)	Wave Direction (θ_m)	Wave period (T_p) (s)	Permeability (%)	G_L (m)	B_z (m)	G_L/B_z	Lee side		Upstream side	
								Rip current (m/s)	Distance from shore (m)	Rip current (m/s)	Distance from shore (m)
1	1	45	14	70.32	225	198	1.138	0.245	45	0.242	45
2	1	45	14	50.13	225	198	1.138	0.196	45	0.413	115
3	1	45	14	33.33	225	198	1.138	0.211	42	0.533	90
4	2	45	14	70.32	225	313	0.718	0.292	45	0.265	45
5	2	45	14	50.13	225	313	0.718	0.243	45	0.480	175
6	2	45	14	33.33	225	313	0.718	0.270	47	0.548	180
7	2	60	14	70.32	225	347	0.648	0.260	47	0.340	155
8	2	60	14	50.13	225	347	0.648	0.275	48	0.565	99
9	3	45	14	70.32	225	462	0.487	0.234	45	0.269	185
10	3	45	14	50.13	225	462	0.487	0.270	45	0.450	155

Table E1-2: Model run permeable pile conditions for 1m x 100m groyne

1m width x 200m length											
Model Run	Wave height (H_s) (m)	Wave Direction (θ_m)	Wave period (T_p) (s)	Permeability (%)	G_L (m)	B_z (m)	G_L/B_z	Lee side		Upstream side	
								Rip current (m/s)	Distance from shore (m)	Rip current (m/s)	Distance from shore (m)
1	1	45	14	70.94	125	198	0.633	0.254	45	0.264	45
2	1	45	14	50.25	125	198	0.633	0.265	46	0.298	48
3	1	45	14	33.33	125	198	0.633	0.231	48	0.422	48
4	2	45	14	70.94	125	313	0.399	0.204	45	0.245	50
5	2	45	14	50.25	125	313	0.399	0.177	45	0.290	95
6	2	45	14	33.33	125	313	0.399	0.153	49	0.459	50
7	2	60	14	70.94	125	347	0.360	0.223	48	0.345	45
8	2	60	14	50.25	125	347	0.360	0.184	47	0.263	98
9	2	60	14	33.33	125	347	0.360	0.187	49	0.451	47
10	3	45	14	70.94	125	463	0.270	0.191	46	0.280	50
11	3	45	14	50.25	125	463	0.270	0.193	45	0.315	100
12	3	45	14	33.33	125	463	0.270	0.239	45	0.530	50

APPENDIX F

SEDIMENT GRADING AND SEDIMENT TRANSPORT ANALYSIS

F1. Sieve Analysis

Table F1-1: Sieve Analysis of Section 1 – South Side Shore

Sieve (mm)	Retained (g)	Total (g)	Cumulative (g)	Retained (%)	Passing (%)
4.750	1.4	1.4	1.4	0.27%	99.73%
2.000	4.7	4.7	6.1	1.17%	98.83%
1.400	1.0	1.0	7.1	1.37%	98.63%
1.180	0.4	0.4	7.5	1.44%	98.56%
0.600	5.6	5.6	13.1	2.52%	97.48%
0.425	36.4	36.4	49.5	9.53%	90.47%
0.300	152.0	152.0	201.5	38.78%	61.22%
0.150	312.2	312.2	513.7	98.86%	1.14%
0.075	5.9	5.9	519.6	100.00%	0.00%
pan	0.0	0.0	519.6	100.00%	0.00%
	Total	519.6			

Table F1-2: Summary of Sieve Analysis Section 1 – South Side Shore

D10	D30	D50	D60	D90	Cu	Cc	Grade
0.160	0.210	0.260	0.300	0.420	1.875	0.919	SP

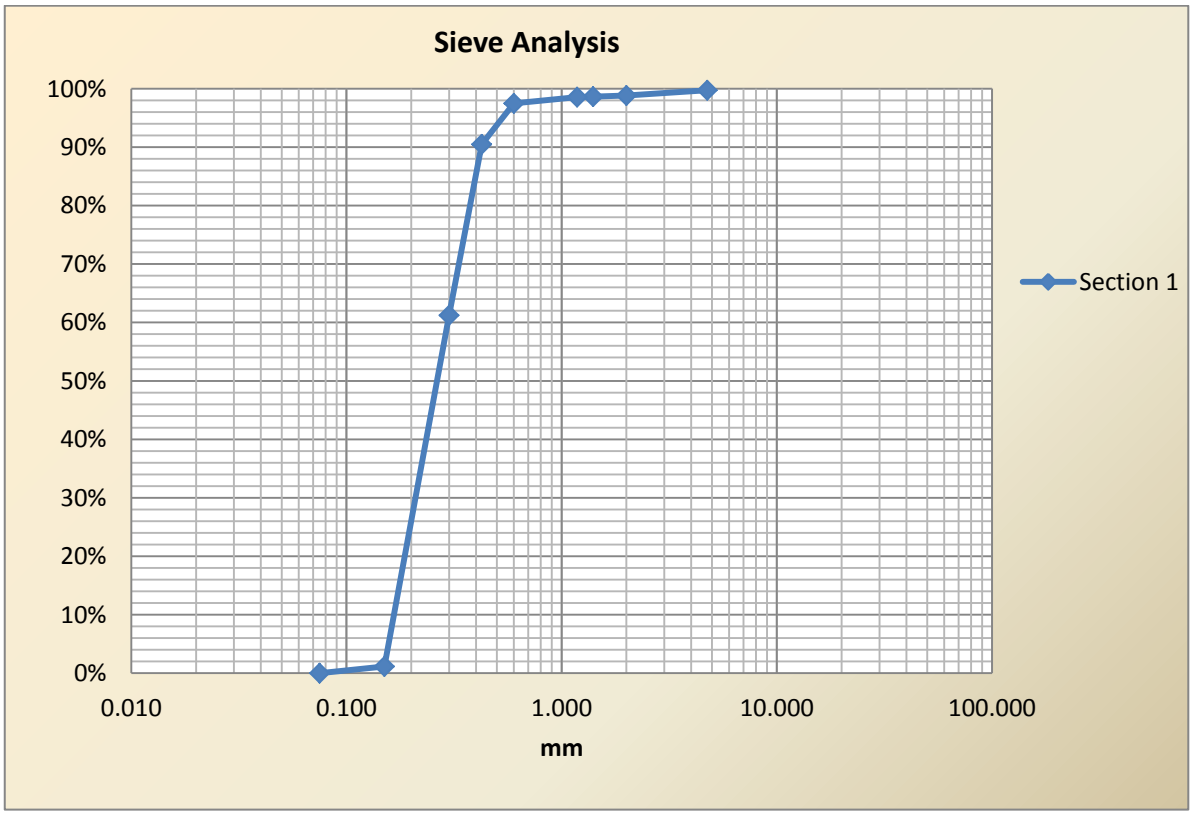

Figure F1-1: Sieve Analysis of Section 1 – South Side Shore

Table F1-3: Sieve Analysis of Section 2 – South Side Middle of Pier

Sieve (mm)	Retained (g)	Total (g)	Cumulative (g)	Retained (%)	Passing (%)
4.750	0.0	0.0	0.0	0.00%	100.00%
2.000	1.7	1.7	1.7	0.33%	99.67%
1.400	0.7	0.7	2.4	0.46%	99.54%
1.180	0.2	0.2	2.6	0.50%	99.50%
0.600	2.6	2.6	5.2	1.00%	99.00%
0.425	15.4	15.4	20.6	3.95%	96.05%
0.300	91.9	91.9	112.5	21.55%	78.45%
0.150	394.5	394.5	507	97.11%	2.89%
0.075	14.8	14.8	521.8	99.94%	0.06%
pan	0.3	0.3	522.1	100.00%	0.00%
	Total	522.1			

Table F1-4: Summary of Sieve Analysis Section 2 – South Side Middle of Pier

D10	D30	D50	D60	D90	Cu	Cc	Grade
0.160	0.195	0.240	0.260	0.380	1.625	0.914	SP

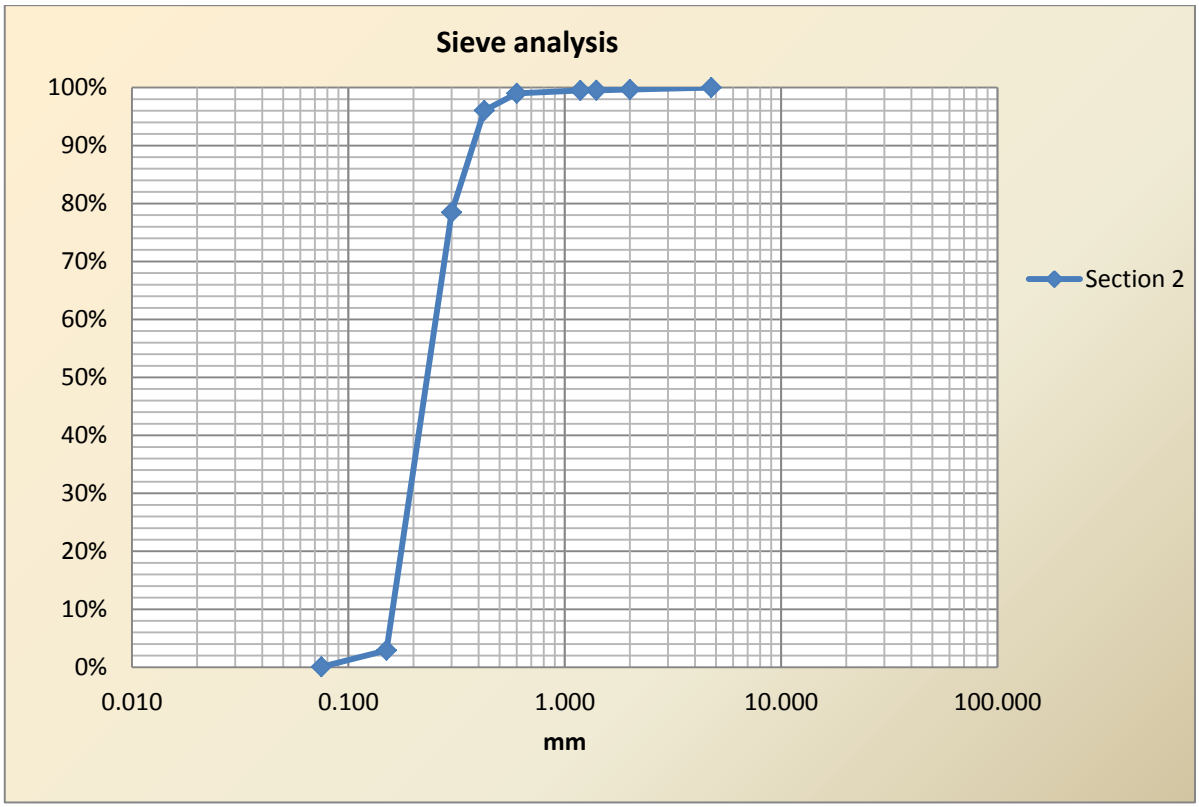

Figure F1-2: Sieve Analysis of Section 2 – South Side Middle of Pier

Table F1-5: Sieve Analysis of Section 3 – South Side ¾ of Pier

Sieve (mm)	Retained (g)	Total (g)	Cumulative (g)	Retained (%)	Passing (%)
4.750	0.1	0.1	0.1	0.02%	99.98%
2.000	1.5	1.5	1.6	0.30%	99.70%
1.400	2	2	3.6	0.68%	99.32%
1.180	0.9	0.9	4.5	0.85%	99.15%
0.600	9	9	13.5	2.56%	97.44%
0.425	33.7	33.7	47.2	8.95%	91.05%
0.300	162.4	162.4	209.6	39.76%	60.24%
0.150	307	307	516.6	98.01%	1.99%
0.075	10.3	10.3	526.9	99.96%	0.04%
pan	0.2	0.2	527.1	100.00%	0.00%
	Total	527.1			

Table F1-6: Summary of Sieve Analysis Section 3 – South Side ¾ of Pier

D10	D30	D50	D60	D90	Cu	Cc	Grade
0.160	0.210	0.270	0.300	0.420	1.875	0.919	SP

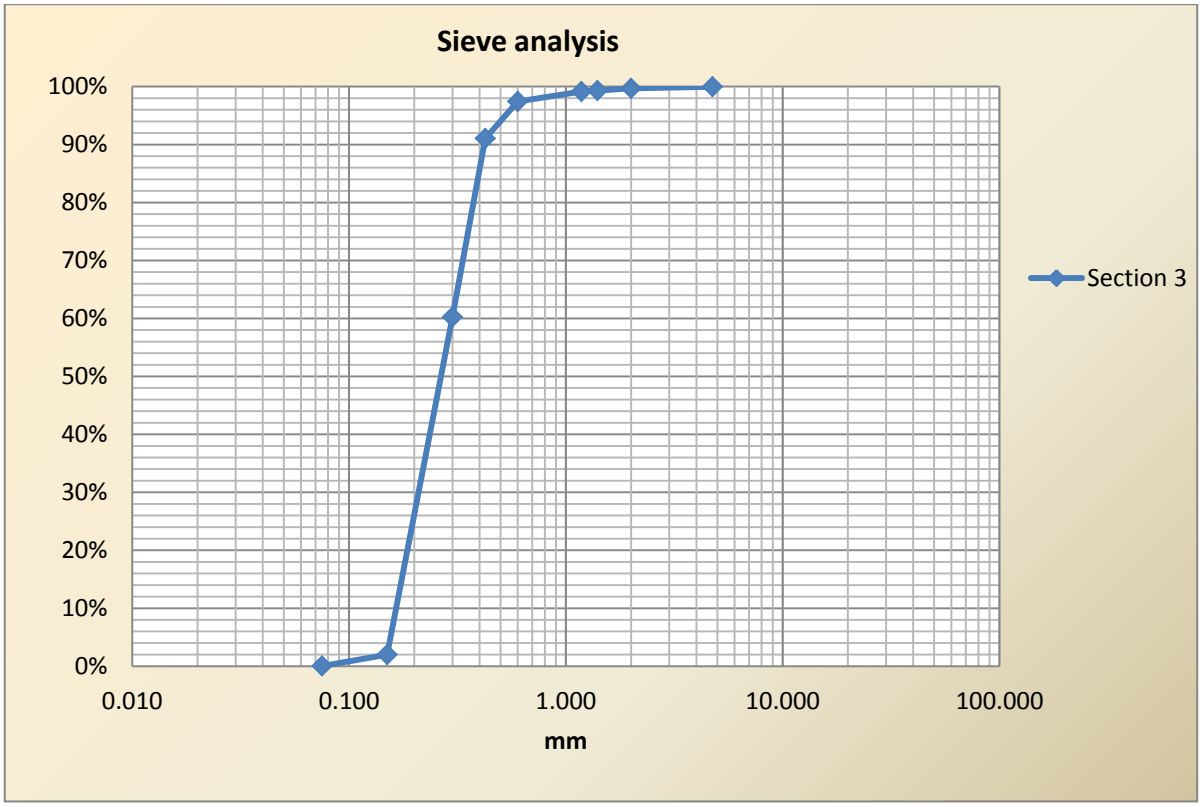

Figure F1-3: Sieve Analysis of Section 3 – South Side ¾ of Pier

Table F1-7: Sieve Analysis of Section 4 – North Side Shore

Sieve (mm)	Retained (g)	Total (g)	Cumulative (g)	Retained (%)	Passing (%)
4.750	0.0	0.0	0.0	0.00%	100.00%
2.000	3.3	3.3	3.3	0.61%	99.39%
1.400	5.5	5.5	8.8	1.62%	98.38%
1.180	1.7	1.7	10.5	1.94%	98.06%
0.600	6.6	6.6	17.1	3.15%	96.85%
0.425	12.9	12.9	30.0	5.53%	94.47%
0.300	125.4	125.4	155.4	28.64%	71.36%
0.150	379.6	379.6	535.0	98.60%	1.40%
0.075	7.4	7.4	542.4	99.96%	0.04%
pan	0.2	0.2	542.6	100.00%	0.00%
	Total	542.6			

Table F1-8: Summary of Sieve Analysis Section 4 – North Side Shore

D10	D30	D50	D60	D90	Cu	Cc	Grade
0.160	0.200	0.240	0.270	0.400	1.688	0.926	SP

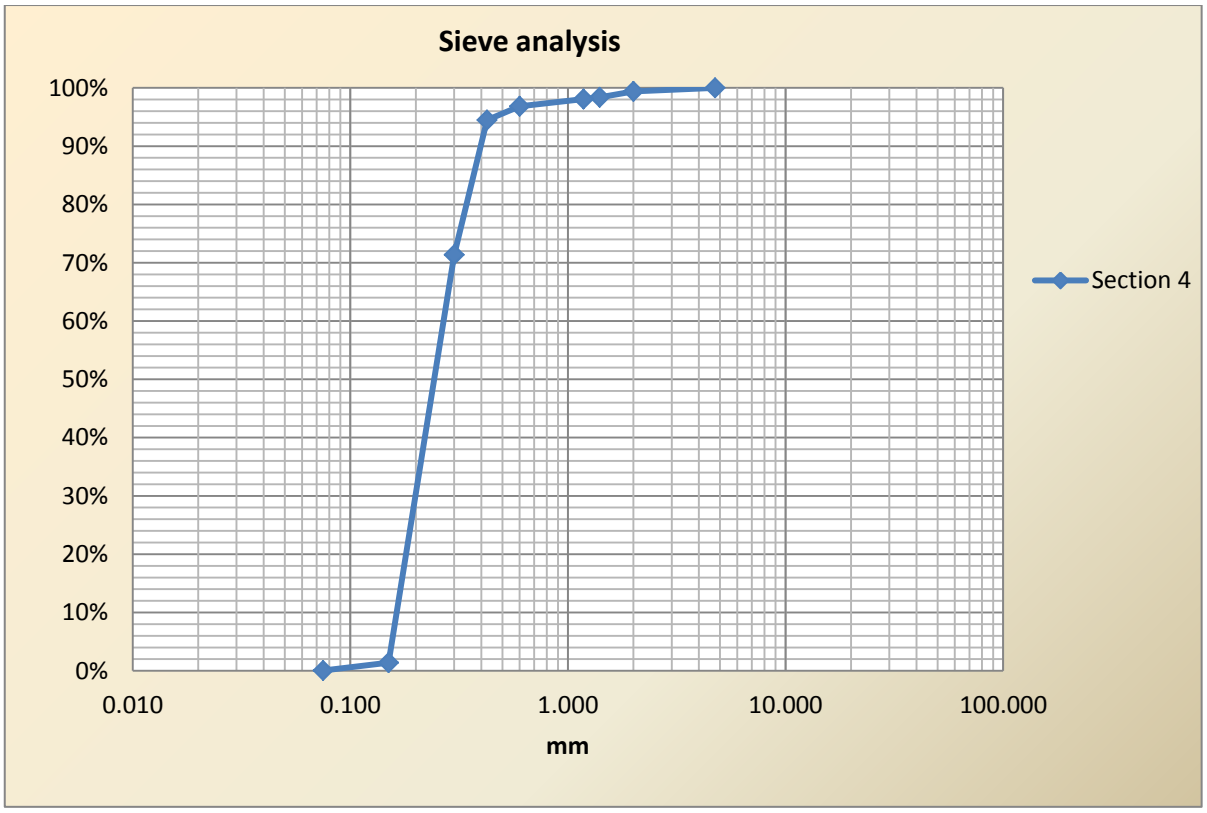

Figure F1-4: Sieve Analysis of Section 4 – North Side Shore

Table F1-9: Sieve Analysis of Section 5 – North Side Middle of Pier

Sieve (mm)	Retained (g)	Total (g)	Cumulative (g)	Retained (%)	Passing (%)
4.750	0.0	0.0	0.0	0.00%	100.00%
2.000	1.2	1.2	1.2	0.22%	99.78%
1.400	3.4	3.4	4.6	0.86%	99.14%
1.180	1.4	1.4	6.0	1.12%	98.88%
0.600	12.0	12.0	18.0	3.35%	96.65%
0.425	30.6	30.6	48.6	9.05%	90.95%
0.300	129.1	129.1	177.7	33.09%	66.91%
0.150	353.6	353.6	531.3	98.92%	1.08%
0.075	5.5	5.5	536.8	99.94%	0.06%
pan	0.3	0.3	537.1	100.00%	0.00%
	Total	537.1			

Table F1-10: Summary of Sieve Analysis Section 5 – North Side Middle of Pier

D10	D30	D50	D60	D90	Cu	Cc	Grade
0.160	0.210	0.250	0.280	0.420	1.750	0.984	SP

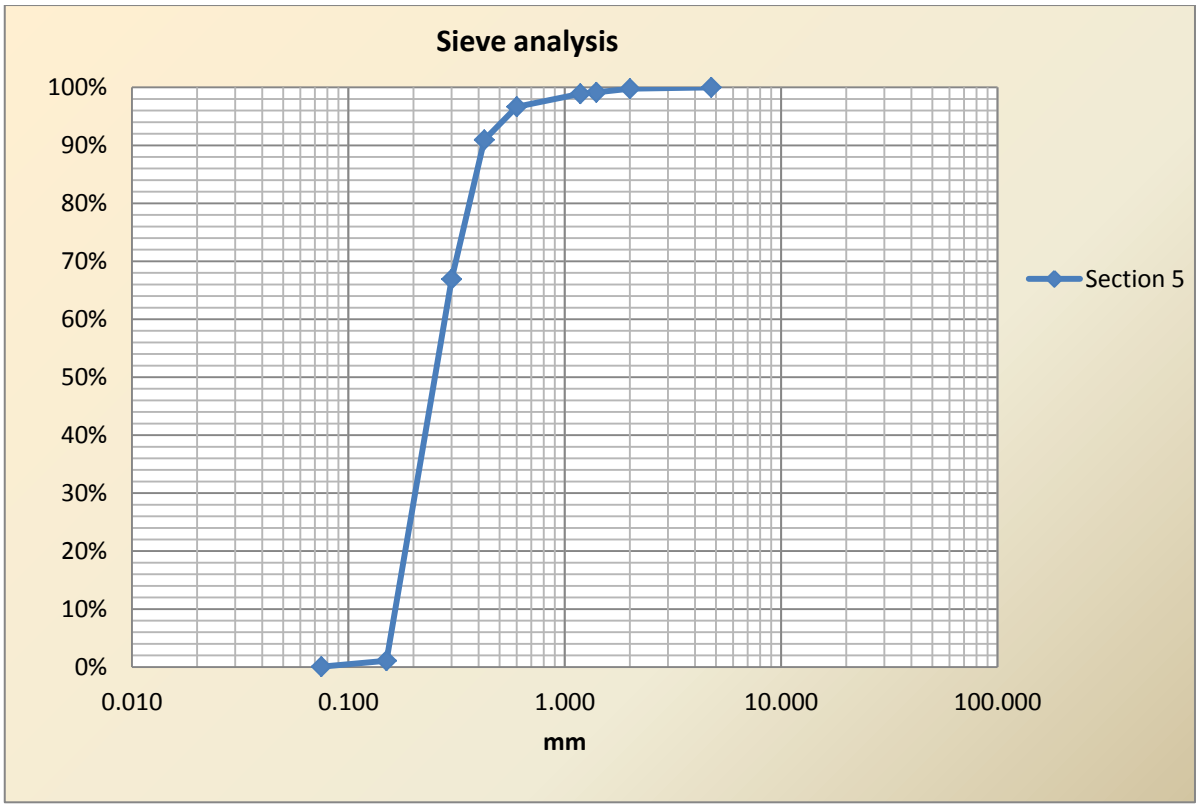

Figure F1-5: Sieve Analysis of Section 5 – North Side Middle of Pier

Table F1-11: Sieve Analysis of Section 6 – North Side ¾ of Pier

Sieve (mm)	Retained (g)	Total (g)	Cumulative (g)	Retained (%)	Passing (%)
4.750	0.5	0.5	0.5	0.09%	99.91%
2.000	3.0	3.0	3.5	0.64%	99.36%
1.400	8.9	8.9	12.4	2.27%	97.73%
1.180	6.0	6.0	18.4	3.37%	96.63%
0.600	52.6	52.6	71.0	13.01%	86.99%
0.425	65.0	65.0	136.0	24.93%	75.07%
0.300	135.9	135.9	271.9	49.84%	50.16%
0.150	266.8	266.8	538.7	98.74%	1.26%
0.075	6.7	6.7	545.4	99.96%	0.04%
pan	0.2	0.2	545.6	100.00%	0.00%
	Total	545.6			

Table F1-12: Summary of Sieve Analysis Section 6 – North Side ¾ of Pier

D10	D30	D50	D60	D90	Cu	Cc	Grade
0.170	0.230	0.300	0.340	0.750	2.0	0.915	SP

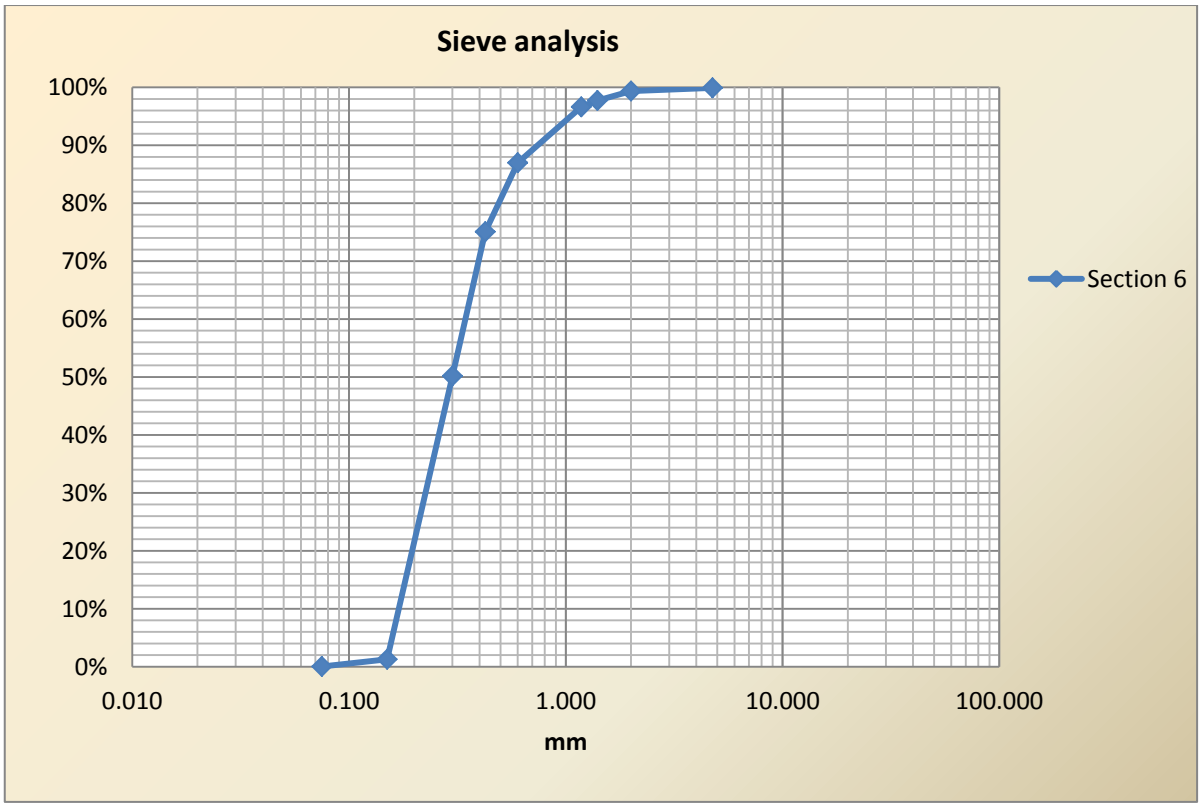

Figure F1-6: Sieve Analysis of Section 6 – North Side ¾ of Pier

Table F1-13: Sieve Analysis of Section 7 – Tip of the Pier

Sieve (mm)	Retained (g)	Total (g)	Cumulative (g)	Retained (%)	Passing (%)
4.750	8.8	8.8	8.8	1.65%	98.35%
2.000	9.0	9.0	17.8	3.34%	96.66%
1.400	16.6	16.6	34.4	6.45%	93.55%
1.180	16.0	16.0	50.4	9.45%	90.55%
0.600	162.6	162.6	213.0	39.94%	60.06%
0.425	119.1	119.1	332.1	62.27%	37.73%
0.300	124.9	124.9	457.0	85.69%	14.31%
0.150	74.9	74.9	531.9	99.74%	0.26%
0.075	1.3	1.3	533.2	99.98%	0.02%
pan	0.1	0.1	533.3	100.00%	0.00%
	Total	533.3			

Table F1-14: Summary of Sieve Analysis Section 7 – Tip of the Pier

D10	D30	D50	D60	D90	Cu	Cc	Grade
0.240	0.380	0.500	0.600	1.150	2.5	1.0	SP

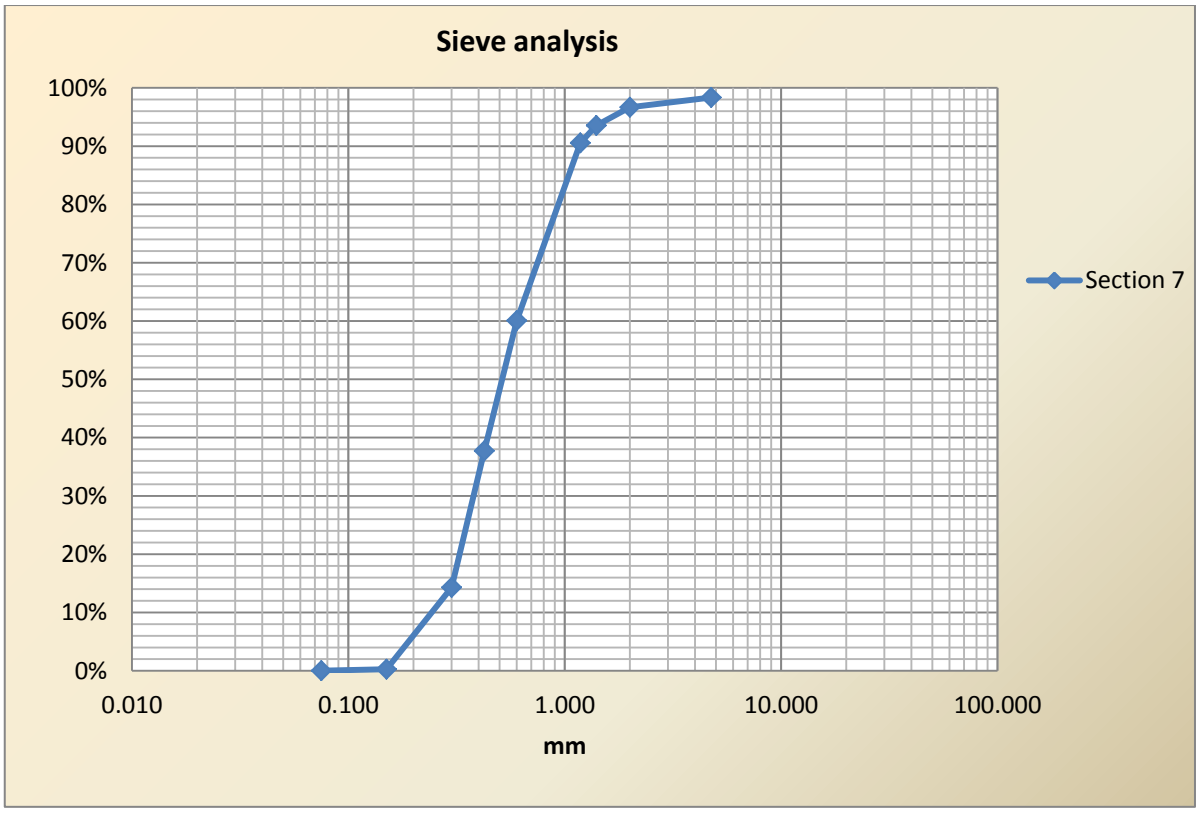

Figure F1-7: Sieve Analysis of Section 7 – Tip of the Pier

C_u and C_c were calculated, in accordance with ASTM D 2487 and AS1726-1993; Unified soil classification system, as follows:

$$C_u = D_{60}/D_{10} \quad \text{(F1-1)}$$

$$C_c = (D_{30})^2/(D_{10} \text{ x } D_{60}) \quad \text{(F1-2)}$$

Unified soil classification:

- The S-shape on the semi-logarithmic graphs denotes a uniform soil
- Percentage majority sand (0.075mm – 2.36mm), "S".
- If $C_u > 4$ and $1 <= C_c <= 3$ then it is a well graded soil "W" else "P".

F2. Sediment Transport Modelling

F2.1 Depth Envelopes

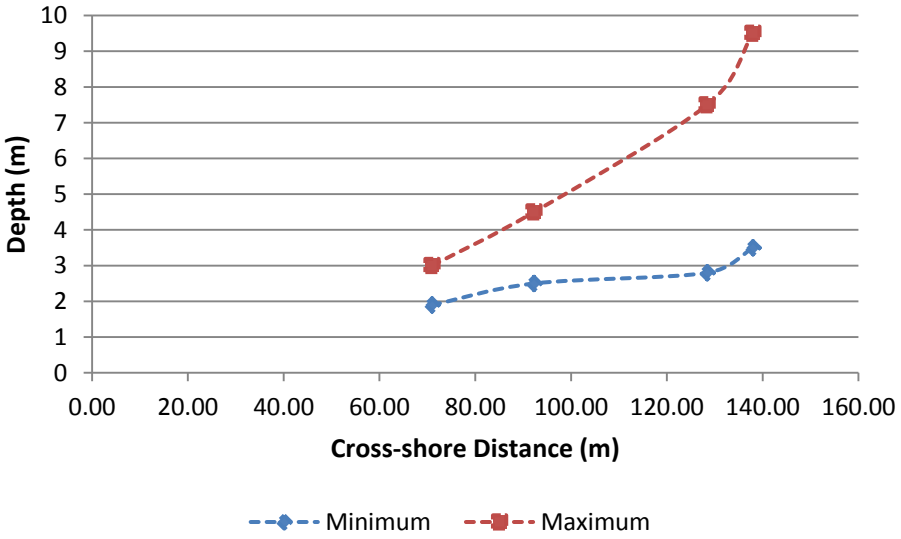

Figure F2-1: Depth envelope of current meters, 10 11 12 & 16 on the North side of the Bay of Plenty Pier. Points are joined to lines for clarity.

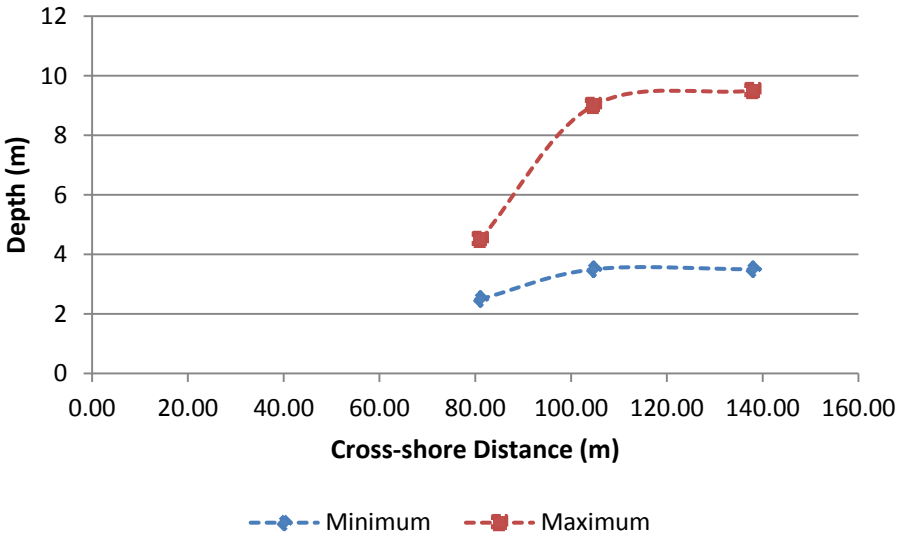

Figure F2-2: Depth envelope of current meters, 14 15 & 16, on the South side of the Bay of Plenty Pier. Points are joined to lines for clarity.

Section F2.2, F2.3 and F2.4 comprise of the equations and flow charts required in calculating the threshold velocities of the sediment grain sizes and the approximated bedload transport for the three separate conditions; Sediment transport due to currents, sediment transport due to waves and sediment transport due to the combination of waves and currents. These sections require the results from the sediment grain analysis and the results from the current meter field test.

The following should be emphasised: The flow models in section F2.2, F2.3 and F2.4 detail what equations were used and in what order. The flow models were created by compiling research on sediment transport and were set up on Microsoft Excel to shorten calculation time.

F2.2 Sediment Transport – Currents

(This section follows in accordance with figure F2.3 & F2.4 flow charts)

Bed shear stress solving:

Nikuradse roughness, k_s, is related to the grain size

$$k_s = 2.5D_{50} \quad \text{(F2-1)}$$

The bed roughness length, z_0, solved initially for rough turbulent flow

$$z_0 = k_s/30 \quad \text{(F2-2)}$$

In the presence of bedforms and tidal flows, the skin friction bed shear stress is a function of the bed roughness solely as seen from the drag coefficient, $C_{D.}$

$$C_D = \left[\frac{0.4}{1+ln\left(\frac{z_0}{h}\right)}\right]^2 \quad \text{(F2-3)}$$

The standard equation relating the bed shear stress, τ_0, to the depth average velocity ($\bar{\upsilon}$) is given by:

$$\tau_0 = \tau_{cs} = \rho_w C_D \bar{U}^2 \quad \text{(F2-4)}$$

The density of water, ρ_w, was taken as 1030 kg/m^3. Equation F2-4 can be used for all current flows, and for skin friction shear stress (τ_{cs}) or total bed shear stress. An additional parameter of importance, known as the shear velocity (u_x), and it is related to τ_0 thusly;

$$u_* = \sqrt{\frac{\tau_0}{\rho}} \quad \text{(F2-5)}$$

To determine the validity of the above z_0, $C_{D,}$ τ_0 and u_x, the original Shields curve made use of a Reynolds number. The Reynolds number must be calculated

$$Re = \frac{u_* k_s}{\nu} \quad \text{(F2-6)}$$

ν is the kinematic viscosity given by

$$\nu = \frac{\mu}{p_w} \qquad \text{(F2-7)}$$

Where μ is the dynamic viscosity of water taken to be, 1.07×10^{-3} Ns/m^2.

There are three flow conditions to consider dependent on the Re

- Rough turbulent, Re > 70
- Transitional Turbulent 5 <= Re <= 70
- Smooth Flow Re < 5

Initially when solving, the flow condition is assumed as rough turbulent, this is to yield z_0, $C_{D,}$ τ_0 and u_x values. Once the flow condition is determined via the Re value, the true z_0, $C_{D,}$ τ_0 and u_x values are solved iteratively as the z_0 equations differ dependent on flow condition.

$$z_0 = \frac{\nu}{9u_*} \qquad [\text{Re} < 5\ ] \qquad \text{(F2-8)}$$

$$z_0 = \frac{k_s}{30} + \frac{\nu}{9u_*} \qquad [5 <= \text{Re} <= 70] \qquad \text{(F2-9)}$$

The accuracy of iteration was carried out by use of a fluctuation error, by dividing the new iteration values by the previous iteration values, till the error reaches zero to two decimal places; Substituting z_0, $C_{D,}$ τ_0 and u_x values as x.

$$\sum_1^n \left(\frac{x_{n-1}}{x_n}\right) \leq 0.00 \qquad \text{(F2-10)}$$

Current threshold velocity solving:

To determine the current threshold velocity or critical velocity, there are two general methods both of which are acceptable to use;

1. The van Rijn (1984) method which is a function of the D_{50} and D_{90} grain sample sizes.
2. The Soulsby (1997) method which is a function of the dimensionless particle size parameter (D^*) and applies to non-cohesive sediment.

Both methods were implemented to allow for a comparative set of values.

The van Rijn (1984) method;

$$\overline{U}_{cr} = 0.19(d_{50})^{0.1} log_{10}(\frac{4h}{d_{90}}) \text{ ,} \quad \text{(F2-11)}$$

for $100 \leq\ d_{50}\ \leq 500\ \mu m$

$$\overline{U}_{cr} = 8.5(d_{50})^{0.6} log_{10}(\frac{4h}{d_{90}}) \text{ ,} \quad \text{(F2-12)}$$

for $500 \leq\ d_{50}\ \leq 2000\ \mu m$

The D_{50} determines which of the equations (equation F2-11 or F2-12) to use for the van Rijn (1984) method.

The Soulsby (1997) method;

$$\overline{U}_{cr} = 7(\frac{h}{d_{50}})^{\frac{1}{7}}[g(s-1)d_{50}f(D_*)]^{\frac{1}{2}} \text{ ,} \quad \text{(F2-13)}$$

for $D_*\ > 0.1$

where:

$$f(D_*) = \frac{0.30}{1+1.2D_*} + 0.055[1 - \exp(-0.02D_*)] \quad \text{(F2-14)}$$

$$D_* = \left[\frac{g(s-1)}{\nu^2}\right]^{\frac{1}{3}} d_{50} \quad \text{(F2-15)}$$

with

$$s = \frac{\rho_s - \rho_w}{\rho_w} \quad \text{(F2-16)}$$

For the kinematic viscosity (ν) refer to Equation F2-7. With respect to the ratio of densities of grain and water (s), the density of sand (ρ_s) was taken as 2650 kg/m^3.

Current bedload transport solving:

Prior to solving for the current bedload transport, two main factors are required;

- The shields critical value (θ_{cr})
- The shields value (θ_s) also known as the entrainment function

A modified version of θ_{cr} was used, following the work of Soulsby and Whitehouse (1997) which is a more explicit form of Shields (1936) work, it is the f(D_*) as written above, equation E2-14;

$$\theta_{cr} = \frac{0.30}{1+1.2D_*} + 0.055[1 - \exp(-0.02D_*)] \quad \text{(F2-14)}$$

For θ_s, τ_0 is required from the bed shear stress solving (Reeve, Chadwick and Fleming, 2004c);

$$\theta_s = \frac{\tau_0}{g(\rho_s - \rho_w)d_{50}} \quad \text{(F2-17)}$$

Please keep in mind that τ_0 in this case refers to the value for the skin friction shear stress, as it is the skin friction shear stress that determines the bedload transport.

Once the θ_{cr} and the θ_s are calculated they can be used to determine the regime of sediment bedload transport, this applies to section F2.1-F2.3, as follows (Reeve, Chadwick and Fleming, 2004c):

- If $\theta_s < \theta_{cr}$, no transport will occur
- If $\theta_{cr} \leq \theta_s \leq 0.8$, then transport occurs with ripples or dunes
- If $\theta_s > 0.8$ then transport will occur as sheet flow, no ripples will be present, flat bed.

There are various bedload transport equations that have been developed, whereby the bedload transport is related to the critical value and the respective entrainment function. A simplified way to denote the relationships is by use of the dimensionless bedload transport rate factor (φ) given below as:

$$\varphi = \frac{q_b}{[g(s-1)(D_{50})^3]^{\frac{1}{2}}} \quad \text{(F2-18)}$$

q_b is equal to the volumetric bedload transport rate per unit width, the SI units are $m^3/m/s$. In 1948 Meyer-Peter and Muller discerned a formula that is still widely used to date:

$$\varphi = 8(\theta_s - \theta_{cr})^{\frac{3}{2}} \quad \text{(F2-19)}$$

Another widely used and far more recent formula is that of Neilsen (1992), given by:

$$\varphi = 12(\theta_s)^{\frac{1}{2}}(\theta_s - \theta_{cr}) \quad \text{(F2-20)}$$

Since both equation F2-19 and F2-20 are commonly used in the field of sediment transport, they were both applied when solving the bedload transport; to give a comparative set of values.

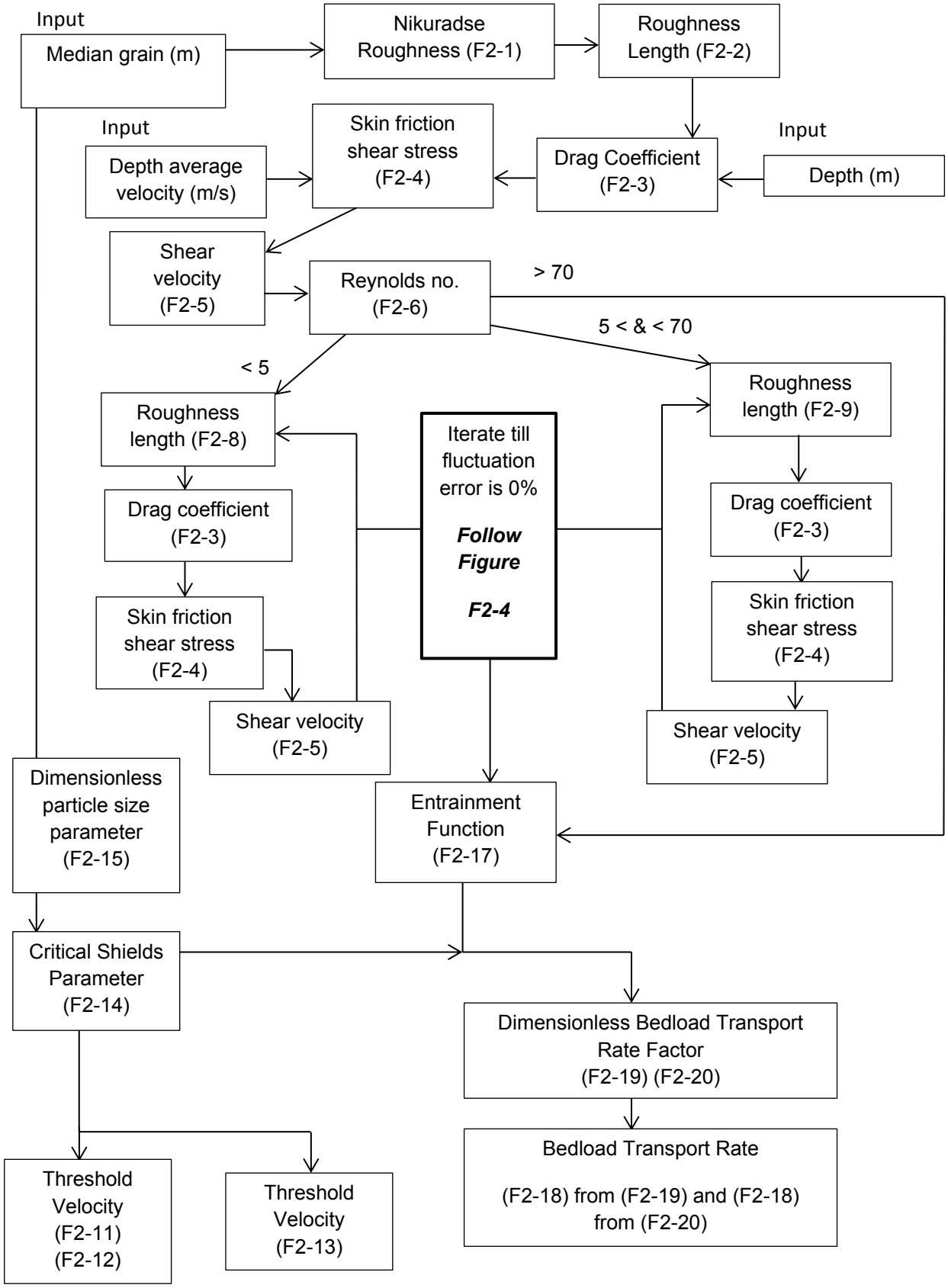

Figure F2-3: Flow chart of determining current bedload transport part 1

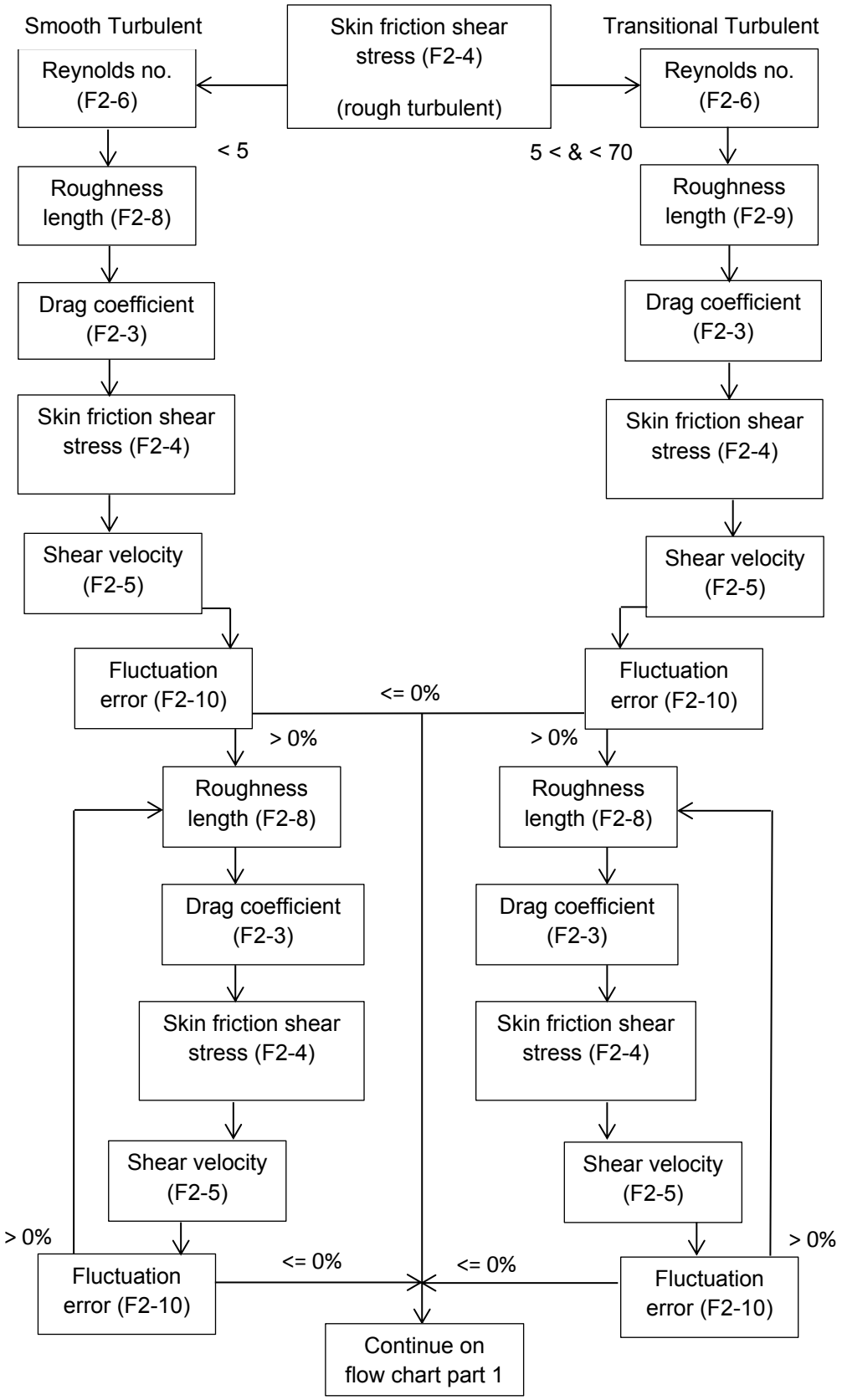

Figure F2-4: Flow chart of determining current bedload transport part 2

F2.3 Sediment Transport – Waves

(This section follows in accordance with Figure F2-5 flow chart)

Bedload transport acts differently for waves than it does for currents. If waves are symmetrical in nature than bedload transport is zero, this is predominately the case when outside the surf zone. However for this study, the area around the groyne is frequently within the surf zone and is characteristically under the influence of steep waves. This wave motion becomes asymmetrical, with longer duration lower velocities in the trough and shorter duration higher velocities in the crest. Under these conditions wave net bedload transport will occur.

Wavelength Solving:

The Port authorities have a wave rider buoy that records direction, wave period and significant wave height. The issue however is that wavelength is not recorded with such devices. Therefore additional solving is required.

The first step is to use linear wave theory to determine the deep water wave characteristics. The key to this is that the period of a wave does not change once the wave has formed. Consequently there will be changes in the speed of the wave which results in changes in its wavelength.

The average wave period, T, from the Port data was determined. From Airy wave equations;

$$c_0 = \frac{gT}{2\pi} \qquad \text{(F2-21)}$$

then

$$L_0 = \frac{2\pi(c_0)^2}{g} \qquad \text{(F2-22)}$$

Where g is the acceleration due to gravity, 9.81 m/s^2. Once the deep water celerity and wavelength have been determined, the wavelengths and celerities at the wave rider buoy (Data site) and the Bay of Plenty Pier (Case study site) can be calculated. The calculation uses a transitional numerical solution of wave dispersion technique described by Goda (2000). It is based on Newton's method, which is given by:

$$x_2 = x_1 - \frac{(x_1 - D\coth x_1)}{(1+D[(\coth x_1)^2-1])} \qquad \text{(F2-23)}$$

where:

$$x = \frac{2\pi h}{L} \qquad \text{(F2-24)}$$

$$D = \frac{2\pi h}{L_0} \quad \text{(F2-25)}$$

h is the depth, in metres. The wave rider buoy depth is at 30m and the test site depth is respect to the values listed in figures F2-1 and F2-2. The best initial estimate is for

$$x_1 = \begin{cases} D \; for \; D \geq 1 \\ D^{\frac{1}{2}} for \; D < 1 \end{cases}$$

This numerical solution using the Goda (2000) technique provides an error of less than 0.05 per cent after three iterations only. Once the wavelengths have been determined for the data site and the test site, the celerity can be determined using Airy wave theory:

$$c = \frac{L}{T} \quad \text{(F2-26)}$$

Threshold bottom orbital velocity solving:

In comparison to the two standard methods of solving current threshold velocity, with regards to waves, there is one preferred method; from the equations of Komar and Miller (1974). It is similar to van Rijn (1984) method in the respect that it is solved as a function of the median grain, it is however also a function of the wave period, *T,* as given;

$$U_{wcr} = [0.118g(s-1)]^{\frac{2}{3}}(d_{50})^{\frac{1}{3}}T^{\frac{1}{3}} \quad \text{(F2-27)}$$

$for \; d_{50} \leq 0.5mm$

$$U_{wcr} = [1.09g(s-1)]^{\frac{4}{7}}(d_{50})^{\frac{3}{7}}T^{\frac{1}{7}} \quad \text{(F2-28)}$$

$for \; d_{50} > 0.5mm$

Where s is the ratio of densities of grain and water as in equation F2-16.

A more roundabout way would be to solve the threshold bottom orbital velocity from θ_{cr} using the critical wave bed shear stress, equation F2-14 and F2-17.

Orbital wave velocity solving:

The first thing required is to determine the non-dimensional water zone; deep water, transitional water, shallow water. Waves act differently depending on the zone they are in. The zones are determined by the ratio of water depth, h, over wavelength, L, (Reeve, Chadwick and Fleming, 2004a);

$\frac{h}{L} \geq 0.5$ Deep water

$0.5 > \frac{h}{L} > 0.04$ Transitional water

$\frac{h}{L} \leq 0.04$ Shallow water

The wave height (H) at the test site is required to determine the orbital velocity; however this requires several steps, starting with the group celerities. The equations used in order are as follows;

Deep water group wave velocity;

$$c_{g0} = \frac{c_0}{2} \quad \text{(F2-29)}$$

Transitional water group wave velocity;

$$c_g = \left(\frac{c}{2}\right)\left[1 + \left(\frac{2kh}{\sinh 2kh}\right)\right] \quad \text{(F2-30)}$$

where:

$$k = \frac{2\pi}{L} \quad \text{(F2-31)}$$

k is the wave number, the unit is rad/m. By applying the concept of a wave crest traveling parallel to the seabed contours, prior to refraction and making the assumption that wave energy is transmitted shoreward without loss due to turbulence or bed friction, this gives:

$$\frac{P}{P_0} = 1 = \frac{Ec_g}{E_0 c_{g0}}$$

where P is wave power, now substituting in the energy (E) per unit area of the ocean

$$E = \frac{\rho g H^2}{8}$$

then

$$\frac{H}{H_0} = \left(\frac{c_{g0}}{c_g}\right)^{\frac{1}{2}} \quad \text{(F2-32)}$$

After calculating the wave heights, the orbital wave velocities can be calculated. As given by:

$$U_w = \frac{a\omega}{\sinh kh} \quad \text{(F2-33)}$$

where:

$$a = \frac{H}{2} \quad \text{(F2-34)}$$

$$\omega = \frac{2\pi}{T} \quad \text{(F2-35)}$$

a is the amplitude, units m, and ω is the radian frequency of the wave, units rad/s.

Wave bedload transport solving:

To determine the wave bedload transport, it is important to first determine the wave skin friction shear stress (τ_{ws}) equation F2-36, given by:

$$\tau_{ws} = \frac{1}{2}\rho_w f_w {U_w}^2 \quad \text{(F2-36)}$$

To solve τ_{ws} requires a wave friction factor (f_w), there are two possible methods for f_w both of which are acceptable to use;

1. The Myrhaug (1989) equation; is an iterative solution that is valid for smooth, transitional and rough turbulent solving. Solved as a function of the roughness coefficient (r), the Reynolds wave number (R_w) and the wave friction factor (f_w).
2. The Soulsby (1997) method; which is an improvement on previous work, solved as a function of the roughness length (z_0) and the semi-orbital excursion (A).

Both methods were implemented to allow for a comparative set of values.

Myrhaug (1989) equation given as:

$$\frac{0.32}{f_w} = \left\{\ln(6.36r\left[f_w\right]^{\frac{1}{2}}) - \ln\left[1 - exp\left(-0.0262\,\frac{R_w[f_w]^{\frac{1}{2}}}{r}\right)\right] + \frac{4.71r}{R_w(f_w)^{\frac{1}{2}}}\right\}^2 + 1.64 \tag{F2-37}$$

where:

$$Re_w = \frac{u_w A}{\nu} \tag{F2-38}$$

$$r = \frac{A}{k_s} \tag{F2-39}$$

and

$$A = \frac{u_w T}{2\pi} \tag{F2-40}$$

The numerical solution using the Myrhaug (1989) equation provides an error of less than 0.08 per cent after three iterations only.

Soulsby (1997) method given as:

$$f_{wr} = 1.39\left(\frac{A}{z_0}\right)^{-0.52} \tag{F2-41}$$

$$f_{ws} = 0.0521(Re_w)^{-0.187} \tag{F2-42}$$

f_{wr} is the rough turbulent wave friction coefficient and f_{ws} is the smooth turbulent wave friction coefficient. The greater of equation F2-41 and F2-42 is selected as the wave friction coefficient. It is not required to solve for the roughness length, use roughness length, z_o, solved from figures F2-3 and F2-4. As for A refer to equation F2-40.

The value for the wave friction coefficient for both methods is then substituted into equation F2-36, to generate two wave skin friction shear stress values, each representing a different method. For the equations that follow both skin friction shear stress values are used.

Refer to and use equations F2-14 – F2-20 to determine critical shields parameter, entrainment function and bedload transport rates for wave bedload transport.

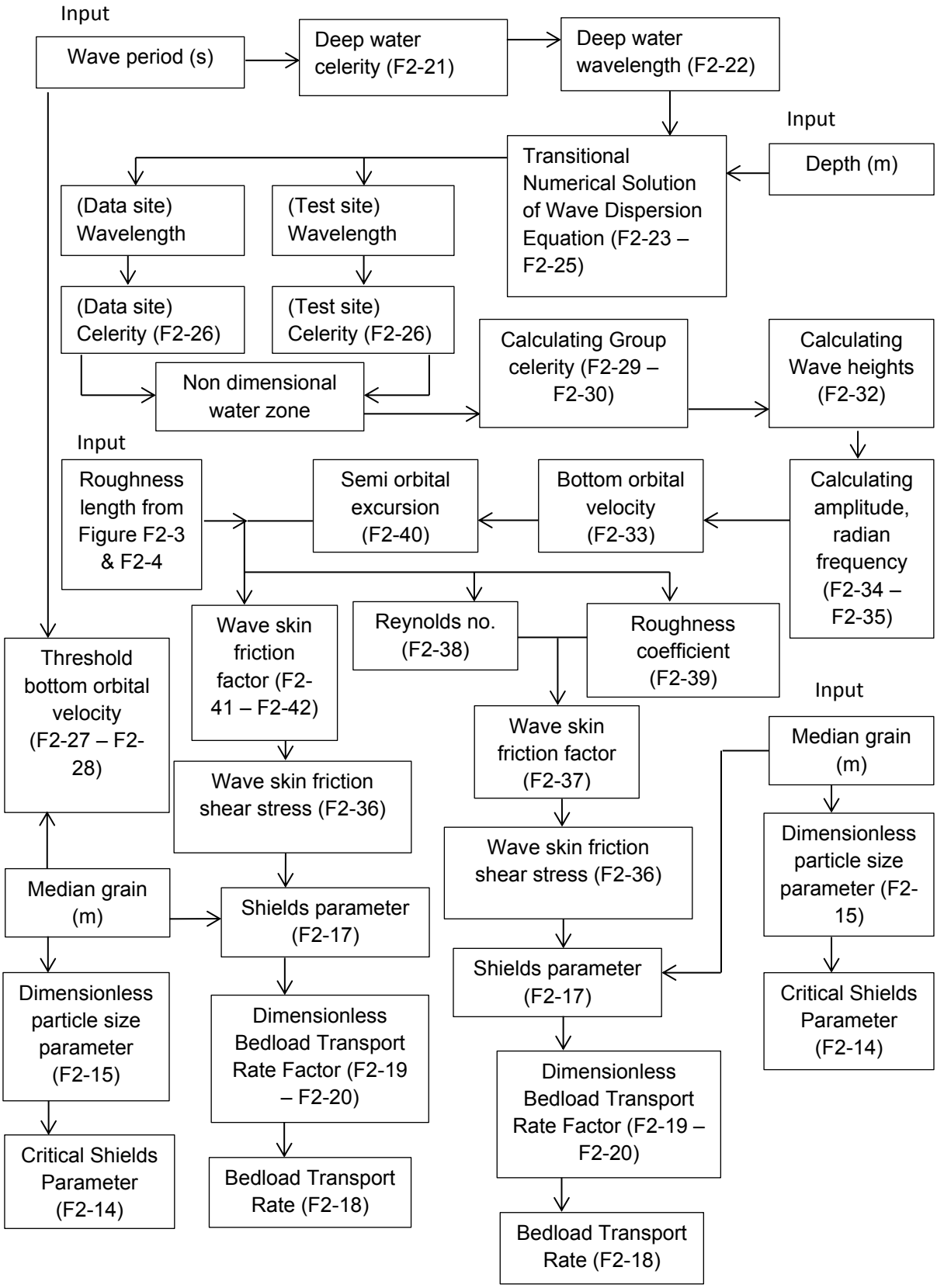

Figure F2-5: Flow chart of determining wave bedload transport

F2.4 Sediment Transport – Combination of Waves & Currents

To calculate bed shear stresses under the action of both waves and currents is far more complex than solving for their individual conditions. When currents and waves co-exist together, they develop a non-linear interaction that takes place between their respective boundary layers. When calculating the resultant bed shear stress it cannot be simply solved by means of vector addition of the two separate bed shear stresses. Through comprehensive analysis of previous theoretical models and data, algebraic expressions were derived (Soulsby, 1995).

The initial solving for Soulsby (1995) algebraic expressions makes use of section F2.1 and F2.2 bed shear stresses, however a report was released by Soulsby and Clarke (2005) documenting a different initial solving with a revised set of algebraic expressions for the resultant bed shear stress. The algebraic expressions in the report were stated to be a better method in fitting to previous models (Soulsby and Clarke, 2005).

Both the algebraic expressions and methods for Soulsby (1995) and Soulsby and Clarke (2005) were applied to this section.

Angle between wave and current directions solving:

One of the key factors in solving for the resultant bed shear stress is the angle of interaction between the wave and current boundary layers; the difference in angle between the propagating wave and the direction of flow. The use of current data is simple as the instruments used had on-board magnetic compasses. The issue however is the propagating waves; the recorded wave directions occurred at the wave buoy which was at a depth of 30 metres. To ascertain the correct direction of wave propagation at the groyne required the use of Snell-Descartes law of refraction:

$$\frac{\sin\alpha}{\sin\alpha_0} = \frac{L}{L_0} \qquad \text{(F2-43)}$$

Wave buoys record the direction waves propagate from but Snell-Descartes law solves using the direction that a wave propagates towards. This requires an angle correction when solving. The end of the groyne and the wave buoy location were determined to be in transitional waters, Snell-Descartes law requires the original medium before refractive deviation. Using the wave buoy recorded direction, the deep water wave direction is determined, then using the deep water wave direction the wave direction at the groyne is determined. For all data, current meters and wave buoy, the nautical bearing was used.

Once the direction of wave propagation is determined, the angle between waves and currents (φ) is calculated.

Combination Bed Shear stress solving, Soulsby & Clarke (2005):

(This section follows in accordance with Figure F2-6 & F2-7 flow chart)

It is important to determine the flow regime as this requires different algebraic expressions due to different turbulent affects occurring on the seabed. For this reason, several checks are required.

1. For $\overline{U}$=0 and U_w=0, there is no flow, therefore mean and maximum shear stress values are given as

   $$\tau_m = \tau_{max} = 0$$

2. For $\overline{U}$>0 and U_w=0, there is current flow only. This then requires the solving of the current Reynolds number (Re_c), given by:

   $$Re_c = \frac{\bar{U}h}{\nu} \quad \text{(F2-44)}$$

   If $Re_c \leq 2000$, then laminar flow is present and the bed shear stress equations are as follows:

   $$\tau_m = \tau_{max} = \frac{3\rho_w \nu \bar{U}}{h} \quad \text{(F2-45)}$$

   If $Re_c > 2000$, then turbulent flow is present and the bed shear stress equations are as follows:

   (rough)

   $$\tau_{mr} = p_w C_{Dr} \overline{U}^2 \quad \text{(F2-46)}$$

   where C_{Dr} is the drag coefficient for rough turbulent flow, equation F2-3.

   (smooth)

   $$\tau_{ms} = p_w C_{Ds} \overline{U}^2 \quad \text{(F2-47)}$$

   Where:

   $$C_{Ds} = 0.0001615\exp[6(Re_c)^{-0.08} \quad \text{(F2-48)}$$

for turbulent flow,

$\tau_m = \tau_{max} = \max(\tau_{mr}, \tau_{ms})$

3. For $\overline{U}$=0 and U_w>0, there is wave flow only. This then requires the solving of the wave Reynolds number (Re_w), given by Equation F2-38.
   If $Re_w \leq 1.5\text{x}10^5$, then laminar flow is present, therefore mean and maximum shear stress values are given as

   $\tau_m = 0$

   $\tau_{max} = \rho_w {Re_w}^{-0.5} {U_w}^2$ (F2-49)

   If $Re_w > 1.5\text{x}10^5$, then turbulent flow is present, therefore mean and maximum shear stress values are given as
   (rough)

   $\tau_{wr} = \frac{1}{2}\rho_w f_{wr} {U_w}^2$ (F2-50)

   where f_{wr} is the friction coefficient for rough turbulent flow, equation F2-41.

   (smooth)

   $\tau_{ws} = \frac{1}{2}\rho_w f_{ws} {U_w}^2$ (F2-51)

   where f_{ws} is the friction coefficient for smooth turbulent flow, equation F2-42.

   for turbulent flow,

   $\tau_m = 0$

   $\tau_{max} = \max(\tau_{wr}, \tau_{ws})$

4. For $\overline{U} > 0$ and $U_w > 0$, then combined wave and current flow is present. Determine the critical current Reynolds number, given by:

   $Re_{c,cr} = 2000 + (5.92 \times 10^5 \times Re_w)^{0.35}$ (F2-52)

   $Re_{w,cr} = 1.5 \times 10^5$ (F2-53)

   If $Re_c \leq Re_{c,cr}$ and $Re_w \leq Re_{w,cr}$, then laminar flow is present then τ_m is given by equation E2-45. T_w is given by:

$$\tau_w = \rho {Re_w}^{-0.5} {U_w}^2 \quad \text{(F2-54)}$$

and

$$\tau_{max} = [(\tau_m + \tau_w|\cos\varphi|)^2 + (\tau_w|\sin\varphi|)^2]^{\frac{1}{2}} \quad \text{(F2-55)}$$

If $Re_c > Re_{c,cr}$ or $Re_w > Re_{w,cr}$, then turbulent flow is present.

Calculating $\tau_{m,r}$ and $\tau_{max,r}$ as follows:

$$T_1 = \frac{\delta}{z_0} = max\left\{a_r \left(\frac{f_{wr}}{2}\right)^{\frac{1}{2}} \left(\frac{A}{z_0}\right), 12\right\} \quad \text{(F2-56)}$$

where $a_r = 0.24$. f_{wr} from wquation F2-41. z_0 from Equation F2-2. A from equation F2-40.

$$T_2 = \frac{h}{\delta} = \frac{h}{T_1 z_0} \quad \text{(F2-57)}$$

$$T_3 = \frac{u_{*e}}{\bar{U}} = \left[{C_{Dr}}^2 + \left(\frac{f_{wr}}{2}\right)^2 \left(\frac{U_w}{\bar{U}}\right)^4\right]^{\frac{1}{4}} \quad \text{(F2-58)}$$

where C_{Dr} is from Equation F2-3.

$$A_1 = \frac{T_3[ln(T_2)-1]}{2ln(T_1)} \quad \text{(F2-59)}$$

$$A_2 = \frac{0.40T_3}{ln(T_1)} \quad \text{(F2-60)}$$

$$C_{Dm} = \left[\left({A_1}^2 + A_2\right)^{\frac{1}{2}} - A_1\right]^2 \quad \text{(F2-61)}$$

$$C_{Dmax} = \left[\left(C_{Dm} + T_3 \frac{U_w}{\bar{U}} \left(\frac{f_{wr}}{2}\right)^{\frac{1}{2}} |\cos\varphi|\right)^2 + \left(T_3 \frac{U_w}{\bar{U}} \left(\frac{f_{wr}}{2}\right)^{\frac{1}{2}} |\sin\varphi|\right)^2\right]^{\frac{1}{2}} \quad \text{(F2-62)}$$

φ is the angle between waves and currents.

$$\tau_m = \rho_w C_{Dm} \bar{U}^2 \quad \text{(F2-63)}$$

$$\tau_{max} = \rho_w C_{Dmax} \bar{U}^2 \quad \text{(F2-64)}$$

Calculating $\tau_{m,s}$ and $\tau_{max,s}$ as follows:

$$T_1 = 9a_s Re_w \left(\frac{f_{ws}}{2}\right)^{\frac{1}{2}} \left[C_{Ds}^2 \left(\frac{\bar{U}}{U_w}\right)^4 + \left(\frac{f_{ws}}{2}\right)^2\right]^{\frac{1}{4}} \quad \text{(F2-65)}$$

where $a_s = 0.24$. f_{ws} from Equation F2-42. C_{Ds} from equation F2-46.

$$T_2 = \left(\frac{Re_c}{Re_w}\right)\left(\frac{U_w}{\bar{U}}\right)\frac{1}{a_s}\left(\frac{2}{f_{ws}}\right)^{\frac{1}{2}} \quad \text{(F2-66)}$$

$$T_3 = \left[C_{Ds}^2 + \left(\frac{f_{ws}}{2}\right)^2 \left(\frac{U_w}{\bar{U}}\right)^4\right]^{\frac{1}{4}} \quad \text{(F2-67)}$$

Calculate A_1 and A_2 from equation F2-59 and F2-60, C_{Dm} from equation F2-61, C_{Dmax} from equation F2-62 except replace all f_{wr} with f_{ws}. Then calculate $\tau_{m,s}$ and $\tau_{max,s}$ from equation F2-63 and F2-64.

If $\tau_{max,r} \leq \tau_{max,s}$, then flow is smooth turbulent and $\tau_m = \tau_{m,s}$, $\tau_{max} = \tau_{max,s}$ else, if $\tau_{max,r} > \tau_{max,s}$, then flow is rough turbulent and $\tau_m = \tau_{m,r}$, $\tau_{max} = \tau_{max,r}$

Combination Bedload transport solving, Soulsby & Clarke (2005):

Refer to and use equations F2-14 to F2-20 to calculate critical shields parameter, entrainment function and bedload transport rates for combination wave and current bedload transport. For the shield/entrainment function (refer to equation F2-17) use the τ_{max} when solving to determine the combination wave and current shield parameter.

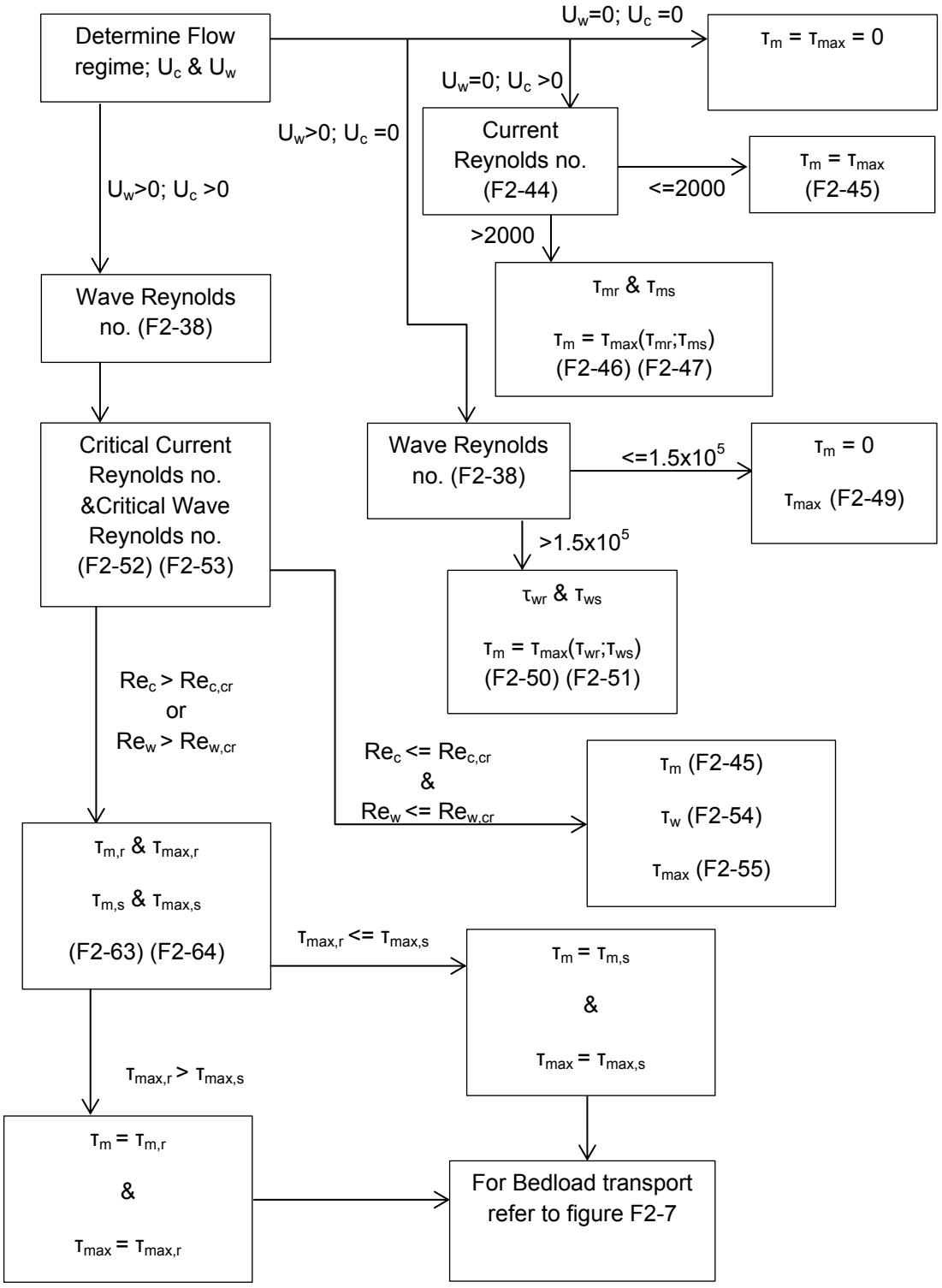

Figure F2-6: Flow chart of determining mean & maximum bed shear stresses for laminar, smooth-turbulent & rough-turbulent wave + current flows

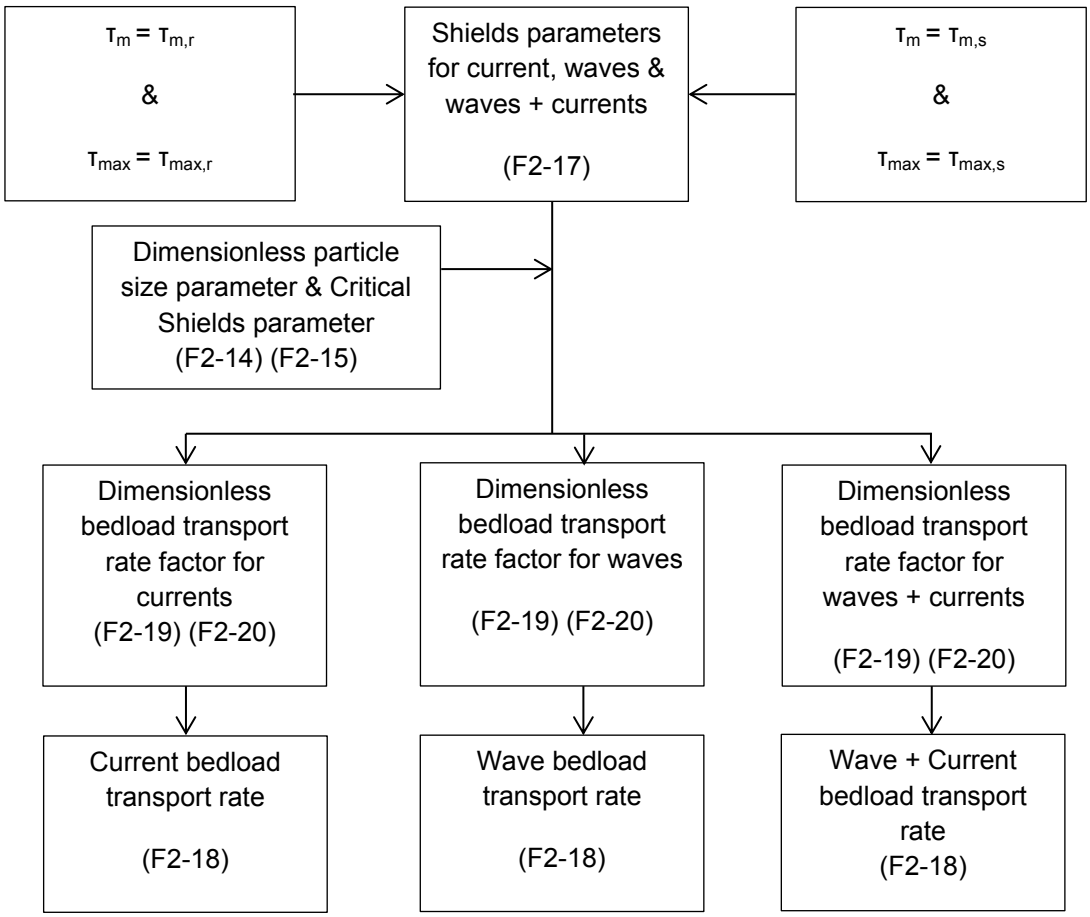

Figure F2-7: Flow chart of determining wave + current bedload transport

Combination Bed Shear stress solving, Soulsby (1995):

The initial solving for Soulsby (1995) algebraic expressions makes use of section F2.1 and F2.2. Follow in accordance with the figure F2-3, F2-4 & F2-5 flow charts up to the current skin friction shear stress (τ_{cs}) and the wave skin friction shear stress (τ_{ws}). Soulsby (1995) algebraic expressions for the mean (τ_m) and maximum (τ_{max}) bed shear stresses are as follows:

$$\tau_m = \tau_{cs}\left[1 + 1.2\left(\frac{\tau_{ws}}{\tau_{cs}+\tau_{ws}}\right)^{3.2}\right] \quad \text{(F2-68)}$$

τ_{max} is given by Equation F2-51 except τ_w is τ_{ws}.

Combination Bedload transport solving, Soulsby (1995):

Refer to and use equations F2-14 to F2-20 to calculate the critical shields parameter, entrainment function and bedload transport rates for combination wave and current bedload transport. For the shield/entrainment function (Equation F2-17) use the τ_{max} when solving to determine the combination wave and current shield parameter.

Table F2-1: Threshold Velocity Data for the South Side of Bay of Plenty Pier

South Side of Bay of Plenty Pier									
Current meter no.	Cross-shore Distance (m)	Shallow				Deep			
		Depth (m)	uc,cr (Soulsby 1997) (m/s)	uc,cr (van Rijn 1984) (m/s)	uwcr (Komar & Miller 1974) (m/s)	Depth (m)	uc,cr (Soulsby 1997) (m/s)	uc,cr (van Rijn 1984) (m/s)	uwcr (Komar & Miller 1974) (m/s)
14	81.10	2.50	0.33	0.52	0.20	4.50	0.40	0.34	0.20
15	104.70	3.50	0.35	0.49	0.21	9.00	0.40	0.36	0.21
16	138.00	3.50	0.38	0.68	0.26	9.50	0.44	0.52	0.26

Table F2-2: Threshold Velocity Data for the North Side of Bay of Plenty Pier

North Side of Bay of Plenty Pier									
Current meter no.	Cross-shore Distance (m)	Shallow				Deep			
		Depth (m)	uc,cr (Soulsby 1997) (m/s)	uc,cr (van Rijn 1984) (m/s)	uwcr (Komar & Miller 1974) (m/s)	Depth (m)	uc,cr (Soulsby 1997) (m/s)	uc,cr (van Rijn 1984) (m/s)	uwcr (Komar & Miller 1974) (m/s)
11	92.27	2.50	0.34	0.63	0.22	4.50	0.37	0.55	0.22
12	128.42	2.80	0.37	0.71	0.26	7.50	0.43	0.56	0.26
16	138.00	3.50	0.38	0.68	0.26	9.50	0.44	0.52	0.26

Table F2-3: Bed Shear Stress Data for the South Side of Bay of Plenty Pier

South Side of Bay of Plenty Pier										
Current meter no.	Cross-shore Distance (m)	Critical Bed Shear Stress τ_{cr} (N/m^2)	Shallow				Deep			
			Depth (m)	Current Bed Shear Stress τ_c (N/m^2)	Wave Bed Shear Stress τ_w (N/m^2)	Maximum (Combination) Bed Shear Stress τ_{max} (N/m^2)	Depth (m)	Current Bed Shear Stress τ_c (N/m^2)	Wave Bed Shear Stress τ_w (N/m^2)	Maximum (Combination) Bed Shear Stress τ_{max} (N/m^2)
14	81.10	0.17	2.50	0.12	5.05	5.44	4.50	0.10	1.15	1.35
15	104.70	0.17	3.50	0.20	3.67	4.10	9.00	0.17	1.22	1.50
16	138.00	0.25	3.50	0.12	5.05	5.45	9.50	0.10	1.58	1.80

Table F2-4: Bed Shear Stress Data for the North Side of Bay of Plenty Pier

North Side of Bay of Plenty Pier										
Current meter no.	Cross-shore Distance (m)	Critical Bed Shear Stress τ_{cr} (N/m^2)	Shallow				Deep			
			Depth (m)	Current Bed Shear Stress τ_c (N/m^2)	Wave Bed Shear Stress τ_w (N/m^2)	Maximum (Combination) Bed Shear Stress τ_{max} (N/m^2)	Depth (m)	Current Bed Shear Stress τ_c (N/m^2)	Wave Bed Shear Stress τ_w (N/m^2)	Maximum (Combination) Bed Shear Stress τ_{max} (N/m^2)
11	92.27	0.18	2.50	0.07	5.67	5.95	4.50	0.07	2.91	3.10
12	128.42	0.25	2.80	0.03	6.50	6.56	7.50	0.02	2.10	2.13
16	138.00	0.25	3.50	0.12	5.05	5.45	9.50	0.10	1.58	1.80

Table F2-5: Bedload Transport Data for the South Side of Bay of Plenty Pier

South Side of Bay of Plenty Pier							
Current meter no.	Cross-shore Distance (m)	Shallow			Deep		
		Depth (m)	Bedload Transport (Meyer-Peter & Muller 1948) q_{b1} (m^3/m/s)	Bedload Transport (Neilsen 1992) q_{b2} (m^3/m/s)	Depth (m)	Bedload Transport (Meyer-Peter & Muller 1948) q_{b1} (m^3/m/s)	Bedload Transport (Neilsen 1992) q_{b2} (m^3/m/s)
14	81.10	2.50	1.90E-04	2.89E-04	4.50	2.01E-05	3.22E-05
15	104.70	3.50	1.22E-04	1.87E-04	9.00	2.40E-05	3.82E-05
16	138.00	3.50	1.86E-04	2.85E-04	9.50	3.03E-05	4.90E-05

Table F2-6: Bedload Transport Data for the North Side of Bay of Plenty Pier

North Side of Bay of Plenty Pier							
Current meter no.	Cross-shore Distance (m)	Shallow			Deep		
		Depth (m)	Bedload Transport (Meyer-Peter & Muller 1948) q_{b1} (m^3/m/s)	Bedload Transport (Neilsen 1992) q_{b2} (m^3/m/s)	Depth (m)	Bedload Transport (Meyer-Peter & Muller 1948) q_{b1} (m^3/m/s)	Bedload Transport (Neilsen 1992) q_{b2} (m^3/m/s)
11	92.27	2.50	2.17E-04	3.31E-04	4.50	7.82E-05	1.21E-04
12	128.42	2.80	2.49E-04	3.80E-04	7.50	4.06E-05	6.48E-05
16	138.00	3.50	1.86E-04	2.85E-04	9.50	3.03E-05	4.90E-05